Aus dem Bereich der Molekularen Zellbiologie
Theoretische Medizin und Biowissenschaften
der Medizinischen Fakultät
der Universität des Saarlandes, Homburg/Saar

The influence of hypoxia in erythropoiesis and morphology of red blood cells in sickle cell disease and hereditary spherocytosis

Dissertation zur Erlangung des Grades
eines Doktors der Naturwissenschaften
der Medizinischen Fakultät
der UNIVERSITÄT DES SAARLANDES
2020

vorgelegt von: Greta Simionato
geb. am: 18.08.1990 in Varese

Tag der Promotion: 19. Oktober 2020

Dekan: Univ.-Prof. Dr. Michael D. Menger

Berichterstatter: Prof. L. Kaestner

Prof. M. Sester

Prof. H. Eichler

To my family.

Contents

4   Discussion   123

Zusammenfassung

Die Lebensfähigkeit menschlicher Zellen hängt in hohem Maße vom Sauerstoff ab, der von den roten Blutkörperchen transportiert und zur Verfügung gestellt wird. In dieser Arbeit wird untersucht, wie Sauerstoff die Physiologie und Pathophysiologie jener roten Blutkörperchen beeinflusst. Die Arbeit ist in zwei wesentliche Teile gegliedert.

Zunächst werden Ergebnisse einer größeren Studie mit Probanden vorgestellt, die in großer Höhe (3450 m) durchgeführt wurde. In dieser Höhe sorgt der reduzierte Luftdruck für eine Abnahme der Sauerstoffsättigung im Blut und führt so zu einer erhöhten Produktion an roten Blutkörperchen (Erythropoese). Nach der Rückkehr aus großer Höhe fällt die Zahl an roten Blutkörperchen nach kurzer Zeit wieder auf das vorherige Niveau Es ist bislang nicht verstanden, ob die neugebildeten roten Blutzellen dazu abgebaut werden. Der hyptothetische Mechanismus der Neozytolyse (engl. Neocytolisis) geht davon aus, dass ausgerechnet die neu gebildeten, roten Blutzellen als erste wieder abgebaut werden, wenn die Rückkehr auf Meeresniveau erfolgt. Die wissenschaftliche Fragestellung, die im Rahmen dieser Studie beantwortet wurde, ist, ob und in welchem Maß Neocytolyse nach einem 3-wöchigen Aufenthalt in großer Höhe stattfindet. Dazu wurden zunächst Untersuchungen an aller Probanden mittels in-vitro Zellkulturen durchgeführt, um sowohl die Erythropoese als auch (neu entstandende) Retikulozyten zu charakterisieren. Die Ergebnisse zeigen eine beschleunigte Reifung der Vorläuferzellen in Zellkulturen bei niedrigerem Sauerstoffgehalt (3%) verglichen mit normaler Atmosphäre (20%) und eine unerwartet verbesserte Überlebensrate der Retikulozyten. Dies stimmt mit dem Ergebnis der Studie überein, dass nach der Rückkehr von der gewählten Höhe keine Neozytolyse, d.h. kein bevorzugter Abbau von neu gebildeten roten Blutzellen, auftrat, was die Hypothese eines selektiven, vorzeitigen Abbaus von unreifen roten Blutzellen widerlegt. Weiterhin wurde in der Zellkultur unter verringerter Sauerstoffgabe eine erhöhte Zahl bikonkaver Zellen beobachtet, was eine typische Gestalt für einen fortgeschrittenen Reifegrad ist. Diese Beobachtung könnte ein Anhaltspunkt dafür sein, dass der Reifeprozess von roten Blutzellen durch die Reduzierung des atmosphärischen Sauerstoffgehaltes begünstigt werden kann. Im Rahmen dieser Arbeit wurde zusätzlich ein Protokoll zur Isolation der Retikulozyten vom Vollblut der Probanden entwickelt, um die pure Zell-RNA jeweils vor und in großer Höhe zu sequenzieren. Jedoch muss die Ausbeute an RNA weiter optimiert werden, um einen detaillierten Vergleich der Gen-Expressions-Niveaus anstellen zu können.

Der zweite Teil der Arbeit konzentriert sich auf die Untersuchung der Morphologie der roten Blutkörperchen bei zwei Arten von Anämie. Aufgrund der hohen Empfindlichkeit der roten Blutkörperchen

gegenüber Formvariationen, mussten die Proben vor jeder experimentellen Manipulation fixiert werden. Dazu musste ein angemessenes Verfahren entwicklelt werden, das im Rahmen dieser Arbeit vorgestellt wird. Zunächst wird auf die Sichelzellenanämie eingegangen, bei der es unter Desoxygenierung des Hämoglobins zur starken Verformung der roten Blutkörperchen (Sichelzellen) kommt. Dies beinträchtigt sowohl deren Funktion als auch Lebensdauer. Eine quantitative Analyse von Zell-Projektionsbildern aus konfokalen Mikroskopieaufnahmen wurde mit Hilfe eines maßgeschneiderten Computerprogramms im Rahmen einer klinischen Pilotstudie der Phase II zur Therapie der Sichelzellanämie durchgeführt. Es konnte gezeigt werden, dass diese Methode in Kombination mit anderen experimentellen Verfahren ein wirkungsvolles Instrument zur Beurteilung des Zellhydratationszustands von Sichelzellenpatienten ist. Daher kann diese Technik zur Beurteilung der Wirksamkeit von Sichelzellen-Therapien oder zur Beurteilung des Zustands der roten Blutkörperchen eines Patienten verwendet werden. Da die roten Blutkörperchen bei verschiedenen Arten von Anämie auch verschiedene Formvariationen aufweisen, wurde eine weitere Blutkrankheit, die hereditäre Sphärozytose, untersucht. In diesem Fall lag der Schwerpunkt auf der automatisierten Formerkennung der roten Blutkörperchen, die in der Regel manuell durchgeführt wird und daher einer Bewertungsinkonsistenz unterliegt. Die Untersuchung nutzt die 3D-Rekonstruktion der Zellen aus konfokalen Mikroskopieaufnahmen und die anschließende Formerkennung mittels künstlicher neuronaler Netze. Die Beurteilung dieses Systems zeigte sowohl eine sehr gute Erkennungsrate, hohe Präzision, eine schnelle Prozesszeit, als auch ein objektives Ergebnis verglichen mit der manuellen Klassifikation. Verglichen mit der Analyse von 2D Mikroskopieaufnahmen von Blutabstrichen, konnten durch die Auswertung korrespondierender 3D Aufnahmen außerdem andere Formspektren abgeleitet werden. Dies legt die Empfehlung nahe, die manuelle Klassifizierung von Zellformen (Stand der Technik) im Kontext von hereditärer Sphärozytose zu überdenken.

Summary

Human cell viability highly depends on oxygen, which is carried and provided by red blood cells. This thesis aimed to investigate how oxygen influences physiology and pathophysiology of red blood cells and is divided in two main parts.

The first one presents results that are part of a larger study performed at high altitude (3450 m). Here, the reduced air pressure causes a decrease in blood oxygenation, which is balanced by an increase in red blood cells production (erythropoiesis). Upon return from high altitude, the amount of red blood cells is restored to the original levels within a few days, which is in contrast with the average red blood cell lifespan of 120 days. The reasons leading to such red blood cells premature clearance are not well understood. A hypothetical mechanism previously proposed is defined as neocytolisis, i.e. the selective clearance of the red blood cells formed at high altitude upon return to sea level. The scientific question of the study was therefore to assess if and how neocytolisis occurs after a 3-week stay at high altitude. The investigations performed in this thesis involved in vitro culture of erythroid precursors of the donors participating in the study to characterize both erythropoiesis and the obtained immature red blood cells, namely reticulocytes. Results highlighted an accelerated maturation of erythroid precursors in cultures performed at lower oxygen (3%) compared to atmospheric oxygen (20%) ones and an unexpected improved cell survival of the obtained reticulocytes. This was in accordance with the finding that after the stay at the chosen altitude no neocytolisis occurred, denying the hypothesis of a higher fragility of cells formed at low oxygen causing their selective premature clearance upon return from high altitude. Moreover, cultures performed at low oxygen resulted in the formation of more biconcave cells, the typical shape of mature red blood cells. This suggests that reducing oxygen levels in cultures may contribute to advance their maturation in vitro. In addition to cell cultures, another objective was to perform RNA sequencing of isolated reticulocytes from whole blood of the donors to compare pre- and high altitude conditions. A protocol for the isolation of a pure fraction of reticulocytes and their RNA was developed. However, total RNA yield needs to be increased to perform an accurate comparison of gene expression levels.

The second part of the thesis focused on studying red blood cell morphology in two types of anemia. Because of the high sensitivity of red blood cells to shape variation, samples were always fixed before any experimental manipulation. A thorough study describing how to perform red blood cell fixation is presented. The first blood disease of study was sickle cell anemia. In this pathology, deoxygenation of hemoglobin causes the deformation of red blood cells to the shape of a sickle that

impairs their functions and lifespan. The quantitative analysis of cell projections from confocal images by means of a customized computer program was employed within a pilot phase II clinical trial for the therapy of sickle cell disease. The obtained results combined with other experimental evaluations showed that red blood cell shape analysis of sickle cell disease patients is a simple but powerful tool to evaluate cell hydration state. Therefore, this technique may be used for the assessment of the efficacy of sickle cell disease therapies or to evaluate the state of red blood cells of a patient. Since red blood cells display shape variations in different types of anemia, a second blood disease was investigated, namely hereditary spherocytosis. In this case, the focus was the automation of red blood cells shape recognition, which is usually performed manually and therefore subjected to evaluation inconsistency. The investigation made use of 3D cell reconstructions from confocal images and automated shape recognition by means of artificial neural networks. System benchmarks showed a good recognition performance, high accuracy, fast processing time as well unbiased results compared to the manual classification. Moreover, the application of 3D imaging in contrast to the traditional 2D-microscopy typically employed in blood smear analysis revealed a different red blood cell shapes spectrum. These results therefore suggest to revise the state-of-the art manual shape classification applied in hereditary spherocytosis.

1. Introduction

1.1 Blood

Blood is a specialized connective tissue consisting of a liquid extracellular matrix, the plasma, and a cellular component that includes Red Blood Cells (RBCs), White Blood Cells (WBCs) and platelets. While simple ancestral animals do not need blood for their vital functions (jellyfish, sponges), most of the living organisms rely on the presence of a circulatory system. Some invertebrates, such as insects or certain types of mussels, retain an open circulatory system containing a fluid called haemolymph, in which different types of hemoglobins (e.g. hemocyanin) are directly dissolved in plasma. Such an open system is efficient when oxygen (O_2) diffusion mainly occurs through the skin (insects) or energy demand is low (crustaceans, non-cephalopod mollusks). Complex organisms like vertebrates require a faster blood flow for their high metabolic activities. For this reason, they developed a closed circulatory system, where the heart pumps blood through vessels to reach the peripheral tissues and returns to the heart trough veins. The structure of the heart is optimized in birds and mammals, where the partitioned atria and ventricles ensure a complete separation of oxygenated from deoxygenated blood. The evolution of such a circulatory system in humans underlines the need for a very efficient blood transport, and the numerous components of blood highlight its multiple functions, making this fluid of primary importance for life [68]. In aerobic organisms, gasses like oxygen and carbon dioxide are continuously exchanged between blood and tissue cells. Oxygen is necessary for cellular metabolism and energy production, while carbon dioxide (CO_2) is the final metabolic product that is removed with expiration. Blood transports such gasses, as well as the dietary nutrients absorbed in the intestine, molecules produced by other organs (e.g. hormones) and waste products, such as urea. It is responsible for the immune response against pathogenic microorganisms, it contributes to tissue regeneration by promoting inflammation, an action mediated by the WBCs, and injury reparation through the activation of platelets (blood clotting). Finally, it regulates body homeostasis by maintaining water content balance, protons concentration, i.e. pH, via buffering systems (mainly bicarbonate buffer) and body temperature by peripheral vasodilation or vasoconstriction [6].

1.1.1 Generalities on blood components

About 55% of blood is composed of plasma, while the remaining 45% is made of the formed elements (RBCs, WBCs and platelets), whose percentage is used to define the hematocrit value. Plasma mainly contains water (90%), organic substances (9%), including proteins, lipids and glucids, and electrolytes (1%), such as chloride, potassium, calcium and phosphate. Proteins regulate blood on-

cotic pressure, which is responsible for the exchange of substances between blood and tissues, while electrolytes determine osmotic pressure. The major plasma protein is albumin (50 to 60% of plasma proteins, 60 kDa) which regulates the oncotic pressure in capillaries and the transport of small hydrophobic molecules. Most of plasma proteins are synthetized by the liver, including the coagulation ones, like fibrinogen and prothrombin [6].

Following a gentle centrifugation, blood appears divided into three layers: a top yellow one containing plasma and suspended platelets; a thin white ring, known as buffy coat, containing Peripheral Blood Mononuclear Cells (PBMCs), i.e. lymphocytes, monocytes and Hematopoietic Stem Cells (HSCs), and a bottom dense layer of RBCs in addition to eosinophils and neutrophils (figure 1). Most of basophilic granulocytes locate between the buffy coat and the bottom layer.
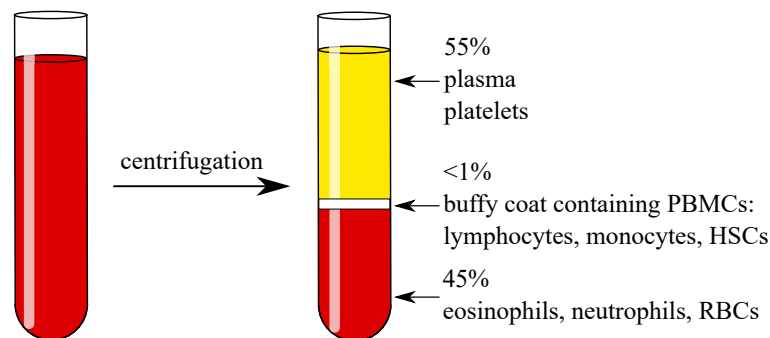
Figure 1: Three layers can be visualized after centrifugation of whole blood. The indicated volume percentages are an average between men and women.

RBCs or erythrocytes are the main cellular component of blood ($> 99\,\%$ of the formed elements), necessary for transporting oxygen to the tissues while removing carbon dioxide. They are considered the simplest type of human cells because they lack both nucleus and other organelles, which are extruded during their maturation to fill the cytoplasm with haemoglobin, the dedicated protein for oxygen transport and responsible for the characteristic red color of these cells. The absence of organelles makes the cytoplasmic compartment fluid, allowing RBCs for a particularly high deformability. This feature is necessary for an efficient blood flow, especially in capillaries, whose diameter is smaller than the one of RBCs. Erythrocytes live for about 120 days and are eventually cleared in the spleen, which acts as a filter system where only deformable and healthy RBCs pass through, while old ones are cleared [10]. Certain blood diseases affect RBCs' life span because of pathophysiological conditions reducing cell deformability and eventually leading to their premature disruption. Such early clearance is not balanced by erythropoiesis (blood cell generation) rate, eventually leading to anemia.

1.2 Erythropoiesis

The formed elements of blood in human adults (RBCs, WBCs and platelets) originate in the Bone Marrow (BM) from pluripotent Hematopoietic Stem Cells (HSCs) [122, 46], which are defined by their ability of both self-renewal and formation of all blood cell types. HSCs reside in specialized niches, either located in the endosteal region (endosteal niche) or in the venous sinusoids of the BM (vascular niche) [173]. These niches are organized in specialized multicellular structures known as erythroblastic islands [13, 5, 109]: here, a central macrophage is surrounded by erythroid precursors at different stages of maturation. Its role is thought to be the regulation of cell maturation by secretion of proliferation and differentiation factors for erythroid cells [66], the phagocytosis of the expelled nuclei and the provision of ferritin to the erythroid precursors. HSCs express CD117, i.e. c-kit, the receptor for the Stem Cell Factor (SCF) that is responsible for cell survival and proliferation. At this stage cells highly depend also on erythropoietin (EPO) activity, a hormone produced by the surrenal gland. Upon binding to its receptor (EpoR), EPO stimulates the commitment of HSCs towards erythroid maturation and promotes cell proliferation and differentiation. HSCs are largely quiescent in adults but can undergo both symmetric and asymmetric mitosis. The first mechanism is to ensure their self-renewal, while the second leads to the formation of Multi-Potent Progenitors (MPP) [97] (figure 2). This latter commit to the myeloid or lymphoid lineage and the respective progenitors undergo rapid mitosis to form unipotent cells, such as Erythroid Burst Forming Units (BFU-E) in the case of the erythroid lineage. Like HSCs, BFU-E express CD34, a surface marker protein thought to regulate cell proliferation and differentiation [154]. BFU-E mature to Erythroid Colony Forming Units (CFU-E), which are negative for CD34 expression [95]. These cells undergo various steps of maturation, during which different precursors can be identified both by morphological features in microscopy and by marker detection of membrane specific Clusters of Differentiation (CD).

The first morphologically recognizable erythroid precursor is the proerythroblast, characterized by a nucleus that occupies 80% of cell volume and has an overall diameter between 12 and 20 μm [124]. Maturation continues with the formation of basophilic erythroblasts, of smaller size, containing condensed chromatin and a basophilic cytosplasm. They express CD71, the transferrin receptor, necessary for iron uptake, which is included in hemoglobin and promotes its synthesis. CD71 expression gradually increases and later decreases until complete disappearance of this receptor in mature RBCs. Another marker for erythroid maturation is CD235a, i.e. glycophorin A, expressed specifically on erythroid cells in increasing amounts during maturation to RBCs [43]. Polychromatic erythroblasts show hemoglobinization and irregularly dense nuclei. Ortochromatic erythroblasts finally extrude the nucleus, originating the reticulocyte, a young red blood cell. This latter detaches from the bone

Erythropoiesis from hematopoietic stem cells in the bone marrow
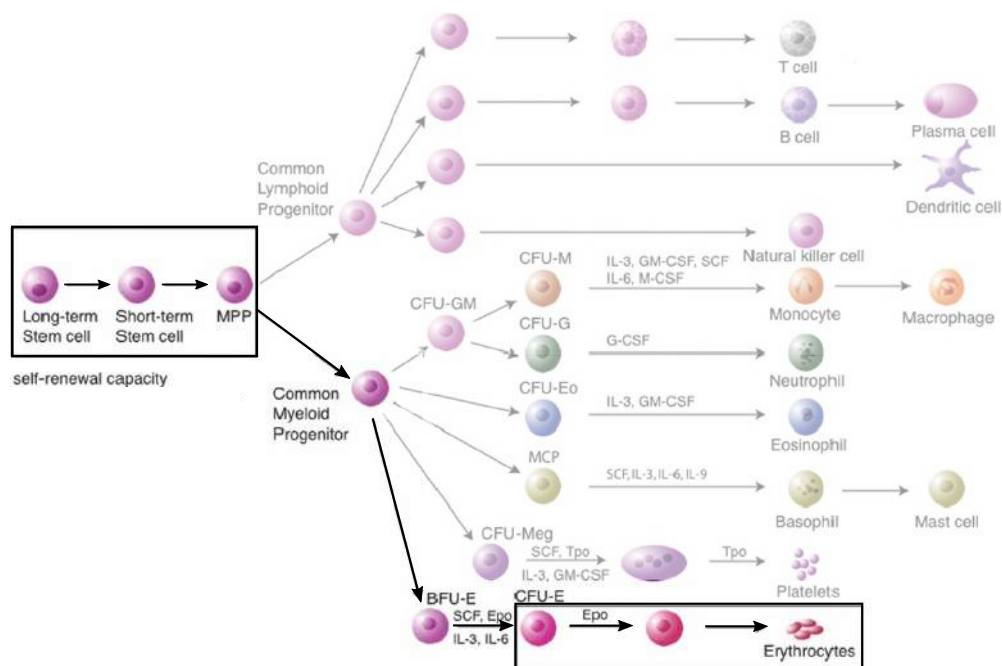
Figure 2: Schematic of hematopoietic progenitors. HSCs undergo self-renewal (long-term stem cell) or commitment to MPP, which proceed to the lymphoid or myeloid lineage to differentiate into all blood cell types. The myeloid progenitor differentiates into a unipotent pogenitor cell unable of self-renewal (BFU-E), which, upon SCF and EPO supplementation, differentiates into CFU-E and following stages until formation of erythrocytes. Adapted from [97].

marrow to be introduced into the blood stream where it completes its maturation within 2 days [30]. At the stage of reticulocytes, only a few mitochondria and remnant RNA are present, gradually completely lost when maturation to erythrocyte occurs (figure 3). Erythropoiesis requires approximately 14 days, yielding more than 10^{12} new RBCs per day [117]. The reasons for reticulocytes maturation occurring in the blood stream rather than in the bone marrow are still unclear and represent a limit for the currently existing cell cultures methods performed *in vitro*.

1.2.1 *In vitro* erythropoiesis

Several cell culture methods have been tested and validated for the commitment of HSCs to erythroid lineage and their differentiation *in vitro* [90, 43, 107]. One of such methods begins with the isolation of Peripheral Blood Mononuclear Cells (PBMCs) from a sample of whole blood. These cells are all circulating erythroid cells with a round nucleus and include HSCs and BFU-E. Cell culture from PBMCs is a non-invasive method to obtain reticulocytes and yields a high number of proliferating erythroblasts compared to other methods [166]. While these cultures achieved full maturation to RBCs in mice [87], from human cultures it is as yet not possible to obtain fully developed erythrocytes,

Bone marrow and erythroid cells
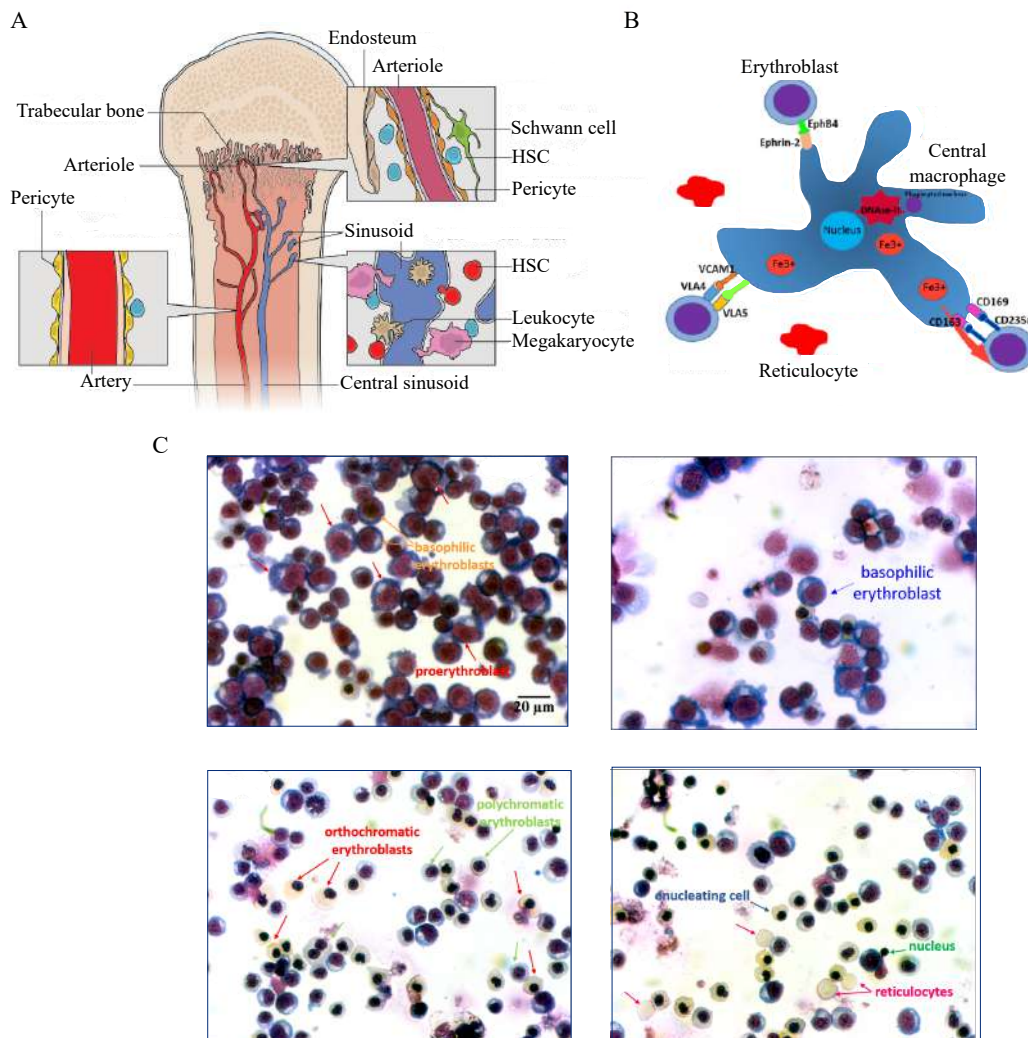
Figure 3: HSCs niche in the BM and committed erythroid progenitors. (A) HSCs are both located in the endosteal part of the BM and more centrally in the vascular sinusoids. Adapted from [173]. (B) Central macrophage in the erythroblastic island surrounded by erythroid precursors at different maturation stages. Adapted from [124]. (C) Examples of stained erythroid progenitors of the bone marrow produced *in vitro*, highlighting nucleus and cytoplasm. Proerythroblasts are the largest cells, differentiating into basophilic cells characterized by a condensed nucleus and in turn maturating to polychromatic and orthochromatic cells. These latter extrude the nucleus, finalizing their maturation to reticulocytes, which are released in the circulation.

meaning cells that lost RNA remnants, do not express CD71 and acquired the typical biconcave disk shape.

The culture protocol, optimized by Sanquin Blood Bank, involves two phases (figure 4). The expansion phase favors proliferation and commitment of PBMCs to the pro-erythroblast stage, thanks to the action of EPO, SCF and dexamethasone, a synthetic glucocorticoid hormone. Glucocorticoids bind their nuclear receptor in order to modulate the transcription of genes that stimulate cell

proliferation but inhibit cell differentiation [90, 168], allowing for the synchronization of erythroid precursors during their maturation process. This step is necessary for the detailed study of erythropoiesis, where experimental analysis are performed on the whole culture population to evaluate its maturation progress. Once the expansion phase is achieved the differentiation phase starts. Here, the medium requires a higher concentration of EPO, the addition of holotransferrin for the acquisition of iron and human plasma, which contains differentiation-inducing factors such as thyroid hormones, in particular T3. Cells themselves also secrete factors that induce terminal differentiation to reticulocytes. The obtained cells display a variety of peculiar morphology, presenting lobes and irregular membrane borders (figure 5).
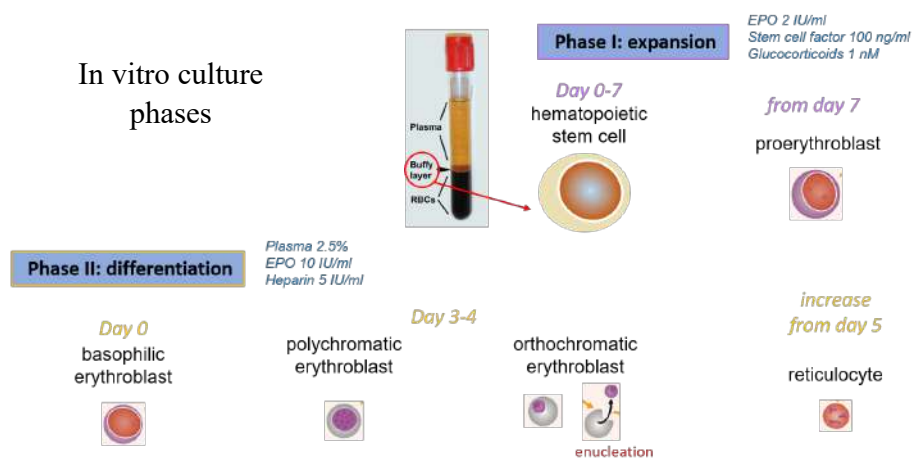
Figure 4: *In vitro* culture of PBMCs. After isolation of the buffy coat, PBMCs, which include HSCs, are set in culture. The first phase, expansion, allows the proliferation of HSCs and commitment to the erythroid lineage, processes stimulated by EPO, SCF and glucocorticoids (dex). After the appearance of proerythroblasts, the differentiation phase involves the addition of plasma, EPO and holotransferrin to bring about the formation of reticulocytes.
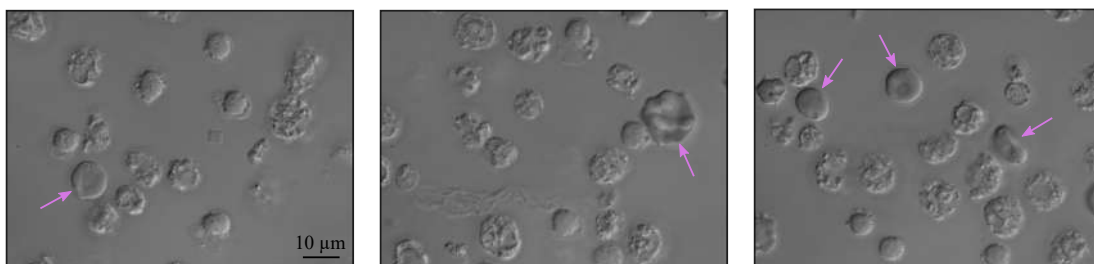
Figure 5: Live imaging in DIC (differential interference contrast) microscopy of reticulocytes (arrows) obtained in culture. Cell membrane presents irregularity, with small invaginations looking like holes on the surface and giving a multilobated aspect. Note the biconcave disk shape of the obtained reticulocytes. Mature RBCs have a smoother membrane and a more evident biconcavity. Pictures from own cultures in collaboration with Thomas Fischer.

1.2.2 Hypoxia in erythropoiesis and neocytolisis

Erythropoiesis is affected by oxygen levels in the body, which depend on air density. Oxygen constitutes 21% of the air, but since air density changes with the altitude, its partial pressure (pO_2) varies. At sea level, atmospheric pO_2 is about 21 kPa, resulting in 13% O_2 in the lungs and about 3% in the bone marrow. At high altitude pO_2 decreases and at 3000 m is equivalent to 13% O_2 at sea level and about 5% at 8848 m (Mount Everest highest summit)[129]. Hypoxia resulting from a stay at high altitude or caused by pathological conditions determines a series of adaptive mechanisms in the body to increase oxygen carrying capacity. Acute hypoxia stimulates a raise in the pulse and hyperventilation, which causes blood alkalosis, a phenomenon that augments hemoglobin oxygen affinity. Diuresis is another effect causing dehydration to increase the hematocrit. Instead, prolonged hypoxia acts on the molecular level to stimulate erythropoiesis by higher secretion of EPO, which is proportional to the degree of hypoxia [51]. The result is an increase in circulating reticulocytes because of the promoted erythroid precursors differentiation by EPO and increased blood flow in the bone marrow. In particular, the activation of the Hypoxia Inducible Factors (HIFs) [151] stimulates, besides EPO production, iron reabsorption and metabolic adjustments, which aim to reduce erythroid precursors ATP demand. This results in a general decrease in protein synthesis and ion transport activity and up-regulation of glycolytic enzymes expression to reduce mitochondrial oxygen consumption. HIFs abundance is regulated by oxygen: for example, the presence of $HIF1\alpha$ subunit of HIF-1 is favored by hypoxia because its proteasomal degradation depends on oxygen [114]. These adjustments cause stress erythropoiesis, where the elevated EPO augments RBCs production and results in a shorter life-span in some species [55]. In addition, it was found in astronauts that during microgravity spaceflights the youngest RBCs (less than 12 days old and defined as neocytes) are selectively destroyed due to a fall of EPO levels [2]. This selective clearance of RBCs was termed neocytolisis (the lysis of neocytes). This phenomenon was also associated to the reduction in RBCs mass occurring in subjects a few days after return from high altitude to sea levels, where a rapid reduction in EPO levels was observed. However, there is no clear demonstration of neocytolisis occurring as a consequence of this in humans. Studies have shown a decrease in RBCs but not in reticulocytes from residents at 4300 m descending to sea levels [141], a normal RBC clearance in subjects acclimatized to hypoxia [140], and explained the decreased RBC mass as a consequence of reduced erythropoiesis [113]. On the other hand, RBCs' faster clearance was seen in subjects upon return from Himalaya [125] and in a study [144] it was found that the youngest RBC fraction on mountaineers was reduced after one day upon return to sea levels. Possible mechanisms for premature RBC clearance have been speculated: anti-oxidant capacity is reduced during prolonged hypoxia, making cells more prone to death upon

return to high oxygen levels where oxidative damage is increased [147]; EPO increases intracellular calcium, which triggers signalling for cell "suicide" [39, 104]; sudden decrease in EPO reduces the expression of CD55 and CD59, known markers conferring protection against macrophage phagocytic activity [144]. Therefore, a better characterization of erythroid precursors formed in hypoxic condition is necessary to explain the possible reasons hypothetically leading to neocytolisis.

1.2.3 Reticulocytes

Reticulocytes are young RBCs, the first introduced in the circulation after erythroid precursors differentiation in the bone marrow. Reticulocytes finalize their maturation to RBCs by loosing about 20% of their membrane within the first days in circulation, along with loss of RNA, mitochondria, lysosomes and ribosomes. Reticulocytes have been classified in four sub-groups according to the expression level of CD71 and detection of RNA [123, 86]. The populations indicate their maturation stage: CD71 high/RNA high represent the youngest reticulocytes, being 0.016% of circulating reticulocytes; CD71 low/RNA high correspond to 0.059%, CD71 negative/RNA high constitute 0.037% and CD71 negative/RNA low 0.55% and represent the most mature reticulocytes [123]. Erythrocytes result CD71 and RNA negative. Therefore, isolation of reticulocytes from RBCs may be based on CD71 and/or RNA positivity. While firstly considered mostly debree, the role of RNA remnants in reticulocytes was assessed and demonstrated to be necessary for the final formation of mature RBCs where it contributes to the acquisition of the biconcave shape, membrane integrity and mitochondrial degradation [93]. Remnant RNA include a few mRNA, miRNA and especially circular RNA, which presence was also detected in aging RBCs [117].

1.3 Red Blood Cells

1.3.1 Morphological characteristics

Red blood cells in stasis suspendeded in plasma are typically biconcave disks, defined as discocytes. This shape holds 25% more cell membrane than the corresponding spherical cell of equal volume [10], therefore optimizing surface to volume ratio to allow for the most efficient gas diffusion inside and outside the cell and to to facilitate RBCs elastic deformations, allowing for unique deformability over 120 days lifespan [41, 84]. However, RBCs can take on several shapes depending on both environmental, e.g. plasma content, pH, osmolality, presence of a pathologic condition, and internal factors, such as impaired cell function, protein expression, presence of a metabolic disorder in the cell. In healthy subjects, RBCs can transform their shape according to the Stomatocyte-Discocyte-Echinocyte sequence (SDE sequence) described in the '70s by Marcel Bessis [14, 96]. This scale

explains RBCs shape changes following specific transitions. The classical discocytes can in fact transform into cup-shaped cells, called stomatocytes, that form upon hypotonicity of the suspending solution, low pH or chemical agents. Stomatocytes are monoconcave cells and their invagination can be mild or pronounced. Bessis classified different degrees of stomatocytes into type I, II and III (figure 6). Some other classification systems include a type IV, the extreme form of stomatocyte, called sphero-stomatocyte. Cells can take on such a shape until they transform into complete spherocytes, a very fragile RBC conformation that is considered a pre-lysis shape [134]. Discocytes can also take on a spiculated shape called echinocyte (from greek, hedgehog), resulting from hypertonicity of the suspending medium, high pH, ATP depletion, echinogenic chemical agents or by contact of cell with glass (glass effect). As for stomatocytes, there exist various degrees of echinocytosis, also divided into three classes (type I, II, III) and an extreme form that is a sphere with small spicules (sphero-echinocytes). The SDE transition describes that a stomatocyte can become an echinocyte only after taking the shape of a discocytes and viceversa. This limitation is due to the structure of the cytoskeleton, which is re-arranged to form each different shape. Indeed, certain blood diseases are caused by cytoskeletal defects (defective protein expression, e.g. spectrin) and the consequence is the presence of an abnormal amount of cells different from discocytes, including peculiar deformed cells caused by the pathophysiological condition. RBCs have also been imaged in flow, where they assume a hydrodynamic morphology following flow properties, taking on shapes like "parachutes", "slippers" or "croissant" [82, 89]. When the diameter of the vessel is larger than a capillary, it is possible to observe a trilobe shape at the walls of the vessel, called knizocyte, resulting from the high shear forces acting on the cells. Such versatility of RBCs to adapt their shape according to the need to stand certain conditions makes microscopic analysis a useful tool to investigate some of their properties and functions.

1.3.2 Cytoskeleton and membrane

Because of the shear forces constantly taking place during blood flow, RBCs evolved a characteristic cytoskeleton able to stand mechanical stress and responsible for their ability to take on different shapes. RBCs' cytoskeleton is primarily composed of spectrin, actin and ankyrin. Spectrin is organized as a mesh of two parallel chains, α and β, which can dynamically rearrange and disassemble to allow for cell shape deformation and adaptation to flow. Ankyrin binds spectrin in order to connect it to membrane integral proteins. Many of these latter are named after their order of appearance on electrophoresis gels: the most important one is band 3 protein (95 kDa), an anion exchanger responsible for CO_2 transport (in the form of bicarbonate anion, HCO_3^-) outside the cell while introducing a chloride anion (Cl^-) to balance intracellular charges. Band 3 is the most abundant protein on red
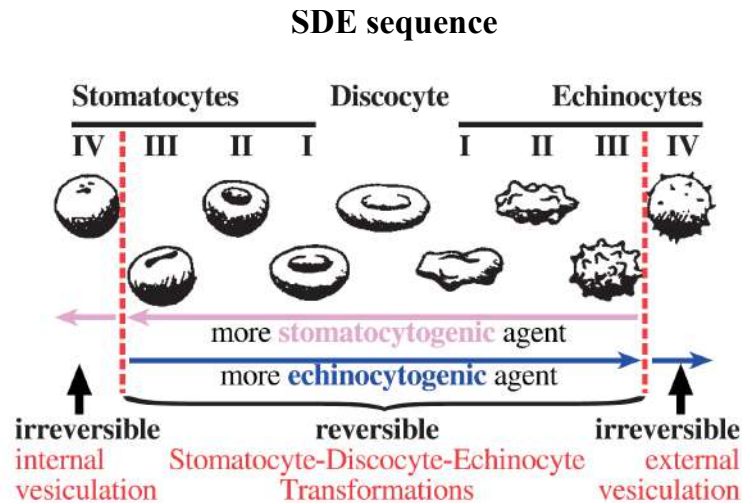
SDE sequence

Figure 6: SDE sequence explaining RBC shape transitions in stasis. Under certain conditions, a discocyte transform into a cup-shaped cell up to the formation of an irreversible shape, the spherocyte (stomatocyte IV); other conditions transform it into a spiculated form which can take on the irreversible sphero-echinocyte shape (echinocyte IV). These transitions necessarily occur according to the indicated order (note colored arrows). Image from [96].

cell membrane, accounting for 1.2 million copies per cell [99] and is essential to maintain red cell stability and morphology because it binds to spectrin through band 4.2 and band 4.1. Moreover, it binds some glycolytic enzymes and deoxy-hemoglobin, which in certain diseases forms precipitates on band 3 known as Heinz bodies. During aging, band 3 molecules tend to form clusters, which were demonstrated to play a role in RBCs clearance [170]. Mutations in band 3 contribute to anemias such as Hereditary Spherocytosis (HS) [130], where red cells lose their biconcave shape and rather assume a spherical-like shape that has reduced deformability and is subjected to hemolysis. Around band 3, other proteins form multi-protein complexes: about 40% of band 3 is organized within the ankyrin complex, that includes Rh blood antigen and the linkage protein 4.2; another 40% constitutes the actin junctional complex, including tropomyosin, tropomodulin, protein 4.1 and adducin, while the rest is in unbound form (figure 7). Actin binds spectrin with the aid of 4.1 and is strengthened by the additional binding of tropomyosin, tropomodulin, dematin and adducin. Protein 4.1 generates a high affinity complex between spectrin and actin and cells lacking it are highly fragile [99]. This protein is synthesized in the form of 4.1b and is gradually converted into 4.1a during cell aging, making the ratio between these two isoforms a RBC age marker [10, 70]. Other important proteins with transport role are Na/K pump, Ca pump, K/Cl exchanger and calcium activated potassium channels, the most known and first discovered being the Gardos channel. RBCs are also mechanosensitive, a property recently associated to a large calcium channel called Piezo-1, which is speculated to be involved in cell volume regulation during flow [75, 39]. Another important protein involved in calcium conductance in RBCs is the non-selective cation receptor NMDAR (N-metil-D-aspartate receptor), which

is activated upon binding of two agonists, aspartate and glycine. NMDAR has also been associated to a possible mechanosensitivity [155]. Calcium intake plays a role in RBCs dehydration triggering potassium efflux. Many researchers focus on studying the role of calcium in RBCs dehydration, which affects certain blood diseases, such as sickle cell anemia (see paragraph Sickle cell disease).
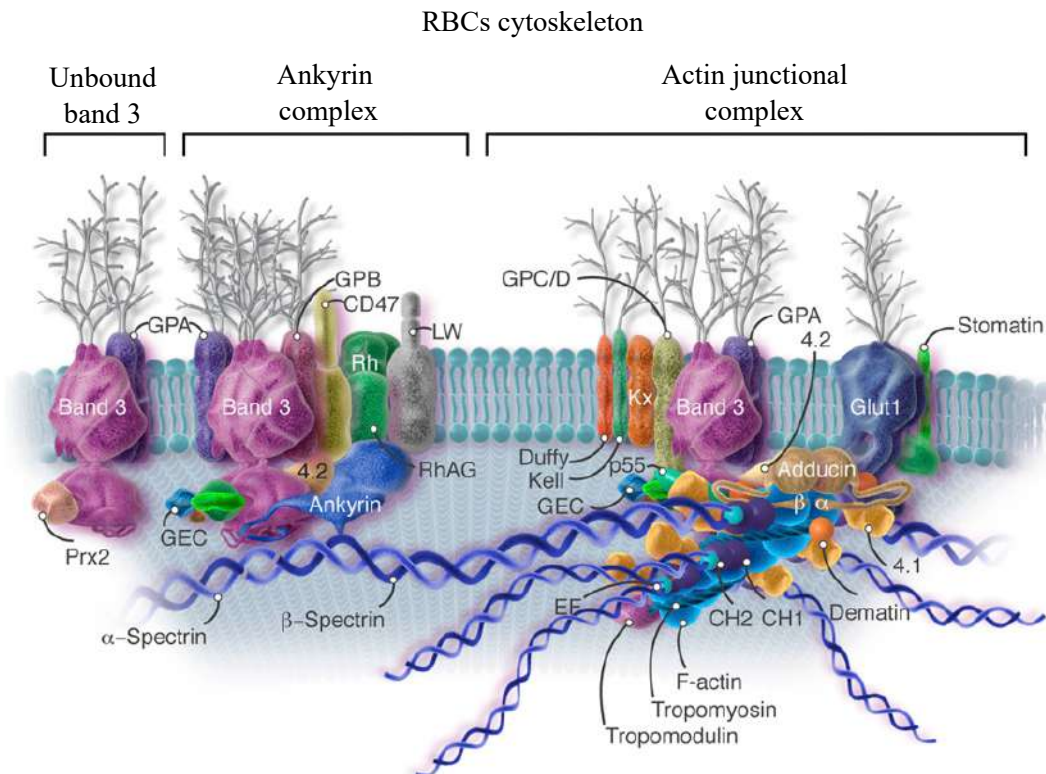
Figure 7: Schematic of RBCs' membrane and cytoskeleton. Spectrin network is bound to the phospholipid bilayer via ankyrin and actin complexes, where connection proteins are present: ankyrin, which is in turn bound to band 3, and protein 4.2, in the first complex, and actin, tropomodulin, tropomyosin, dematin and adducin in the second, in addition to glycophorins (GPA, GPB, GPC/D), carrying blood group antigens. Image modified from [99].

1.3.3 Hemoglobin

Hemoglobin (Hb) is a large metalloprotein (64 kDa) [101] with a quaternary structure composed of four subunits, the globins. Different genes code for a globin type and the protein assembly occurs with two globins of the same type, for example in adult hemoglobin (HbA) two globins α with two globins β (figure 8). Each of these units contains a heme group, the prostetic part of the protein, made of a porphyrin, i.e. a structure of four pyrrolic rings, where an atom of iron ($4\,Fe^{2+}$) is bound at the center and is essential for the binding of oxygen to hemoglobin. This transition atom cannot bind oxygen in the ferric state (Fe^{3+}), forming metahemoglobin [6]. Oxygen binding is reversible and depends on oxygen concentration. In particular, the quaternary structure of Hb has the property to

allow the cooperative binding of oxygen: when the first atom of iron binds a molecule, the affinity of the other atoms increases and viceversa when one atom of iron releases its oxygen molecule. The dissociation curve of Hb shows that Hb saturation occurs when the partial pressure of oxygen increases: first the amount of oxygen binding Hb increases rapidly, then it slows-down, eventually reaching a saturation plateau (figure 9). This occurs because when Hb binds oxygen it changes conformation to the oxygenated R-state (relaxed) in contrast to the deoxygenated T-state (tense), which has less affinity for oxygen (figure 8. The mechanism behind the dissociation curve of Hb is fundamental for an efficient gas exchange in the body because oxygen is easily released when erythrocytes travel through peripheral deoxygenated tissues, while it is bound while flowing through areas exposed to high oxygen levels (lungs and arteries) [163].

1.3.4   Bohr effect

In addition to the cooperative binding of oxygen, the increased acidity in peripheral tissues as a result of CO_2 and other metabolic products formation contributes to the release of oxygen by Hb. This results in a shift of the dissociation curve to the right at lower pH, and viceversa, to the left at higher pH, known as Bohr effect (figure 9). Also increased temperature and the presence of 2,3 diphosphoglycerate (2,3-DPG) induce Hb oxygen release. 2,3-DPG is an allosteric regulator which binds deoxy-Hb (T-state) and stabilizes it, meaning that Hb must bind more oxygen to get to the R-state [34].

1.3.5 CO_2 transport and Haldane effect

CO_2 has different means of transport than oxygen. About 10% is dissolved in plasma and therefore removed with expiration; 30% binds to terminal amino groups (NH_2) of proteins, including Hb, forming carbamino-Hb; the remaining 60% is transported as dissolved CO2 into bicarbonate (HCO_3^-). CO_2 accesses red cell from peripheral tissues through diffusion; once entered, it is converted to carbonic acid (H_2CO_3) by cytosolic carbonic anidrase and easily dissociates into HCO_3^- at pH=7.4. On the contrary, in the lungs HCO_3^- is converted to CO_2 to allow its removal through expiration. Protons forming in erythrocytes are buffered by Hb, whose binding causes a loss of its oxygen affinity. Therefore, H^+ act as allosteric regulators of Hb and explain the Bohr effect. Conversely, deoxy-Hb has a higher affinity for H^+, meaning that oxygen release facilitates CO_2 transport. The ability of deoxy-Hb of transporting more CO_2 is known as Haldane effect [38]. The equilibrium of CO_2 and HCO_3^- molecules contributes to buffer plasma pH and is reproduced *in vitro* in cell cultures.

Molecular structure of hemoglobin
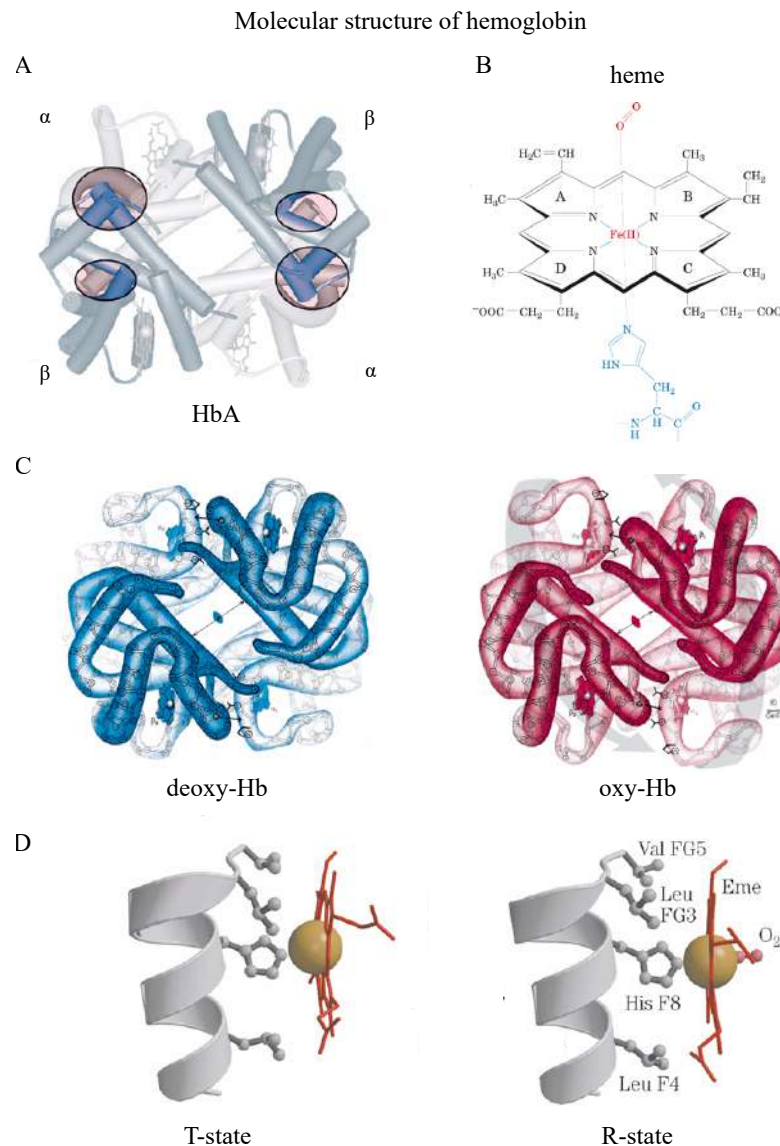
Figure 8: Molecular structure of hemoglobin. (A) Quaternary structure of HbA, with α and β chains. (B) Heme group, made of a porphyrin with an atom of Fe^{2+} binding O_2. (C) Deoxygenated and oxygenated Hb. Oxygen binding causes β chains to approach each other. (D) T-state of deoxyHb has low affinity for oxygen and Fe^{2+} is in proximal position to the porphyrin; R-state of oxyHb has the Fe^{2+} in the same plane of the porphyrin, increasing its oxygen affinity. Images (A), (B), (D) from [133] and (C) from [22].

1.3.6 Types of human hemoglobins

Hemoglobin synthesis occurs during maturation of hematopoietic cells and involves the expression of several variants. HbA, the adult hemoglobin, is the most abundant in mature erythrocytes of adults. In immature erythroid cells fetal hemoglobin (HbF) is more expressed, dropping during terminal RBCs maturation to about 1% of total Hb expression in adult RBCs. HbF has higher affinity for oxygen because it does not bind 2,3-DPG, making an efficient oxygen delivery to the fetal RBCs from the erythrocytes of the mother [38]. Despite the advantageous oxygen binding, HbF half-life is reduced
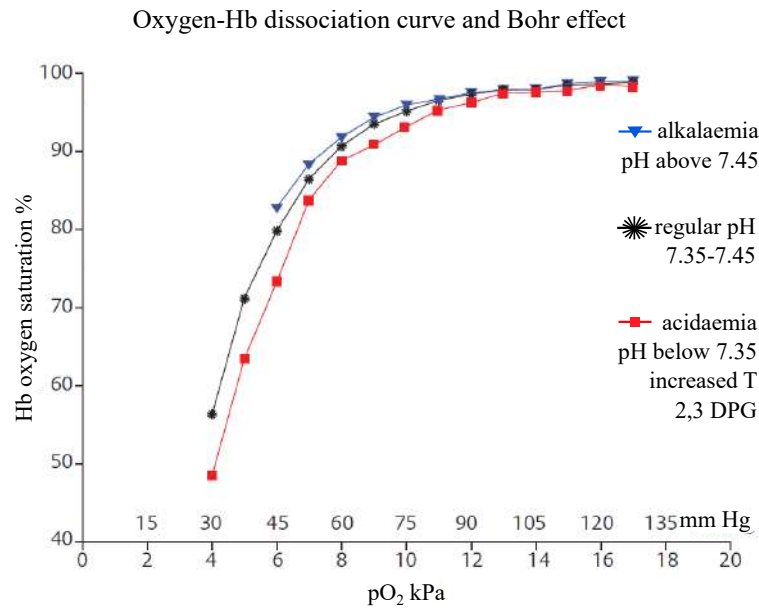
Figure 9: Oxygen-Hb dissociation curve and Bohr effect. Hb increases its affinity for oxygen with the increase of its tension (pO_2) until saturation of its heme groups. Changes in pH cause a shift of the saturation curve: to the left at alkaline pH, meaning faster saturation and therefore more oxygen affinity, and to the right at acidic pH, meaning a decrease in Hb oxygen affinity. Increase in temperature and the presence of 2,3-DPG reduce it as well. Adapted from [34].

compared to HbA and the higher affinity implicates a reduced oxygen release in peripheral tissues. HbA containing α and β chains is coded by genes in chromosome 16 and 11, respectively, while HbF contains γ globins instead of β ones, coded in the β-locus, which also includes the gene for δ chains [54, 158]. This latter globin type together with α globins is included in HbA2, which accounts for 2-3 % of Hb levels in adults. Muscles contain myoglobin, a monomeric form of HbA, that is the Hb variant with the highest affinity for oxygen.

1.3.7 Haemoglobin abnormality and anemia

Certain genetic mutation cause abnormal Hb molecules or abnormal Hb expression, which eventually impair its function, affecting tissue oxygenation and causing anemia. An example are α and β-thalassemia. Here, α-globins are expressed in low supply, causing high oxygen affinity of Hb and therefore an impaired tissue oxygenation. The severe form of α thalassemia causes an excess of β globins, which form a tetramer of β chains, called hemoglobin H (HbH). This Hb form precipitates on cell membrane, causing oxidative damage to RBCs. β-thalassemia is the prevailing form of this disease, where the gene for β chains is mutated often in the promoter region, resulting in less β-globin expression. Disease severity varies from minor (heterozygous) to major (homozygous), this latter resulting in severe anemia that often requires transfusions [26]. Anemia is also caused by defects in Hb protein which impair RBCs function and survival. The most known example is certainly Sickle

Cell Disease (SCD).

1.3.7 Sickle cell disease

SCD is the first discovered molecular disorder [128, 48]. In this pathology, a mutation occurs in the HbA gene (β-chain in chromosome 11), causing the substitution at position 6 of glutamic acid with valine that generates a defective protein called sickle hemoglobin (HbS) [49, 45, 121]. Because of the hydrophobic properties of valine, hemoglobin in its deoxygenated form is not soluble and "hides" from water molecules by binding to a hydrophobic pocket of other HbS, creating a solid fiber that deforms cells and eventually affects their functions by destroying the cytoskeleton [120]. Once HbS is reoxygenated such fibers disaggregate, making the process reversible. RBCs expressing HbS are subjected to continuous shape changes caused by the formation and disassembly of HbS complexes, transforming from normal discocytes to abnormal "sickle" cells (figure 10).
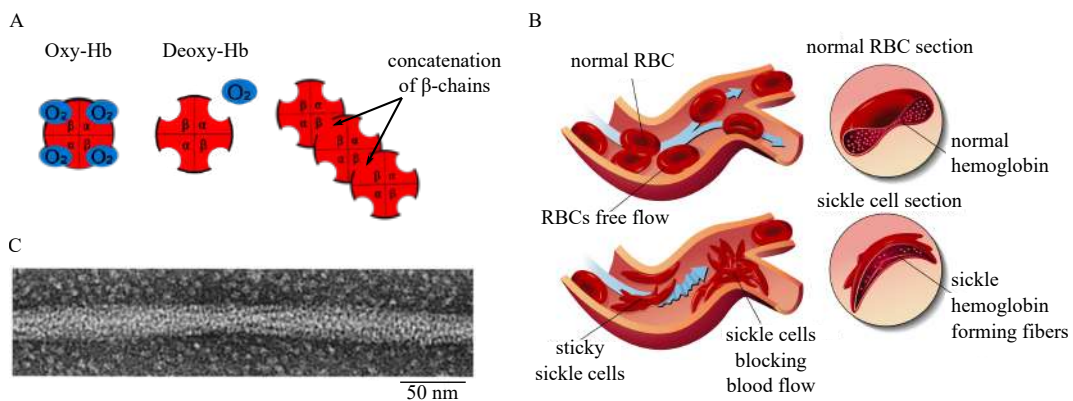
Figure 10: Representation of hemoglobin (Hb) defect in SCD. (A) While in its oxygenated state HbS is in a normal configuration, the deoxygenated form binds to the β chains of other deoxy-HbS. (B) Consequence of sickling on RBCs shapes. While oxygenated soluble HbS preserves discocyte shape, deoxygenation deforms cells to the sickle shape, impairing blood flow due to reduced deformability and cell adhesion of sickle cells to blood vessels. (C) Fiber of deoxy-HbS imaged in TEM from [45]. Images (A) and (B) adapted from [36] and [35].

Repeated cycles of deoxygenation-reoxygenation eventually lead to the irreversibility of the sickle shape [11], (figure 11). These sickling-unsickling process highly reduces RBCs deformability, impairing blood flow, and the additional damages caused to the cytoskeleton affect the flow also in oxygenated tissues despite oxygenated HbS conformation is normal. The resulting mechanical stress that RBCs experience shortens their lifespan to an average of only 14 days [120].

HbS does not bind oxygen, therefore its free electrons are taken by oxygen molecules, forming superoxide anion. This provokes several cellular damages, such as meta-HbS formation, which binds on cell membrane band 3 protein, forming crystals (Heinz bodies). As a consequence, gas exchanges are impaired and phosphatidylserine is exposed, triggering premature cell death that leads to anemia.

A

Oxygenated cells   Deoxygenated cells   Presence of ISCs in oxygenation

B

Typical sickle aspect of ISCs
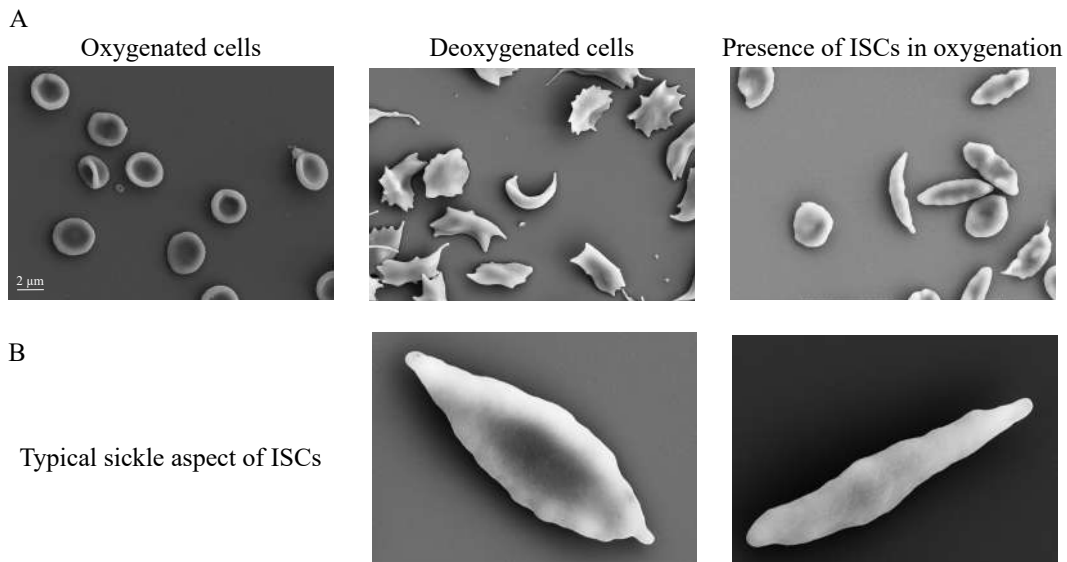
Figure 11: Scanning Electron Microscopy (SEM) of samples from SCD patients. (A) RBC shapes in oxygenated form looking like regular biconcave disks; various deformed cells upon artificial deoxygenation; typical Irreversible Sickle Cells (ISCs) after several cycles of deoxy-reoxygenation in the blood. (B) Zoom of single ISCs. Despite the lack of HbS fibers, at this stage the shape deformation cannot be recovered. The resulting cells are non-deformable, affecting blood flow. Images from own experiments.

Sickle cell disease is therefore affected by high oxidative stress and inflammation [19].

The kinetics of HbS molecule aggregation was thoroughly described [49, 31, 44, 37, 119]. The speed of formation and disassembling of the fibers directly depends on HbS concentration within the cell: the higher the concentration the faster the fiber formation and viceversa. In particular, the rate of formation is exponential and depends on the development of "nucleation sites", where the first HbS molecules start to aggregate. A nucleation site is made of 7 HbS molecules which form a structure (domain) where other HbS can easily bind, resulting in a faster sickling in cells with high concentration of HbS. In this case, when cells flow through deoxygenated tissues multiple nucleation domains form at the same time, while low concentrations may form a single nucleation site. This explains the variety of deformed cells instead of only sickle shapes that can be observed under prolonged deoxygenation (figure 12). Each of these shapes is therefore an expression of the speed of HbS fiber formation.

The presence of the fibers both depends on HbS protein expression levels and cell hydration state. Moreover, sickling itself triggers cell dehydration, enhancing the rate of fiber formation. This additional feature is caused by the characteristic abnormal calcium permeability seen in SCD patients' RBCs [47, 159]. This high calcium up-take is mediated by a conductive cation transport pathway, named P*sickle* [21, 10], activated by deoxygenation. The channel(s) involved in its activation are still unknown. P*sickle* increases intracellular calcium 6 to 10 folds, resulting in the activation of the Gar-
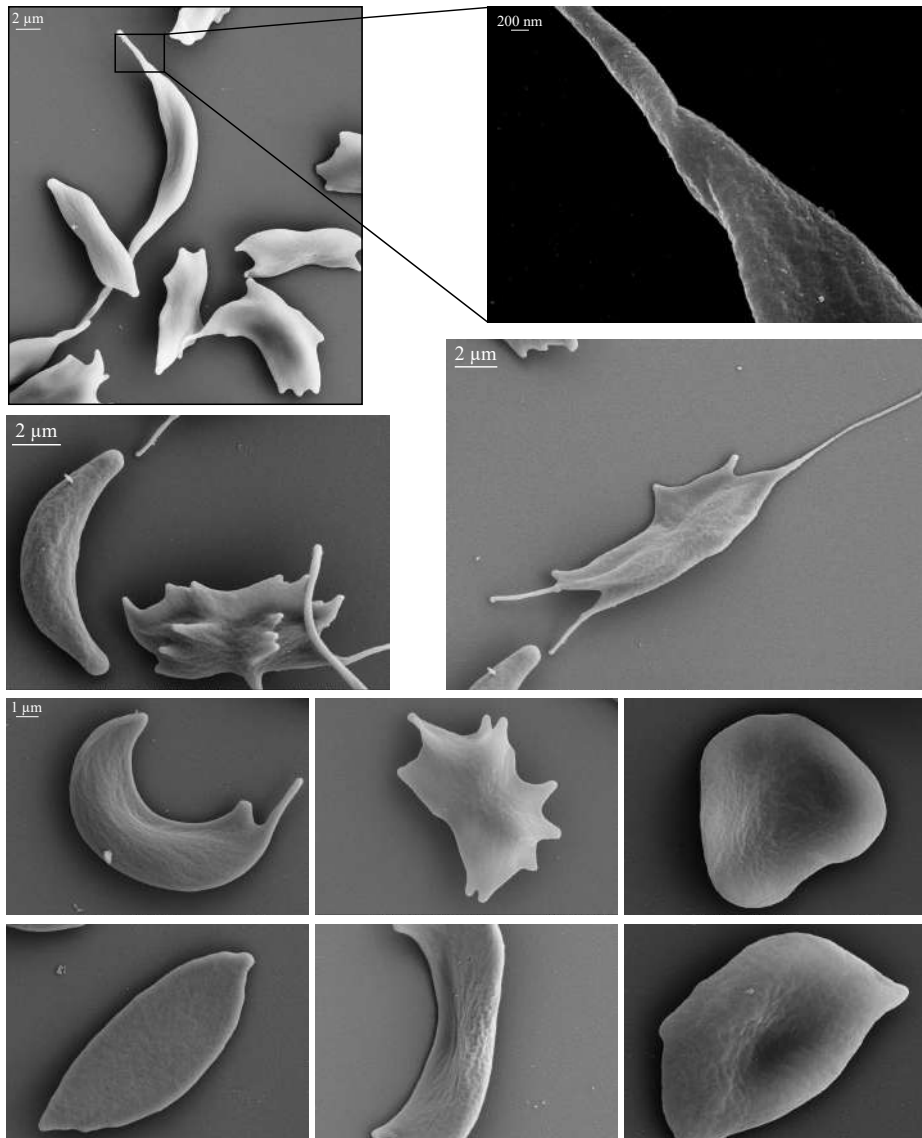
Figure 12: SEM of artificially deoxygenated RBCs from SCD patients. Note the various shapes of cells depending on HbS concentration within each cell, which determines the speed of formation from a different number of nucleation sites. Artificially deoxygenated cells are not ISCs but can return to the discocyte shape up to a certain number of deoxy-reoxygenation cycles. In samples prepared from whole blood of patients only ISCs can be observed, exclusively with a sickle shape. This is explained by the fact that in flow, HbS fibers don't completely disassemble by the time of their return to deoxygenated tissues, meaning that at least a main nucleation site remains, where HbS molecules bind and form several aligned HbS fibers. Images from own experiments.

dos channels, which determine potassium efflux and, the activation of KCC cotransporter, therefore causing cell dehydration. This pathophysiological pathway increases RBCs' osmotic fragility and enhances the chances of sickling due to dehydration. In fact, a slower reversal of sickle shapes to discocytes upon reoxygenation in dehydrated cells has been shown to occur despite the absence of HbS fibers, promoting the formation of Irreversible Sickle Cells (ISCs) [47]. Calcium overload is also associated with patients' crisis, oxidative damage, enhanced cell adherence to vasculature, and ATP

depletion because deoxy-HbS binding to band 3 protein inhibits the activity of glycolytic enzymes. The lack of ATP affects ion pumps functions including calcium pumps, preventing cells to recover their volume [19].

1.3.7   Sympthomatology and treatments

As mentioned above, the presence of HbS has severe consequences on RBCs functions and survival. The impaired blood flow causes episodes of Vaso-Occlusive Crisis (VOCs) that may be associated with severe pain triggered by inflammation and dehydration. Swollen limbs, micro-infarcts, impaired bones, organ development and functions, splenomegaly and jaundice are consequences of such compromised flow and tissue oxygenation. Because of the various complications, patients affected by SCD often suffer from depression, and the therapy includes psychological support [26].

Sickle cell disease mutation is spread in the African continent as a result of resistance of subjects with sickle cell trait, i.e. the heterozygote carriers of HbS mutation, to malaria infection caused by *Plasmodium falciparum* [131, 139]. Immigration phenomena and improved life quality of patients increased the frequency of SCD, accounting for 300 000 births in the world in 2017, possibly increasing up to 400 000 in 2050 [132]. Currently, treatments allow a life expectancy of more than 60 years. However, life quality is often poor. The spread of the disease increases the global need for efficient therapies to support the quality of their life. Current treatments are preventive approaches against VOCs and include chronic administration of hydroxyurea, which favours HbF expression. HbF does not contribute to HbS fiber formation during sickling and many of the patients with SCD already naturally express higher levels compared to healthy subjects as an adaptive response to the mutated Hb. However, some patients remain refractive to hydroxyurea or suffer from side effects [78]. Other available therapies include infection prophylaxis and hydroxycarbamide, which has been hypothesized for a number of side effects [139]. A recent trial aiming to prevent RBCs dehydration concluded that the drug Senicapoc, a blocker of Gardos channels, reduces hemolysis. However, it failed to prevent VOCs [9].

1.3.8   NMDAR and memantine: a clinical trial for a new therapy for SCD

Cell hydration is fundamental in SCD to delay HbS sickling. Water content equilibrium is regulated by the interaction of membrane proteins (e.g. ion channels and pumps) responsible for the influx and/or efflux of ions. In SCD the conductance generated by P*sickle* resulted to be determinant in the sickling process and it is known to involve a higher calcium permeability. N-methyl D-aspartate receptor (NMDAR) is an ionotropic receptor with conductance for cations, previously found to be

involved in calcium overload in sickle cells. Therefore it could hypothetically be part of P*sickle* [77, 63]. NMDAR is a heterotetrameric protein made of the subunits GlutN1 and GlutN2 and opens upon binding of glycine and glutammate. NMDA is a substance that mimics the agonist action of glutammate only in this particular receptor, that is the name [40]. NMDAR is mostly known for its activity in neurotransmission in the brain, but is also expressed in other cells and organs, including RBCs. During erythroid maturation its expression drops down to a number of about 30 receptor per cell in RBCs of healthy subjects, but it was found to be of about 300 in patients with SCD, where also the channel activity is up-regulated during VOCs [104]. NMDAR is more abundant in reticulocytes [104, 103], making young cells paradoxically more susceptible to irreversible sickling and hemolysis in SCD. Due to its involvement in calcium overload and knowing that dehydration is a crucial trigger of sickling (Senicapoc trial), targeting NMDAR could be a new alternative therapeutic approach. A blocker of NMDAR activity, memantine (MEM) is already in use for Alzheimer's disease treatment [171, 110] and therefore a good candidate drug already approved and commercialized to administer to SCD patients (figure 13).

1.3.9 Other anemias: hereditary spherocytosis

Hereditary Spherocytosis (HS) is a blood disease involving defects in cytoskeletal proteins. As an autosomal dominant genetic inheritance-based disease is the most common hemolytic anemia in subjects of north European ethnicity. However, 20 % of cases are *de novo* mutations. The defective protein may be spectrin, ankyrin, band 3, proteins 4.1 and 4.2 or a combination of multiple mutations in these proteins. The most common mutations are in spectrin, where the α-spectrin one is mild and β-spectrin is very severe [26]. Ankyrin deficiency is accompained, as a consequence, in spectrin deficiency. Less common are mutations in band 3 and 4.2. The genetic defect mostly translates into a deficiency of the mutated protein and therefore, RBCs do not have a cytoskeleton providing an appropriate cell deformability. Moreover, patients' membrane abnormalities cause sodium leak into the cell and such increased permeability requires energy to re-establish the ionic membrane steady-state of the gradient. In an environment like the spleen, relatively acidic and hypoglycemic, cells do not produce enough energy, and the failure in maintaining membrane equilibrium results in membrane loss through vesiculation [130]. The reduction of cell surface area transforms the biconcave disk shape into a rounder cell. Such deformed RBCs are defined "spherocytes" because on blood smears they appear round and devoided of the typical central pallor observed in discocytes. Spherical cells are less deformable, hence more susceptible to hemolysis and thus bringing to anemia. In some cases the effect is mild or completely absent because cell loss is balanced by enhanced erythropoiesis. Other

Effect of memantine on NMDAR action
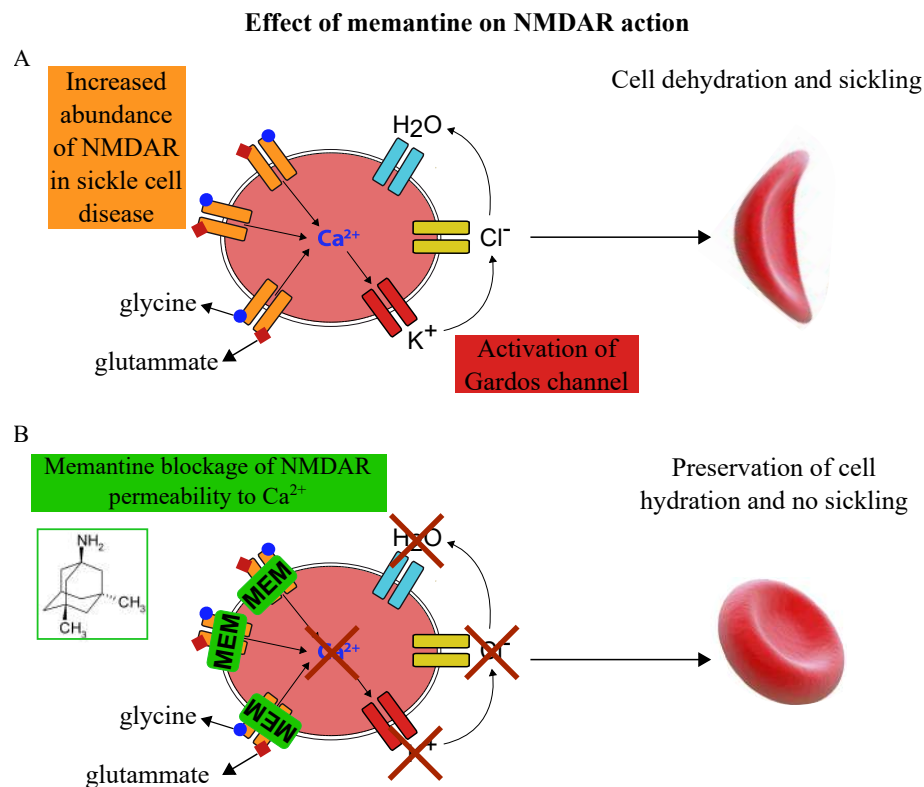
Figure 13: Schematic of NMDAR and memantine action. (A) After binding of its ligands (glycine and glutammate), NMDAR gets activated, allowing calcium ions to enter the cell and bind to the Gardos channel, a calcium-activated potassium channel. Potassium efflux is followed by chloride an eventually water, causing cell dehydration and increasing the chance for sickling. In sickle cell disease RBCs, NMDAR abundance is higher than in healthy RBCs. (B) Memantine bond physically blocks ion permeation, avoiding the activation cascade of the channels, therefore preserving cell hydration and shape. Images adapted from [67] and wikimedia.

typical complications involve splenomegaly, reticulocytosis and hyperbilirubinemia (which can require exchange transfusions). Considering the variable symptomatology and the numerous mutations, HS is an heterogeneous disease. The diagnosis of HS is based on the combination of family clinical history and physical examination for splenomegaly or jaundice, followed by laboratory tests, such as morphological observation in blood smears, reticulocyte count, measurement of MCHC (¡36 %) but confirmation is given by osmotic fragility testing. Protein quantification is done by SDS-page and mutation identification via next-generation sequencing of target genes. However, some of the test are either not sufficiently specific or not cost-effective or easy to realize [26]. Blood smear is a simple, fast and cheap technique. However, spherocytes can be observed in a large variety of diseases and can also result as an artifact of blood smear technique. More accurate and sensitive diagnostic methods are desirable. The only existing treatment is splenectomy, which improves cell survival, reduces anemia, reticulocyte count and hyperbilirubinemia, but not the presence of spherocytic cells.

1.4 Cell shape analysis: Overview on current methods

This thesis dedicates a study on unbiased RBC automated shape recognition applied to both healthy and diseased subjects. Characteristics morphological deviations are used to name several types of anemia, e.g. "sickle cell" disease, hereditary "ellyptocytosis", "stomatocytosis" and "spherocytosis". Blood smear was the first technique used to study such shape deformations [169, 100] and the additional assessment of cell size and hemoglobin distribution contributed to define typical morphological features in different blood diseases. This state-of-the art technique is based on smearing a droplet of blood on a microscope slide. After drying, cell nucleus as well as hemoglobin are stained and inspected by means of microscopy. This approach is a routine test in hospitals as a preliminary diagnostic method for blood diseases. However, considering the advances occurred both in computing and microscopy, it is currently possible to make use of more sophisticated methods for an accurate detection of the complexity of surface details, improving the understanding on the shape variability of RBCs. Studies on methods for the automation of blood smear analysis have been published [152, 164, 156]. The advantage of automation is the unbiased high-throughput outcome that delivers more statistically relevant results in a time-efficient manner. For comparison: manual classification of cells on a blood smear usually accounts for about 200-300 cells in total, while automated systems process thousands of cells within a few seconds or minutes. The automated approaches for image recognition make use of machine learning techniques (see 1.6.1).

In the field of microscopy, advanced imaging allows to obtain 3D reconstructions of cells, e.g. confocal, holographic or scanning ion conductance microscopy. While the two latter techniques produce 3D images of the top of the cell surface, confocal microscopy provides a 360 degree view, revealing shape details of the whole surface with a fine cell border definition and the possibility to measure cell volume. However, manual cell shape classification in 3D is highly time-consuming because each scan must be rotated for the full visualization of the shape, requiring special 3D viewers and elaborated image processing steps for the reconstruction. Therefore, an important prerequisite for the automated classification is the implementation of all relevant preprocessing steps in an automated manner. Finally, the automation of cell shape recognition is based on machine learning techniques.

1.4.1 Basics about machine learning

The term "Machine Learning" (ML) was coined in 1959 by Arthur Samuel, an American engineer considered the pioneer of artificial intelligence [111]. ML, in fact, is a branch of artificial intelligence that consists of an ensemble of algorithms working together to learn how to recognize patterns/trends within a given dataset and to generate predictive results. ML is used in a variety of fields, such

as finance, search engines, email filtering, facial recognition systems or autonomous driving[118].
Basically, it is helpful to solve general problems that rely on correlation and, for this reason, it is
close to certain human performances. Currently, related techniques are steadily developing, especially
in diagnostics, where for some particular diseases ML outperforms the interpretations of physicians
[157]. Moreover, in the field of microscopy [3, 7, 73, 165] ML is used e.g. for cell shape recognition
and classification by means of automated segmentation (organelles, plasma membrane, nucleus). ML
is a suitable approach to overcome the lack of quantitative methods to recognize the large variety of
occurring shapes of RBCs. The here proposed approach for 3D RBC recognition is based on Artificial
Neural Networks (ANN).

1.4.2 Artificial Neural Networks

Becoming popular in the '80s, ANNs are computing systems inspired by the structure of the biological
brain with the aim to perform complex tasks [92], such as pattern recognition. Similar to biological
neurons, an ANN is composed of particular processing nodes, called neurons, that are interconnected
to each other through edges, which correspond to the biological synapses (figure 14). Edges have
a weight, representing the amplification or attenuation of a signal. Similar to the synapses, each
artificial neuron receives signals from other neurons, each with a corresponding weight (intensity); it
sums all of them up and, in the most simple case, when the sum exceeds a defined threshold it gets
activated.
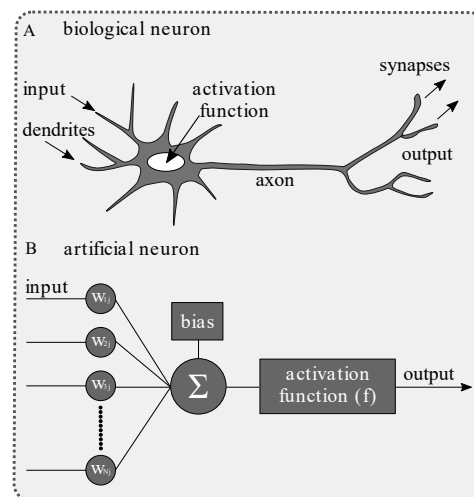
Figure 14: Representation of (A) a biological and (B) an artificial neuron. In (A) the input stimulus
comes from the signal of other neurons transferred to the dendrites. The stimulus is then processed
by the cell that transmits it over the axon to the synapses (connection point) with other neurons. (B)
Artificial neurons receive data by multiple inputs. Each input is multiplied by a weight (Wj), then
summarized and elaborated by applying a mathematical activation function, resulting in an output
signal. A constant signal (bias) can be applied for each neuron to increase the degrees of the system.

Consequently, each activated neuron sends its signal to next layer of connected neurons. This reflects the activity of biological neurons, in which a received stimulus exceeding the membrane depolarization threshold (-55 mV) triggers the action potential while, on the contrary, a stimulus below the threshold is ignored. However, for ANNs, the threshold is usually replaced by sophisticated mathematical activation functions, with non-linear and/or linear characteristics.

An ANN is always organized in so-called layers, each containing a certain number of neurons: the input layer, which serves as a memory for the received digital input data that will be processed (e.g. time-series or images); one or more hidden layers, which represent the black box of the system and contain all linear and non-linear mathematical transfer functions; the output layer, which provides the desired output value either by means of classification or regression (15).
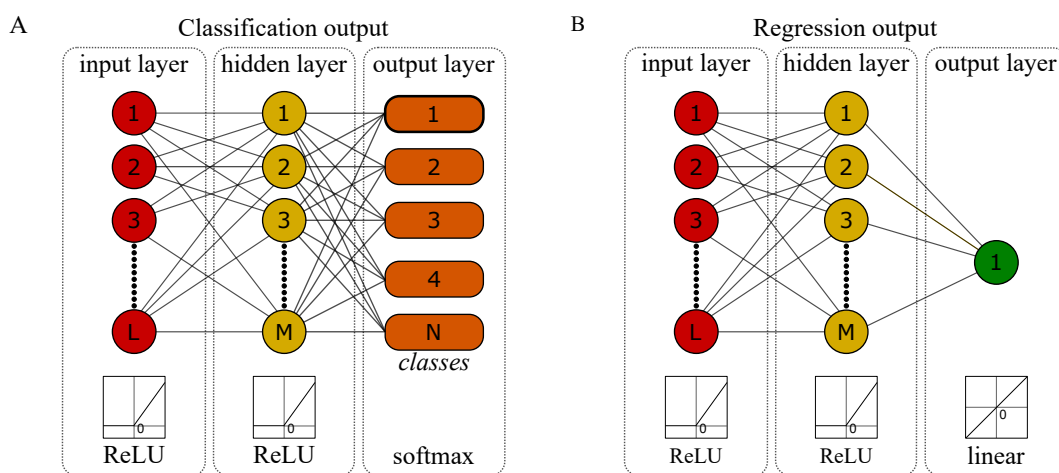
Figure 15: General architecture of ANNs and types of output. Each circle represents a neuron, while any connection line (edge) has a weight assigned and adjusted by the ANN. Since the used toolbox involves the first hidden layer into the the input layer by default, the input layer also exhibits a transfer function. (A) The classification ANN elaborates the data leading to a discrete number of classes, each representing a certain type of shape. (B) The regression ANN contains a single-neuron in the output layer, resulting in a continuous scale. The activation functions of the hidden layer (ReLU) are chosen as non-linear for both types. Conversely, the function that produces the output can both be linear or non-linear according to the desired result.

In this project (see Material & Methods), the input layer already contains the first hidden layer, which assigns weights to the input data and transfers the information of each neuron to the second hidden layer using a particular activation/transfer function, in this case the Rectified Linear Unit (ReLU, [88]). This non-linear function rectifies any input, meaning that negative numbers are set to zero while positive values remain unvaried. Both layers are fully connected (dense layers). The second hidden layer has the same structure of the first hidden layer and was added to increase the complexity of the system to improve the ability to detect complex patterns. The output layer in case of a classification contains multiple neurons, i.e. classes, which are cross-linked by a non-linear activation function

(softmax). Therefore, the number of output neurons corresponds to the number of expected classes. In the case of a regression, the output layer consists of a single neuron exhibiting a linear transfer function. This allows to map the result onto a linear and continuous scale, e.g. from 0 to 1. For RBCs 3D shape recognition, both output types were designed: the classification output was used to recognize pathological shapes, while the regression was employed as the output for shapes owing to the SDE sequence (see Material & Methods for a detailed description).

1.4.3 Learning

Learning is a mathematical optimization process that adapts all weights and bias terms with respect to a certain data-set. In the ANN here presented, based on supervised learning only, this process occurs as follows. In the very first step, all degrees of freedom (weights and bias terms) of the ANN are randomly initialized. Several input data are then presented, each containing a certain label that represents the perfect system response (output). During the learning process, all deviations of the ANN output from the expected output are compared and all degrees of freedom (weights and bias terms) are updated in a way that the ANN predictions get closer to the expected ones. For instance, an often cited algorithm which performs this optimization task is the so-called "back-propagation" algorithm [91]. This automatic updating algorithm allows to revise and adapt weights through iterations of the whole process and constitutes the basis of the learning process [127, 27]. In particular, the back-propagation or any other optimization algorithm make use of the so-called "loss function" that is a measure of the performance, i.e. the precision of the network. This step occurs during the training process of an ANN. Moreover, the updates of all free parameters are not performed for each individual input but rather for a certain batch of inputs. The smaller the batch-size, the more often the network is updated and the longer the training lasts. Moreover, if the batch-size is too small, the networks gets sensitive to particular features of certain inputs which is not advantageous for general use. In contrast, if the batch-size is too large, small details remain unconsidered during training and the network shows some kind of "low pass" behavior.

The "back-propagation algorithm" includes an optimization function, in the case here presented the so-called "gradient descent" algorithm. The goal of such a function is to force the loss function towards the global minimum during the training process. The update of all free parameters is usually done batch-wise. If all batches are processed, a so-called epoch is concluded, i.e. all training data is fully processed. A certain number of epochs is usually required for convergence, however, it is never clear if the global minimum is actually found (figure 16, A, B). Indeed, different random initializations (different random seeds) can lead to different paths within the high dimensional "loss-function landscape", meaning that the minimum found may be local instead of global. Several approaches
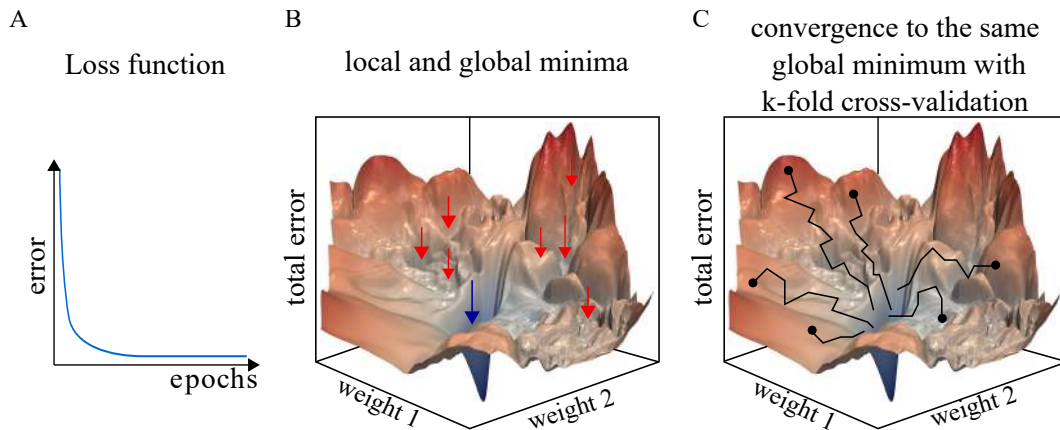
Figure 16: Loss function. (A) The error is minimized at every epoch until (optimally) reaching the global minimum. At this point the iterations stop and the training is concluded. (B) Representation of the loss function as a landscape in two dimensions (weight 1 and weight 2), underlining the presence of several local minima (red arrows) that may be erroneously assumed to be the global minimum (blue arrow), hence resulting in a non-optimal ANN training. (C) The application of methods such as k-fold cross validation enhances the confidence of the convergence towards the global minimum. The principle relies on parallel initialization (k times) of the ANN with different random seeds (black circles). For simplicity, all random seeds in the figure converge to the same global minimum. Adapted from [94].

exist, such as the "k-fold cross-validation" to estimate the convergence of the training process towards the global minimum. Using such an approach, the network is trained k-times in parallel and the performance of all obtained networks is later compared [27]. Such statistical method can result in a higher confidence of an ANN model, especially if many training runs lead to the same or very close results (figure 16, C).

The choice of the loss function is related to the purpose of the network. For mutual exclusive classification purposes, Cross-Entropy (CE) is often used and was chosen here as the loss function for RBC shape classification (pathological shapes). For regression problems, a loss function with continuous value range is required. Examples are the Mean Absolute Error (MAE) or Mean Squared Error (MSE). The latter was chosen for the regression of RBC shapes on a continuous scale (shapes owing to the SDE sequence).

To resume, figure 17 represents the algorithms involved in the ANN designed in this thesis.

1.4.4 Training data

The training data is a subset of the whole acquired data provided to the network for the learning process. For supervised learning, the dataset used for training is usually split in two parts: 70-90% of the data are introduced to the network together with their corresponding expected outputs (labels). The network is therefore trained until the output is as close as possible to the expected one, i.e. until
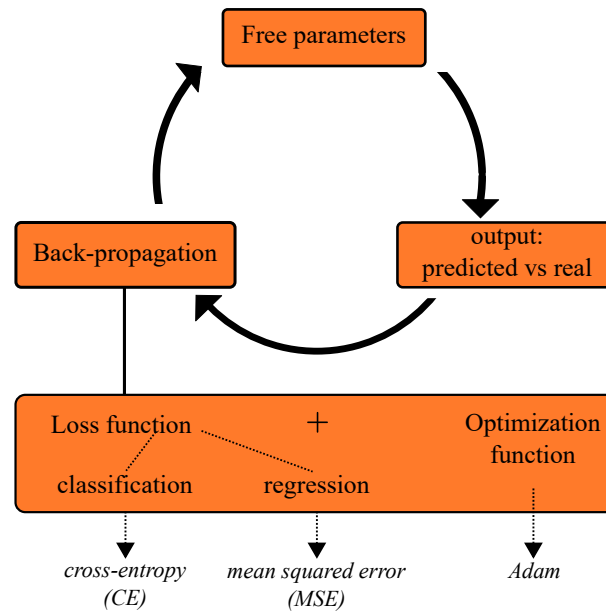
Figure 17: Schematic of the employed algorithms for the ANN training. The activation function produces an output which is compared to the expected output by the back-propagation algorithm. In particular, the loss function, represented by the CE or MSE, calculates the error between predictive and expected output. The optimization function therefore re-calculates the free parameters (weights and bias) in order to minimize the error at next iteration. Adam is an example of an optimization function (see Material & methods).

the minimization of the error. Consequently, the remaining 10-30% of the data are used to validate the network, checking if the outputs are valid also for data that the network has never seen. For this reason, a network is tested by evaluating both the training and the validation datasets (figure 18).
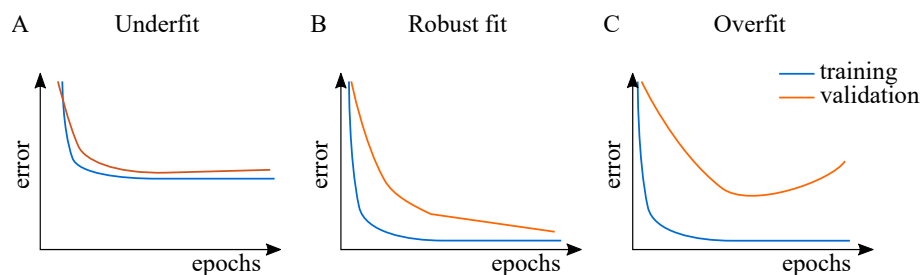
Figure 18: Examples of curves showing the accuracy of the learning process. The training curve is obtained from a training dataset and compared to the validation curve obtained from a test dataset. (A) Representation of an ANN underfitting the data because of, e.g., a too low number of epochs applied. (B) Example of correct data fitting, where the accuracy in both training and validation results from a good number of epochs. (C) Despite the training data is recognized with high accuracy, the error during the validation test remains high, showing the ANN is overfitting the training dataset and therefore is not accurately recognizing the test dataset.

It can occur that the error increases at a certain epoch, an indication for the over-training of the network. In this case the ANN is too well trained on the details of the training dataset and therefore will not perform well on test data. Underfit and overfit of the data may occur for several reasons:

a badly chosen training and validation dataset, a wrong number of set epochs, a sub-optimal ANN architecture, a bad initialization number (random seed). Therefore, the ANN resulting performance highly depends on fine-tuning all these parameters and components.

2. Material & methods

2.1 Material

2.1.1 Chemicals

The chemicals used throughout this work are listed in Table 1.

Table 1: Chemicals. PB=Pacific Blue, PE=Phycoerythrin, PerCP=Peridinin Chlorophyll Protein Complex, Cy5.5=Cyanine5.5, FITC=Fluorescein-5-isothiocyanate.

Reagent	Provider	Stock concentration
Antibody anti-human CD71 PB	Miltenyi Biotec, Germany	used 1:100
Antibody anti-human CD71 FITC	Miltenyi Biotec, Germany	used 1:100
Antibody anti-human CD235a PE	Biolegend, USA	$0.2\,\mathrm{mg}/ml$
Antibody anti-human CD45 APC	BD Biosciences, USA	used 1:200
Antibody anti-human CD34 PerCP-Cy5.5.	BD Biosciences, USA	$12\,\mu\mathrm{g}/ml$
Antibody anti-human fetal hemoglobin FITC	BD Biosciences, USA	used 1:5
Antibody anti-mouse isotype control IgG1k PB	Biolegend, USA	$100\,\mu\mathrm{g}/ml$
Antibody anti-mouse isotype control IgG1 PE	R&D Systems, USA	used 1:200
Bovine Serum Albumin (BSA)	Sigma Aldrich, USA	n.a.
Calcium chloride	Carl Roth, Germany	1 M in distilled water
CASYton®	Schärfe System GmbH, Germany	n.a.
CD71 MicroBeads, human	Miltenyi Biotec, Germany	n.a.
CellMask™Deep Red	Life Technologies, USA	$0.5\,\mathrm{mg}/ml$
CellQuin	Sanquin, The Netherlands	n.a.
Chloroform	Sigma Aldrich, USA	$\geq 99.5\%$
Dexamethasone	Sigma Aldrich, USA	1 mM in absolute ethanol

Reagent	Provider	Stock concentration
Difco Red	Sigma Aldrich, USA	n.a.
Difco Blue	Sigma Aldrich, USA	n.a.
DRAQ5	Abcam, UK	5 mM
EDTA	Invitrogen™, USA	0.5 M, pH=8
Eosin-5'-maleimide (EMA)	Invitrogen™, USA	$0.5\,\text{mg}/ml$
Erythropoietin (EPO)	ProSpec, USA	$6.66\,\mu\text{g}/ml$
Ethanol	Merck, Germany	100%
Ficoll®-Paque	GE Healthcare, USA	100%
Glucose	Sigma Aldrich, USA	n.a.
Glutamate	Sigma Aldrich, USA	n.a.
L-glutammine	Merck, Germany	n.a.
Glutaraldehyde	Sigma Aldrich, USA,	25% in water
	Merck, Germany	25% in water
	Fluka, Germany	25% in water
	Sigma Aldrich, USA	50% in water
Glycine	Carl Roth, Germany	n.a.
Heparin	MP Biomedicals™, USA	5000 IU/ml
HEPES	Carl Roth, Germany	n.a.
Holotransferrin	Sanquin, The Netherlands	$70\,\mu\text{g}/ml$
Hydrogen peroxide	Merck, Germany	30% in water
Isopropanol	Sigma Aldrich, USA	$\geq 99.5\%$
KCl	Carl Roth, Germany	n.a.
$KHCO_3$	Merck, Germany	n.a.
K_2HPO_4	Merck, Germany	n.a.
Memantine Mepha® (MEM)	Mepha Pharma, Switzerland	10 mM
Methanol	Merck, Germany	100%
$MgSO_4*7H_2O$	Grüssing GmbH, Germany	n.a.
NaCl	Sigma Aldrich, USA	n.a.
$NaHCO_3$	Sigma Aldrich, USA	n.a.
NH_4Cl	Grüssing GmbH, Germany	n.a.
O-diasidine	Sigma Aldrich, USA	n.a.
Omniplasma	Omnipharma S.A.L., Lebanon	n.a.

Reagent	Provider	Stock concentration
Osmium tetroxide	Sigma Aldrich, USA	2% in H_2O
PBS	Gibco Life Technologies	1X
	Sigma Aldrich, USA	1X
Penicillin-Streptomycin	Sigma Aldrich, USA	$10.000 \, \mu g/ml$
Percoll	GE Healthcare, Sweden	100%
PKH67	Sigma Aldrich, USA	0.9-1.1 mM
TRIzol Reagent BD	Sigma Aldrich, USA	n.a.
Trypan blue	Sigma-Aldrich, USA	0.4%
Triton X-100	Sigma-Aldrich, USA	n.a.
Sodium dithionite $Na_2S_2O_4$	Sigma Aldrich, USA	n.a.
Stem cell factor (SCF)	ITK Diagnostics BV, The Netherlands	$10 \, mg/ml$

2.1.2 Instruments

Table 2 resumes the equipment of various laboratories, where different experimental procedures were performed.

Table 2: Instruments

Instrument	Model	Provider
Blood analyzer	RapidLab 1265	Siemens, Germany
Centrifuge	Rotina 420R 4706	Hettich Zentrifugen, Germany
Cytocentrifuge	Cytospin II	Shandon, USA
Confocal head	CSU-W1	Yokogawa Electric Corporation, Japan
Confocal laser beam	LU-NV Laser Unit, 647 nm	Nikon, Japan
Coulter counter	Casy® Model TTC	Schärfe System GmbH, Germany
CO_2 incubator	Heracell™240i	Thermo Scientific™, USA
Critical Point Dryer	CPD 030	Bal-tec™, USA
Culture hood	Safe 2020	Thermo Scientific™, USA
Digital camera	Orca-Flash 4.0	Hamamatsu Photonics, Japan
DNA/RNA analyzer	Bioanalyzer 2100	Agilent, USA
FACS sorter	FACSCalibur	Becton Dickinson, USA
Flow cytometers	FACS Canto™II	BD Biosciences, USA
	Gallios	Beckman Coulter, USA
	CyFlow Cube 5n	Sysmex, Japan
Glove box	Invivo2 Hypoxia Workstation 400	Ruskinn Technology Ltd, UK
Illumina	HiSeq 2500	Illumina®, USA
Magnetic stand	MACS MultiStand	Miltenyi Biotec, Germany
Microscope	Eclipse Ti	Nikon, Japan
Microscope set-up	Leica DM-2500	Leica Microsystems, Germany
Microcentrifuge	Eppendorf Micro Centrifuge 5415 C	Brinkmann Instruments, USA
Microscopy objective	CFI Plan Apo Lambda 60x oil, NA=1.40	Nikon, Japan
Microscopy objective	Plan Apo TIRF 100x oil, NA=1.49	Nikon, Japan
Magnet	OctoMACS™separator	Miltenyi Biotec, Germany
Osmometer	Type 6	Loser Messtechnik, Germany
pH-meter	S20 SevenEasy™	Mettler-Toledo, USA
Rotator-mixer	Grant-bio PTR-35	Grant Instruments, England
SEM	Zeiss Supra 50 VP	Zeiss, Germany
Sputter coater	CCU-010 HV compact coating unit	Safematic, Switzerland
Vortexer	Vortex-Genie™2	Scientific Industries Inc., USA

2.1.3 Consumables

The consumables adopted for experiments are listed in Table 3.

Table 3: Consumables

Consumable	Provider
CASYcups	Schärfe System GmbH, Germany
Eppendorf tubes	Eppendorf, Germany
Falcon tubes	Greiner Bio-One, Austria
MACS MS columns	Miltenyi Biotec, Germany
Microscopy coverslips 24x60 mm	VWR™, France
Microscopy mounting medium	Merck-Millipore, USA
Microscopy slides 76x26 mm	Thermo Fischer Scientific, USA
Petri dishes	Greiner Bio-One, Austria
Pipettes	Gilson, USA, Eppendorf, Germany
Pipette tips	Greiner Bio-One, Austria
Pipettes for cell cultures	Sarstedt, Germany
Precision scale	Sartorius, Germany
Spheromeres CA20®	Microbeads, Norway
6-well plates	Greiner Bio-One, Austria
96-well plates, V-bottom	Sigma Aldrich, USA

2.1.4 Laboratory kits

The used ready kits, resumed in Table 4, included experimental protocols suggested by the producers.

Table 4: Kits

Use	Kit	Provider
Cytospin cell stain	Differential Quick Stain Kit	PolySciences, USA
RNA extraction	miRNeasy Serum/Plasma kit	Qiagen, Germany
DNA library preparation	CATS Total RNA-Seq Kit v2	Diagenode, Belgium
PKH67 stain	PKH67 Fluorescent Cell Linker	Sigma Aldrich, USA

2.1.5 Solutions

The solutions used are resumed in Table 5.

Table 5: Buffers used

Solution	Reagent	Concentration	
HEPES buffer	NaCl	132	mM
	KCl	6	mM
	$MgSO_4 \cdot 7\,H_2O$	1	mM
	K_2HPO_4	1.2	mM
	HEPES	20	mM
RBCs lysis buffer	NH_4Cl	155	mM
	$KHCO_3$	12	mM
	EDTA	0.1	mM
PBS	NaCl	137	mM
	KCl	2.7	mM
	Na_2HPO_4	10	mM
	KH_2PO_4	1.8	mM
Tyrode	NaCl	135	mM
	KCl	5.4	mM
	glucose	10	mM
	HEPES	10	mM
	$MgCl_2$	1	mM
	$CaCl_2$	1.8	mM
Benzidine	o-Dianisidine	1% in methanol	
HbF staining buffer	PBS	1	X
	FBS	1	%
	NaN3	0.1%	
Citrate/phosphate buffer, pH=5	citric acid	50	mM
	Na_2HPO_4	50	mM
MACS buffer pH=7.2	PBS	1	X
	BSA	0.5%	
	EDTA	2	mM

2.1.6 Softwares

Different applications for data processing were performed with the softwares listed in Table 6.

Table 6: Softwares

Software	Application	Provider
Adobe Illustrator	Image processing in vector graphics	Adobe Systems Incorporated, USA
Blender2.80	3D vector graphics	Blender Foundation, The Netherlands
FACSDiva™	Flow cytometry data analysis	BD Biosciences, USA
FlowJo™v10	Flow cytometry data analysis	BD Biosciences, USA
ImageJ	Image processing	Wayne Rasband (NIH), USA
Inkscape	Image processing in vector graphics	Free Software Foundation, USA
LAS V4.3	Microscope image acquisition	Leica, Germany
Matlab® R2017a	Programming & statistics	Mathworks, USA
NIS elements	Microscope image acquisition	Nikon, Japan
Origin® 2017	Data analysis and graphing	OriginLab, USA
Prism 8	Graphing & statistics	GraphPad Software, USA
Vision 4D 2.12.6	3D vector graphics	Arivis, Germany

2.2 Methods

2.2.1 Neocytolisis: design of a study to assess the effect of return from high altitude on RBCs and reticulocytes

The assessment of the role of oxygen in erythropoiesis was part of a larger study performed in collaboration between Saarland University (Prof. Dr. Lars Kaestner), University of Heidelberg (Prof. Dr. Heimo Mairbäurl) and Zurich University (Prof. Dr. Anna Bogdanova). The main purpose of this research was to confirm the phenomenon of neocytolisis occurring on neocytes, i.e. young RBCs, upon return from high altitude. Twelve healthy male volunteers in their 20ies were recruited for the study and monitored pre-altitude, during high altitude and post-altitude (figure 19). The donors living in Heidelberg (114 m above sea level) were exposed to a 3-week stay at the High Altitude Research Station at the Jungfraujoch (3450 m) in Switzerland to allow an increase in erythropoiesis. Their RBCs were labelled with the isotope ^{15}N-glycine before the stay and with the isotope ^{13}C-2-glycine after two weeks of stay in Jungfraujoch. Regular measurements of the ratio ^{15}N/^{14}N and ^{13}C/^{12}C by mass spectroscopy in heme allowed to follow RBCs lifespan during the control pre-altitude phase, during high altitude and post-altitude. The use of these specific isotopes allowed for an age-cohort cell labeling because of their incorporation in the heme and proteins of newly forming cells after ingestion. Analysis on plasma content, blood count, characterization of reticulocytes by flow cytometry, hemolysis assays, calcium permeability, oxidative stress and RBCs density measurements were performed to understand any possible mechanisms involved in this phenomenon.

Saarland University participated by performing the isolation of reticulocytes for transcriptome analysis of cells before and at high altitude and *in vitro* cell cultures to assess the exclusive role of oxygen in erythropoiesis, since in these conditions no changes in EPO amount could occur. For this purpose, cultures from PBMCs isolated from these donors were performed by comparing standard culture conditions, i.e. at atmospheric oxygen (20 % O_2) with cultures at low oxygen (3 % O_2). Oxygen concentration of this latter actually reflects the physiological average concentration of oxygen in the bone marrow at sea level. The representative amounts of oxygen would therefore rather be 3 % O_2 versus lower oxygen levels, but the *in vitro* system was designed and optimized for hyperoxia and for this reason 20 % O_2 represented the control condition. Besides the tests at high and low oxygen, additional cultures were performed on PBMCs isolated after the 3-week stay at high altitude to evaluate any changes caused by the hypoxia experienced by the donors. Therefore, pre-altitude cultures at 20 % O_2 were compared to pre-altitude at 3 % O_2 and to high-altitude isolated PBMCs cultured at 20 % O_2. Samples from these two comparison sets were named as follows:

i) "20 % O_2" and "3 % O_2" for the comparison between pre-altitude PBMCs;
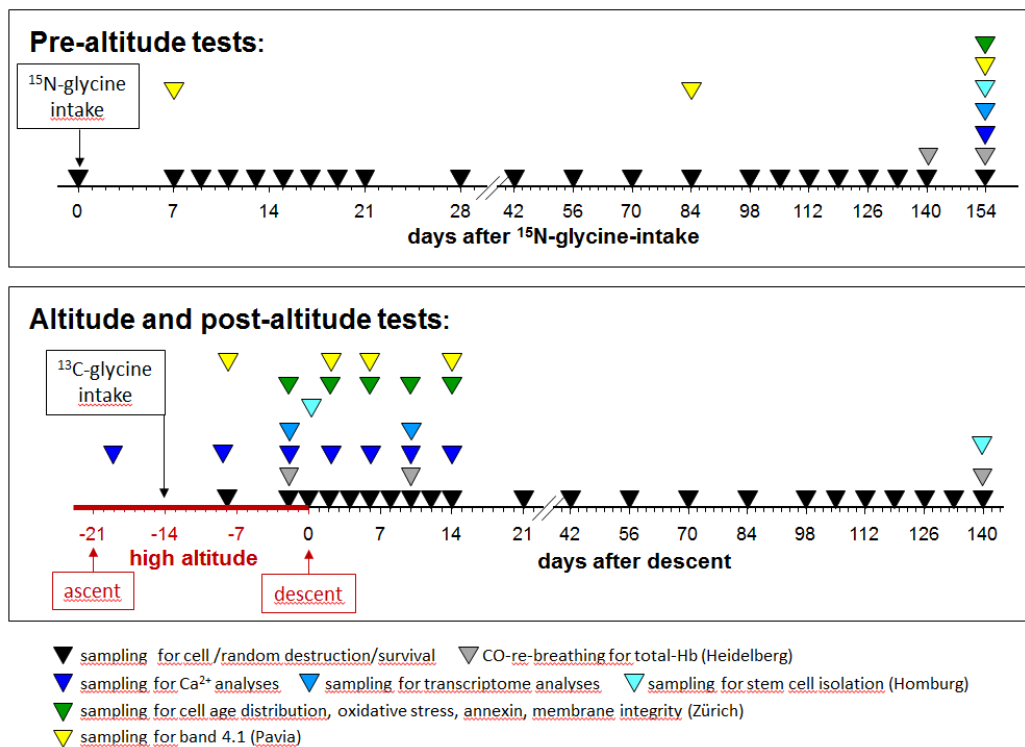
Figure 19: Timeline of the study showing all the experimental measurements plan. The study was divided into two phases: the control pre-altitude phase, when cells were labeled and tested until day 154 to check that no traces of labeled glycine were left; high altitude and post-altitude phase followed, starting from day -21 (day of ascent) to day 0 (day of descent) until day 140 to follow RBCs lifespan. Samples for stem cell cultures were collected at day 154 pre-altitude and day 0 post-altitude.

ii) "Pre" (pre-altitude) and "JJ" (Jungfraujoch) for the comparison between sea level and high-altitude-isolated PBMCs.

Cultures were performed on all 12 donors, divided in two culture rounds at 6 months distance. Only 5 donors were included for final statistical analysis because the 3 different culture conditions were performed simultaneously, canceling any possible difference occurred during the two culture rounds.

2.2.1.1 PBMCs isolation

PBMCs are located in the buffy coat, primarily including lymphocytes; only 0.16 % are HSCs (CD34+). In 1 ml of blood there are about 1 million PBMCs, meaning 1600 HSCs. For an efficient culture, it is necessary to isolate at least 8000 HSCs, hence to start with 5 ml of blood. PBMCs isolation was performed by centrifugation with ficoll, a polysaccharide with density of $1.077 \, g/ml$ at 20 °C that is used as an intermediate layer between buffy coat and RBCs (figure 20). In this way, it is technically easier to pipette out the buffy coat from contaminant RBCs. The method consisted in diluting at least 5 ml of blood with an equal amount of PBS to reduce its viscosity for pipetting. For the study, 27

ml of blood were used to ensure a sufficient amount of PBMCs for cultures. One part of this blood was added to 2 parts of ficoll in a tube, pipetting ficoll at the bottom and blood on top. This step requires a particular slow pipetting to avoid blood to mix with ficoll. Centrifugation for 30 min at room temperature and 400 g was following, setting no brake to avoid any friction causing the mix of the separated blood layers. Plasma was therefore at the top followed by a visible buffy coat ring, ficoll and, at the bottom, RBCs. After pipetting the ring out, three washes were done for 5 minutes at 500 g with PBS filled until the top of the tube to remove residual platelets. Cells were therefore subjected to a step for the specific lysis of RBCs (which are mostly reticulocytes) with the "RBCs lysis buffer" added to the cell pellet for 5 to 10 minutes at room temperature. After washing cells with PBS, the purified pellet could be either frozen or directly plated in Petri dishes for culture.
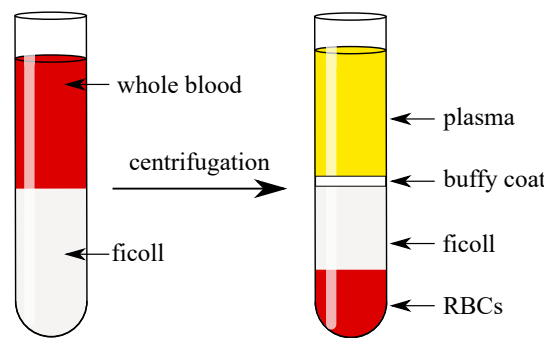
Figure 20: Schematic of PBMCs separation by ficoll. Blood is carefully pipetted on top of a layer of ficoll and after centrifugation results located between the buffy coat and RBCs.

2.2.1.2   Culture conditions

The following protocol was applied to cells cultured both at atmospheric oxygen (20 % O_2) and low oxygen (3 % O_2). The incubators were humidified and set at 37 °C and 5 % CO_2.

2.2.1.3   Expansion phase

In vitro cell culture included two phases, the first stimulating cell division (expansion phase) and the second their differentiation (differentiation phase). Isolated PBMCs were plated in a concentration of 5 to 10 million cells/ml in CellQuin medium supplemented with 2 IU/ml of EPO, 1 μM dexamethasone and 100 ng/ml of SCF. This counted as the "day 0" of expansion. Half of the medium was refreshed every second day in each Petri dish until day 7 or 8, when proerythroblasts come up. While they appear and are clearly recognized under a microscope by their large size, all lymphocytes progressively die, making the culture pure of erythroid progenitors. From day 7 or 8 cell count was monitored every day to maintain cell density to 1 million cells/ml to avoid spontaneous differentiation that occurs at higher cell density. Therefore, cells were constantly diluted with fresh medium

until the necessary number for following analysis was reached.

2.2.1.4 Differentiation phase

Differentiation was starting between day 12 and 14 of expansion. To follow this phase the last day of expansion was renamed as the "day 0" of differentiation. Cells were first centrifuged and washed once with PBS to remove traces of dexamethasone and SCF which inhibit differentiation. Afterwards, differentiation medium was added and calculated to plate cells at a density of $2\,million/ml$. Medium was CellQuin additioned of $5\,\%$ human plasma, $10\,IU/ml$ EPO, $5\,IU/ml$ heparin and $700\,\mu g/ml$ holotransferrin. Fresh or frozen plasma came from any donor cause no immune response could occur in the culture. During differentiation, the medium was refreshed, meaning a half change, at day 2 and day 5. At day 12-13 cell maturation was complete, resulting in a culture where most of cells enucleated, therefore becoming reticulocytes.

2.2.1.5 Coulter counter

Cell count and volume measurements were performed in a Casy count, a microfluidic device where cells flow suspended in an isotonic solution containing electrolytes. The current in the solution is measured and when a cell passes through the microchannel an increase in electric impedance is recorded. In this way it is possible to count how many particles pass and relate the electrical resistance to their volume. Cell samples were measured by resuspending the cells in Petri dishes, collecting $20\,\mu l$ and diluting them into 10 ml of CASYton solution. Cell count and volume measurements were set to record all particles with diameter above $4.5\,\mu$m. These measurements were done starting from day 8 expansion every day until day 0 differentiation to monitor cell density in the culture. From this moment, cell count was performed at day 3, 6, 9 and 13 of differentiation, when samples were collected for following experiments.

2.2.1.6 Flow cytometry and sorting

Flow cytometry is a technique based on the combination of a fluidic and an optical system, which includes light scattering and fluorescence measurements [112] (figure 21). A cell suspension introduced in a flow cytometer is sucked into the fluidic system and directed to a narrow aperture where a single-cell stream forms. Each cell is here hit by a laser and the incident light is scattered and recorded. In particular, Forward scatter (FSC) is the light collected along the same axis of the laser beam, while side scatter (SSC) is the light collected at 90°C from the laser beam direction. These measurements correlate with cell size and structure complexity, respectively and are typically used

in the analysis to distinguish different cell populations. Besides these parameters, flow cytometers measure fluorescence emitted by fluorophores used to tag cells for specific detection. Eventually, this technique provides a series of information on cell samples, e.g. the detection of different surface markers. The analysis is also highly efficient in terms of number of cells because the instrument easily detects thousands of cells/second, providing robust statistics and revealing rare cells (it is possible to record millions of cells in one experiment).
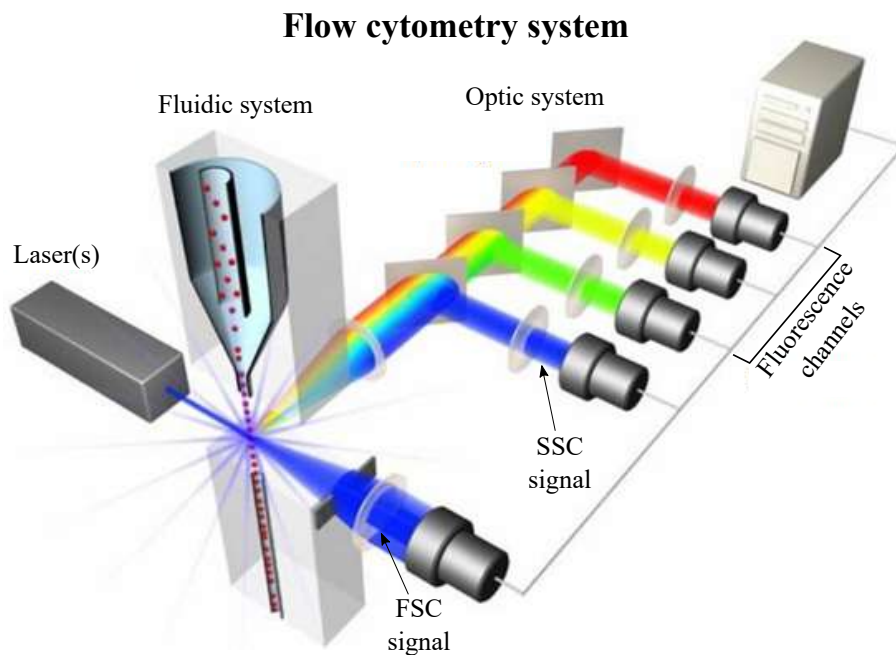
Figure 21: Flow cytometry principle. Samples are collected into a fluidic system that directs cells through a narrow aperture, where they flow singularly. A laser hits each cell and the scattered light is measured by a detector in front of the laser beam (FSC) an at 90° C (SSC). Each signal including any fluorescence detection is recorded by respective detectors for each fluorescence channel. Adapted from [17].

Flow cytometry was applied for different analysis:

- Assessment of cell markers presence during differentiation in culture, from day 0 and every 3 days, to compare cultures at $20\,\%\,O_2$ with $3\,\%\,O_2$ and to the high altitude PBMCs ("JJ" versus "Pre" altitude);

- Detection of HSCs by staining CD34 during high altitude and post-altitude;

- Detection of HbF in cord blood while studying glutaraldehyde autofluorescence.

2.2.1.7   Staining procedures

Culture samples were collected after cell count to be consistent with the number of stained cells between samples during the days of analysis. After collection, cells were placed in 96-well plates

containing 200 000 cells/well. An equal volume of HEPES buffer was added to each well and the plate was centrifuged for 2 min at 2000 g to remove medium traces. After discarding the supernatant, cells were stained for CD71 and CD235 expression assessment and for nuclear staining to distinguish erythroblasts from enucleated reticulocytes. CD71 and CD235 were marked by antibody-anti CD71 and anti-CD235 conjugated with Pacific Blue (PB) and Phycoerythrin (PE), respectively in order to perform a double staining in the same well. Nuclear staining was performed with DRAQ5 dye that marks DNA and RNA. As negative control, a well per sample was stained with isotype controls for CD71 and CD235, while an unstained sample was used to set the gating for DRAQ5. Master mixes for all culture samples were prepared in HEPES buffer supplemented with 0.5% BSA.

Table 7: Antibodies and dyes used for flow cytometry analysis on cell cultures.

Staining	Fluorescence channel	Stock dilution
CD71 isotype	PB	1:200
CD235 isotype	PE	1:200
CD71	PB	1:100
CD235	PE	1:200
DRAQ5	APC	1:2500

$100\,\mu$l of antibody mixes were added to each well, mixed and cells were placed in the fridge covered with aluminium foil for 20 minutes. Afterwards, cells were spinned down as described before and resuspended in $100\,\mu$l of HEPES buffer, except for the wells dedicated to DRAQ5 staining, where a master mix was added prior to flow cytometry analysis.

For the analysis of HSCs from the 12 donors performed both at high altitude and post-altitude $10\,\mu$l of fresh blood were diluted in 1 ml PBS and antibody anti-CD34 was added for 25 min at room temperature before the measurements.

In another experimental context, an intracellular staining for HbF was applied on cord blood by fixing $10\,\mu$l for 10 min in either 0.05 % or 1 % cold GA in PBS. A suggested protocol from the antibody supplier was followed: after one wash with 5 ml HbF staining buffer, cells were washed once and permeabilized with 1 ml of 0.1 % Triton X-100 for 10 min. After another wash, cells were resuspended in 0.5 ml HbF staining buffer and $10\,\mu$l of this suspension were incubated for 20 min at room temperature with the antibody against HbF. Following 3 washes, cells were resuspended in $500\,\mu$l of staining buffer.

Table 8: Antibodies used for flow cytometry analysis on stem cells and cord blood.

Staining	Fluorescence channel	Stock dilution
CD34	PerCP-Cy5.5	1:200
HbF	FITC	1:5

2.2.1.8   Flow cytometry analysis

The measurements were performed with the flow cytometer FACSCanto for cell cultures, with CyFlow Cube 5n for HSCs and Gallios for HbF measurements. The software integrated in the flowcytometers was FACSDiva. FSC and SSC were used to gate cultured cell population from debree and to distinguish the population of nucleated cells and extruded nuclei. Within the gated populations 10 000 events were recorded for cell culture differentiation samples, 5 million for CD34+ (HSCs) cell detection and 100 000 for HbF and GA tests. Each sample was measured together with its respective control sample, i.e. an isotype for antibody measurements, except for HbF and cell dyes, where the negative control was an unstained sample. Data analysis was performed with the software Flowjo_v10. FSC and SSC were used for cell population detection in addition to a single cell gating to exclude any cell duplets. Example graphs of cell culture analysis are given in figure 22.

2.2.1.9   Cytospin staining procedure

For microscopy evaluation of cell maturation, 100 000 cells were collected and placed into a cytospin centrifuge (Cytospin II Shandon) for 5 minutes at 72 g. Cytospin is a special centrifuge for microscopy slides, where cells can directly be spun on the glass, which mostly dries during centrifugation. Afterwards, the obtained cytospun cells were stained for nucleus, cytoplasm and hemoglobin. This procedure included immersion steps under a fume hood of the glass slides at room temperature for exact amounts of time in the order indicated in table 9.

Table 9: Giemsa/benzidine staining solutions and procedure for cytospin staining.

Solution	Immersion time
methanol	4 min
benzidine	2 min
hydrogen peroxide	2 min
demi water	rinse
difco red	4 min
difco blue	40 sec

Benzidine solution consisted of 1% O-diasidine in methanol. After staining in difco blue, a rinsing step was performed to wash out the excess color with demi water for 1 min 35 sec. Eventually, Hb resulted red-brown, nuclei were purple-blue, and cytoplasm of younger erythroid precursors purple

Example FACS staining data
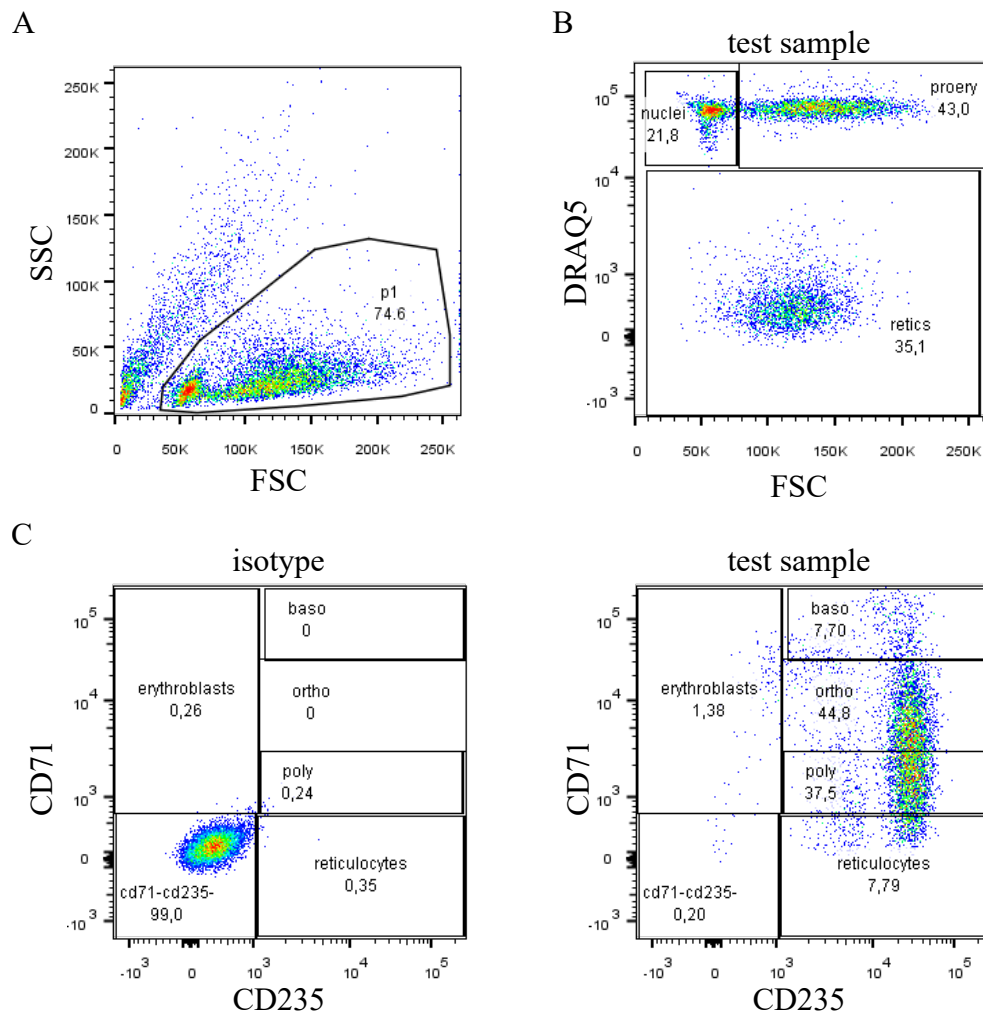
Figure 22: Representative graphs obtained by flow cytometry during differentiation. (A) SSC vs FSC to identify cell populations. P1 refers to cell culture population. (B) Nuclear staining with DRAQ5 plot with FSC. Nucleated cells (proery) can be distinguished from nuclei and enucleated cells (retics) which are negative for DRAQ5. Note the reduced FSC of nuclei and retics compared to nucleated cells. (C) Isotype control staining and CD71 and CD235 expression of a test sample.

(figure 23). Slides were let dry and then covered for microscopy observation.

2.2.1.10   Glucose, lactate and ion measurements

For metabolic activity tests, $300\,\mu$l of culture medium were collected from sample Petri dishes and measured in RapidLab instrument, which relies on amperometric and Ion Selective Electrode (ISE) analytical measurements for glucose and lactate, and ions, respectively.

Cytospun and stained cultured cells

Day 0   Day 6

reticulocyte
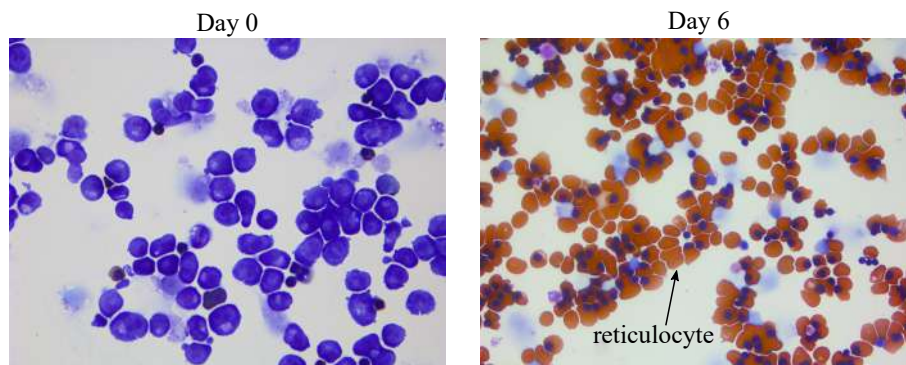
Figure 23: Example of stained cultured cells at day 0 and day 6 differentiation. At day 0 erythroblasts with a large purple/blue nucleus and purple cytoplasm can be observed. At day 6 advanced differentiation shows cells with a condensed nucleus containing Hb and formed reticulocytes.

2.2.1.11   Spectrophotometry for hemoglobinization assessment

Cell hemoglobinization was followed at day 0, 3 and 6 for all cultures conditions by collecting 150 000 cells/ culture condition. Each sample was divided in 3 equal amounts that were added in a 96-well plate for spectrophotometry measurement. Cells were therefore spinned down to remove culture medium and lysed with $20\,\mu$l distilled water. Prior to the measurement, $100\,\mu l/ml$ of a reagent mix containing 0.5 mg/ml o-Phenylenediamine dihydrochloride, $1\,\mu l/ml$ H_2O_2 and 0.1 M citrate/phosphate buffer adjusted to pH=5 were added to each well in a timed manner. After observing the first samples turning yellow (between 2 and 5 minutes), the reaction was stopped with $20\,\mu l/ml$ $8\,M\,H_2SO_4$ in each sample, controlling that the incubation time of each well with the reagent mix was the same. A row in every plate was used to add only the reagents as a blank. Each plate was therefore analyzed in an ELISA photometer by measuring the absorbance at 492 and 620 nm. Finally, every triplicate sample was averaged and the absorbance at 420 nm was subtracted from 620 nm and the blank to remove any background signal besides Hb.

2.2.1.12   HPLC

High-Performance Liquid Chromatography (HPLC) was employed in the dedicated facility for Hb expression assessment at day 13 differentiation on all cultures, with the particular interest to observe the expression of HbF. Collected cells were at least 5 million per sample and were washed from cell medium and resuspended in 1 ml PBS before lysis prior to the measurements.

2.2.1.13   Measurement of cell deformability

The Automated Rheoscope and Cell Analyzer (ARCA) is a rheometer additioned with a microscope used to measure cell deformability [42]. It was applied at day 13 differentiation as a functional assay for the obtained reticulocytes. In this device cells are spun to apply shear stress that induces their deformation. Cell elongation is therefore measured as the ratio of cell axis (length and width), thus being close to 1 for round cells and higher for more elongated cells. Samples collected from cell cultures were washed from the medium and resuspended in HEPES buffer, introduced in the ARCA for automated imaging at shear stress set to 10 Pa. The embedded software is provided with an option to automatically exclude nucleated cells, which are not deformable and therefore of no interest for the experimental condition. Average deformability value and standard deviation were used to compare the three culture conditions on the 5 cultured donors.

2.2.2   Methods employed for RNA isolation from purified reticuolcytes

2.2.2.1   Reticulocytes enrichment from whole blood

Reticulocytes enrichment was applied to fresh blood from the 12 donors before and at the day of descent for following RNA isolation and sequencing. Magnetic-activated Cell Sorting (MACS) separation is a magnetic beads-based method for the enrichment of cell types, such as CD71+ cells. The technique makes use of magnetic micro-beads that bind to the antibody against CD71, used to tag the cells of interest. These samples are therefore loaded onto columns containing larger magnetic beads and positioned on a permanent magnet. The columns serve to create a strong magnetic field to retain microbeads-labeled CD71+ cells, since the magnetic field of the microbeads would not be sufficient. After washing out non-labeled cells, removal of the columns from the magnet allows to elute the desired cells, obtaining an enriched percentage in the sample. MACS® Column Technology provided a protocol optimized for a certain number of labeled cells for each column type. For the study, MS columns were used and the amount of blood was tested between 20 and 160 μl. The steps involved blood centrifugation and suspension into degassed MACS buffer at 4°C with the addition of microbeads. Several tests were performed, diluting microbeads concentration of 8, 20, 40, 80 an 160 times. This staining was simultaneously performed with a fluorescent antibody anti-CD71 FITC and with anti-CD45, 1:200 dilution, for WBCs staining for 15 minutes at 4°C in rotation. After one wash, cells were loaded on the columns and the separation was performed as indicated by the protocol, with three washes to remove unlabeled cells and a final flush to collect the enriched sample. After first trials, the amount of blood used for the enrichment of reticulocytes from 6 pre and high altitude samples was 80 μl with a 20 times diluted microbeads and CD71 antibody staining to 1:50. These

experiments involved the collaboration of Laura Hertz.

2.2.2.2   Reticulocytes sorting

Enriched samples were checked on a FACS sorter to first detect the percentage of obtained reticulocytes. The threshold for the population to sort was therefore established based on corresponding unstained control samples signal to sort CD71+, CD45- cells. Sorting of "pre" and "JJ" was done on 6 samples at a time, requiring a minimum collection of 200 000 reticulocytes for next experiments. These measurements involved the collaboration of Laura Hertz.

2.2.2.3   RNA extraction from sorted reticulocytes

RNA extraction was performed both with the classical TRIzol-based method and with a special kit for total RNA extraction including miRNA. TRIzol is a solution which preserves RNA integrity while breaking down cellular structures. Sorted cell pellets were resuspended in different amounts of TRIzol, from $300\,\mu$l to $20\,\mu$l in different experiments testing the best concentration, and snap frozen in liquid nitrogen before storage at -80°C. For RNA isolation, frozen pellets were later thawed to room temperature and chloroform was added in proportion with the amount of TRIzol used as suggested by the company provider. A centrifugation step followed to separate cell components into an upper colorless aqueous phase containing RNA and an organic phase containing DNA, proteins and lipids. After transferring the aqueous phase, RNA was precipitated with ethanol, centrifuged, let fully air dry by keeping the sample lid open and finally resuspended in water. The procedure with the kit was similar. Sorted reticulocytes pellets were snap-frozen in liquid nitrogen and stored at -80°C. After thawing the samples, QIAzol lysis reagent was added. Next steps included addition of chloroform, centrifugation to separate the aqueous phase with RNA, its precipitation with ethanol on a spin column followed by centrifugation steps for ethanol removal and final RNA elution from the column with water.

2.2.2.4   RNA quality check by bioanalyzer

The bioanalyzer is an automated electrophoresis technique for DNA and RNA quantification, advantageous over the nanodrop spectrophotometer because of its high sensitivity for low concentration of nucleic acids. RNA is fluorescently labelled and the detected signal is related to its concentration. At the end of the electrophoretic run, a gel-like image and an electropherogram are generated, allowing to check the peaks and ratio of 18 and 28S RNA, indicated by the RNA Integrity Number (RIN). The eukaryote total RNA pico kit was chosen for this analysis.

2.2.2.5   Library preparation

DNA library preparation for following RNA-Seq was performed on 6-donors in both RNA samples from pre-altitude and high altitude ("JJ"). A step for both cytoplasmic and mitochondrial ribosomal RNA (rRNA) depletion was included in the library kit, requiring a minimum amount of 10 ng of RNA. From the obtained samples, 80 ng of RNA per samples were used.

Library preparation steps involve RNA fragmentation to reduce the size of nucleotides to sequence, addition of a poly-A (adenine) tail to 3' ends and retro-transcription to produce a cDNA (complementary DNA) filament (figure 24). In particular, retro-transcription with this kit involves the use of the reverse transcriptase from Moloney Murine Leukemia Virus (MMLV), which is able to perform template switching [174]. During cDNA first-strand synthesis, upon reaching the 5' end of the RNA filament, this reverse transcriptase adds a few more nucleotides, mostly C (cytosine) to the newly synthesized cDNA strand. This extra bases are used as template switching anchoring sites for the transcriptase. In fact, an oligonucleotide sequence including complementary G bases binds to the oligo-C and the transcriptase switches filament, synthesizing the remaining complementary bases of this oligo-sequence. This mechanism is useful to synthesize the full RNA sequence and to add sequence "adapters", which are later used for RNA-seq. Prior to the sequencing, a pre-amplification PCR step is also included in the protocol to increase the amount of cDNA. This experiments were done in collaboration with Franziska Drews and Marcello Piritano from the research group of Prof. Dr. Martin Simon.

2.2.2.6   RNA-Seq and analysis

Transcriptome sequencing was performed with Illumina technology by the bioinformatics group of Prof. Dr. Andreas Keller. The methodology consists in a cluster generation for the amplification of the cDNA library, based on the added adapters working as amplification primers. This step is followed by repeated sequencing (reads), which in the tested samples reached 5 million. Data analysis consists in grouping all the reads with similar structures, creating contiguous sequences, which are later mapped on the human genome for gene expression detection and quantification.

2.2.3   Study of RBCs fixation

2.2.3.1   Fixatives

Cell samples can be stored for long time when fixed with specific reagents. The most used are formaldehyde (FA) and glutaraldehyde (GA) (figure 25), either employed singularly or in combination, and osmium tetroxide, mostly used in electron microscopy applications. The first two molecules

Creation of a DNA library for RNA-Seq

RNA filaments fragmentation

Poly-A tail addition

AAAAAAAAAAAAAAA

3'-adaptor TTTTTTTTTTTTTTTTTV ⎤
5'-adaptor rXrXrX ⎦ primers

Reverse transcription

AAAAAAAAAAAAAAA
V TTTTTTTTTTTTTTTTT

forming cDNA

5'-adaptor binding
and template switching

XXX AAAAAAAAAAAAAAA
XXX TTTTTTTTTTTTTTTTT

reverse filament
forward filament

Pre-amplification PCR

XXX AAAAAAAAAAAAAAA
XXX TTTTTTTTTTTTTTTTT

Figure 24: Steps involved in library preparation. Isolated total RNA is first reduced into fragments, following a dephosphorilation step for poly-A tail binding to 3' end of all fragments. Reverse transcription is performed with a primer of poly-T complementary to poly-A including an adaptor sequence. When reverse transcriptase reaches the 5' end of the RNA filament, a few additional C bases are added by the transcriptase to the formed single-strand cDNA. The second primer can therefore bind with its G nucleotides to C, causing the template switching of the transcriptase, which synthesizes the complementary filament of this primer, including its adapter sequence. The library cDNA is then formed and a final PCR steps is performed to obtain and amplify double-strand DNA. Image modified from CATS Total RNA-seq v2 manual.

bind to amino groups, while osmium tetroxide fixes lipids. The result is the crosslinking of molecular cell structures, retaining cell morphological properties. GA is preferable to FA for RBCs fixation (see Results) and was here used to study how to preserve their original shape in the most accurate manner. For this reason, RBCs were fixed in different GA concentrations. Moreover, different GA suppliers were tested because cell fixation was performed in different laboratories with the batches indicated in table 10).

2.2.3.2 Measurement of osmolality

Glutaraldehyde was diluted in either PBS or NaCl according to the desire application to concentrations between 0.05% to 1% and the osmolality of each solution was measured. The osmometer was

formaldehyde   glutaraldehyde
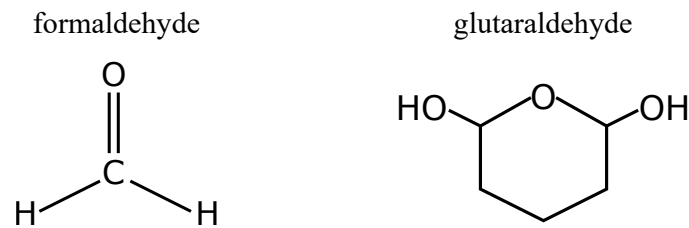
Figure 25: Molecular structure of formaldehyde and glutaraldehyde, showing the single and the double aldehyde (R-CHO) group, respectively.

Table 10: Glutaraldehyde tested suppliers

Supplier and grade	Mode of storage	Batch & employment
Sigma, grade I, 25 %	-20°C, >1 year storage	batch 1, fig. 52, 53 and RBCs' shape transitions by osmolality
Sigma, grade I, 25 %	-20°C, fresh batch	batch 2, fig. 52, 53, 55, cultured reticulocytes and HS patients
Merck 25 %	room temperature, >1 year	batch 3, fig. 52, 53
Fluka 25 %	room temperature, >1 year	MemSID trial and SEM samples
Sigma, grade I, 50%	-20°C	batch 4, fig. 52, 53, 55 and healthy subjects

checked for zero display with distilled water prior to each measurement. Each solution was diluted 1:10 to have a 110 μl sample for the measurement.

2.2.4 Methods applied for the morphological characterization of RBCs of sickle cell disease patients upon memantine treatment

2.2.4.1   Deoxygenation of blood

Deoxygenation of RBCs can be performed by decreasing Hb oxygen affinity or by physical removal of the gas. The first method can be realized by reducing Hb with sodium dithionite, while the second consists in incubating cells in a closed environment where the amount of oxygen is controlled. The difference between these methods is the speed of deoxygenation that causes different RBC shapes formation. In fact, sodium dithionite rather then "sickle" forms "mosaic" cells [8], i.e. cells with a polygonal aspect presenting Heinz bodies. The incubation in a chamber, such as a glove box, where oxygen levels are monitored, allows the formation of sickle cells, including several other sickled shapes containing fibers of HbS distributed in different orientations. In both methods, re-exposition of

RBCs to atmospheric oxygen triggers a back transition to the biconcave disk, therefore it is necessary to fix cells under deoxygenation to preserve their formed shapes. It was demonstrated that sodium dithionite reduces oxygen at a very fast rate, while nitrogen addition in a glove box allows a slow deoxygenation, necessary for the organization of HbS fiber [8]. Since slow deoxygenation forms actual sickle cells, deoxygenation in a glove box was later used to obtain artificially made sickle RBCs for first morphological analysis experiments.

2.2.4.2 Fast deoxygenation via sodium dithionite

Sodium dithionite ($Na_2S_2O_4$) is a toxic, inflammable powder with a characteristic pungent smell. Thanks to its reducing power, it was used to deoxygenate RBCs in a concentration of 2 % according to [8]. To a drop of fresh blood from SCD patients placed on a microscopy slide a drop of dissolved sodium dithionite in PBS was added and the glass slide was immediately sealed with a coverslip for microscopy examination. A lower concentration, 0.25 % dithionite, was additionally tested for comparison.

2.2.4.3 Slow deoxygenation by nitrogen

PBS additioned with 25 mM $NaHCO_3$, pH=8.05 at 37 °C was prepared and incubated overnight in a glove box with 1 % O_2, temperature set at 37 °C, humidity at 74 % and 5 % CO_2. The day after, $100 \, \mu$l of whole blood from SCD patients and at least one healthy control were diluted in respective Petri dishes containing 2 ml of deoxygenated medium in the glove box and left in deoxygenation for 8 hours. The slow oxygen diffusion through the dish caused the complete sickling of cells, leading to the formation of different deformed shapes depending on their speed of HbS fibers formation. After deoxygenation, $100 \, \mu$l of each sample were fixed in 1 ml deoxygenated 1 % glutaraldehyde in PBS inside the glove box and removed after 5 minutes. Fixed cells were therefore rotated for several hours. Glutaraldehyde solutions were deoxygenated when sample deoxygenation was starting. Control samples were incubated in the same conditions in a regular cell culture incubator, both for patients' samples and controls and later fixed in the same manner at atmospheric oxygen. A test on deoxygenation in the presence of calcium and memantine was performed. In order to activate NMDAR, the used medium for deoxygenation was supplemented with 1.8 mM $CaCl_2$, $300 \, \mu$M glutammate, $300 \, \mu$M glycine and $50 \, \mu$M memantine.

2.2.4.4   Morphological study on SCD patients undergoing MemSID trial: design of the study

At University of Zurich in the research group of Prof. Dr. Anna Bogdanova, the phase II Clinical Trial to Study the Safety and Tolerability of Memantine Mepha® in Sickle Cell Disease Patients (MemSID) was performed for 12 months on 6 adults with SCD, all homozygous for HbS. The study was conducted at the Clinic of Medical Oncology and Hematology at the Zurich University Hospital to evaluate the safety and tolerability of memantine in a small cohort of patients. The design of the trial included 5 phases, resumed in figure 26.
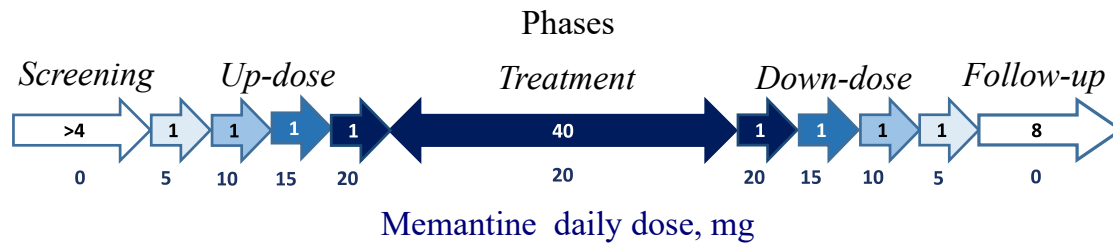
Figure 26: Design of MemSID trial. After a minimum of 4 weeks of screening, MEM was administered in increasing doses every week for 4 weeks to reach the maximal dose of 20 mg/day (up-dose), followed by the treatment phase for 10 months. After decreasing the dose to 0 in the course of other 4 weeks (down-dose) patients were monitored over next 8 weeks (follow-up phase).

Personal participation in the trial was within a secondment of the RELEVANCE project and included thorough confocal microscopy image acquisition and analysis of samples regularly collected and stored throughout the trial. The objective was to obtain quantitative data on sickle cell morphological characteristics and involved the use of programming tools, realized with the collaboration of Dr. Viviana Claveria.

2.2.5   General methods applied in multiple studies

2.2.5.1   RBCs samples fixation for storage and microscopy

2.2.5.2   Cultured cell fixation

At day 13 differentiation, cultured cells were spun down to remove extra medium and resuspended in $10\,\mu$l of this latter for fixation in 1 ml 0.1% GA in PBS and placed in rotation for at least 2 hours. Cells were stored at room temperature.

2.2.5.3   SDE shapes formation for studying cell fixation with GA

Blood was drawn with informed consent from 3 healthy donors via finger prick blood sampling in tubes containing $5\,\mu$l of EDTA 1.6 mg/ml. $30\,\mu$l of each sample were therefore resuspended in 1 ml of different concentrations of NaCl solution to induce specific shape transitions: $0.9\,\%$ NaCl (290

mosmol/kg H_2O) was used to keep discocyte shape and 0.4% NaCl (131 mosmol/kg H_2O) to induce sphero-stomatocytes formation. Intermediate shapes were obtained by suspending cells in 0.5% NaCl (stomatocytes type I and II) and 2.5% NaCl (echinocytes type I and II, 800 mosmol/kg H_2O) solutions. $20\,\mu$l of each cell suspension were fixed in 1 ml of 0.1% and 1% GA solution in NaCl. In order to fix cells with the desired shape, each glutaraldehyde solution was prepared to have a total osmolality equal to the osmolality of the NaCl solution used to induce each shape. Fixed cells were placed in a rotator-mixer at room temperature for at least 2 hours. Corresponding living cells for shape comparison were suspended in the different NaCl solutions just prior imaging.

For the automated shape detection via ANN, RBCs shape transitions were induced in the same manner to produce the SDE training data, using 5 healthy volunteers. Echinocytes type III were additionally formed by exploiting the glass effect on live cells (see CellMask staining).

For microscopy measurements, stored fixed samples were washed out from GA suspension solution. Cells were centrifuged at $2000\,$g for 5 minutes, washed three times with 1 ml of each respective NaCl solution used to induce the different shapes and eventually resuspended in 1 ml of the same solution.

2.2.5.4 MemSID trial SCD sample preparation

$5\,\mu$l of fresh blood were fixed in 1 ml of 1% GA solution and stored at room temperature. All the samples collected by the end of the treatment were washed 3 times in PBS with centrifugation for 3 min at 10 000 g between each wash.

2.2.5.5 Brightfield microscopy

Brightfield images of both live and fixed cells were acquired with a 50x oil objective on an inverted microscope.

2.2.5.6 CellMask staining

$5\,\mu$l of CellMask Deep Red plasma membrane stain were added to each sample, which was kept in rotation at room temperature. Staining time varied according to the application. For 3D imaging of fixed cells the staining was performed overnight, but for shape comparison with living cells, samples were stained for only 5 min due to CellMask toxicity. This dye is amphipathic, preferably binding to the membrane but can also be internalized into the cytoplasm, increasing cell fluorescence signal. Three washes were performed prior to imaging.

Echinocytes type III were induced by exploiting the glass effect, occurring when living RBCs are suspended in an isotonic solution deprived of BSA. Therefore, $10\,\mu$l of blood were suspended in 1 ml PBS and labeled with CellMask Deep Red. Following 3 washes, cells were resuspended in PBS and placed on a glass slide for confocal microscopy.

For tests on ANN automated 3D shape recognition, $5-10\,\mu$l of whole blood from other healthy volunteers and patients with hereditary spherocytosis were fixed in 1 ml of either $1\,\%$ or $0.1\,\%$ GA, stained as described above and imaged. Patients' samples were fixed and shipped from Fondazione IRCCS Ca' Granda Ospedale Maggiore Policlinico (Milan) and University Medical Center Utrecht (The Netherlands) with the same protocol described here.

2.2.5.7   EMA staining

Eosin-5'-maleimide (EMA) is typically used to stain band 3 protein [80] as it binds its Lys430. The method is normally applied on living cells and was here performed to test any effect of fixation. Therefore, both fresh and GA fixed RBCs were employed. $2\,\mu$l of fresh blood or fixed cells were added to $50\,\mu$l EMA supplemented with 10 mM $CaCl_2$ and incubated at room temperature for 2 hours in rotation [161]. Samples were then washed 3 times with 1 ml of tyrode solution at 300 g for 2 min. Each sample was therefore resuspended in 1 ml of tyrode solution and imaged in confocal microscopy with a 100x oil objective and an excitation wavelength of 488 nm. GA autofluorescence was examined at 647 nm.

2.2.5.8   PKH67 staining

Another membrane staining was assessed to study its compatibility with fixed cells, PKH67. The applied protocol suggested by the manufacturer was based on the use of $10\,\mu$l of packed cells stained with $0.5\,\mu$l PKH67 to incubate at room temperature for 5 min. Afterwards, 3 washes followed before resuspension in 1 ml PBS. Living cells were resuspended in PBS supplemented with $0.1\,\%$ BSA for imaging.

2.2.5.9   Confocal microscopy

Confocal microscopy is a technique that uses a focused laser beam to reduce the depth of field of an image by detecting the fluorescence signal exclusively coming from the focal plane [58]. The

applications go from protein co-localization to 3D imaging since the enhanced z resolution allows to take several images of a cell at different focal planes. Afterwards, such images can be re-stacked to obtain a 3D cell reconstruction. The principle consists in utilizing a pinhole, i.e. a narrow aperture, as a spatial filter for the emitted fluorescence of the sample. In this way, the fluorescence emitted by the sample is sent to a detector through the pinhole, thus reducing the signal to the photons exclusively coming from the focal plane and not from regions above or below it, as it occurs in a conventional fluorescence microscope. This can be realized by, e.g. two approaches: laser-scanning and spinning disk confocal microscopy. In the first, the focused beam is directed to small areas to scan point by point the whole sample surface; in the second, two aligned disks between the dichroic mirror are equipped with multiple pinholes and spin to scan all sample surface. The advantage of this method is the speed of imaging, since it is based on multi-point scanning.

Confocal microscopy principle
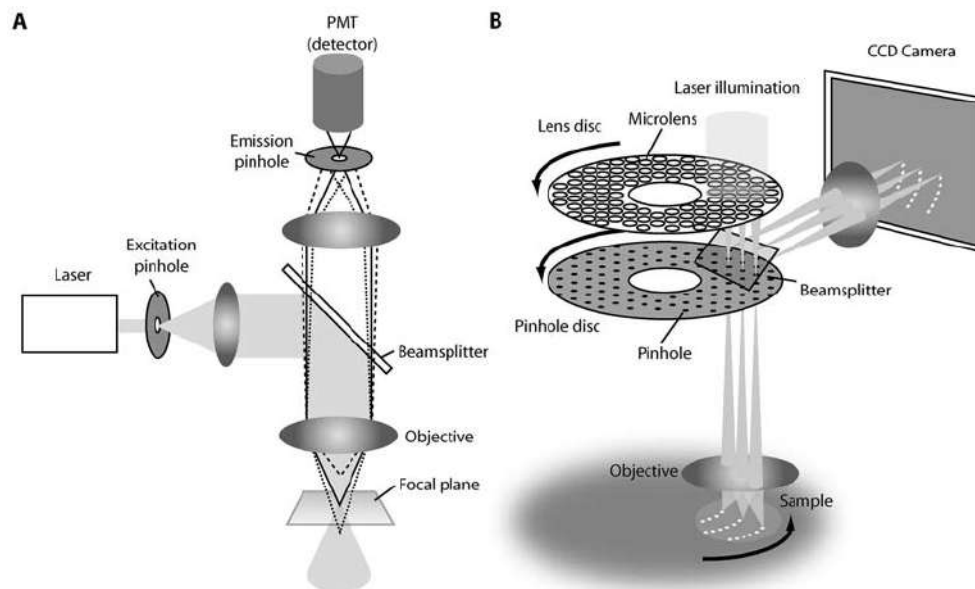
Figure 27: Principle of confocal microscopy. (A) Single-point scanning confocal microscope. The pinhole allows the light coming from one focal plane to be focused on the digital camera, canceling out the light coming from other focal planes. A first pinhole is used as a spatial filter for the laser beam and a second for the emitted fluorescence of the sample. (B) Multi-point scanning confocal microscope (spinning disk microscope), where the spinning disks with several pinholes increase the scanning speed. Image from [58].

2.2.5.10 3D imaging

Each labeled sample was placed in between two glass slides together with $20\,\mu$m diameter beads as spacers for imaging on top of a $60X$ oil objective of an inverted microscope. A diod laser emitting at

647 nm was used as a light source for imaging. Z-stack scanning were realized with steps of 300 nm for a 20 μm Z-range. Confocal image generation was performed with a spinning-disk based confocal head and image sequences were acquired with a digital camera.

2.2.5.11   Examination of autofluorescence quenching

To test GA autofluorescence quenching, fixed cells were permeabilized with 1 ml 0.1 % Triton X-100 for 10 min, washed and resuspended in 1 ml PBS. 200 μl of this suspension were added to 800 μl of 0.4 % trypan blue in PBS. After 15 min of incubation at room temperature, cells were washed twice and imaged in the confocal microscope as just described.

2.2.5.12   Sample preparation for scanning electron microscopy

Cell preparation for electron microscopy is delicate and requires a series of steps to preserve their morphological characteristics. Each sample must be dried out of all cell water content to avoid cell collapsing during a step in the vacuum and the dehydration process must be gradual. As a first step, stored fixed samples resulting in 0.2 % hematocrit were diluted 1 to 100 in PBS and placed in a cytospin centrifuge for 6 minutes at 600 rpm. Cell density was later checked at the optical microscope to confirm a proper cell distribution (no cells overlapping or too close), therefore each glass slide was mounted on a holder immersed in PBS to avoid cell drying. After 3 washes in PBS by mixing up and down the sample holder, this latter was placed in a solution of 1 % osmium tetroxide and left for at least 30 minutes at room temperature to allow lipid fixation. The holder was then washed 3 times in PBS, leaving the sample holder in for a few minutes. Afterwards, sample dehydration was performed in ethanol in gradual steps, starting from 30 minutes in 70 % ethanol, followed by other 30 minutes in 80 % and a final incubation for at least 1 hour in 100 %, in this last case in fridge covering the sample with parafilm. The dehydrated sample was then ready for the critical point drying, a process during which the dedicated instrument gradually substitutes ethanol with liquid CO2 and evaporates it in a final step at 40° C and at a pressure of 80-85 bars to finalize cell dehydration. At this point, samples were inserted in a sputter coater, i.e. a machine coating cell surface with a metal, in this case platinum, to make it homogeneously conductive. The chosen film thickness at the end of the process was 4 nm. Ready samples were finally mounted on the dedicated SEM holder for imaging.

2.2.5.13   SEM imaging

Scanning electron microscopy is based on the use of an electron beam as a source for creating an image of a sample. The electron beam is generated by applying high voltage to heat an e.g. tungsten

lamp until it releases electrons. Such beam has an undulating nature like the light, but at much smaller wavelength than this latter, allowing for higher resolutions (the theoretical limit is 0.2 nm). Samples need to be conductive in order to send electrons to the detectors. Two main types of electrons can be distinguished: Back-Scattering Electrons (BSE), i.e. reflected electrons from the beam as a result of the elastic interaction with the sample, and Secondary Electrons (SE), which correspond to the electrons released by the sample as a result of non-elastic interactions with the beam. BSE travel through the sample, moving deeper according to the weight of the atoms they hit: the lighter the deeper and viceversa. When many electrons pass through the sample only a few are re-emitted, and the image appears dark. Therefore, the lighter the image, the heavier the atoms. SE come from the surface of the sample and therefore provide an image of its topology. The detectors for BSE and SE are different: the first is located on top of the sample, while the second on the side. The choice for one or the other depends on the desired image effect: BSE is ideal for visualization at high magnifications because it provides a better contrast, while SE creates a 3D effect on the images. This detector is a scintillator converting the received electrons into light before the creation of the image and is the most commonly used. To create a picture, the electron beam is moved through a pattern of points on the sample, scanning each area, which depends on the dimension of the beam that is regulated by the condenser. SEM works in vacuum to avoid the interaction of air molecules with the electron beam, possible contaminations and to provide a better detection of BSE and SE. The voltage applied can enhance the resolution because it accelerates the electrons and needs to be adjusted for the desired images. Here, 5 to 10 kV with SE detector and occasionally BSE were used and typical magnifications were 5000 to 10000 X.

2.2.5.14   Confocal image processing for analysis of projected areas, eccentricity and solidity

Confocal imaging was preferred to brightfield microscopy because it provides a more defined border detection, especially important for spiky cells, where each spicule is oriented in different directions, making it impossible to focus each cell surface detail. In addition, confocal imaging abolishes the problem of different focal areas within a cell and between cells in the same image, since the obtained projected image is always the maximum intensity projection. Despite the fact that projected area, eccentricity and solidity are 2D parameters strongly dependent on cell position with respect to the microscopy slide, confocal projections make their analysis more accurate than brightfield microscopy. A semi-automated Matlab routine was used to enable the detection and extraction of the mentioned geometrical characteristics in individual RBCs. From the stack of images obtained, the maximum pixel intensity value was identified for each (x,y) position and projected at z=0, i.e. on a single plane in order to obtain 2D images with homogeneous background and cell border. Automated detection of

cell border from confocal images is simple because of the application of binarization, i.e. an image processing step where a grey scale is transformed into an image made of only 2 colors (black and white). The requirement for this step is to set a pixel intensity value as a threshold to establish where is cell border. This threshold was set to 80 out of 255 values of the grey scale and the identified objects (RBCs) were set to pixel value 1 (white), while the background to pixel value 0 (black). The coordinates of cell borders were defined as the positions of the interface between the objects and the background. The number of pixels inside the cell border was defined as the cell projected area, A. The major and the minor axis, a and b respectively, of an ellipse that fits to the cell contour and its eccentricity ε were obtained. Eccentricity is defined as

$$\varepsilon = \sqrt{1 - \left(\frac{a}{b}\right)^2}$$

where $\varepsilon = 0$ represents a perfect circle and $\varepsilon = 1$ a line. This value is used as a measure of cell elongation. A third parameter was obtained as the ratio of cell projected area, A, and the area of the smallest polygon that can contain the binarized cell, Ap, defined as solidity, s, where

$$s = \frac{A}{Ap}$$

Solidity is a measure of the roughness of a cell, meaning how "spiky" are its borders. $s = 1$ indicates a perfect smooth surface, while cells with $s < 1$ have some degree of roughness which is increased as s decreases. Once area, eccentricity and solidity from all cells of each sample were obtained, small objects, overlapped and highly drifted cells were filtered out by setting a maximum as well as a minimum projected area accepted values. The majority of non-applicable detections were removed in this first filtration step. Figure 28 shows the detection of these 3 cell features. These image processing steps were performed in collaboration with Dr. Viviana Claveria.

2.2.5.15 2D cell shape manual classification

Detected cells were subjected to a manual and individual scrutiny for their classification and to filter out remaining non-applicable detections. The classification was based on three groups: 1) "non-sickle" cells, that included all shapes within the SDE transition scale, i.e. discocytes, echinocytes and stomatocytes; 2) "sickle", meaning clear sickle cells and additional shapes mostly forming during *in vitro* deoxygenation, described by [37]; 3) "others", to include additional shapes (e.g. teardrop cells), and deformed cells without a clear known shape observed in SCD (figure 29). Eccentricity was used as a reference value to distinguish discocytes from ellyptocytes: cells with $\varepsilon = 0.7$ were classified as
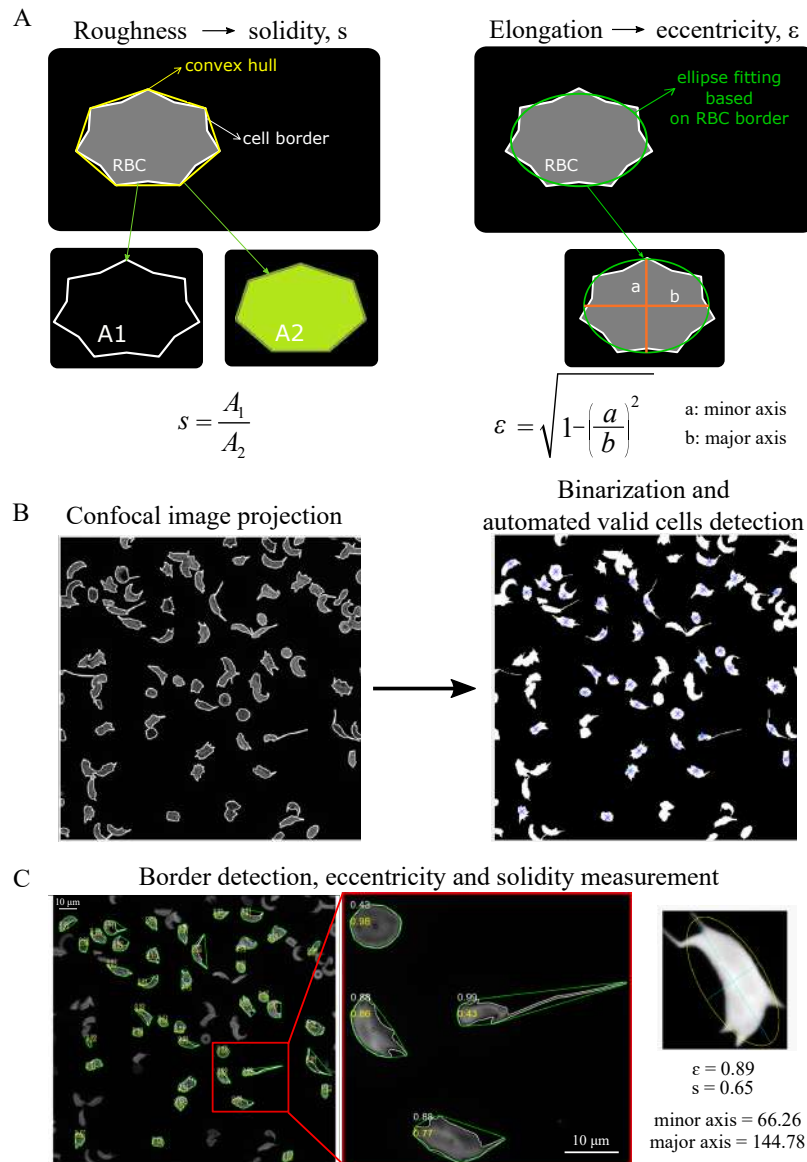
Figure 28: Image processing from confocal projections. (A) Scheme showing solidity, representing cell border roughness, and eccentricity, a measure of cell elongation, with their respective equations. (B) Example of an image projection of SCD cells previously deoxygenated *in vitro* with fluorescence intensity corresponding to cell labeling (note more staining on cell membrane); on the right, corresponding image after binarization, showing automatically selected cells (marked with x). (C) Border detection of each cell and measurement of eccentricity and solidity. The chosen sample of deoxygenated SCD RBCs can clearly show the different values between highly sickled and deformed cells from regular discocytes.

ellyptocytes and therefore included in the group "others". As shown in figure 29, cell shape is not a sufficient parameter for differentiation of SCD RBCs from healthy ones. The addition of quantitative measures with projected area, eccentricity and solidity allows for the detection of other differences.

Figure 29: Example shapes in (A) patients with SCD and (B) healthy subjects. Patients and healthy donors "non-sickle" class show morphological variance, where a defined and smooth biconcave shape can be observed in healthy RBCs, while not as smooth in patients. As well, the category "others" in SCD patients includes a variety of deformed cells, while in healthy rare elongated cells such as elliptocytes.

2.2.5.16   Plots

The distribution of the projected area values among the population of RBCs for each sample was obtained by using the probability density function estimation based on a normal kernel function, where Gaussian smoothing and bandwidth values set by default in Matlab were not changed.

2.2.5.17   Statistical analysis

Data from MemSID trial comparing three different time points were analyzed for statistical significance by unpaired one-way ANOVA test. Whiskers of the box plots of projected area and eccentricity include maximum and minimum values of the distributions divided in quartiles, while solidity includes 95% of the distribution interval. Each distribution included between 500 and 1000 cells. Plots of eccentricity vs projected area and solidity vs projected area show mean value and standard deviation.

For *in vitro* erythropoiesis data, two-tailed paired t-tests were used for comparison between atmospheric ($20\,\%$ O_2) and low oxygen cultures ($3\,\%$ O_2) or atmospheric oxygen from cells isolated before (samples "Pre") and from high altitude (samples "JJ"). For hemoglobinization and Hb type evaluation in the three conditions in comparison, one-way ANOVA was used. Plots show mean values and standard deviation from a total of 5 donors. Statistical significance is indicated with stars, where one star corresponds to $p \leq 0.05$, two stars $p \leq 0.01$, three $p \leq 0.001$ and four $p \leq 0.0001$. Omitted stars or the indication ns stand for non significant results, i.e. $p > 0.05$.

2.2.6   Methods applied in the study on the automated 3D classification of RBCs' shapes in hereditary spherocytosis

2.2.6.1   Confocal image processing for single cell 3D reconstruction

A custom written MATLAB routine was used to crop single cells in each image and perform their 3D reconstruction to enable the visualization of the 3D shape. Each original 3D image containing 68 planes had a resolution of $0.11\,\mu\text{m/px}$. In z direction, the piezo stepper had a maximal resolution of $0.3\,\mu\text{m}$. This difference between the dimensions caused the 3D reconstruction to have a mismatch in scaling. To overcome this issue, the z-dimension was rescaled by adding artificial planes via interpolation to obtain the same resolution as in x-y-plane. The 3D re-scaled image was then made of isotropic voxels, i.e. the same edge length for each direction. After rescaling, the offset was removed by subtracting the minimum intensity value. Therefore, the intensity values were normalized to 1. In this way, fluorescence intensity values were adapted to a range from 0 to 1 in every image, making it possible to apply the same absolute threshold to each of them. Since the microscope records many cells at the same time within each field of view, single cells had to be cropped. For this purpose, the image stack was first collapsed (summed in z-direction) to obtain its projection on a single plane. Afterwards, a threshold for binarization was applied to allow to segment and crop each cell singularly. The chosen cropping area was 100 px x 100 px. After cropping, each image plane was finally re-stacked in z-direction to obtain single-cell 3D reconstructions. The software for this step was written in collaboration with Dr. Stephan Quint and Dr. Revaz Chachanidze.

2.2.6.2   Design of a 2-stage supervised ANN with classification and regression outputs

The training can either occur in a supervised or unsupervised manner, meaning that the data are either fully evaluated beforehand (manually) or self-learned exclusively by the network. Since the shapes of RBCs are mostly known, the supervised approach was here chosen. In particular, as mentioned in Introduction, two types of output were designed: a regression one to recognize shapes owing to the

SDE sequence and a classification one for the recognition of all other shapes (mostly pathological ones). To obtain two different output types it is necessary to design two different ANNs. Since in this project the two networks were consecutive, the whole system was defined as a 2-stage ANN. Mathematically, a regression is represented by floating points (rational numbers) which were here placed on a continuous scale. In this 2-stage ANN the output layer was made of a single neuron that gave as an output a value between -1 and +1 by applying a linear function. This choice for shapes within the SDE sequence was motivated by the observation that RBCs in 3D do not show their transitions from one shape to another in a discrete manner as described by Bessis, but are rather continuous. Therefore, this scale was proposed in this project as a progression of Bessis' classification of RBCs, where SDE shapes were divided into specific degrees of stomatocytes and echinocytes (see "Morphological characteristics" in Introduction). On the contrary, the second approach involving a classification output was applied to all the shapes not owing to the SDE scale. In this case any possible shape transition is currently not known, therefore they could only be assigned to a specific class.

2.2.6.3   3D cell shape manual classification

Each 3D re-meshed cell reconstruction was rendered in Blender 2.80 for cell shape visualization and individual manual classification. Since the 2-stage ANN was trained with a chosen shape dataset, cells had to be first labeled. Therefore, SDE shapes were carefully selected to be assigned to a specific position on the continuous scale and for this purpose Bessis classification and other indicative shape criteria [96, 81] were used. In particular, SDE shapes were manually selected as follows: "discocytes", i.e. clear biconcave and symmetric discs; "stomatocytes type I", i.e. monoconcave cells, "stomatocytes type II", i.e. monoconcave cells with a deeper invagination, "spherocytes", i.e. spherical cells; "echinocytes type I", crenated cells still keeping their biconcavity, "echinocytes type II", meaning cells with forming spicules and "echinocytes type III", i.e. cells with more than 25 spicules. For the classification output the chosen shapes were: "knizocytes", i.e. cells with three lobes, "keratocytes", a category including several damaged RBCs, "acanthocytes", meaning echinocytes and sphero-echinocytes with irregular spicules, and "multilobated" cells, representing early reticulocytes. A class for exclusion of an artifact that can occur upon fixation, i.e. the presence of "cell clusters" (cells sticked to each other), was added. Each class of the training dataset contained a minimum of 10 cells to a maximum of 200 cells. Any other shape beyond the chosen classes was not introduced for the training process due to low occurrence and lack of identification into a known shape type in literature. This shape variability was particularly observed in 3D-reconstructed cells of patients with HS. For this reason, an additional class for "unknown" shapes was added. This class was the only one not trained with a dataset, but it was ruled out by setting an accuracy threshold to the neural network,

meaning that all cells below 70 % accuracy were automatically classified as "unknown". This passage was created to reflect the uncertainty of a human observer encountering unclear shape types (figure 30).
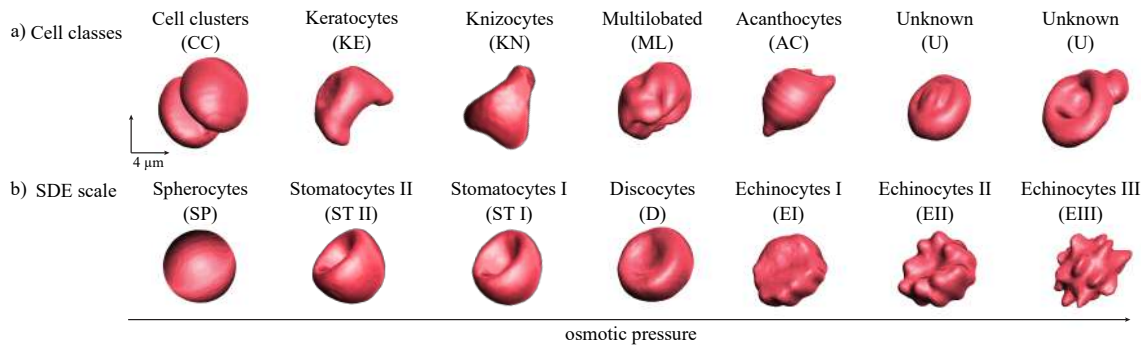

Figure 30: Example 3D reconstructions of RBCs used to train the 2-stage ANN. (A) Representative shapes for the classes. The class "unknown" shows here two example shapes but included a large variety of other shapes. (B) Example cells with shapes owing to the SDE scale, selected as representative of Bessis' classification.

Both classification and regression outputs were therefore trained using the described shape classes. However, while the classification assigned every cells to a defined class, the regression output assigned each SDE shape a score in order to create a continuous scale. The score was between -1 ("spherocytes") and +1 ("echinocytes type III"), with intermediate scores for the shapes in between: -0.67 for "stomatocytes type II", -0.33 for "stomatocytes type I", 0 for "discocytes", +0.33 for "echinocytes type I" and +0.67 for "echinocytes type II" (figure 31). The advantage of this method was that any cell that was not easy to define by eye, e.g. a "stomatocyte type I" or "type II" could be left out from the training dataset because, provided a successful ANN training, it was later automatically assigned a score by the ANN.

2.2.6.4   Spherical harmonics as data type for the ANN

The input data for the ANN were neither the 3D images nor the renderings but rather a transformed representation that reduced the amount of data while obtaining the characteristic details. This allowed for simple ANN structures, hence an optimized learning performance as well as training (classification process). 3D images in a computational sense are numbers organized in a matrix in 3 dimensions, where any mathematical operation applied corresponds to a modification of the original image. Each unit in a 3D matrix of a 3D image is a voxel with coordinates in x, y and z dimension. If a 3D RBC reconstruction is rotated in a certain position, the 3D matrix will have different coordinates. Using 3D data in this form would affect the training of the ANN by each cell rotation. Same relates to cell translation in the field of view. Rotation and translation are features that highly affect the per-
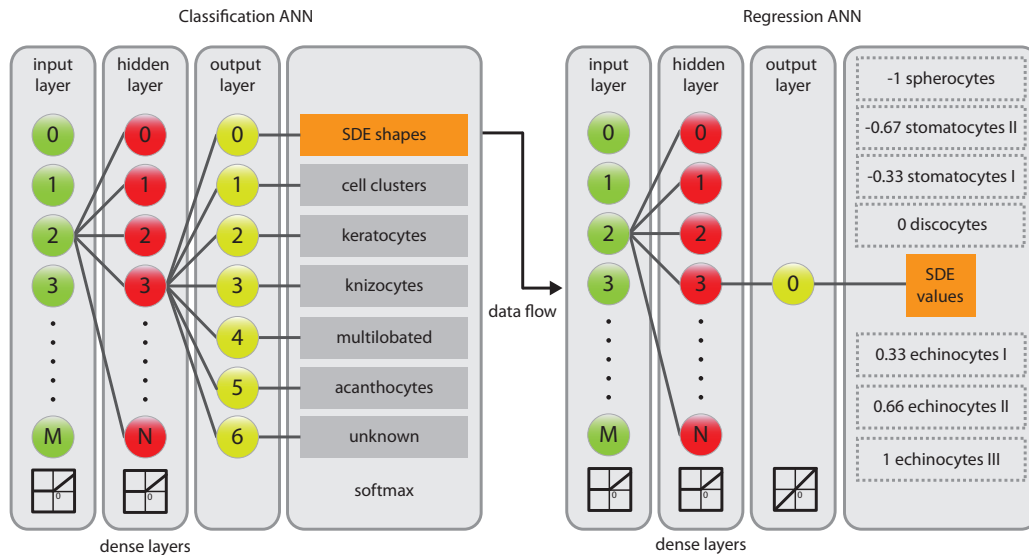
Figure 31: Two-stage ANN: the first output was the classification of RBCs. All the input data resulting in the class "SDE shapes" were additionally flowing to the second ANN that would output a score, assigning a position in the SDE scale that corresponded to each shape transition. SDE=stomatocyte-discocyte-echinocyte scale.

formance of cell shape recognition, but it is possible to overcome both issues by applying a set of mathematical functions to the 3D image, known as Spherical Harmonics Analysis (SHA) [79]. This particular transformation has the peculiarity of making the analyzed object invariant to rotations while simultaneously reducing the amount of data. The SHA finally collapses all data to a single-dimension vector, which can be directly processed by an ANN without any need for further processing (such as convolution). In order to transform the 3D reconstructions of single cells into their SH components, each 3D reconstructed cell was firstly vectorized by applying a threshold to transform the defined cell membrane into an iso-surface (mesh of organized points and edges). Originating from this representation, the SHA algorithm of Kazhdan [79] was then applied. The obtained spectrum from each 3D reconstruction resulted in 544 components, which corresponded to the size of the input layer of the used ANNs. Each component was therefore assigned a weight by the 2-stage ANN, some components resulting more relevant than others in defining a cell shape. The whole 2-stage ANN was therefore organized as follows: 544 neurons for the input layer in both the classification and regression ANN; 54 for the hidden layer of the classification and 544 for the regression; 7 neurons in the output layer of the classification network representing shape classes and 1 neuron for the regression-type ANN. An example of the whole work-flow of the system applied to each image is given in figure 32.
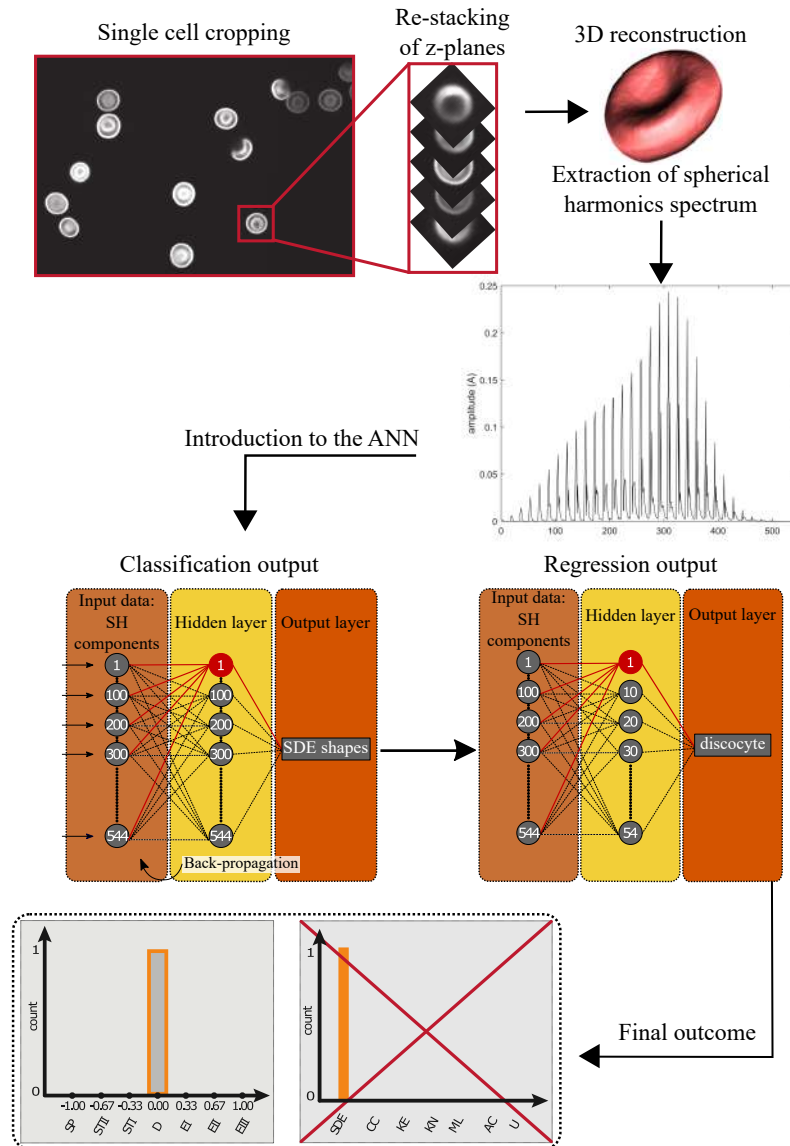
Figure 32: Scheme of the whole work-flow for 3D automatic RBC shape recognition by the 2-stage ANN. After obtaining confocal image stacks of cells, each image was projected onto a plane for single cell cropping. Therefore, each cell was re-stacked to obtain its 3D reconstruction. The obtained image was then transformed into the corresponding spherical harmonics spectrum, which collapsed the characteristics of interest to a low dimensional representation that is invariant with respect to rotation and translation but included all relevant information for shape recognition. Each spectrum was provided to the 2-stage ANN, where each neuron of the input data was one component of the spectrum. The example cell has a discocyte shape, so the data do not stop at the first classification stage but proceed to the second ANN which places the cell onto the SDE scale with the score 0.

2.2.6.5   Training and validation

After manual classification, the ANN was trained with Keras, an open source framework for an easier use of Google Tensorflow with Python. The amount of data manually selected was very low for an optimal ANN training, which requires thousands of cells. Besides taking an interminable amount of time, this is not practically applicable on rare cells. Therefore, a data augmentation step was applied,

a typical approach to dramatically increase the amount of data artificially. In this case, data augmentation was performed by applying a superposition between several SH spectra of cells of the same class or in between neighboring types on the SDE scale. For example, 20 % of one spectrum (cell 1) was added to 80 % of another spectrum (cell 2), creating a new spectrum that therefore represented a new cell which was a mixture of both. The augmentation applied accounted for 2000 interpolations, meaning that each shape class finally contained 2000 cells (real and artificially created cells). In the case of SDE shapes, cell spectra were also interpolated between neighboring shape types, i.e. echinocytes type I with echinocytes type II and these latter with echinocytes type III, and so on. 80 % of the training of the ANNs was actually used to train, while the remaining 20 % was used to validate the learning process. In order to obtain the best performing 2-stage ANN, k-fold cross validation was used by training each of the 2-stage ANN with 100 random seeds. The best random seeds were chosen to be used in the perspective of re-training the ANN for a larger cell dataset. As mentioned in Introduction, the loss function for the classification ANN was the CE, while for the regression ANN the MSE. The chosen optimization function was Adam, a specialized gradient descent algorithm [85]. Adam stands for "adaptive moment" and has the advantage over other systems to adapt the learning rate during the training, enhancing the chance to find the global minimum.

2.2.6.6   Automated 3D shape-classification in healthy subjects and patients with HS

Once the 2-stage ANN was validated, a total of 25 healthy subjects and 11 patients affected by HS was automatically classified by the 2-stage ANN. The number of classified cells varied between a minimum of 400 until a maximum of 2000 cells per sample. Results of the automated shape recognition were compared with a manual check of the shapes in each class, including the SDE shapes, by randomly picking 200 cells per sample. Finally, in the case of 3 patients the shape distribution in 3D was compared to the counts on corresponding blood smears.
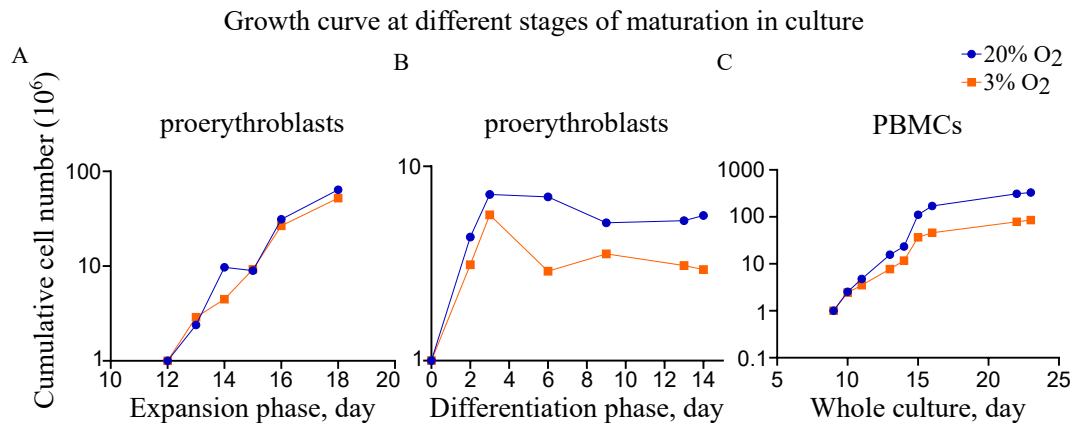
3. Results

3.1 The role of oxygen in erythropoiesis and neocytolisis

This first chapter describes the results on cell cultures at two different oxygen concentrations to assess the role of oxygen in erythropoiesis and a method for reticulocytes isolation and RNA extraction for RNA-Seq. The objective of both experimental applications focused on understanding the possible mechanisms leading to neocytolisis.

3.1.1 Varying oxygen concentration during cell erythropoiesis in culture

Culture protocol was developed for growing cells in regular incubators at atmospheric oxygen ($20\,\%\,O_2$). However, physiological concentrations in the bone marrow reach on average $3\,\%\,O_2$ and this may impact expansion and differentiation of cells in culture, either resulting in a higher cell number due to a better expansion and cell survival or failing because culture protocol was optimized for a hyperoxic ($20\,\%\,O_2$) condition. Therefore, PBMCs of a test donor were incubated at different maturation stages in $20\,\%\,O_2$ and $3\,\%\,O_2$ to verify if cells could grow and survive at low oxygen (figure 33). Three conditions were tested: (i) proerythroblasts expanded from day 0 to day 8 in $20\,\%\,O_2$ and moved to low oxygen at day 9 until day 18 to test the impact of oxygen on cell expansion potential; (ii) expanded proerythroblasts in $20\,\%\,O_2$ moved to low oxygen at day 0 differentiation to test the effect on differentiation phase; (iii) directly isolated PBMCs to test the whole culture at low oxygen. Growth curves and cell volumes were monitored to compare $3\,\%\,O_2$ cultures with the control condition at atmospheric oxygen. Results showed that cultures can be performed at any protocol phase, but are affected both in terms of cell number and volume. In particular, at low oxygen expansion is reduced, an effect that is more evident on HSCs from isolated PBMCs, where the lower expansion affects cell number until the end of differentiation. Proerythroblasts expanded in hyperoxia and later incubated at low oxygen did not result in a high difference in cell number. However, this may become more obvious if cells would be expanded for a longer period of time. In fact, at day 18 a larger difference appears, especially in terms of cell volume, which severely reduced from 493 fl in hyperoxia to 220 fl at low oxygen. During differentiation cell number is reduced to more than half the amount of cells in hyperoxia, resulting in a ratio of 2.4 times at day 6 differentiation. At this stage cells divide until day 3 differentiation, when cell mitosis occur to reduce cell volumes before nuclei expulsion and terminal maturation. However, at day 14 cell number was reduced only 1.9 times. Volumes throughout differentiation were not affected, therefore cells reduced their size in a similar manner until they reached 200 fl at the end of differentiation. Therefore, the strongest effect occurs on stem cells, where

expansion at low oxygen leads to 4 time less cell number compared to hyperoxia. Cell volumes are also reduced of about 10 fl but are comparable at the end of differentiation.

Figure 33: Growth curve on a single donor to compare culture efficiency at different maturation stages. (A) PBMCs expanded at $20\,\%\,O_2$ and moved to $3\,\%\,O_2$ at proerythroblast stage resulted in 1.2 times reduced cumulative cell number. (B) Incubation of cells at differentiation stage (day 0 differentiation) decreased cell number of 2.4 times in $3\,\%\,O_2$ at day 6 differentiation but resulted in 1.9 time difference at terminal differentiation (day 14). (C) Isolated PBMCs directly incubated at low oxygen resulted in 4 time less cell yield compared to the corresponding culture in hyperoxia.
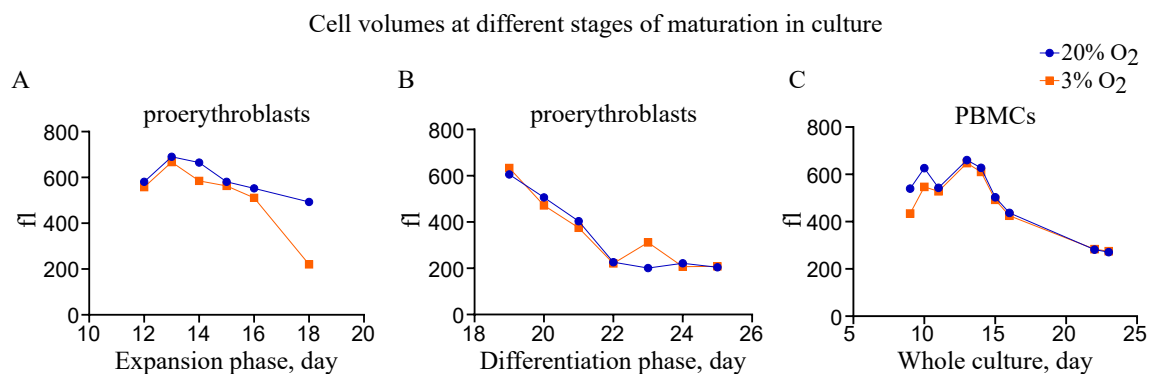
Figure 34: Volume curves on the tested donors at different stages of cell culture. (A) Cells incubated at proerythroblast stage in $3\,\%\,O_2$ reduced their volume in a clear manner at day 18 expansion, indicating a likely tendency to spontaneous differentiation during prolonged expansion phase. (B) Differentiation did not cause relevant volume changes. (C) The complete culture performed at low oxygen resulted in smaller cells during expansion but same final volumes reached at the end of differentiation.

3.1.2 Reversible effect of oxygen on cell growth and volume

After verifying that cell cultures at $3\,\%\,O_2$ were possible at any maturation stage and getting first hints on its effect on cell number and volumes, a test to determine if changes in oxygen levels could affect cell growth was performed. Stem cells from PBMCs placed both in $20\,\%\,O_2$ and $3\,\%\,O_2$ were moved from $20\,\%\,O_2$ to $3\,\%\,O_2$ and viceversa at the stage of proerythroblasts (day 7 expansion),

respectively. Figure 35 shows growth curves and cell volume changes throughout cultures in these 4 conditions until terminal differentiation.

Complete cell maturation at different oxygen levels
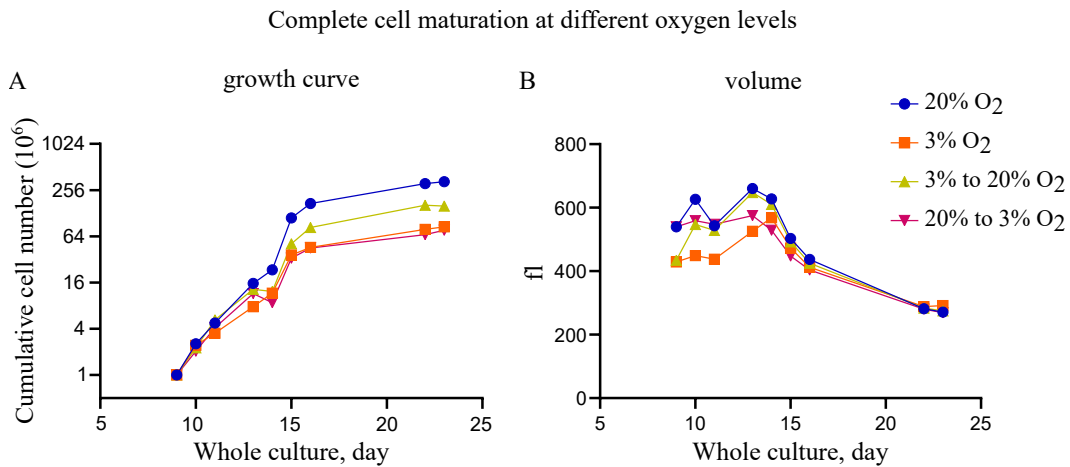
Figure 35: Cell maturation after culture exchange of oxygen levels. (A) Growth curves comparing cell number in 4 conditions. Cells placed from low oxygen ($3\,\%\,O_2$) to hyperoxia ($20\,\%\,O_2$) recovered their expansion potential, however not reaching cell number from the culture performed in hyperoxia only. Conversely, cells moved from hyperoxia to low oxygen reduced their expansion potential. (B) In accordance with the effect on cell growth, cell volumes also recovered after moving cells to higher oxygen and viceversa reduced after changing to lower oxygen.

The effect of oxygen level on both cell expansion potential and cell volumes is reversible. Cells grown to proerythroblasts in hyperoxia when moved to low oxygen reduced their expansion potential and cell volume and viceversa for cells placed from low oxygen to hyperoxia. Recovery from low to high oxygen was however not reaching the amount of cells obtained from cultures performed only in hyperoxia, resulting in 2 times less cell amount by the end of differentiation (day 23 corresponding to day 9 differentiation), showing that stem cell potential is affected. The effect on cell growth on the culture moved to low oxygen occurred after 6 days of incubation at $3\,\%\,O_2$, where cell amount was reduced by 3 times compared to the corresponding culture in $20\,\%\,O_2$ and resulted in 4.3 times less at day 23. This latter culture resulted in 1.4 times less grown than the culture exclusively performed at $3\,\%\,O_2$. This means that sudden hypoxia affected proerythroblasts more than stem cells, underlining a direct stem cell adaptation to oxygen levels, which occurs only in part in proerythroblasts. Cell volumes from $3\,\%\,O_2$ cultured cells were fully recovered after 3 days in $3\,\%\,O_2$, while the decrease in cells moved from $20\,\%\,O_2$ to $3\,\%\,O_2$ did not affect them as the cultures initiated at $3\,\%\,O_2$.

3.1.3   Characterization of erythroid precursors grown at high and low oxygen and comparison with the precursors from high altitude

3.1.3.1   Growth and volume curves

PBMCs isolated from 5 healthy donors were both cultured at $20\,\%\,O_2$ and $3\,\%\,O_2$. Cultures at $20\,\%\,O_2$ were also compared to cultures of PBMCs isolated from the participating donors after 3 weeks at high altitude, performed as well at $20\,\%\,O_2$. Growth curves show significant differences throughout the cultures, confirming preliminary results obtained from single donors where hypoxia affected cell expansion and volume, which resulted decreased (figure 36). Comparison between pre-altitude isolated PBMCs ("Pre") with high-altitude PBMCs from Jungfraujoch ("JJ") resulted in an enhanced growth of cells from high altitude, where two time points were significantly different, corresponding to day 12 expansion and day 9 differentiation. Day 13, 16 and 26 (terminal differentiation) correspond to P values of 0.053, 0.052 and 0.0516, respectively. Considering cell adaptation to oxygen levels obtained from preliminary cultures, the higher growth is a hint of more stem cell presence (CD34+ cells) among the isolated PBMCs, meaning that high altitude may promote CD34+ cells mobilization.
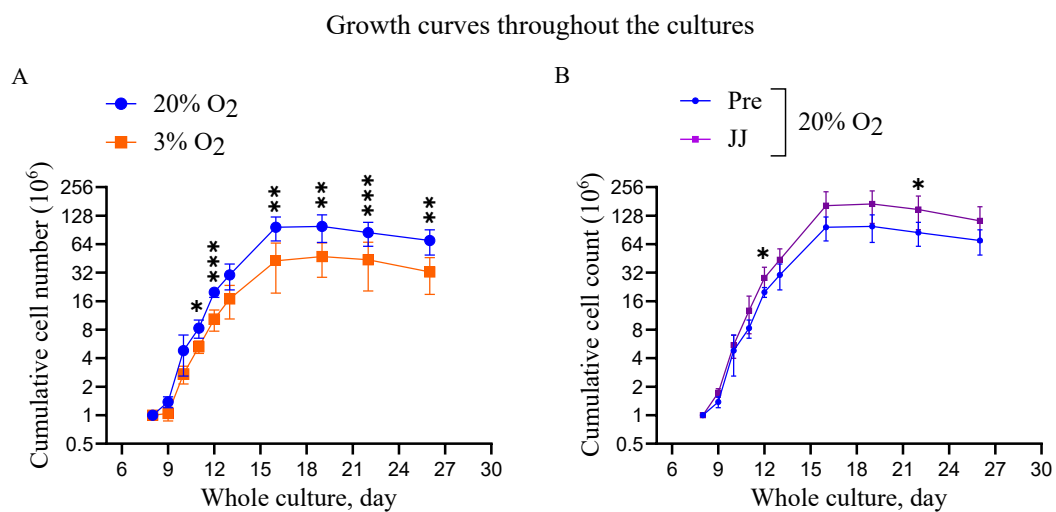
Figure 36: Growth curve from 5 donors in different oxygen conditions. (A) Donors were cultured at high and low oxygen and significant differences exist in several time points throughout the culture. (B) Pre-altitude ("Pre") and high altitude ("JJ") in comparison show a higher cell yield in cultures from JJ PBMCs, with significant time points at day 12 expansion and day 9 differentiation.

Indeed, analysis performed at high altitude by flow cytometry staining of CD34+ cells confirmed an increased amount of circulating stem cells occurring from 1 day after the ascent ("1 JJ") and maintained until day "18 JJ" (figure 37). The apparent average increase during the stay at high altitude is not significant. After descent CD34+ cells per-mille dropped already at day 1 post-altitude (1 post) from 0.1-0.2‰ to about 0.02‰ in whole blood, confirming the immediate response of these

cells to oxygen levels as seen at day "1 JJ". These dropped levels are maintained after 5 weeks (day 36 post) and correspond to the amounts indicated in literature [83]. PBMCs from high altitude were isolated at time point "18 JJ".
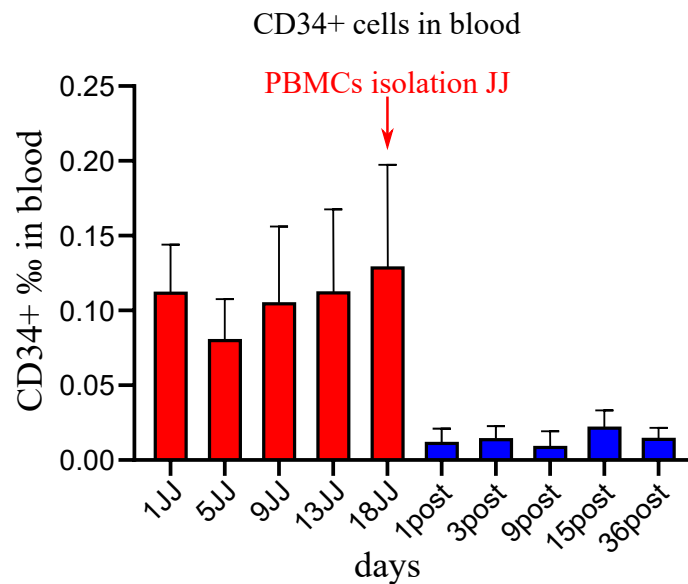

Figure 37: Flow cytometry measurement of CD34+ cells at high altitude ("JJ") and post altitude. An immediate increase in CD34+ cells occurs upon one day of ascent ("1 JJ") and is maintained throughout the stay at "JJ". Conversely, a sudden decrease after one day from the descent ("1 post") was observed and resulted maintained after 5 weeks ("36 post"). "18 JJ" was the day when PBMCs for "JJ" cultures were isolated.

In terms of volume, cells were larger at $20\,\%\,O_2$ compared to $3\,\%\,O_2$ during the whole expansion phase until day 0 differentiation (corresponding to day 13 in the scale of figure 38), when cells start to reduce their volume for their final maturation. No differences existed between "Pre" and "JJ" cultures, underlining the direct adaptation of cells to oxygen conditions and supporting the likely mobilization of stem cells into circulation responsible for their enhanced cell growth.

3.1.3.2   Hemoglobinization and hemoglobin type expression

Cells were characterized during differentiation to evaluate hemoglobinization and hemoglobin types expression. By day 6 differentiation hemoglobinization did not result different in both high and low oxygen cultures and "Pre" compared to "JJ". Only at day 0, high and low oxygen cultures showed a significant difference, suggesting an accelerated differentiation of cultured cells at low oxygen (figure 39).

At the end of differentiation, HPLC was used to detect any differences between hemoglobin types expression, which resulted in a significant increase in HbF in cultures at $3\,\%\,O_2$ also reflected by a significant decrease in their HbA expression (figure 40). HbA2 also increased in $3\,\%\,O_2$. No

Cell volume throughout the cultures
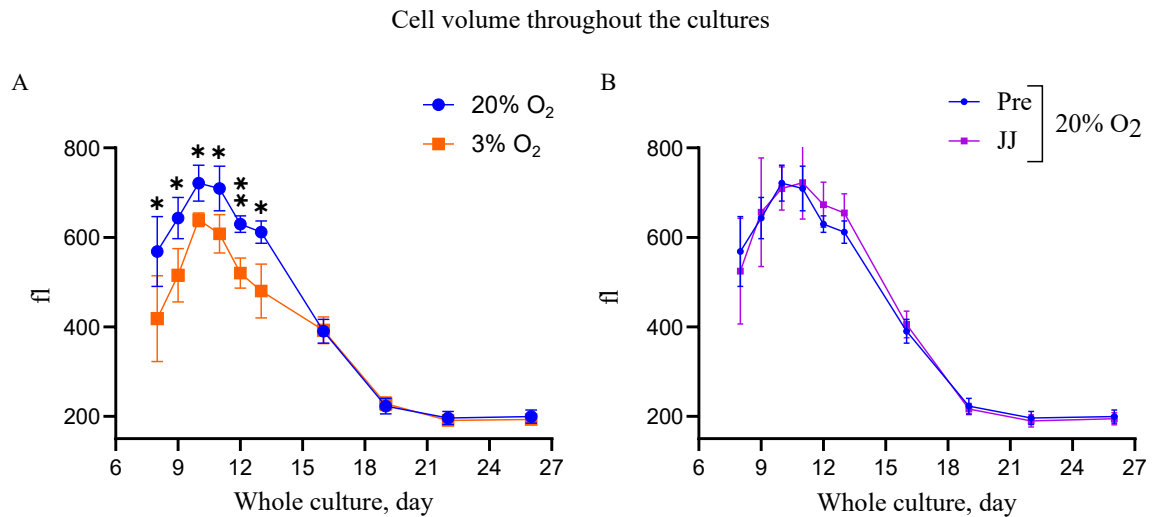
Figure 38: Cell volume throughout the cultures. (A) Cell volumes significantly decreased in cultures at low oxygen during expansion but overlapped with $20\,\%\,O_2$ cultures during differentiation. (B) No difference resulted between "Pre" and "JJ" cultures.
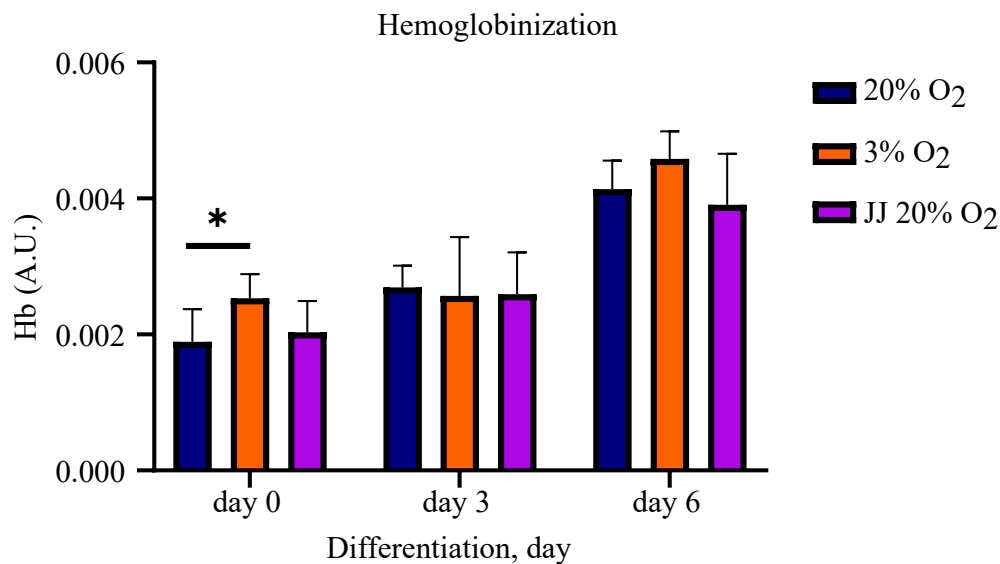

Figure 39: Spectrophotometrical measurement of Hb content at three time points during differentiation, comparing high and low oxygen cultures with "JJ". At day 0, a significant difference existed between $20\,\%\,O_2$ and $3\,\%\,O_2$ cultures, indicating an acceleration of cell differentiation at low oxygen. However, in next days cells hemoglobinization resulted similar among all conditions.

significant difference was observed between "Pre" and high altitude "JJ".

Cytospun cells were additionally observed to visualize cell morphology and intracellular Hb. Cells revealed a fastened differentiation in cultures at low oxygen at day 0, where reduced cell diameters, hemoglobinization and the premature appearance of reticulocytes were observed (figure 41).

Hemoglobin expression at terminal differentiation
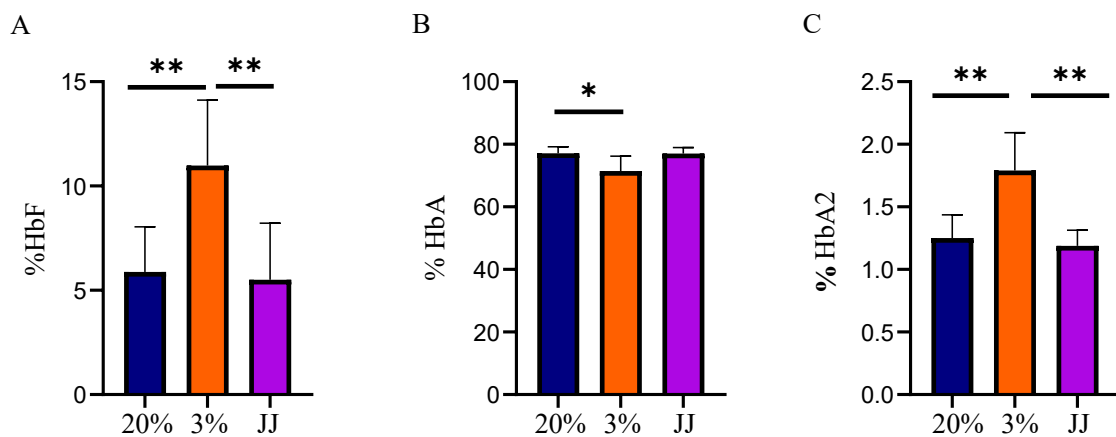
Figure 40: Comparison between different Hb types expression at the end of differentiation (day 13). (A) HbF expression resulted to be the double in low oxygen cultures, while (B) HbA decreased of about 10%, accompained with an increase (C) in HbA2. "Pre" and "JJ" cultures were not different.

Cytospins at day 0 differentiation
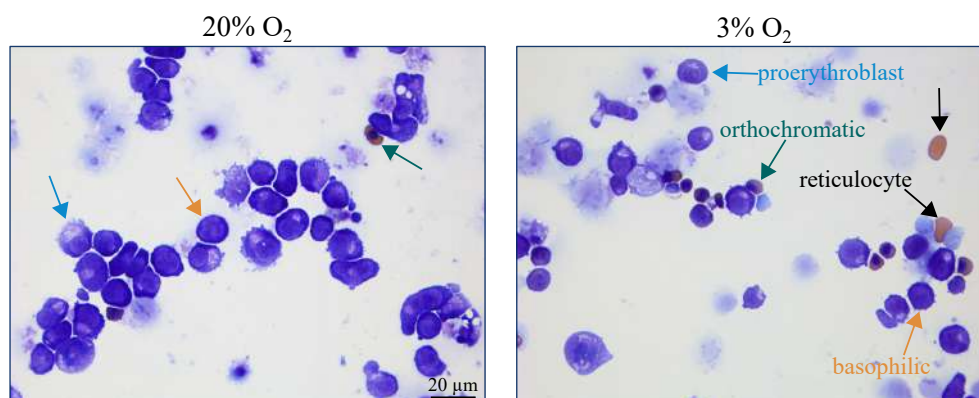
Figure 41: Example cytospins from one donor at $20\,\%\,O_2$ and $3\,\%\,O_2$. At day 0, smaller and hemoglobinized cells (orthochromatic erythroblasts) were observed in samples cultured at low oxygen, with the appearance of some reticulocytes despite the presence of glucocorticoids preventing spontaneous differentiation. No reticuloyctes were observed in cultures at $20\,\%\,O_2$, where proerythroblasts to basophilic erythroblasts prevailed.

3.1.3.3   Assessment of enucleation via flow cytometry

Enucleated cells correspond to reticulocytes, which are negative for nuclear staining. Forward scatter and nuclear staining allowed the gating of nuclei (smallest forward scatter), nucleated cells and reticulocytes. Their ratio represented enucleation efficiency and reticulocytes survival. Cultures at $20\,\%\,O_2$ and $3\,\%\,O_2$ showed significant differences in such ratios, starting from day 0 differentiation. In particular, a higher percentage of reticulocytes appeared in cultures at low oxygen, indicating an accelerated differentiation (figure 42).

At day 13 the amount of reticulocytes was similar. However, cells in hyperoxia eventually expelled

Enucleation throughout differentiation
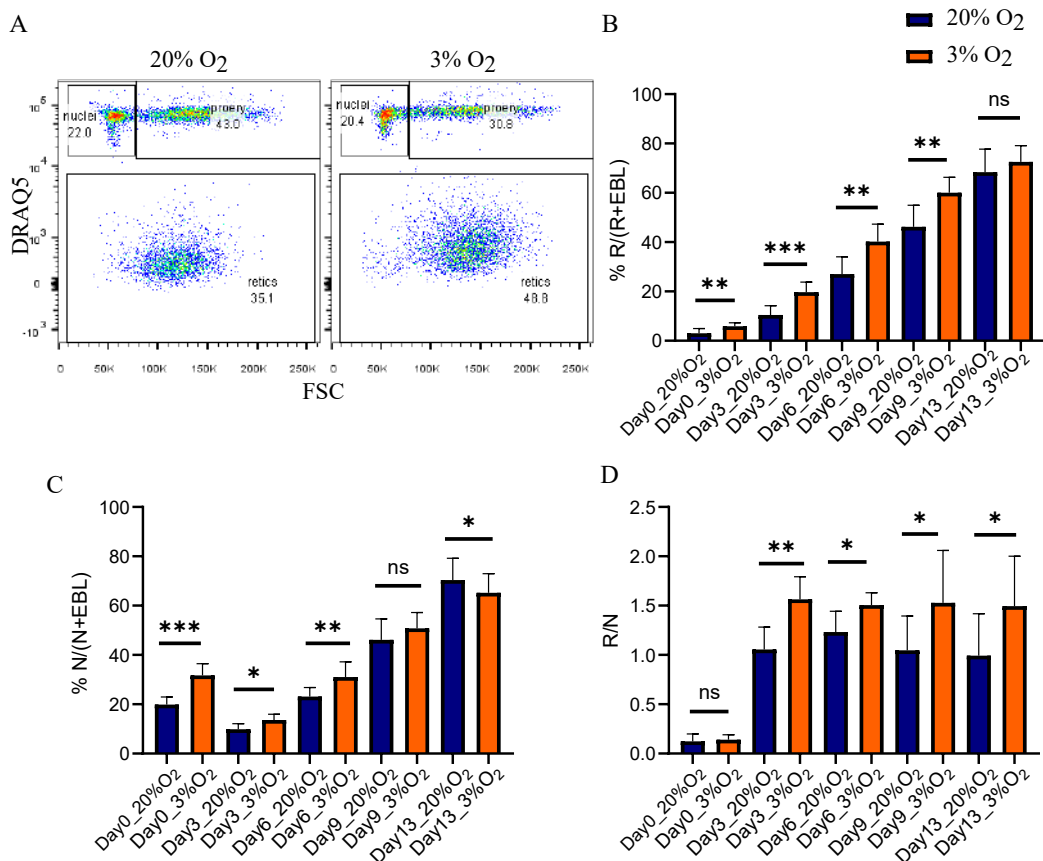
Figure 42: Enucleation efficiency at $20\,\%\,O_2$ and $3\,\%\,O_2$. (A) Flow cytometry raw data from one donor cultured at $20\,\%$ and $3\,\%\,O_2$. The example is from day 9 differentiation. (B) The percentage of reticulocytes over the whole cell population showed a higher amount of reticulocytes at low oxygen in each day of differentiation, except for day 13 which was not significant. (C) The percentage of enucleated cells was higher at $3\,\%\,O_2$ until day 6 differentiation, becoming similar by day 9 and eventually higher in cells differentiated at $20\,\%\,O_2$. (D) The ratio of reticulocytes over expelled nuclei showed that reticulocytes in $3\,\%\,O_2$ were surviving longer than the ones formed at $20\,\%\,O_2$. R=reticulocytes, EBL=erythroblasts, N=nuclei.

more nuclei, but the ratio of reticulocytes over nuclei (R/N) was higher in cells at $3\,\%\,O_2$. This indicates that in hypoxic condition reticulocytes were more stable, i.e. survived better throughout the whole differentiation.

The same comparison between pre and high altitude samples demonstrated that no difference occurred in cell enucleation, both in terms of rate of reticulocytes formation and survival (figure 43).

3.1.3.4   CD71 and CD235 expression

Evaluation of markers of differentiation CD71 and CD235 was used to detect different cell populations in both high oxygen, "Pre" and "JJ" cultures, and low oxygen ones (figure 44). A significant difference existed at day 3 in the amount of formed reticulocytes, more abundant in low oxygen cul-

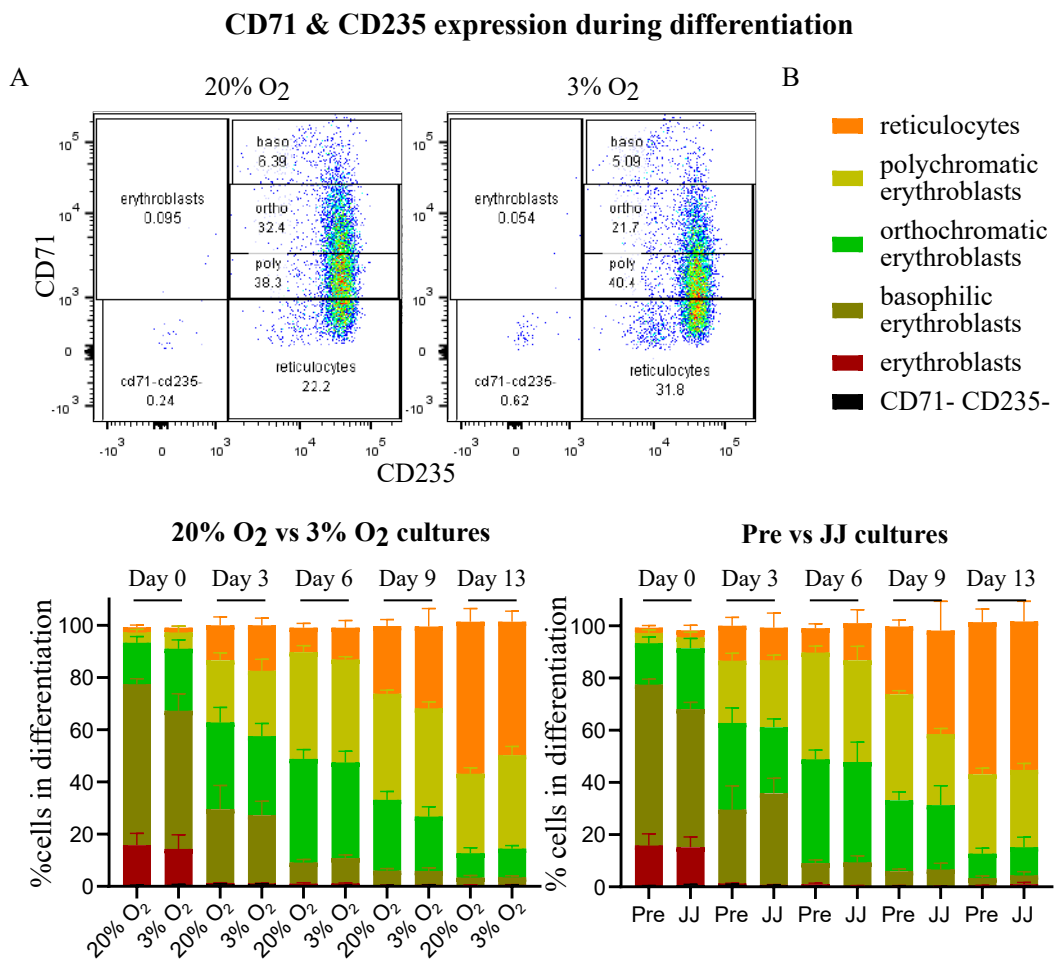**Enucleation throughout differentiation**
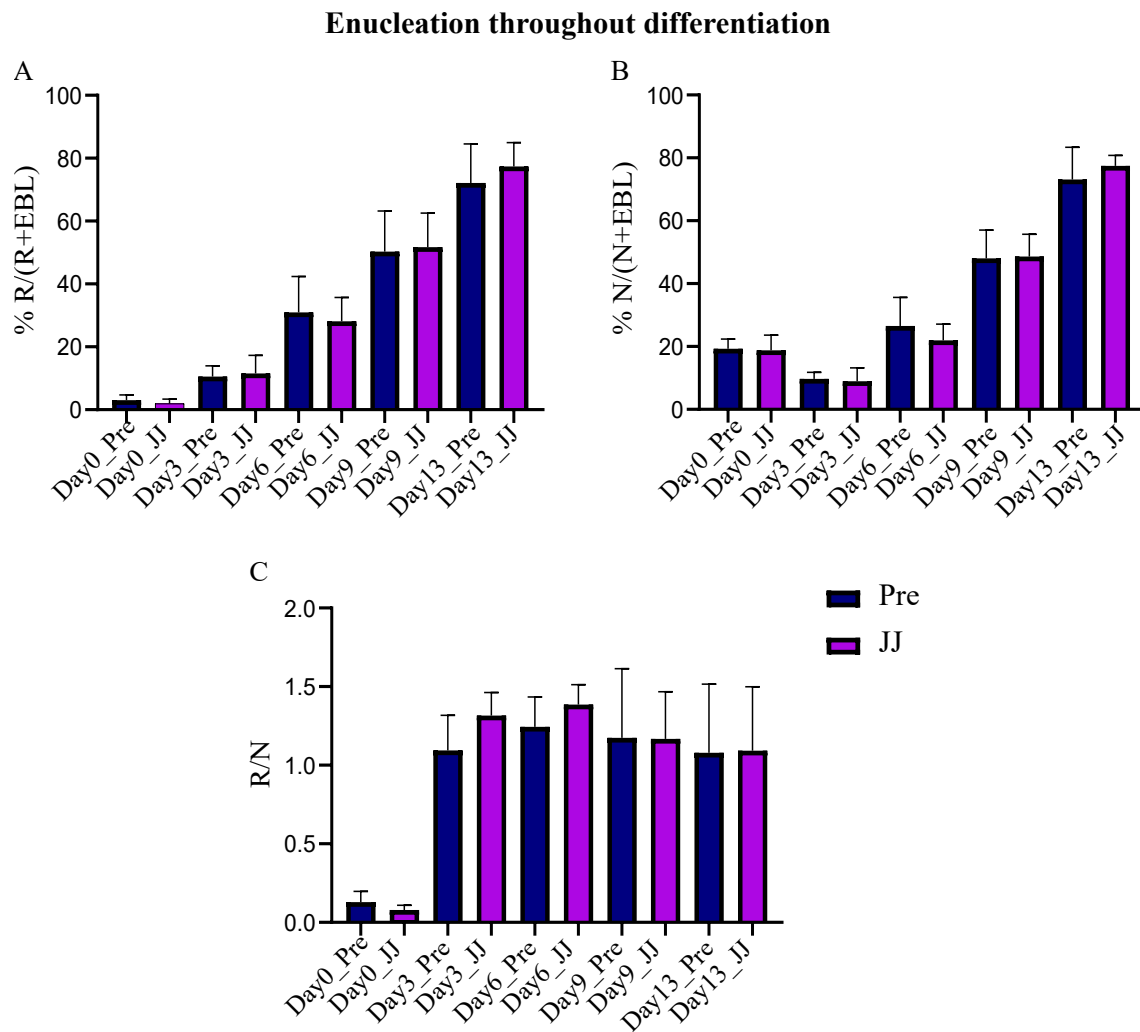
Figure 43: Enucleation efficiency in pre-altitude samples compared to high altitude ones. Amount of reticulocytes (A), expelled nuclei (B) and reticulocytes survival (C) did not differ between the two conditions. R=reticulocytes, EBL=erythroblasts, N=nuclei.

tures. At day 6, P=0.054 and next days the difference was not significant. This is in accordance with the reticulocytes assessed by nuclear staining, where the amount was similar but the enucleation was overall higher in high oxygen cultures. Between "Pre" and "JJ" no significant differences were observed throughout differentiation.

3.1.3.5 Metabolic activity

Considering the different oxygen availability for cells at $20\,\%\,O_2$ and $3\,\%\,O_2$, measurements on glucose and lactate levels of the culture medium were performed throughout differentiation. Glucose consumption resulted higher in cells cultured at $3\,\%\,O_2$ and so lactate production (figure 46), thus glycolysis resulting the preferred pathway for energy production in cells cultured at low oxygen.

Ions concentration in the medium was additionally evaluated by checking sodium and potassium

Figure 44: CD71 and CD235 expression assessment via flow cytometry. (A) Flow cytometry raw data on a donor at day 9 differentiation cultured in 20,% and 3 % O_2. (B) Expression of CD71 vs CD235 throughout differentiation in both 20 % vs 3 % O_2 and Pre-altitude vs "JJ" cultures at 20 % O_2. Reticulocytes were significantly more abundant at day 3 differentiation (P=0.05) and mostly at day 6 (P=0.054), but not in next days, underlining a faster differentiation that did not result in a higher number of formed reticulocytes at day 13. No difference was observed between "Pre" and "JJ".

ratio and chloride content. Na/K ratio during differentiation had similar trends between high and low oxygen, but was significantly lower for 3 % O_2 cultures. Chloride showed instead an increase in 20 % O_2 cultures and steady levels at 3 % O_2.

3.1.3.6   Cell morphology comparison by 3D confocal imaging

Morphological evaluation of fixed cultures cells was performed by confocal microscopy at day 13. A very small percentage of cells acquired a monoconcave or, more rarely, a biconcave shape and resulted to be higher in low oxygen (figure 47). This may indicate a more advanced maturation of reticulocytes cultured in this condition and may explain their better survival observed in the data on cell enucleation.

Metabolic activity
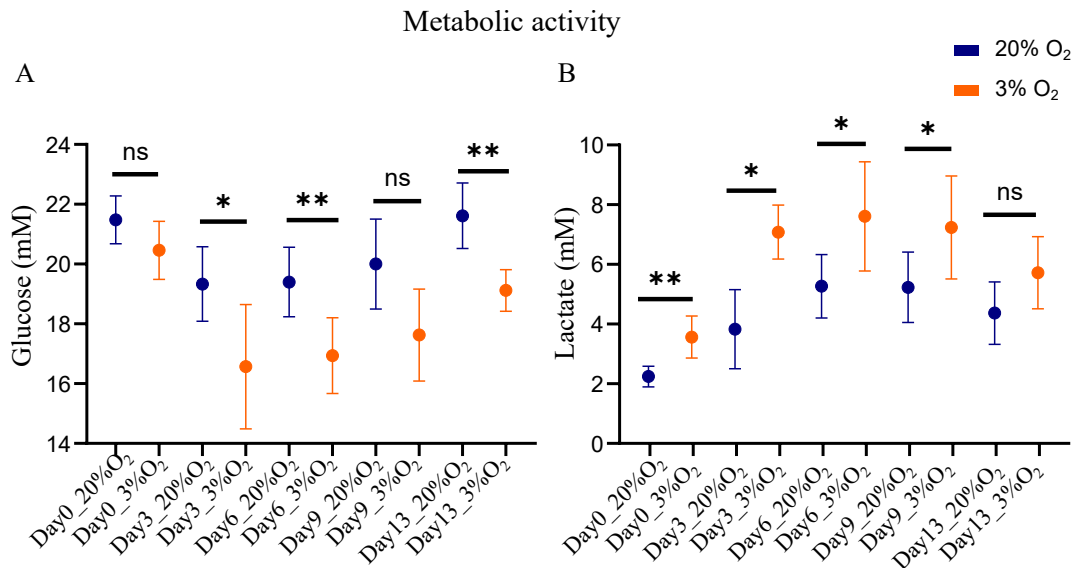
Figure 45: Metabolic activity at $20\,\%\ O_2$ and $3\,\%\ O_2$. (A) Glucose consumption during differentiation showing significantly lower amount of glucose in cell medium at day 3 (when last mitosis occur), day 6 and day 13. (B) Lactate production was significantly higher at low oxygen from day 0, except for day 13.

Ion concentration in culture medium
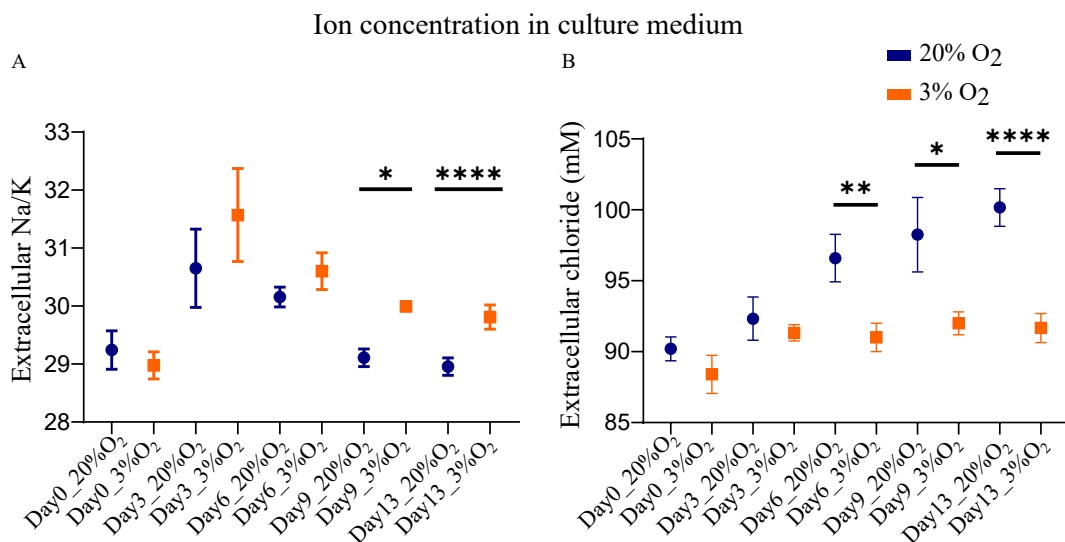
Figure 46: Ion content measurements. (A) The ratio of Na and K resulted significantly higher at day 9 and 13 in cells at low oxygen. (B) Chloride concentration was significantly lower in low oxygen cultures in the last days of differentiation. While extracellular chloride increased in cells at high oxygen throughout differentiation, it remained steady in cultures at low oxygen.

3.1.3.7   Cell deformability measurement

A functional assay was performed at day 13 differentiation by ARCA methodology to assess cell deformability under controlled shear stress. Results comparing the three culture conditions are shown in figure 48, where cell elongation was measured as the ratio between the two axis representing cell length (A) and width (B). No significant differences were observed between each condition.

3D cells
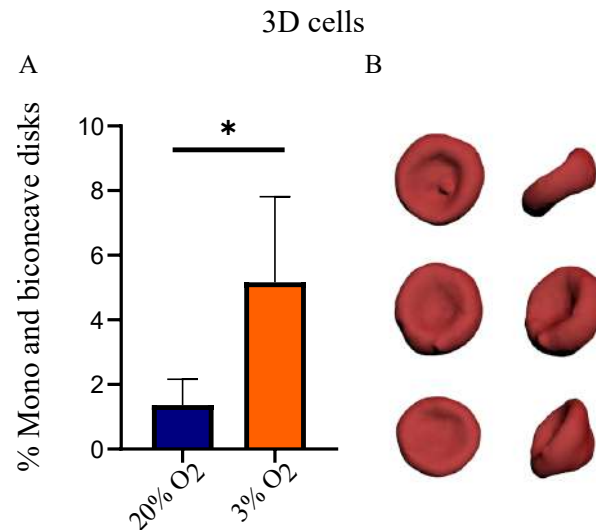
Figure 47: 3D confocal imaging showed a clear distinct number of monoconcave and biconcave shapes. (A) Percentage of such cells was more than doubled in cultures at $3\%\,O_2$. (B) Example of biconcave and monoconcave cultured reticulocytes.

Deformability at terminal differentiation
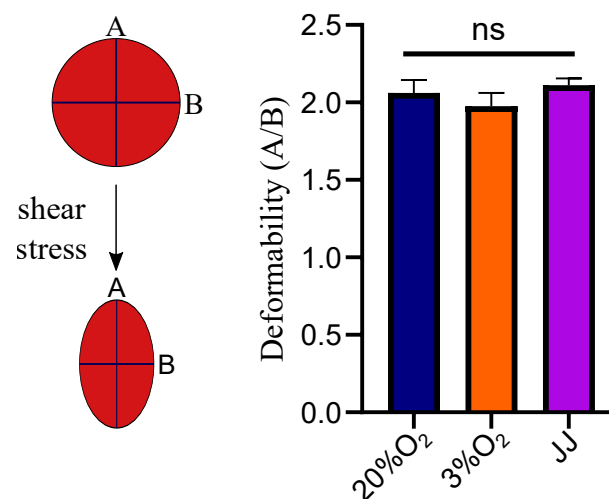
Figure 48: Deformability of cultured reticulocytes at day 13 differentiation. Deformability is measured by evaluating cell elongation under shear stress as the ratio between cell length (A) and width (B). No significant differences between each culture condition were observed. Error bars represent standard deviation from the mean.

3.1.4 Towards RNA-Seq of reticulocytes pre and high altitude

3.1.4.1 Reticulocytes enrichment

Reticulocytes enrichment is a useful step when requiring a time-efficient isolation of a sufficient number of cells for RNA-Seq. MACS separation from whole blood was here employed and resulted in a maximal 70% enrichment, reproducible between 60 an 70% for a 20 times dilution of the microbeads, which resulted more efficient than the company recommended concentration.
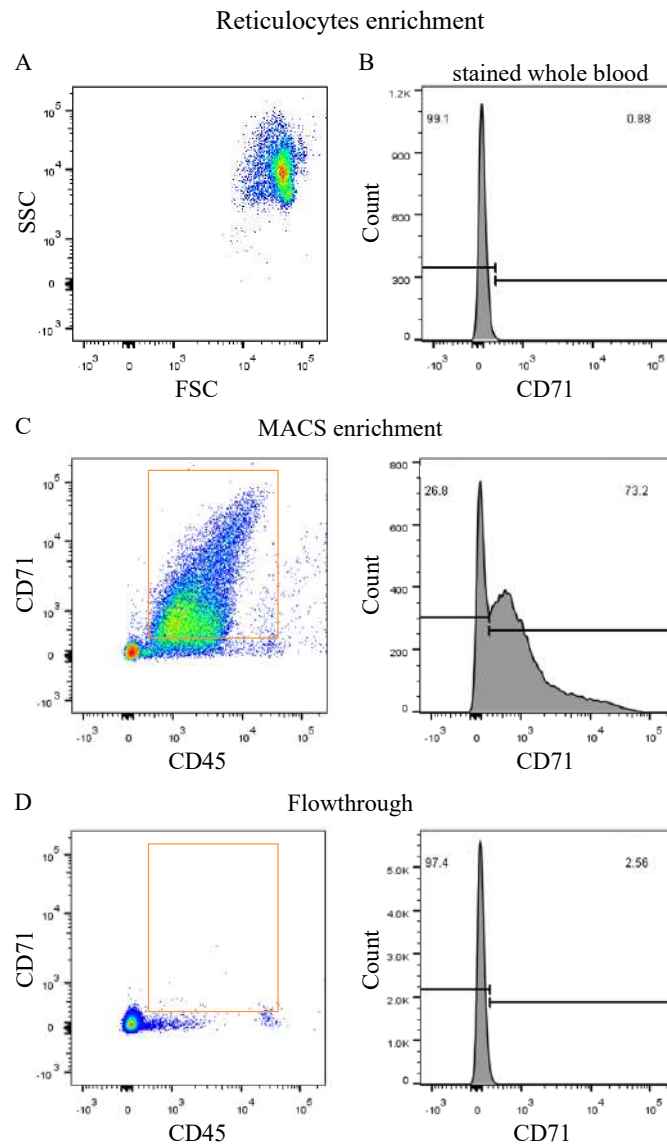
Figure 49: Reticulocytes enrichment by MACS checked by flow cytometry. (A) FSC and SSC were used to visualize blood sample population including a mixture of reticulocytes, RBCs, WBCs and platelets. (B) Control sample of whole blood stained with CD71, showing a very low percentage of reticulocytes in the sample. (C) Sample after MACS enrichment. On the left, in orange the population of reticulocytes, corresponding to 73%, as shown by the histogram on the right. (D) Relative flowthrough of sample (C), showing that only 2.6% of reticulocytes were flushed out.

Checks on the flowthrough, i.e. the discarded non-labeled cells, demonstrated that most of reticulocytes were retained in the labeled sample (figure 49).

3.1.4.2   Reticulocytes sorting and RNA isolation

The outcome of the total RNA isolation from reticulocytes was a low yield, but this result was expected since reticulocytes contain only RNA remnants. Table 11 shows the number of sorted cells and the corresponding total obtained RNA from the 6 donors tested at pre-altitude and end of high

altitude ("JJ").

Table 11: Sorted reticulocytes and RNA amounts

Donor	Sorted reticulocytes number	RNA (ng)
1 Pre	212 000	156
2 Pre	185 000	160
3 Pre	200 000	336
4 Pre	200 000	162
5 Pre	196 000	126
6 Pre	200 000	150
1 JJ	3 million	407
2 JJ	550 000	276
3 JJ	2.5 million	662
4 JJ	600 000	455
5 JJ	800 000	278
6 JJ	800 000	488

Reticulocytes number and consequently RNA amounts from high altitude samples resulted to be higher in high altitude samples, indicating an increased number of young (CD71+) circulating reticulocytes. The obtained RNA amount in each sample was far higher than the minimum required for the rRNA depletion (minimum 10 ng), a step performed before library preparation since it constitutes 90% of total RNA. A bioanalyzer was used to perform RNA quality check. In most of the preliminary test samples 18S was resulting in a higher peak than 28S, indicating RNA degradation. In this case in fact the band of 18S includes fragmented 28S, which migrates faster in the gel allocating together with 18S. The use of the kit lead instead to a higher peak for 28S, with a ratio of 2.1 between 28S and 18S and general RIN values above 8 in the 6 samples pre-altitude (figure bioanalyzer). However, in some samples almost no peak was detectable.

High altitude samples resulted in more degradation, as seen by the presence of a middle peak between 28S and 18S. While observing inverted peaks and their almost total absence in some samples, RIN were always both higher than 3 (strongly degraded RNA) and 5 (partially degraded RNA) and no RNA smear typically observed in degraded samples was observed. The slight degradation may therefore indicate reticulocytes RNA loss rather than necessarily RNA fragmentation occurred during the experimental procedure.

3.1.4.3   RNA sequencing results

Library preparation followed rRNA depletion. No hemoglobin depletion was performed due to the intention to check for Hb types, such as HbF expression. End of high altitude stay relative to pre-altitude, resulted statistically significant for EPO Receptor Signaling pathway depletion (P=0.035).

RNA quality check with bioanalyzer

A

RNA isolation with
TRIzol

RIN: 7.2
28S/18S=0.7

B

RNA isolation by kit

RIN: 9.9
28S/18S=2.1

RIN: 7.5
28S/18S=1.3
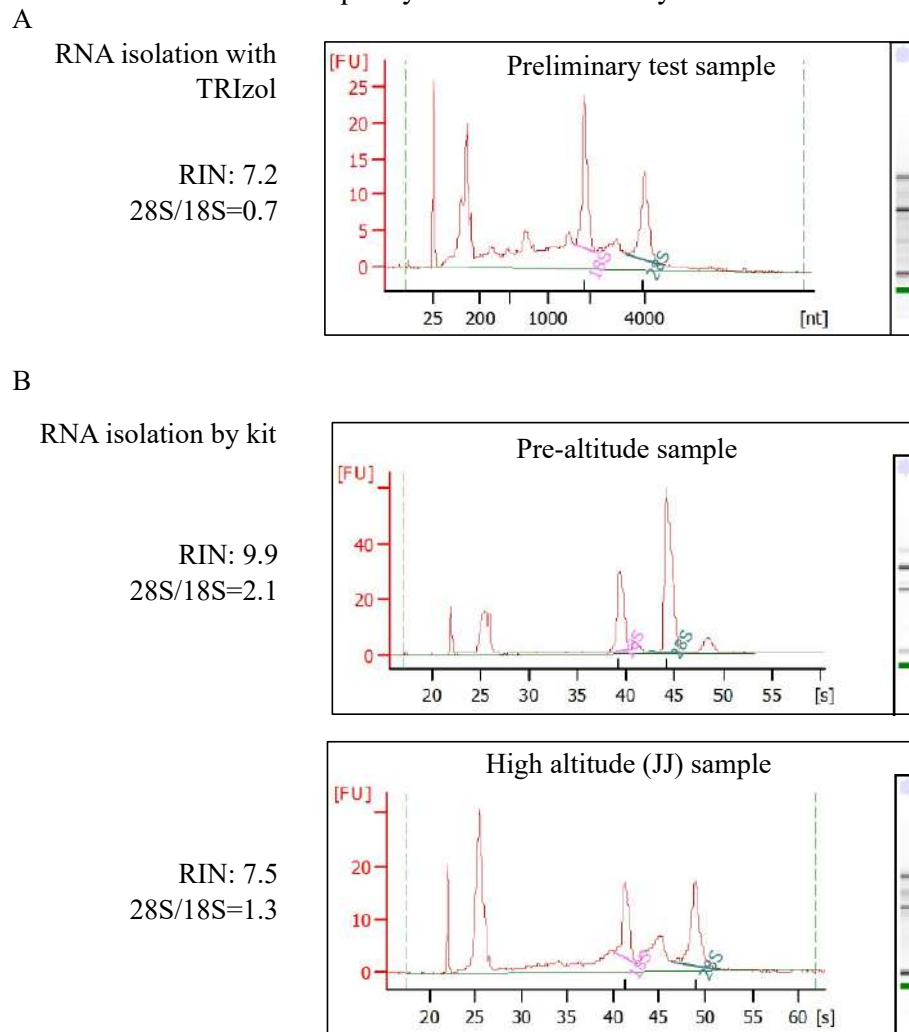
Figure 50: RNA quality check with a bioanalyzer. (A) RNA obtained with TRIzol-based method showed in any tested sample a higher peak for 18S than 28S, with a ratio 28S over 18S of 0.7. (B) RNA isolation performed with the miRNAeasy kit resulted in a higher ratio, where 28S was more abundant. In samples from high altitude ("JJ") this ratio was reduced, indicating more RNA degradation products. RIN=RNA integrity number.

No Hb type difference was detected and between 9 and 27% of the reads could not be mapped to specific genes in the different samples.

3.2 Studies on RBCs' morphology

3.2.1 Methodological considerations on RBCs fixation

3.2.1.1   Choice of the fixative

Cell fixation is a tool for the preservation of morphological structure and ultrastructure. While applications such as SEM necessarily require fixation prior to imaging, traditional microscopy and confocal microscopy do not. However, especially for RBCs which are particularly susceptible to shape changes, immediate fixation of fresh blood provides an advantage to avoid artifacts formation due to temperature, time and means of transportation and when dealing with patients with rare anemias this becomes almost a necessity [105, 67]. In the context of rare blood diseases, the analysis of RBCs shape is a simple but powerful tool to get an impression of the pathology and its impact on RBCs' health. Not every fixative works with the same efficiency. Figure 51 shows an example at SEM of a sickle cell fixed in 1% formaldehyde compared to a cell fixed in 1 % glutaraldehyde. In formaldehyde cell membrane resulted clearly damaged, proving this fixation modality not to be ideal for RBCs. A personal communication with Dr. Emmanuel Terriac confirmed poor shape preservation in formaldehyde and paraformaldehyde with RBCs, where he observed cell lysis. While he experienced FA mixed with GA to be successful, here only GA was later employed and investigated for its use on RBCs.

Fixative effect on RBCs

Formaldehyde (FA)   Glutaraldehyde (GA)
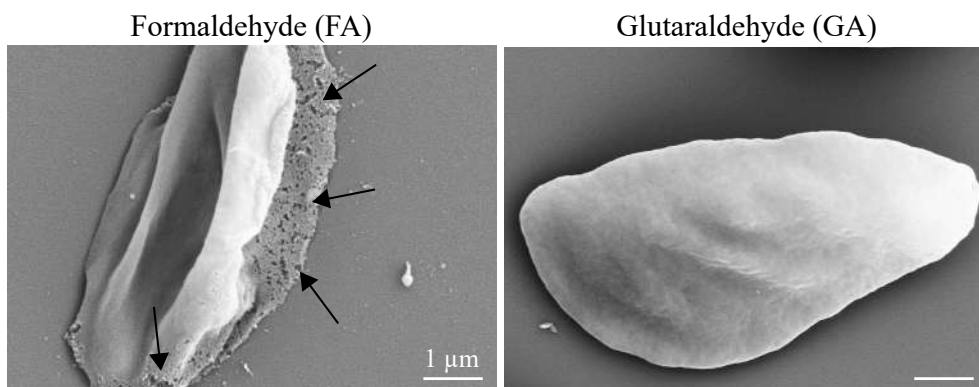
Figure 51: Effect of fixation by formaldehyde (FA) and glutaraldehyde (GA) on sickle cells imaged in SEM. FA-fixed RBC resulted in clear membrane ruptures (arrows), with large holes on the whole cell length. This result is an artifact because a living cell with such holes would immediately lyse. Fixation in GA demonstrated instead to preserve membrane integrity, even on fragile RBCs such as sickle cells.
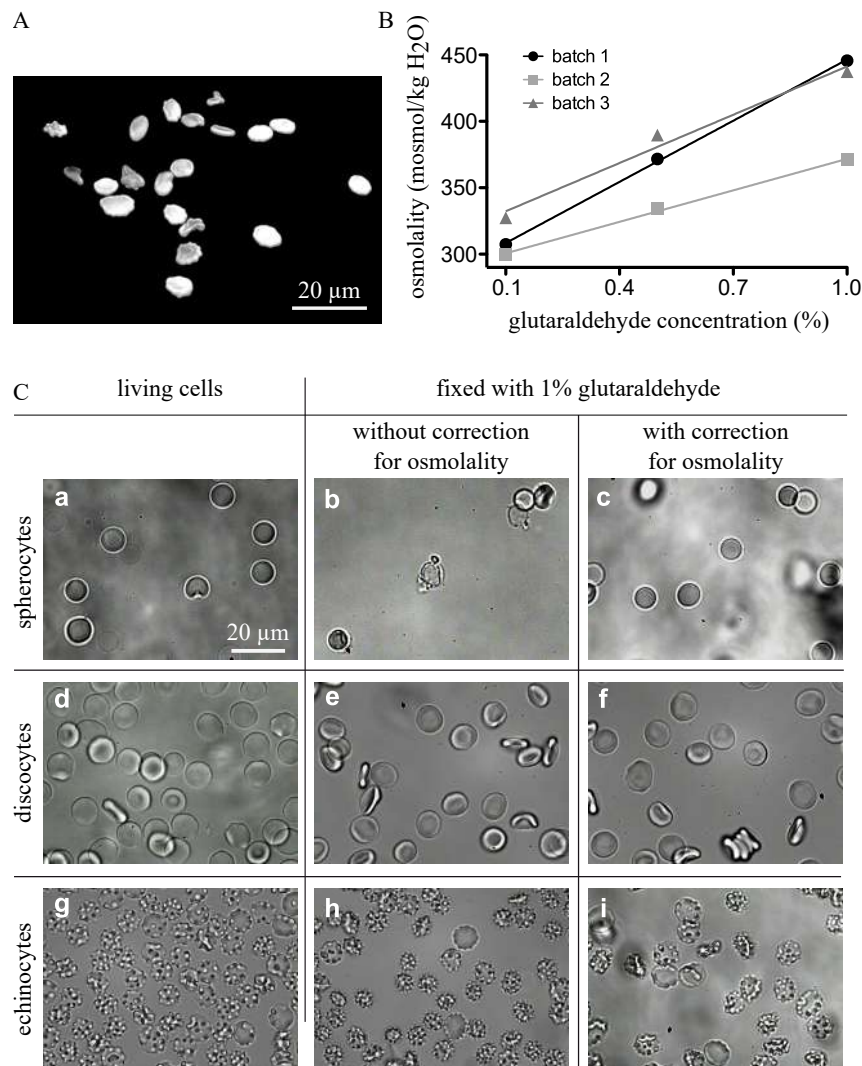
3.2.1.2 Osmotic effect of GA

The highest concentration of GA tested was 1%. After suspending RBCs in solutions with specific osmolality, the addition of GA determined a different expected shape (figure 52). The reason for such changes was due to the increase in the osmolality of the solution containing GA, which corresponds to about additional 100 mOsmol, having therefore an impact on RBCs water fluxes. Fixation in 1% GA occurs almost immediately, within 1 second [162], but water flux through cell membrane during this time can be relevant. To solve this problem, the dilution of the buffer concentration to have the same osmolality of the suspension solution after addition of 1% GA proved to be useful for a correct shape preservation. However, different GA batches used to prepare the same GA-concentrated solutions revealed different osmolality (figure 52, B). This means that the calculated concentration from the stock of GA is nominal but not realistic. Indeed, GA tends to polymerize with its own molecules, reducing the number of single GA molecules responsible for the osmotic effect. Hence, the calculated concentration is not exact and it is rather useful to measure the osmolality of the solution before its use, making sure that after the addition of GA it corresponds to the same osmolality of the original suspension solution. Exploiting the osmotic effect on RBCs to manipulate their shape transitions was useful to investigate the importance of osmotic pressure. In particular, spherocytes revealed to represent the most "sensitive" shape: their tolerated range for appropriate fixation resulted to be very small, only between 127 and 145 mOsmol/kg H_2O. Discocytes tolerate a wider osmolality range, being the most stable RBC shape, showing biconcavity from 210 to 380 mOsmol/kg H_2O, but being flattened and occasionally showing irregular borders at high osmolality. Ideally, discocytes should be suspended in a solution of 290 mOsmol/kg H_2O, the osmolality used when correcting GA solutions.

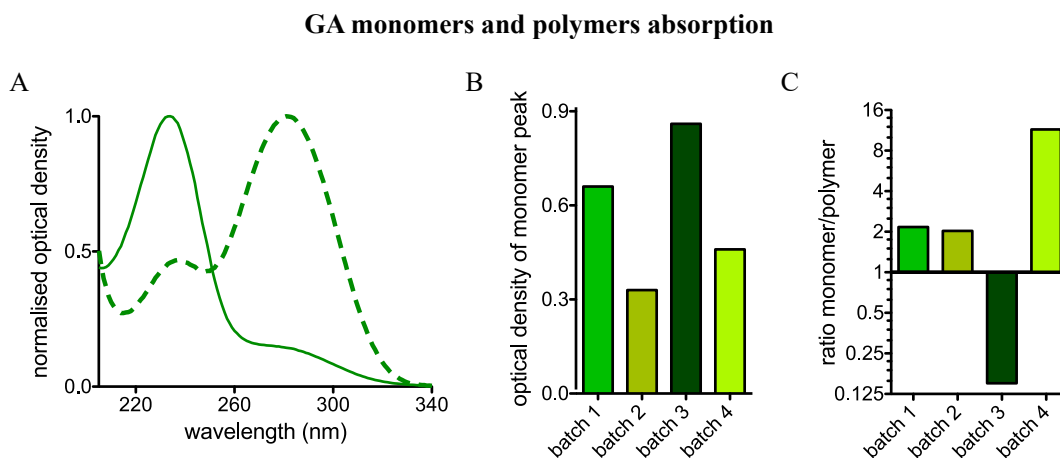### 3.2.1.3 Monomers and polymers

As mentioned before, GA can polymerize with its own molecule, a process that is accelerated by raising the temperature and occurring during storage time [137, 56, 138, 135]. The extensive studies on GA fixation properties performed in the '60s [64, 143, 145] generated controversy whether monomers or polymers are responsible for the crosslinking of cell structures and which one results in a better fixation quality. The tests here performed were based on commercial GA, which always contains a certain extent of polymer presence. It is possible to obtain only monomeric GA by applying a distillation step. However, fixation with different GA batches, containing a different monomer to polymer ratio, resulted in appropriate fixation. Such ratio was measured by UV-absorption spectroscopy since monomers have an absorption peak at 280 nm, while polymers at 235 nm. Figure 53 shows differences in this ratio for 4 tested batches. Moreover, batch 1 and 2 ratios looking similar show different

Effect of osmolality on RBCs fixation

Figure 52: Osmotic effect of GA on RBCs fixation. (A) RBCs from a patient affected by piruvate kinase deficiency showing a flattened aspect and spiky borders due to the high osmolality of 1% GA solution, causing cell dehyration which resulted in echinocyte formation. Here, the echinocyte aspect is very mild because it occurs as a simultaneous dehydration while cells get fixed. (B) Measurement of osmolality of GA solutions in different concentration from three different batches. Osmolality changes linearly but each batch showed different slopes and especially osmolality, despite the nominal GA concentration was the same. (C) Brightfield microscopy of living cells (a-d-g) compared to fixed in 1% GA with and without correction for osmolality. Spherocytes burst upon sudden osmotic pressure change with the addition of 1% GA (b), but can be preserved after correction (c) with the same concentration of GA; discocytes preserved their biconcave shape, however showing a flattened aspect as a result of cell dehydration (e); echinocytes increased their degree of spikes formation (h) transforming from type II to type III, but were preserved when fixed with corrected GA (i). Adapted from [1].

optical density of the monomers (figure 53, B), indicating different concentrations between batches despite the same nominal concentration. Therefore, it is important to evaluate the single GA solutions prior to their use.
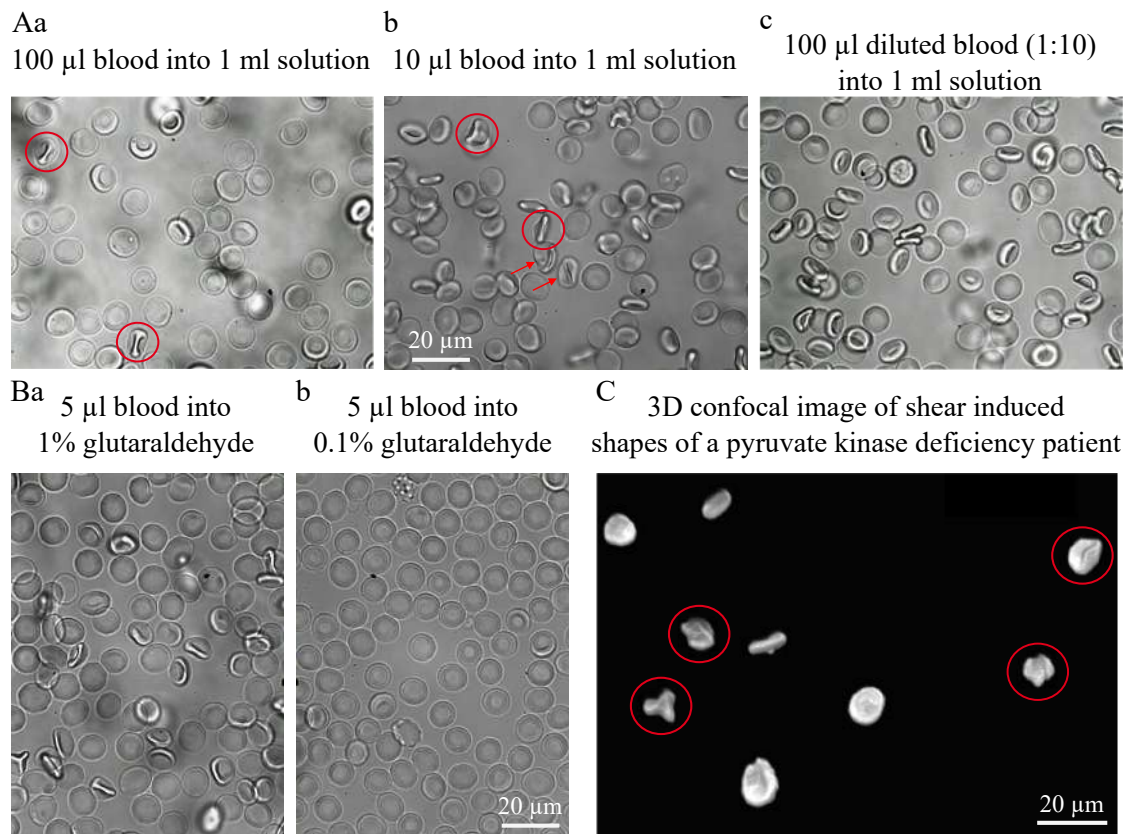
GA monomers and polymers absorption

Figure 53: Assessment of the monomeric and polymeric GA in 4 batches by UV-absorption spectroscopy. (A) Normalized optical density of two GA batches in distilled water. Monomers (solid line) have an absorption peak at 280 nm, while polymers (dashed line) at 235 nm. (B) Monomer absorption peak in 4 GA batches with nominal GA concentration to 1% in distilled water. (C) Monomers to polymers ratio for the same 4 batches from 1% GA solutions in distilled water. These experiments were done in collaboration with Asena Abay. Adapted from [1].

3.2.1.4   Effect of shear stress on artifacts formation

RBCs in flow assume a hydrodynamic shape and the applied shear stress determines a certain shape change. In particular, it was demonstrated that at high shear, RBCs can transform into a trilobe shape [89], in blood smears commonly known as knizocyte [15]. Tests of RBCs fixation at 0.1% and 1% GA showed in this latter the presence of knizocytes, which were completely absent in samples fixed at 0.1%. Therefore, the presence of such shapes was an artifact. It is important to be aware of this aspect because certain blood diseases result in the formation of knizocytes in stasis [14]. The fact that such shapes were observed only at 10 times higher GA concentration reflects the faster fixation occurring at 1% compared to 0.1% GA, this latter fixing cells after their relaxation to static shape that follows pipetting into the fixative solution. However, it is possible to reduce shear stress by pipetting gently and using large pipette tips when fixing at 1% GA. Also the dilution of RBCs prior to fixation resulted in a lower amount of knizocytes formation, explained by the reduced blood viscosity that decreased shear stress [52].

Shear stress shapes formed during fixation

Aa
100 µl blood into 1 ml solution

b
10 µl blood into 1 ml solution

c
100 µl diluted blood (1:10)
into 1 ml solution

Ba   5 µl blood into
1% glutaraldehyde

b   5 µl blood into
0.1% glutaraldehyde

C   3D confocal image of shear induced
shapes of a pyruvate kinase deficiency patient

Figure 54: Effect of shear stress on RBCs shape deformation. (A) Examples of RBCs from a healthy donor fixed in 1% GA and comparison of the amount of knizocyte formation: 100 and 10 μl fixed in 1 ml of blood showed the presence of knizocytes (a, b), not observed after a 1 to 10 dilution of blood prior to fixation. (B) The comparison of 1% with 0.1% GA solutions confirmed that such shapes are an artifact of shear, since they did not appear in 0.1% fixed cells from the same donor. (C) Example in 3D of a sample from a patient affected by pyruvate kinase deficiency showing knizocytes after fixation in 1% GA. Adapted from [1].

3.2.1.5   Autofluorescence of GA affecting cell staining: Quenching of GA autofluorescence

GA induces strong autofluorescence on a wide spectral range. Tests comparing the effects of monomer and polymer on GA autofluorescence where carried out (figure 55) and revealed that their mixture covers a wide range of emission wavelengths (figure 55, A, batch 2) compared to the almost exclusive monomeric GA (batch 4). This should be considered for fluorescence staining, where a considerable background fluorescence adds to the desired measured signal. A possibility to reduce it is by addition of trypan blue to fixed cells, a method previously suggested [98]. Here, a test by fluorescence spectroscopy was performed, showing trypan blue absorbance at the emission wavelengths of GA, reducing its signal (figure 55, C). Trypan blue was also compared to Hb absorption spectrum. Images before and after quenching (figure 55, B) showed a marked reduced background fluorescence of GA,

however, not totally depleted. 3D-imaging of RBCs (figure 55, D) compare the exclusive GA signal at 561 nm with the one from CellMask staining at 647 nm, highlighting by the presence of a WBC (circled) the different degree of autofluorescence in different cell types.

Glutaraldehyde autofluorescence
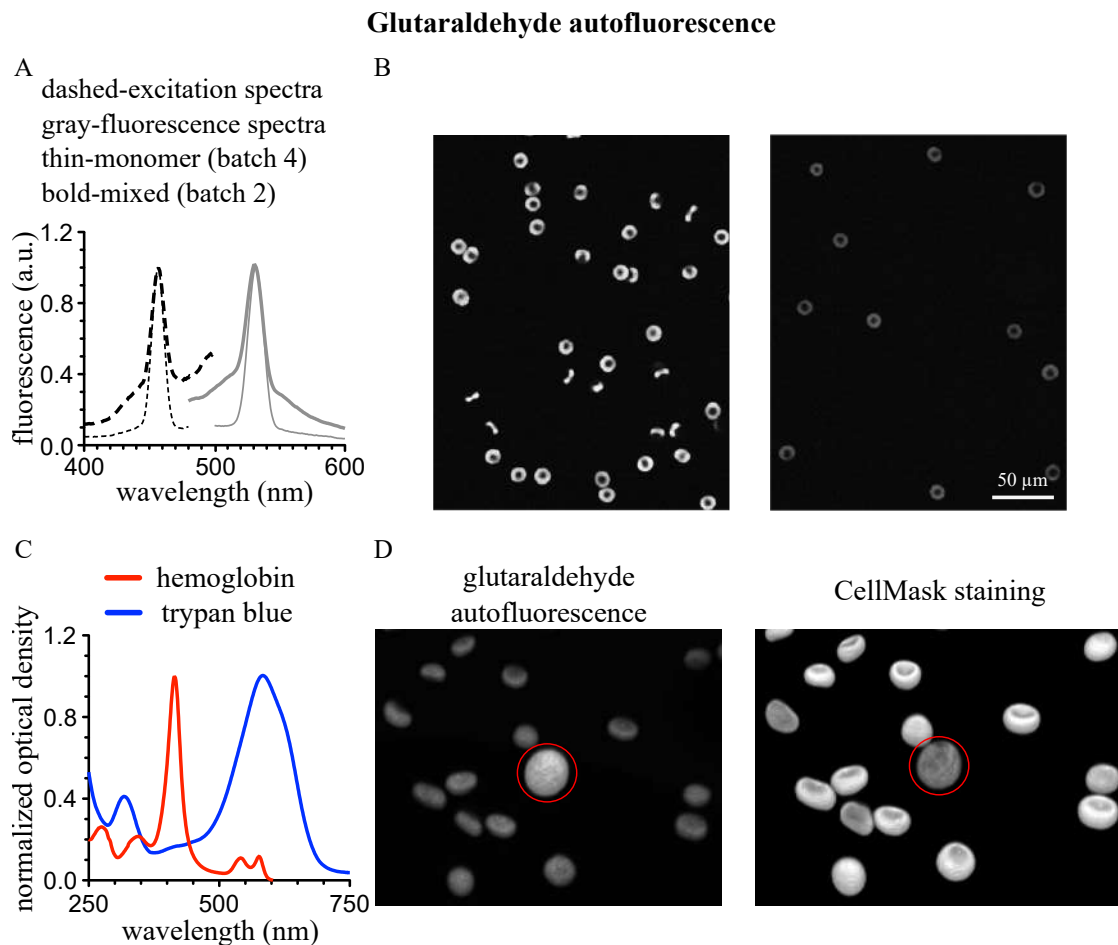
Figure 55: GA autofluorescence. (A) Fluorescence spectrum of two different GA batches, showing their absorption and emission peaks. Batch 4 has a higher monomer presence and results in a tighter band compared to batch 2 that contains a mix of monomers and polymers. (B) Confocal image planes before (left) and after (right) quenching with trypan blue. (C) Normalized absorption spectrum of trypan blue compared to the one of Hb. (D) Autofluorescence intensity differing between cell types, being stronger in WBCs than RBCs and related 3D image at 647 nm showing CellMask staining. These experiments were done in collaboration with Asena Abay. Adapted from [1].

3.2.1.6   Compatibility of EMA staining with fixed cells

In addition to autofluorescence, tests to evaluate different staining protocols were performed on fixed cells. EMA staining is one of the most common RBCs fluorescence stainings employed to evaluate band 3 protein abundance in blood diseases, e.g. hereditary spherocytosis. Figure 56 shows the comparison between living stained cells (figure 56, A) in a healthy donor, where EMA caused shape transition to echinocytes. Therefore, it could be interesting to stain fixed cells to maintain RBCs

original morphology. However, tests showed that staining after fixation resulted in some stained and non-stained cells. In particular, high cell autofluorescence corresponded to very low EMA signal, indicating a possible binding competition between the two molecules (figure 56, B). To confirm this effect due to the prior fixation, a test was performed on cells first stained with EMA and then fixed, resulting in an homogeneous staining with echinocytes formation as for living cells.
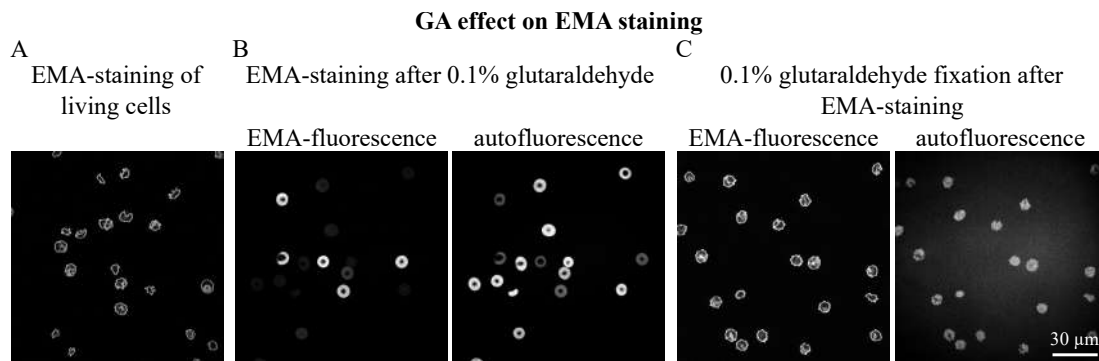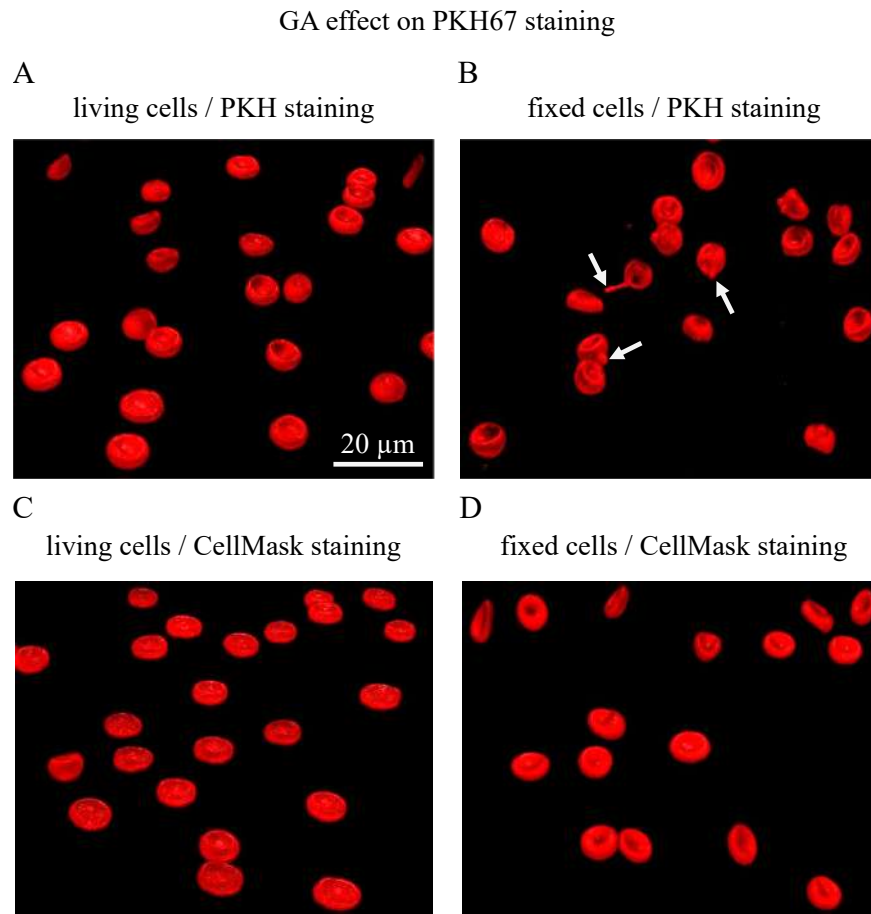

Figure 56: EMA staining assessment on fixed cells. (A) Living cell staining is homogeneous and resulted in the formation of echinocytes. (B) Fixed cell staining showed the preservation of discocytes but resulted in a selective EMA staining of cells, where the ones with higher autofluorescence (right image) showed less EMA signal (left). (C) Confirmation of the effect of GA fixation in EMA staining heterogeneity: cells stained with EMA when living and later fixed showed the same characteristics of (A). Adapted from [1].

3.2.1.7   Membrane staining with PKH67 on living and fixed cells

While CellMask can be used on both living and, due to its cytotoxic effect, preferably fixed cells, PKH67 membrane staining did not result as efficient on fixed cells. Figure 57 shows living cells imaging of PKH67-stained cells (A) and corresponding fixed cells at 1% GA (B), which showed the formation of a sort of membrane filaments. This was also observed at 0.1% GA (not shown). Cell-Mask on fixed cells resulted in a good staining (D), although occasional dye accumulation occurred when staining with 0.1% GA. These inconsistent effects on the quality of membrane staining in fixed cells may be due to the different monomer/polymer ratio of the various GA batches.

3.2.1.8   Effect of GA on intracellular staining by assessing HbF concentration in cord blood

After assessing the impact of fixation on membrane dyes, a test with an intracellular antibody staining for the detection of HbF was performed. HbF staining can only be done after fixation because it requires cell membrane permeabilization. Figure 58 shows the base signal of living cells in flow cytometry in FITC channel (A) compared to basal signal from fixed cells in 0.05% GA (B), the concentration suggested by the manufacturer of the antibody. A comparison with cells fixed in 1% GA showed a higher background signal ((D), note the exponential scale of fluorescence signal), but

GA effect on PKH67 staining

A

living cells / PKH staining

B

fixed cells / PKH staining

C

living cells / CellMask staining

D

fixed cells / CellMask staining

Figure 57: Membrane staining of living an fixed cells. (A) PKH67 living cell staining compared to (B) fixed cells in 1% GA, where the formation of protrusions like filaments can be observed. (C) Staining with CellMask on living cells looking as efficient as on (D) 1% GA-fixed RBCs. Adapted from [1].

the major effect was on the antibody anti-HbF between these two concentrations. In fact, cord blood staining showed 97% of cells positive for HbF when fixed with 0.05% GA (C), while it decreased to only 1.7% in the sample fixed with 1 %, i.e. a 20 times higher concentration (E). This reflects the important effect of GA in masking the epitopes recognized by anti-HbF antibody, making it crucial to use the correct amount for efficient intracellular staining.

3.2.1.9   Emphasis on sickle cell fixation

For the later studies on sickle cells within the clinical trial MemSID, a final check of GA fixation effect on sickle cells was performed. In fact, GA consumes oxygen during its crosslinking reaction [62], an effect that can also be visualized by the color of cell pellets, which become darker several hours after fixation indicating the formation of methemoglobin. To verify that GA deoxygenation of Hb in fixed cells would not affect RBCs shape of SCD samples, fixation with 1% GA was performed both on oxygenated and deoxygenated SCD RBCs left for 8 hours in a glove box and there fixed.

Effect of GA concentration on intracellular staining (HbF)
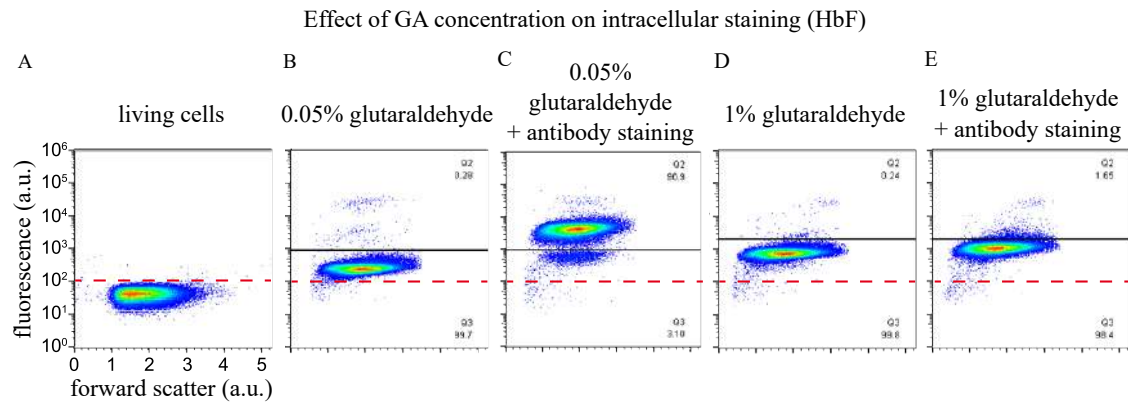
Figure 58: HbF detection by flow cytometry in cells fixed at different GA concentrations over the same fixation time and conditions. (A) Background signal of live cells in FITC. (B) Autofluorescence of GA at 0.05% concentration. (C) Related antibody signal, revealing 97% HbF positive cord blood cells. (D) Autofluorescence signal for 1% GA fixed RBCs and related HbF signal (E), showing an extremely reduced percentage of positive cells. Adapted from [1].

Figure 59 shows that oxygenated RBCs from SCD patients preserved their biconcave shapes despite Hb deoxygenation due to GA, demonstrating that once cells are crosslinked, no cellular structure is affected.

3.2.1.10   Effect of fixation on cell projected area

After confirming that cell shape could be maintained with the due attention to osmolality, shear stress and verifying it does not affect sickle cell shape, one quantitative microscopy parameter was assessed to compare living and fixed cells. Despite no shape difference was observed between living and fixed cells, projected area was unavoidably changing in relation to the GA concentration used (figure 60). This parameter was chosen since it was used for morphology analysis of SCD patients involved in the clinical trial MemSID, and is in general a common parameter in microscopy. Results showed that GA reduces projected area in relation to different fixation concentrations, affecting projected areas distributions. In particular, the reduced areas of fixed cells can be imagined as the effect of cell shrinkage notably caused by fixatives [59]. Interestingly, cells fixed in 0.1% GA resulted in lower projected areas. However, it has to be taken into account that this is a 2D parameter, which partially reflects cell shrinkage. Once again, fixation demonstrated the delicate sensitivity of RBCs' morphological properties.

GA for oxygenated and deoxygenated sickle cells fixation
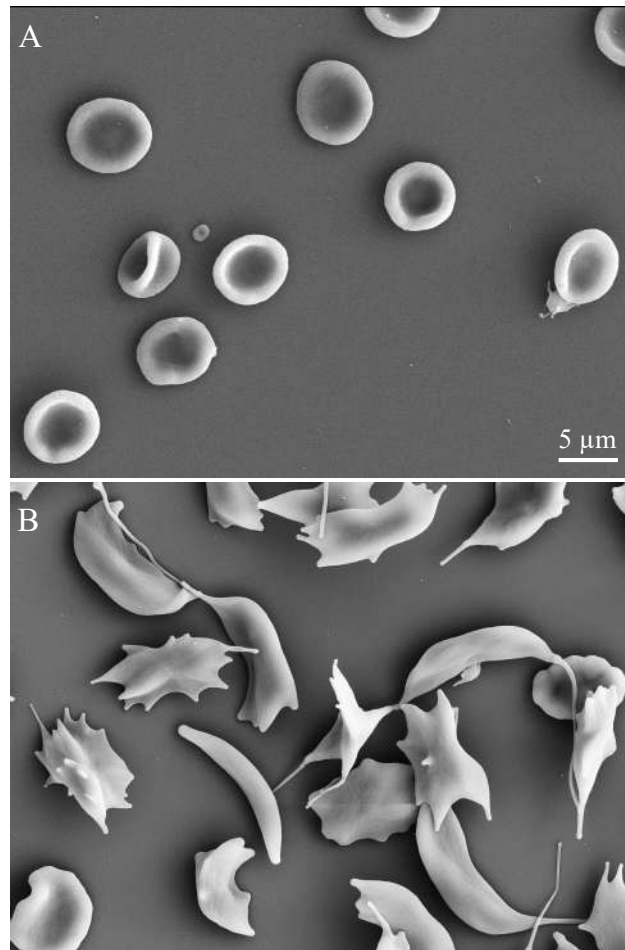
Figure 59: Comparison of (A) oxygenated and (B) fully deoxygenated sickle RBCs from a patient fixed in 1% GA, showing that despite GA Hb deoxygenation, fixed cells do not undergo any shape modification after fixation. Adapted from [1].

3.2.2 Morphological characterization of RBCs of sickle cell disease patients upon memantine treatment

3.2.2.1   Characterization of RBCs from SCD patients in deoxygenation: HbS reduction with sodium dithionite

Two methods of deoxygenation where compared to induce sickling of SCD RBCs during deoxygenation: fast and slow deoxygenation with sodium dithionite and nitrogen, respectively. Sodium dithionite reduces HbS inducing its release of oxygen. A concentration of 2 % caused the precipitation of HbS on the membrane, detected by the formation of Heinz bodies and the shape transformation into "mosaic cells". These cells were not sickling because HbS deoxygenation occurred too rapidly and prevented the crystallization of HbS into a fiber. Trials with 0.25 % dithionite lead to an extent the formation of sickle cells since the lower concentration decreased the deoxygenation rate (figure 61).

Projected area changes upon cell fixation in GA
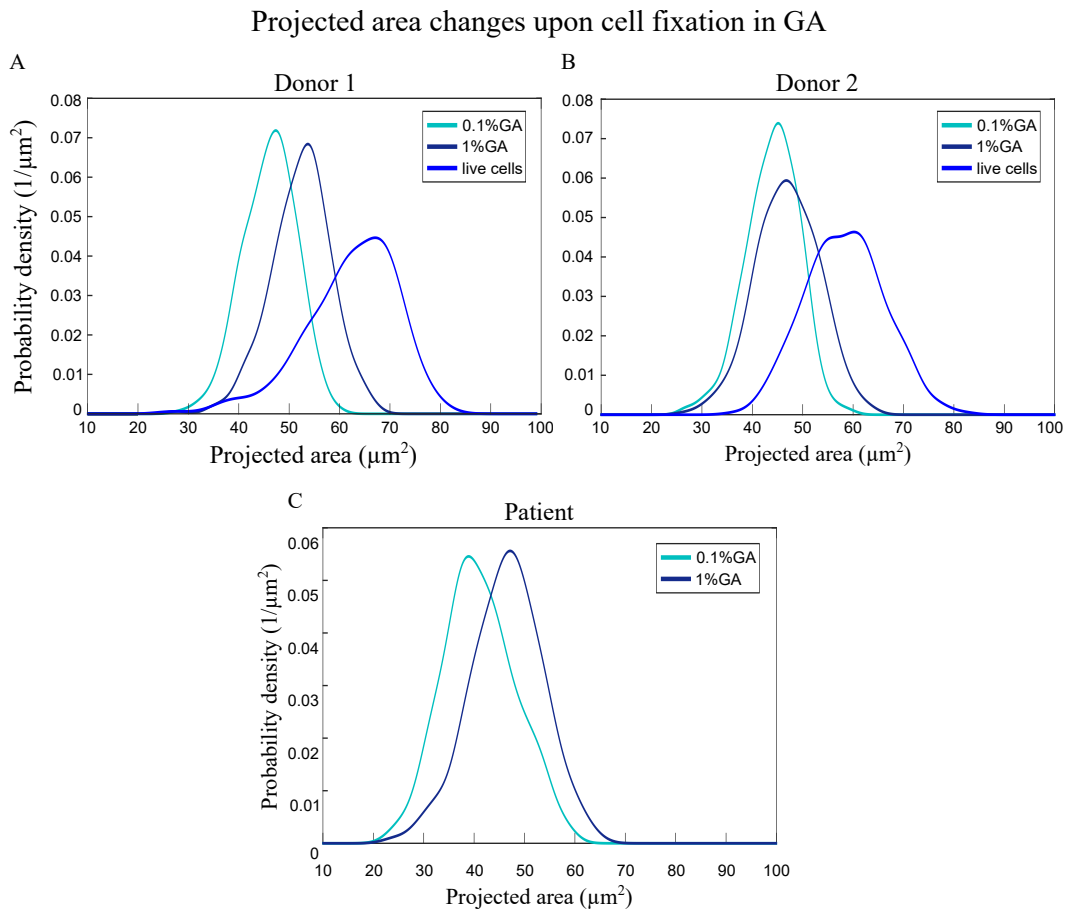
Figure 60: Effect of fixation on cell projected area in 3 donors. (A) and (B) are samples from healthy donors tested for living and fixed cells from the same blood withdrawal, (C) is a fixed sample from a patient affected by hereditary spherocytosis sent by Fondazione IRCCS Ca' Granda Ospedale Maggiore Policlinico (Milan). Note that cells fixed in 0.1% GA have distributions shifts towards smaller projected area values compared to cells fixed in 1% GA.

Slow deoxygenation achieved by substitution of oxygen with nitrogen to a constant concentration of $1\% \ O_2$ resulted in cell sickling. Sickle or spiky cells formed depending on HbS concentration.

Due to non-sickling of cells if dithionite was used at higher concentration and because of morphological transformation of healthy RBCs into echinocytes with the lower concentration, slow deoxygenation in a glove box was chosen as a method for sickling, adding the possibility to fix deoxygenated cells for following microscopy.

3.2.2.2   Effect of deoxygenation on RBC morphology

To understand the impact of projected area, eccentricity and solidity on cell analysis, tests on 2 SCD patients were done and compared to 3 healthy controls under atmospheric oxygen and deoxygenation. Results showed clear changes in the distributions of these 3 parameters (figure 62).

Projected area resulted in a dramatic shift towards larger values compared to healthy subjects distribu-

Deoxygenation of RBCs with sodium dithionite
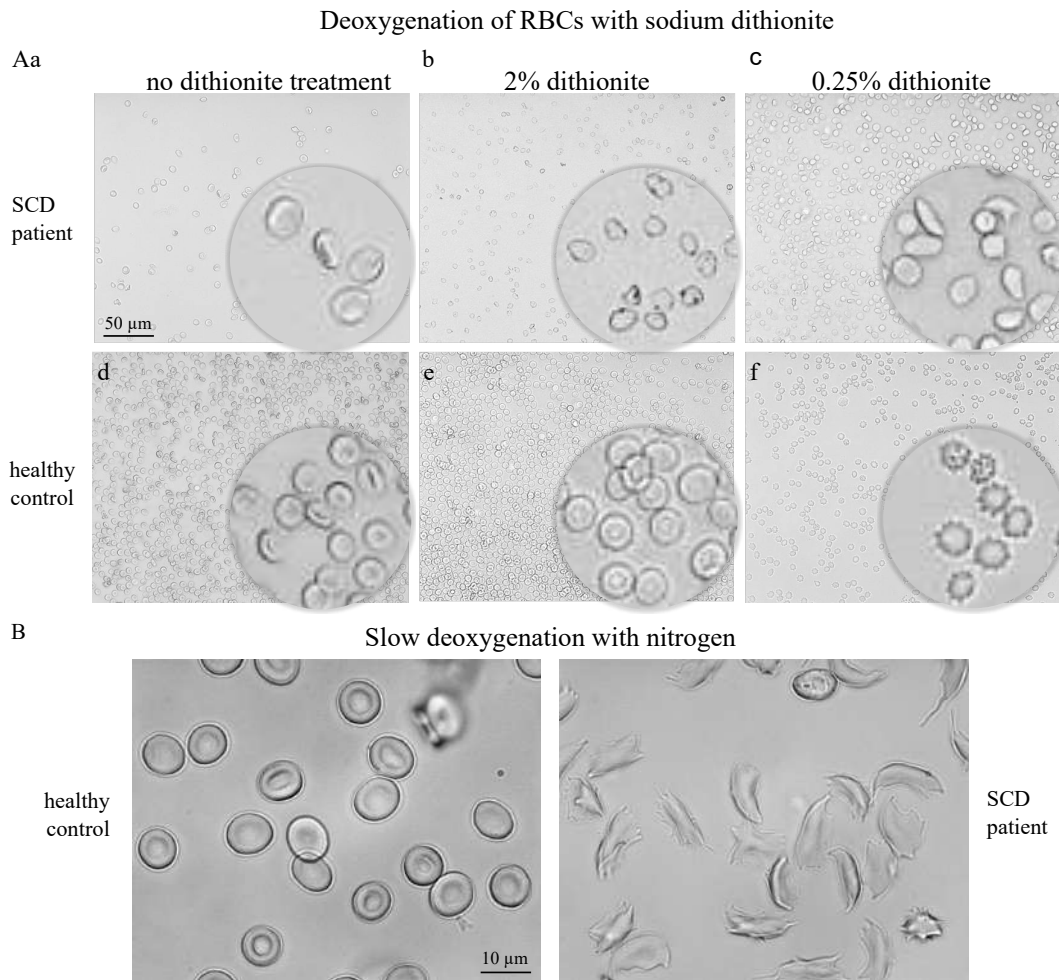
Figure 61: Effect of (A) fast and (B) slow deoxygenation of Hb on RBCs. (A) Fast deoxygenation: (a) biconcave shapes preservation in a control SCD sample not subjected to deoxygenation; (b) "mosaic cells" forming after treatment with 2 % dithionite with the presence of Heinz bodies (dark spots on the membrane); (c) 0.25 %-treated samples with a small degree of sickling due to a slower rate of deoxygenation of HbS, allowing the formation of HbS fibers that deform cells; (d) Non-treated healthy control. (e) High concentration of dithionite not affecting RBCs, while (f) lower concentration transforming healthy RBCs into echinocytes. (B) Slow deoxygenation showing normal RBC morphology in healthy control and cell sickling in a SCD patient.

tions, showing that HbS fiber formation stretched cell membrane. On the other hand, the distribution got overall wider, including cells with smaller projected areas, thus indicating the presence of highly dehydrated dense cells. Eccentricity and solidity shifted towards values for highly elongated cells (closer to 1) with very spiky borders (closer to 0). Plots of solidity of healthy subjects were separated into two graphs for a better visualization. All three parameters have similar values in healthy subjects. Cell shapes were also subjected to manual classification to investigate the degree of sickling, showing that about 90 % transformed to sickle shapes with a small percentage of intermediate shapes between healthy and sickle. A very small amount of cells maintained a discocyte shape, different between donors due to dependency on differential HbF expression.
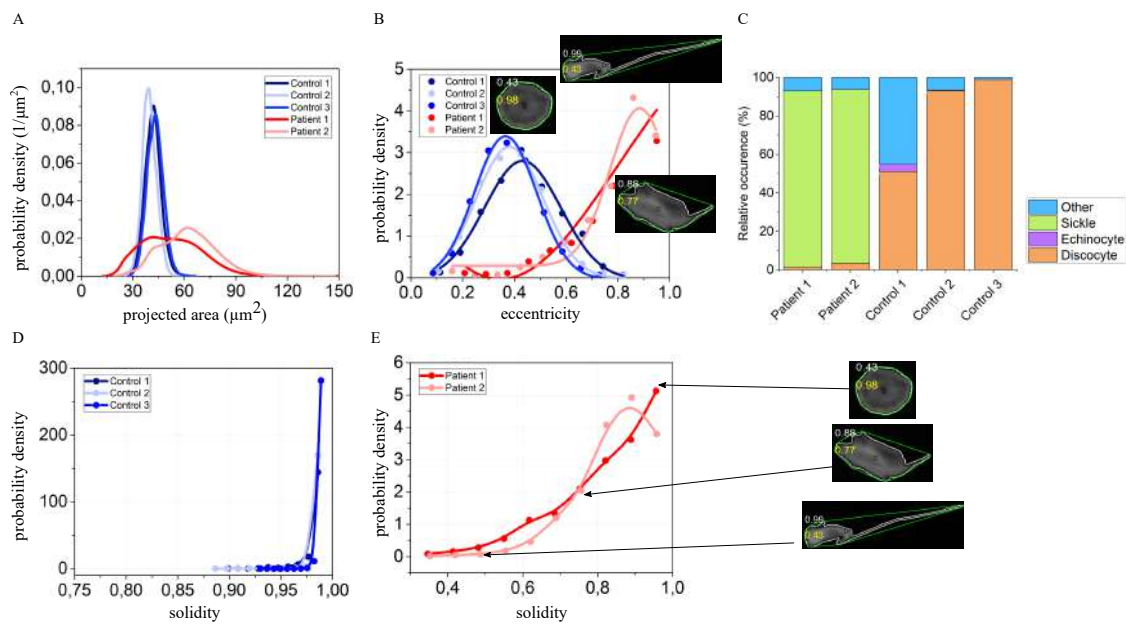
Figure 62: Effect of deoxygenation on morphological characteristics. (A) Projected area distribution of SCD patients is wider and centered towards larger values compared to healthy subjects, highlighting the heterogeneity of formed sickle cells. (B) As a demonstration of its meaning, eccentricity values increased to almost a perfect fitting ellipse (value 1) around sickle cells, a marked difference with regular discocytes. (C) Cell shape classification showed that the vast majority of cells sickle, while a number is unclassified (others) and a small portion of cells remained discocyte. One of the healthy donors showed a certain degree of shape deformations, while the others mostly stayed as discocytes. (D) Healthy controls and (E) SCD patients plots of solidity, as well showing a large change leading to extremely high cell roughness (close to 0) in highly sickled cells.

3.2.2.3   Effect of the presence of memantine on SCD RBCs shapes in deoxygenation

A test to verify the involvement of calcium in inducing sickling was done in addition and in absence of memantine on one of the patients at the follow-up phase of the clinical trial (figure 63). Incubation for 6 hours in a medium containing calcium caused the sickling of most of cells. However, a number maintained a biconcave shape. In particular, discocytes were found to be 14 % in the sample treated with memantine and only 4 % in the non-treated one on a count of 400 cells per sample. These cells did not sickle because they expressed more HbF, which does not form fibers. However, the fact that more cells did not sickle upon addition of memantine demonstrated that preservation of cell hydration by reducing cation permeability, including calcium, through NMDAR decreases the chance of sickling of other cells that express HbS.

3.2.2.4   Projected area, eccentricity and solidity in healthy subjects

To be able to understand the effect of MemSID trial on patients' RBCs' morphological characteristics, 3 healthy donors were analyzed after fixation of fresh cells directly following blood drawing (figure

Effect of MEM on number of discoytes after 6 hours of deoxygenation
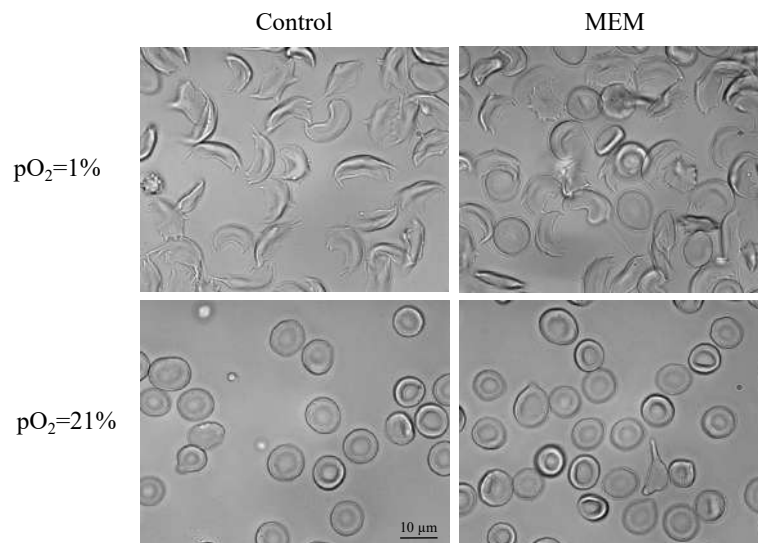
Figure 63: Test on the effect of calcium on SCD RBCs sickling upon MEM action on NMDAR of a patient. In a calcium-containing medium supplemented with NMDAR agonists glutammate and glycine, cells sickle less, leading to a 14 % discoytes in the MEM-treated sample versus 4 % in non-treated control. At atmospheric oxygen no shape change occurred, demonstrating no effect caused by calcium-supplemented medium and MEM on cellular morphology.

64).
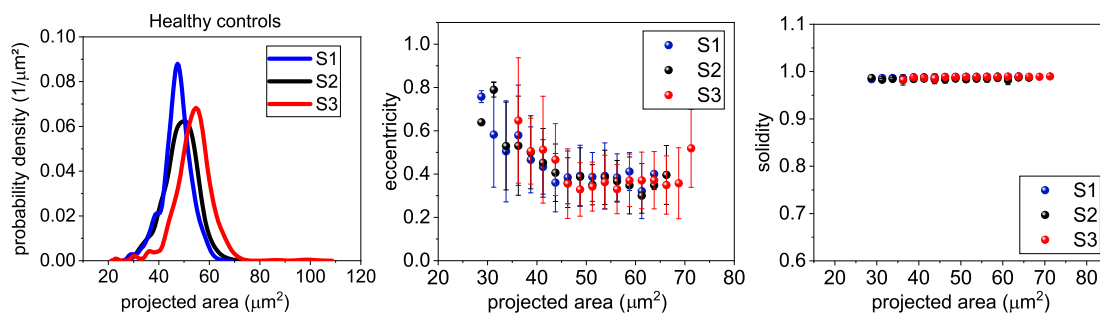
Figure 64: Plots of projected area distributions, eccentricity and solidity vs projected area in 3 healthy subjects (S1, S2, S3). (A) Note the variability between subjects shown by the shifts in projection values. However, each probability density distribution had a similar width. (B) Eccentricity vs projected area showed average roundness to be about 0.4 for discoytes. A population of elongated cells existed for RBCs with smaller projected areas. (C) Solidity values were mostly at 0.99.

3.2.2.5   Projected area, eccentricity and solidity in treated patients

To examine patients, probability density distributions for projected area, eccentricity and solidity were assessed at three time points of the trial: pre-treatment (pre), end of treatment (end) and 2 months follow-up (post) from stored fixed samples (for representative images in 3D, see figure 80 in Appendix). Statistical tests demonstrated significant differences between "pre" and "end" phases and between "end" and "post" phases. Projected area plots resulted in a shift towards smaller values at the

end of the treatment, similar to healthy controls, and reduced the extension of the distribution (figure 65, see standard deviations on box plots). This means that cell heterogeneity caused by sickling was decreased by the treatment as a consequence of overall maintained cell hydration. After two months from treatment suspension (post phase) RBCs distribution shifted in the direction of the original condition (pre-treament) in P1, while its median values in P2 and P4 got even more reduced. All patients maintained a significant difference with the pre-treatment condition, revealing a preserved effect of memantine on RBCs stability. However, a difference existed between "end" and "post" phase in three patients, showing that treatment suspension is affecting RBCs state.
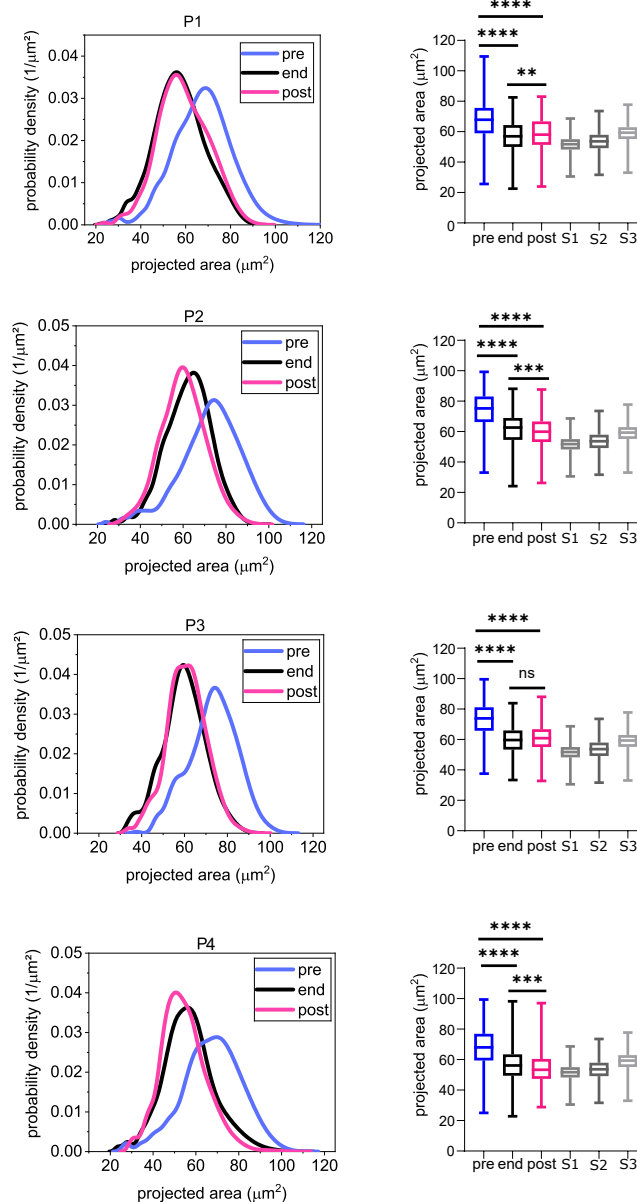
Figure 65: Probability density distributions of cell projected area in the 4 patients (P1, P2, P3, P4) completing the trial and relative box plots together with 3 healthy subjects (S1, S2, S3). All patients showed a shift from pre-treatment phase to the end of the trial. Such shift were mostly maintained although there was a significant difference in three patients between "end" and "post" phases. Box plots highlight projected area distributions becoming tighter by the end of the treatment, demonstrating an improvement in cell homogeneity. P=patient, S=subject. Pre=pre-treatment phase, end=end of treatment, post=two-months follow-up post-treatment.

3.2.2.6   Eccentricity

Eccentricity plots versus projected area reflect healthy subjects distributions, with smaller values of projections related to higher elongation. However, the treatment visibly improved the circularity of all kinds of cells, a feature not only maintained post-treatment but eventually improved (figure 66). Patient 3 resulted in fact in a significant difference only in the post phase, while for P4 no differences occurred. The presence of more circular cells after suspension of memantine explains that their hydration is maintained, preventing sickling and related shape deformations to occur.

3.2.2.7   Solidity

Solidity in cells from patients is a less sensitive parameter compared to deoxygenated cells, ranging from 0.90 to 0.99 in SCD RBCs. However, some RBCs appeared rough, with values close to 0.5. The treatment resulted in smoother cell borders for high projected areas in P1 (solidity vs projected area plot, figure 67). For P2 and P3 a significant improvement occurred only post treatment, while maintained in P4. This patient had overall a rather homogeneous solidity distribution throughout each tested phase, but a significant difference resulted between "pre" and "end" phases, maintained post treatment. Interestingly, this change appeared as a worsen solidity of RBCs. Considering no significant differences occurred in eccentricity, the meaning of such change may highlight a higher cell resistance to sickling events, reduced by the improved cell hydration but still occurring during cell lifespan and eventually deforming cells without causing their lysis.

3.2.2.8   Analysis of P5 and P6

Two other patients, P5 and P6, were recruited for the trial but did not finalize it. Their anticipated treatment suspension gave the opportunity to explore which morphological parameters are firstly influenced by memantine. After 1 month, a significant difference resulted in projected area and solidity distributions.

P6 rapidly responded to this effect, while P5, who continued for another month, resulted in a smaller effect (figure 68). Despite the differential response to the drug, cell projections distributions resulted reduced in their width and shifted to smaller values as observed for P1 to P4. Solidity resulted as well in a significant difference, with larger deviations in the distribution: similarly to P4, this may be related to the variety of cells in the whole population, where existing sickle cells were progressively substituted by smoother cells and cells previously affected by sickling events co-existed thanks to their improved life-span by increased cell hydration. Eccentricity did not show any difference, suggesting that this parameter is an indication for the long-term effect on cell morphology by MEM.

3.2.2.9   RBCs' shape occurrence and manual classification upon MemSID trial

Furthermore, cell shapes were compared to projected areas in the three time points. RBCs of different sizes corresponded to ranges of projected areas, but figure 69 underlines that most sickle dense cells corresponded to the smallest values, in accordance with the higher elongation seen in plots of eccentricity.

The visualization of the occurrence of sickle cells in the three phases suggests a decrease in sickle cells upon treatment, statistically evaluated in figure 70, where the amount of discocytes significantly increased by the end of the treatment, even more in the post phase. Sickle cells decrease showed a P value of 0.056 only in the post phase. This difference with discocytes can be explained by the fact that some deformed cells not clearly sickle were classified rather in the group "others" to avoid wrong sickle cell evaluation, thus counting as "others" some possibly actual "sickle" shapes.
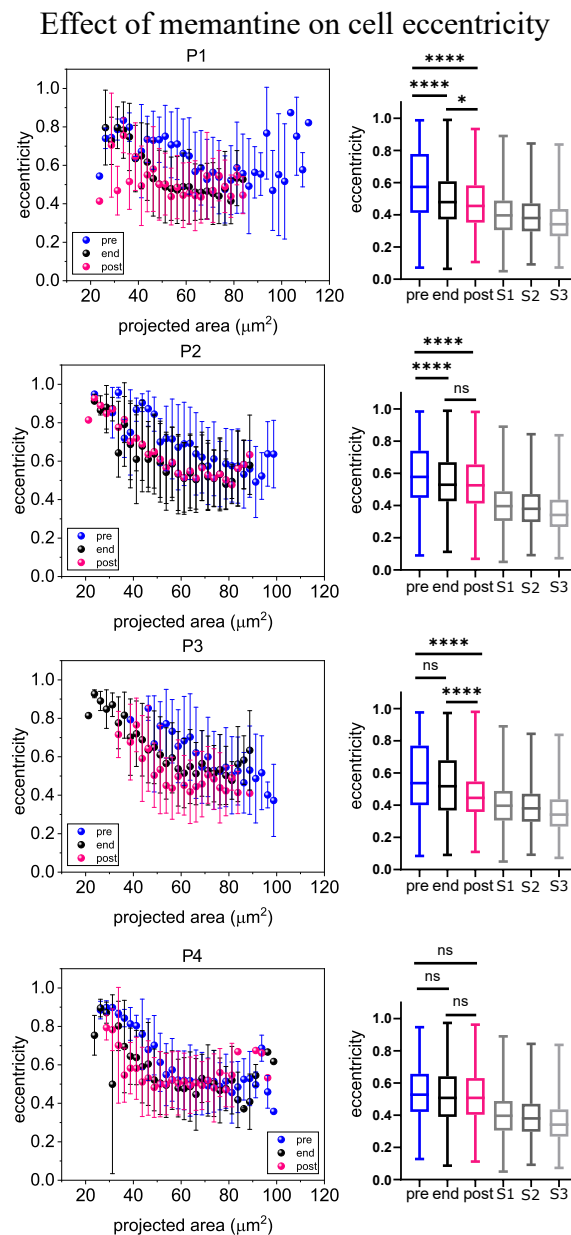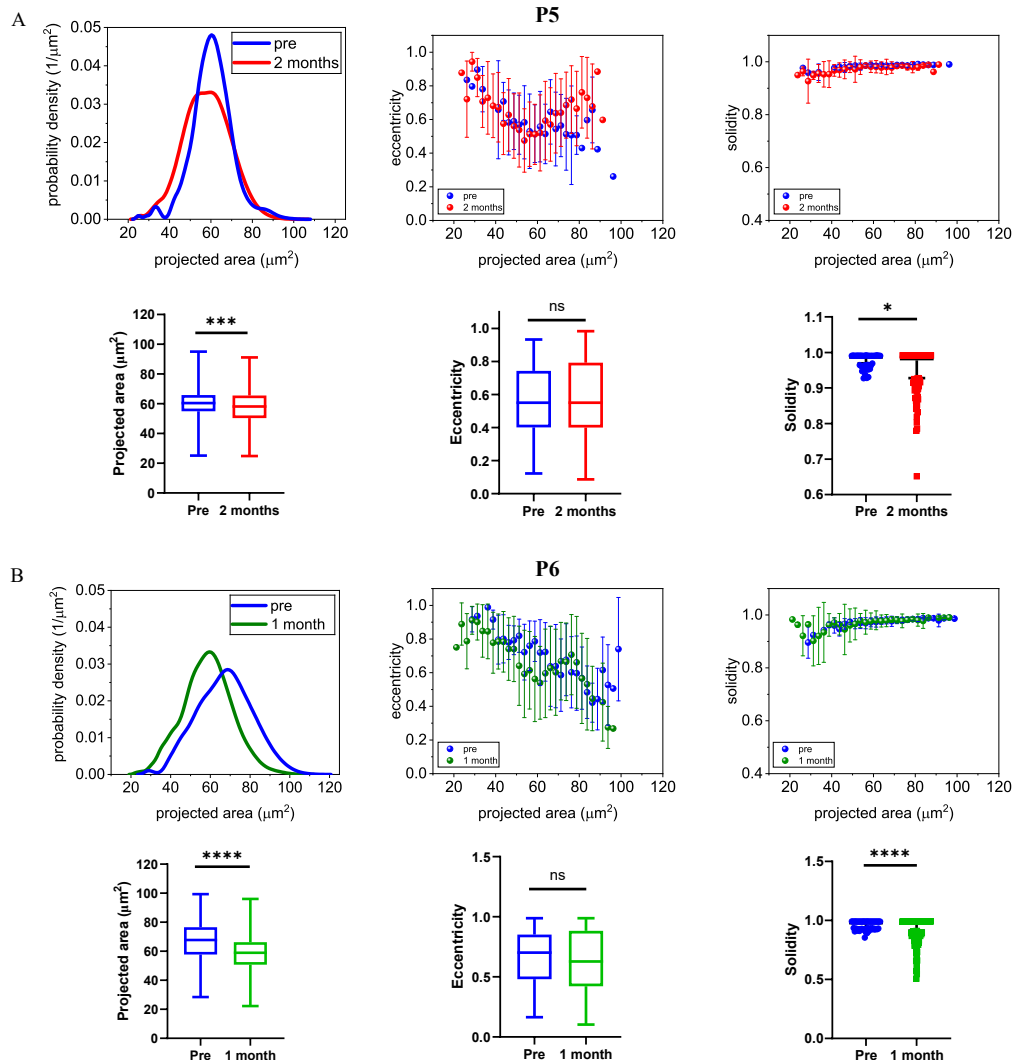
Figure 66: Cell eccentricity vs projected areas during the phases of treatment and relative eccentricity distributions box plots in the 4 patients (P1, P2, P3, P4) completing the trial with 3 healthy subjects (S1, S2, S3). Note that cells with the lowest projected areas were more elongated. Except for P4, all patients showed a significant decrease in cell eccentricity in the end-phase, maintained or improved in the post-phase. This change in cell roundness is a sign of less cell sickling, and the preservation of this feature after suspension of the treatment is an indication of improved cell survival. P=patient, S=subject. Pre=pre-treatment phase, end=end of treatment, post=two-months follow-up post-treatment.
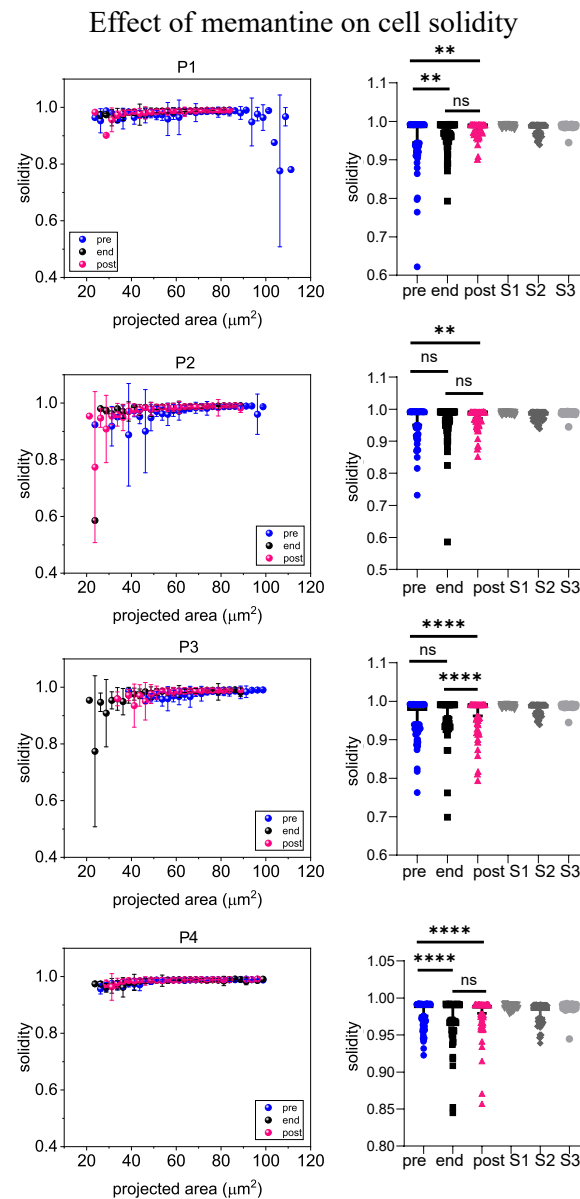
Figure 67: Plots of solidity vs projected area in the 4 patients (P1, P2, P3, P4) concluding the treatment and related solidity distributions box plots with 3 healthy subjects (S1, S2, S3). Each patient shows a significant change in cell solidity upon treatment, preserved or improved post-treatment. Solidity highlights patients' border roughness: P1 showed rough cells for higher projected areas in the pre-teatment phase, disappeared upon treatment, while P2 and P3 showed higher roughness for lower projected areas. P4, although not characterized by particular cell roughness values, resulted in significant difference between the phases. These apparent solidity worsening may actually indicate a higher cell resistance to sickling events during their prolonged lifespan upon treatment. P=patient, S=subject. Pre=pre-treatment phase, end=end of treatment, post=two-months follow-up post-treatment.

Morphological analysis on patients which suspended the treatment

Figure 68: Projected area, eccentricity and solidity distributions of cells from the 2 patients suspending the treatment (P5 and P6).(A) Analysis on P5: projected area distribution and related box plot, as well as solidity plots show a significant difference upon 2 months of treatment, while eccentricity did not change. (B) Analysis on P6: projected area and solidity changes already occurred with one month treatment, while eccentricity did not highlight any significant change.

With respect to P5 and P6, the short memantine administration period had an effect on cell shapes as well. The overall occurrence of sickle cells increased in P5. This may be explained by a higher survival of the existing cells that were affected by previous sickling events, in accordance to solidity showing an increase in cell roughness. P6 resulted in a slight increase in the number of discocytes for lower projected areas.
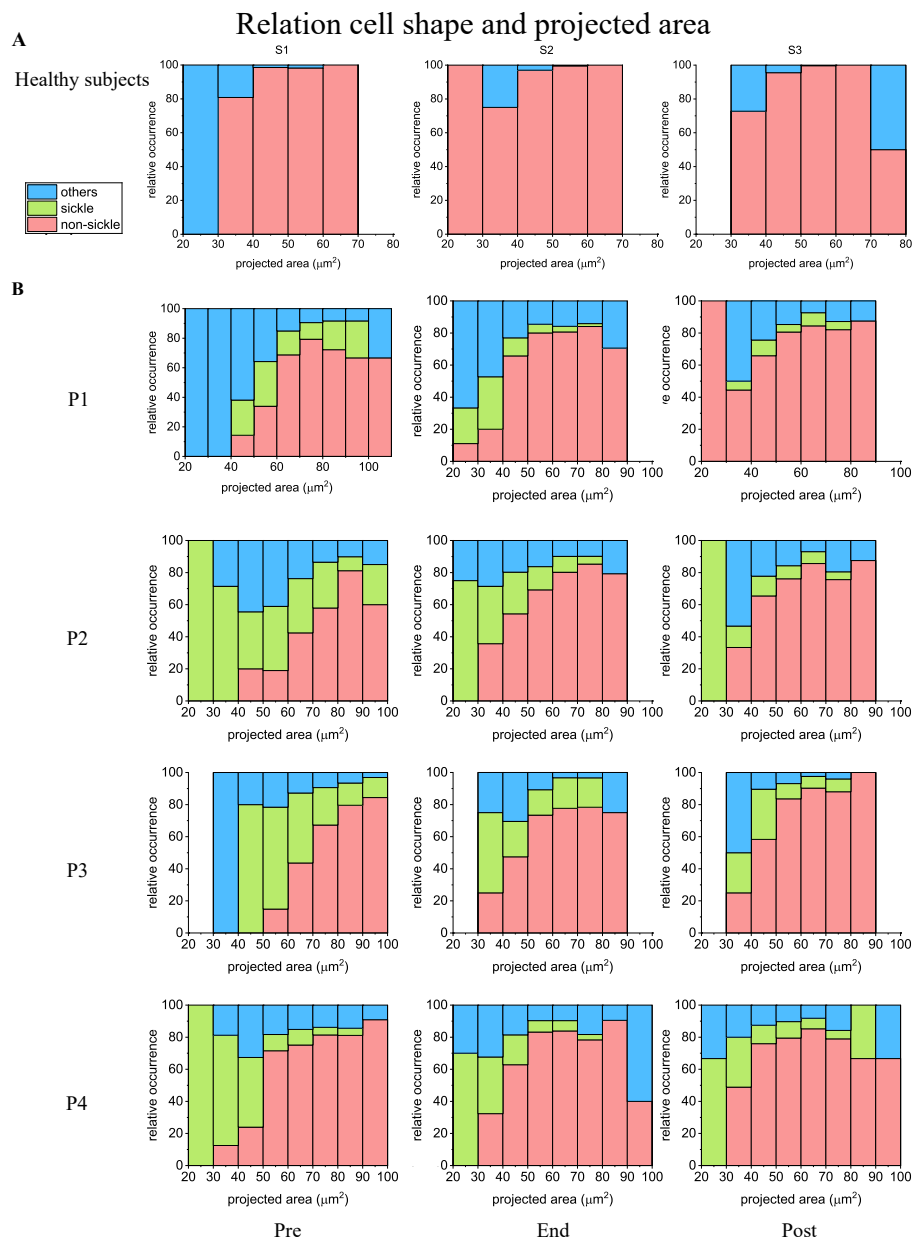
Figure 69: Shape occurrence at different projected areas in healthy subjects compared to the 4 treated patients. (A) Healthy subjects shape distributions were mostly "non-sickle" cells, i.e. discocytes. A small portion of slightly deviated cell shapes (elongated) was detected. Sickle cells were absent. (B) Shape occurrence in patients in the different phases of the treatment (Pre, End, Post). Note that most sickle cells corresponded to lowest projected areas. By the end of the treatment the amount of such cells was reduced, being replaced by "non-sickle" shapes. This effect remained upon treatment suspension (post treatment follow-up phase).

Evaluation of cell shape changes during the treatment
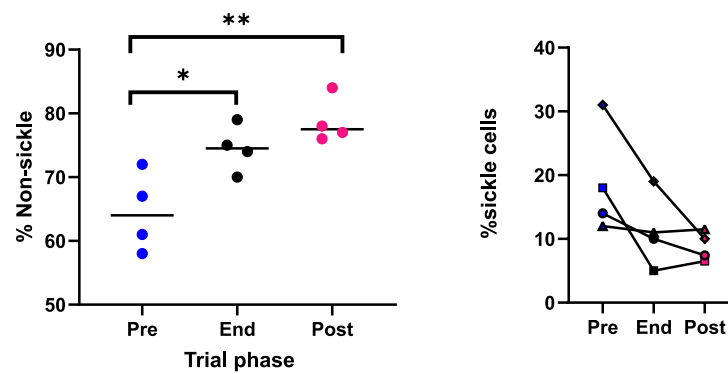
Figure 70: Cell shape changes evaluation for the 4 patients concluding the treatment. The number of "non-sickle" cells increased significantly and was not only preserved in the post-phase, but resulted even higher, demonstrating an improved cell survival due to less sickling events, where both present and new formed cells maintained their hydration. The number of sickle cells decreased in all patients but was not statistically significant (P=0.056 in post phase), probably due to cells classified as "others" that reduced the accuracy of cell count during manual classification in all trial phases.
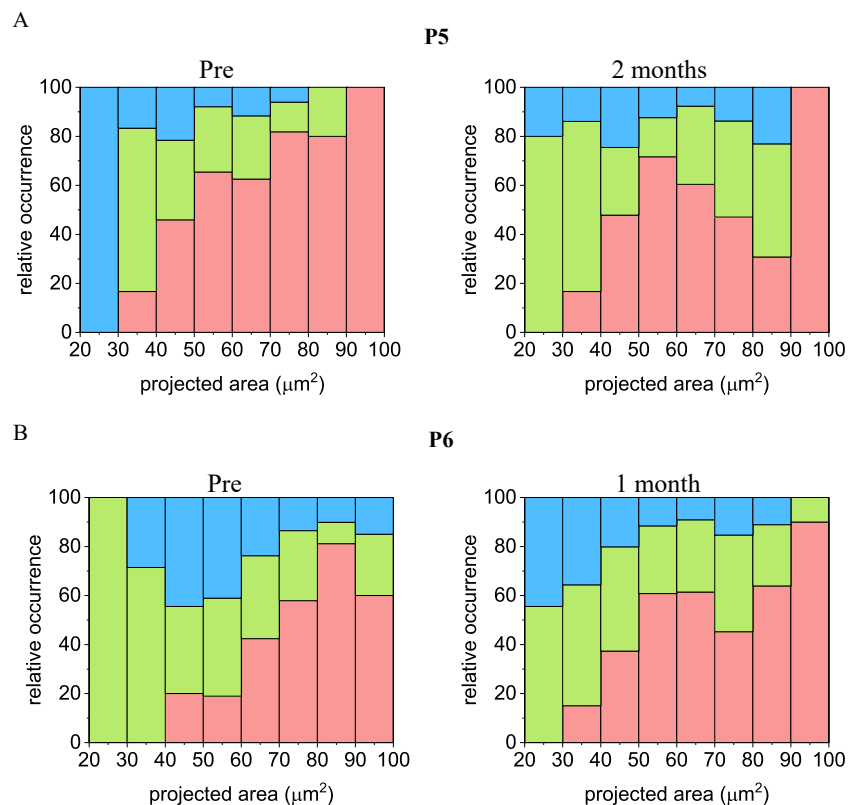
Figure 71: Shape occurrence related to projected area in the 2 patients suspending the treatment. (A) P5 in the pre-treatment phase and after 2 months. Note that the occurrence of "sickle" cells increases during this period and may be a result of improved survival of cells previously affected by several deoxygenation-reoxygenation cycles. (B) P6: pre-treatment compared to 1 month of under memantine administration. Here, a slight increase in "non-sickle" cells occurrence is noticeable.

3.2.3   Automated 3D classification of RBCs' shapes in hereditary spherocytosis

3.2.3.1   3D shapes in comparison with classical smears

Cell orientation induces to think cells to have a certain morphology, while the possibility to rotate 3D reconstructions of 360° reveals not only the actual shape but also a higher cell surface complexity, making it difficult to assign cells to a specific shape type. The automated classification applied here for SDE shapes aimed to eliminate such difficulties by assigning cells a score that represents their transition state. In fact, while there are energy minima where certain cell configurations are preferred [96], the transitions from one shape to another showed a continuous nature. As a consequence of these first observations, the examination of samples from patients affected by HS (see table 12 for details on mutations) revealed the complete absence or a very limited amount of spherocytes (figure 72), often comparable to the amount in healthy subjects. In blood smears, several cells appear circular and devoided of the central pallor, giving the impression of being fully spherical. In 3D, most of these spherocytes were actually stomatocytes of various types or other shapes that appeared fully round according to their rotation. In particular, the comparison in 3 patients with different mutations causing HS lead to a count of (figure 72): A=11 %, B=8 %, C=10 %, while in the corresponding 3D images for: A=2.5 %, B=0 %, C=0.08 %, mostly reflecting the amount observed in healthy subjects (0 % to 0.3 % counted in 25 control samples). Of note, patient B was the only one with the highest amount of spherocytes in 3D within the group of 11 patients. Rather, other cell morphologies became of more interest in 3D because of their exclusive presence in patients' samples: the class "acanthocytes" included echinocytes with different features, such as squared or polygonal, flattened and occasionally mushroom-shaped cells (figure 73). All these type of shapes were collected into this single class for training the 2-stage ANN since they have not been yet classified in literature.

Table 12: Information related to the presented 5 patients affected by HS. They were all heterozygous for their mutations. As indicated in the results of SCD MemSID trial, P stands for "patient".

HS patient	Mutation	Corresponding protein
P1	*SLC4A1*	band 3
P2	*SLC4A1*	band 3
P3	*ANK-1*	ankyrin-1
P4	*SPTA1*, *SLC4A1*	spectrin α, band 3
P5	not identified	n.a.
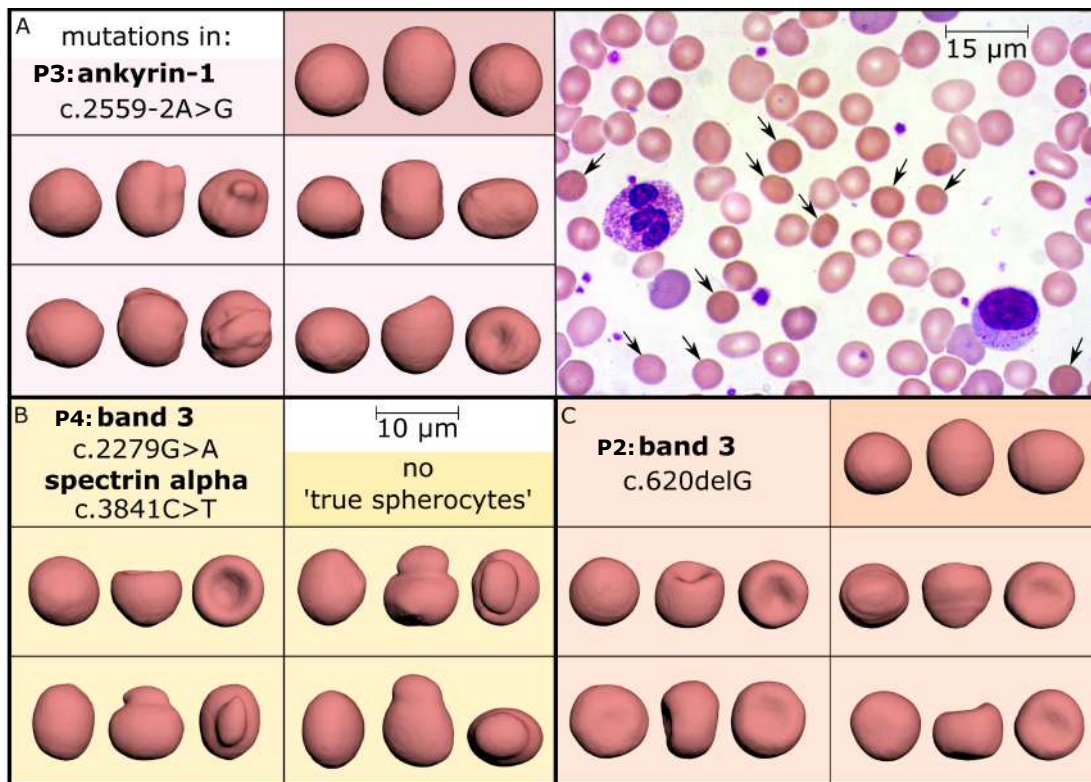
Figure 72: Example of 3D-reconstructed true and pseudo-spherocytes in patients (A), (B), (C) affected by HS: (A) left: 3D images, right: corresponding blood smear showing spherocytes (arrows) from a patient with mutation in *ANK-1*. Each box in every panel shows perpendicular rotations of the same cell. Darker-colored boxes represent true spherocytes, which were completely absent in (B).
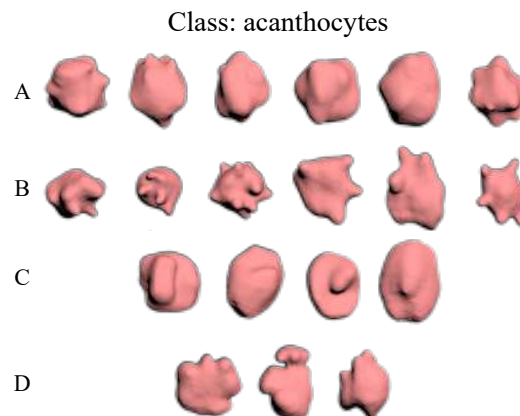

Figure 73: Example of cells included in the class "acanthocytes". (A) Quadratic and polygonal echinocytes. (B) Typical acanthocytes as described in literature. (C) Flattened echinocytes with irregular spikes formations. (D) Mushroom-shaped and irregularly spiky cells.

3.2.3.2   Training and validation performance of the 2-stage ANN

The optimization of the learning process is the key for a well-performing neural network. Providing a sufficient amount of training data, avoiding redundancy, choosing the right functions and tuning the

parameters such as number of epochs, number of hidden layers and interpolations for data augmentation, allowed to obtain an accurate ANN performance. Training and validation curves for each ANN of the 2-stage system are shown (figure 74), while examples of 3D shapes, corresponding SHA and related automated positioning in the SDE scale are shown figure 81 in Appendix.
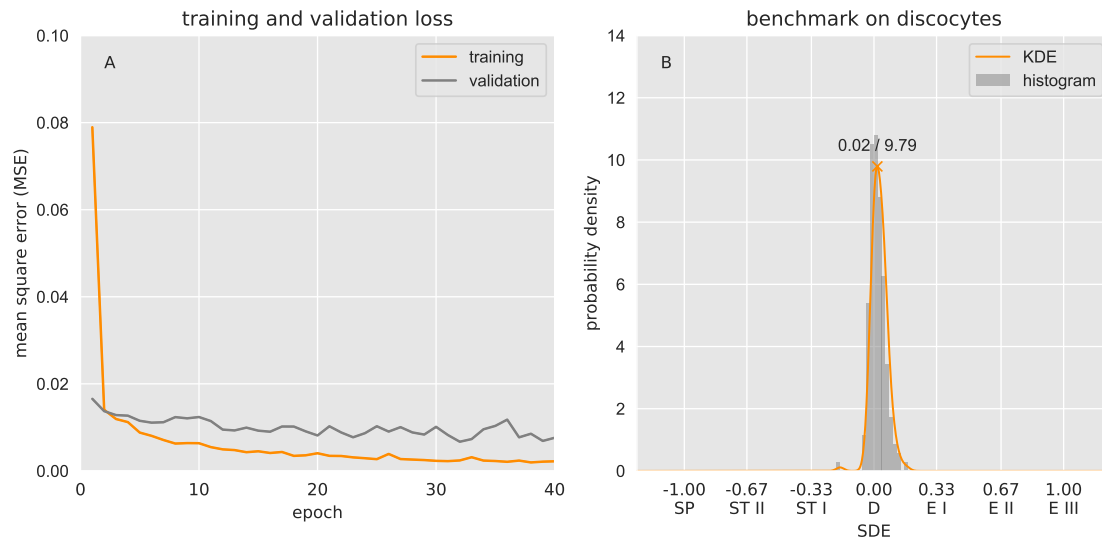
Figure 74: Training and validation for ANN regression output (SDE scale). (A) Training and validation curves with an optimal fitting that minimizes the MSE. (B) Plot of the probability density function of a group of test discocytes, showing an excellent allocation of such shapes at the expected position on the SDE scale.

For the regression type ANN, the MSE converged to 0, both during training and validation, confirming the high learning performance of the network for SDE shapes. The benchmark on discocytes highlighted the resulting cell distribution within a narrow interval around 0 (where they should be located).

For the classification ANN, the training was evaluated with the CE (figure 75) but also by assessing the categorical accuracy, which represents the fraction of correct predictions by the 2-stage ANN over the total. Finally, a confusion matrix was generated for evaluation of which cells were correctly and non-correctly classified by comparing the actual class (y direction) to the predicted class (x direction). For example, 1% "acanthocytes" were predicted as "unknown" cells.

After verifying training and validation of both ANNs, tests on healthy subjects and patients were run to see if reproducible results on a large set of new data could confirm the quality of the automated classification.
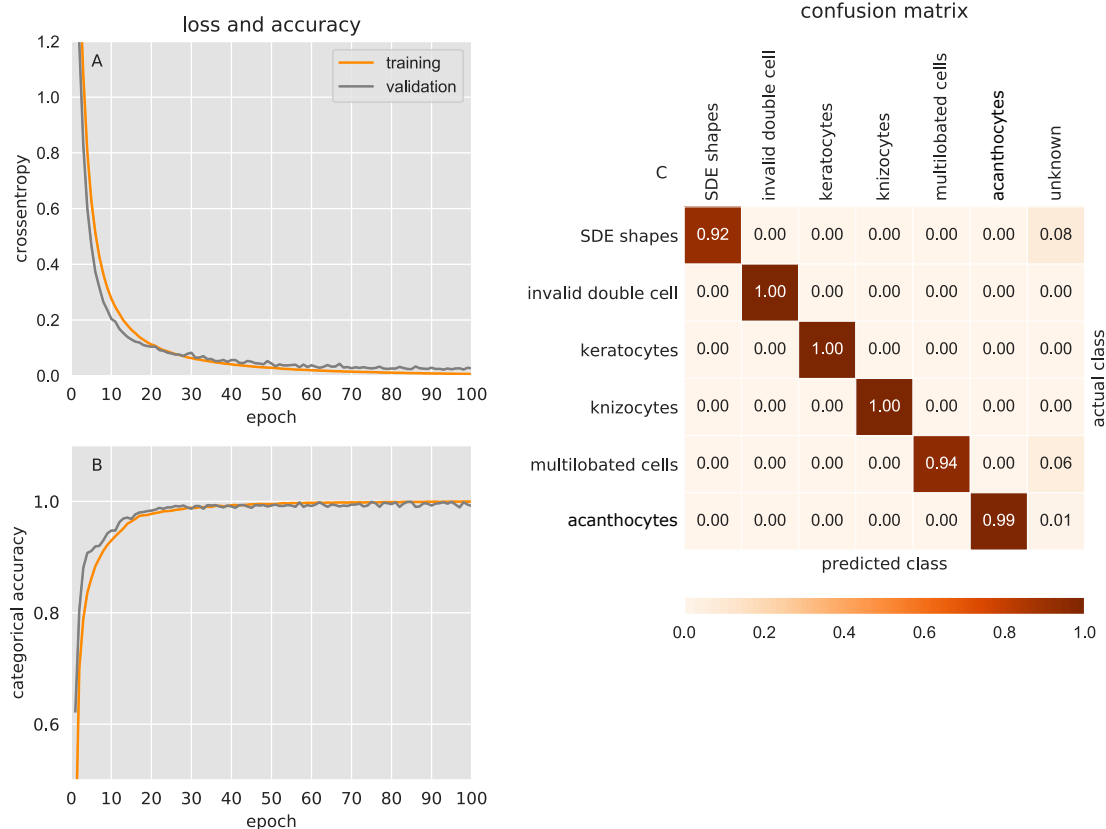
Figure 75: Training and validation curves for the 2-stage ANN classification output. (A) The loss function (CE) converged to 0 and the process was aborted after 100 epochs both for training and validation. The categorical accuracy is a measure of how many cells were correctly placed in the classes and is shown in (B). It almost approached 100 % for the tested cells. (C) Confusion matrix showing that classes were almost precisely recognized. Three of them were fully correct.

3.2.3.3   Tests on healthy and patients' samples

As expected and previously confirmed by visual inspection of 3D reconstructions, the distribution of healthy subjects was allocated in the discocyte range. Among the 25 examined subjects, some showed small peaks of stomatocytes, completely absent in other subjects. Occasional keratocytes and knizocytes appeared. Knizocytes can be an artifact of fixation, however not observed for fixed cells in $0.1\,\%$ GA and therefore taken into account only in samples fixed at this concentration. Figure 76 resumes results from 5 healthy subjects.

In the case of patients, confirming what was observed by visual inspection, the allocation of cells at the position of spherocytes (score +1) was none. The automated classification of 5 patients is shown in figure 77: cell distribution profiles were visibly different from healthy subjects, showing a wider cell shape distribution over the SDE scale and a shift towards stomatocytes. In particular, P3 had a large amount of stomatocytes and corresponded to (B) in figure 77. While expecting a common trend towards a high number of spherocytes in patients affected by this anemia, each patient showed
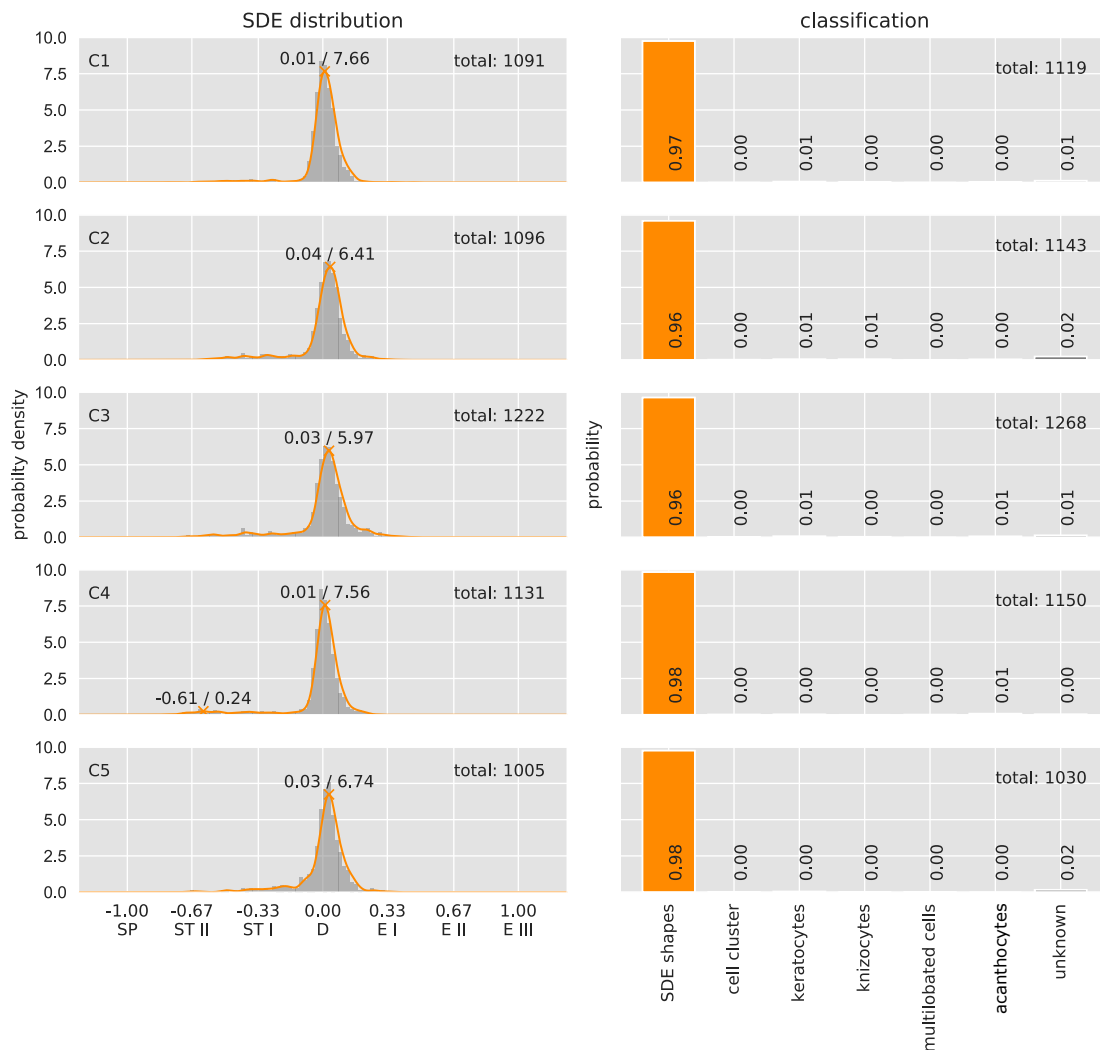
Figure 76: Probability density distributions of 5 healthy subjects and related shape classification. All subjects clearly show similar distributions, where cells were allocated at the discocyte position on the SDE scale. In subject C4 (control 4) a small amount of stomatocytes was present. The classification plot showed cells in the SDE class, while the other classes were almost totally empty.

different shapes distribution. In fact, the mutations causing the disease involved different genes. The classification profile resulted in a larger shape distribution between classes, especially in the class of "acanthocytes", which includes several deformed echinocytes. A considerable percentage of cells was classified as "unknown", due to the lack of existing classes for other deformed shapes. The chosen 5 patients were the ones with the largest number of imaged cells in order to obtain statistically relevant results (minimum 1000 cells per patient). Besides the individual differences, according to the automatic 3D shape recognition by ANNs, patients affected by HS tend to have a wide SDE distribution and non-classifiable deformed shapes.
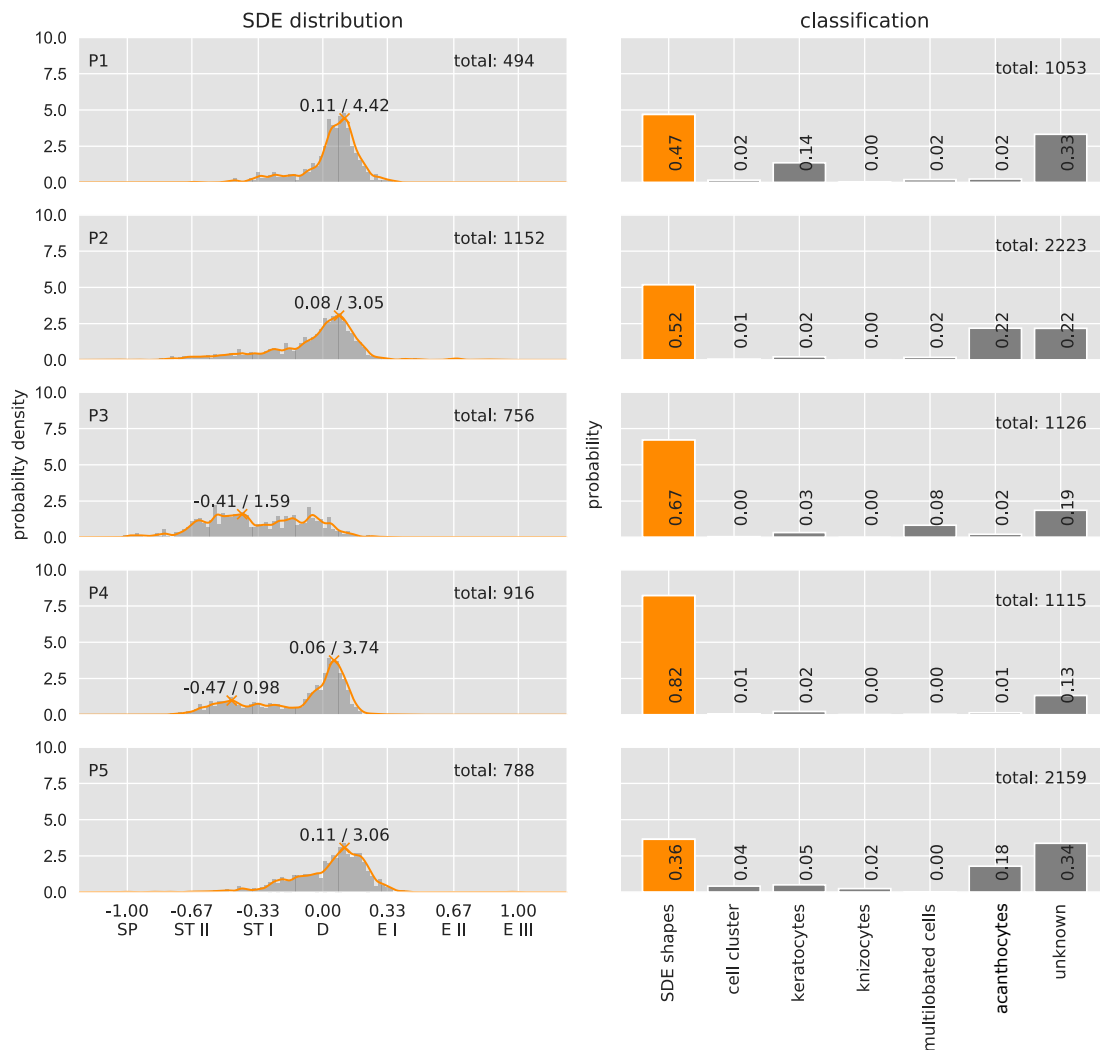
Figure 77: Example of 5 patients with HS. Different shape distributions may reflect the molecular cause of the disease, but a shift towards stomatocytic shapes can be observed in all the patients. The classification resulted in several cells in the "unknown" class and a considerable amount of "acanthocytes" in the case of 2 patients.

Finally, to validate such results, 200 cells from both healthy and patients were randomly picked and manually checked. A confusion matrix for all classes was created, also including SDE shape types (figure 78).

The validation on healthy subjects and patients confirmed the accurate recognition performance of the 2-stage ANN. Most of the errors were in the classes and this is expectable considering that the number of cells for the training was reduced compared to the number of cells within the SDE scale that were artificially created by osmolality. Moreover and maybe more importantly, dividing shapes in discrete classes is not the right choice for 3D shape recognition because each cell may have features of different classes that do not allow a complete allocation to a specific class. In fact, the error here

Figure 78: Confusion matrices of all shapes resulting from the comparison of automated and manual shape recognition. SDE shapes demonstrated an excellent recognition accuracy, from lowest value as 78 % up to 100 %. Cells owing to specific classes showed a higher recognition error, partly due to the larger amount of unknown shapes, especially occurring in patients, partly due to the less defined shape features that could allow a clear allocation into a class. The error obtained in such classes was therefore related to the intrinsic inaccuracy of the training data.

observed was due to recognition uncertainty, which brought to the placement of cells in the class "unknown".

Discussion

4.1 The role of oxygen in erythropoiesis & neocytolisis

This study aimed to understand how erythroid precursors are affected by oxygen levels. The relevance of this scientific question relates both to physiology and laboratory methods for the *in vitro* production of RBCs. On one hand it aimed to understand which mechanisms during erythropoiesis could lead to a hypothetical neocytolisis after high altitude and on the other hand, on understanding the reasons behind the current impossibility to differentiate cultured reticulocytes to mature RBCs, considering that cultures are performed at $20\,\%\,O_2$ oxygen, which is a hyperoxic condition and therefore may affect cells by oxidative stress. Since it is not possible to follow erythropoiesis in the bone marrow, both questions required to study erythroid maturation *in vitro*. The difference and the advantage with the *in vivo* situation is that a controlled culture system allowed to evaluate the exclusive impact of oxygen on cell expansion and differentiation, while hypoxia in the bone marrow also results in increased EPO affecting cell maturation. Some studies evaluating oxygen levels effect in erythroid progenitor cultures were performed with the three-phases culture systems starting from CD34+ cells instead of all PBMCs [167, 71, 146] (detailed comparisons follow below), but none were done with the two-phase system designed by the researchers of Sanquin, making experiments worthed for a comparison.

4.1.1 High and low oxygen test at different phases of cell maturation

Before starting the experiments with the actual donors of the study, a single-donor preliminary test was done to assess cell ability to expand and survive at $3\,\%\,O_2$ in different cell maturation phases. Results showed that cells can grow at any phase and are all affected by oxygen levels in terms of reduced cell growth and volume, meaning that the most profound effect is on HSCs expansion potential. Vlaski et al. [167] have also observed this, but their cultures resulted in a higher yield in hypoxic cells, where cultures at $20\,\%\,O_2$ were compared to cultures at $5\,\%\,O_2$ and $1.5\,\%\,O_2$. However, their experimental protocol involved a step where cells were temporary moved to atmospheric oxygen because they observed cells could not survive at low oxygen despite the initial increase in cell growth. Moreover, they performed phase II and III at either atmospheric oxygen or at $13\,\%\,O_2$, which is a physiological condition in the lungs but not in the bone marrow ($3\,\%\,O_2$ at sea level). These important differences may explain the discrepancies with the results obtained here. Ishikawa and Ito [71] previously assessed BFU-E colony expansion potential comparing cultures at atmospheric oxygen with $7\,\%\,O_2$, also resulting an in increased growth at low oxygen. This was confirmed in other

hematopoietic progenitors, e.g. Bradley et al., [23], who observed an increased colony formation in granulocyte-macrophage progenitors both in mouse and human cells and in mouse fibroblasts in hypoxia. Rich et al. [142] confirmed a higher colony formation for both BFU-E and CFU-E and, besides explaining it with the reduced toxicity of oxygen, they implied a higher response to EPO in hypoxia.

All these cultures stopped at BFU-E and CFU-E stages and aimed to demonstrate an improved cell survival at lower oxygen concentrations than atmospheric one caused by the reduced oxidative stress. However, besides this advantage over hyperoxia, cultures in hypoxia were compromised when oxygen levels were very low: Cipolleschi et al. [33] observed less BFU-E expansion and also inhibition of CFU-E formation at $1\%\,O_2$. Therefore, a fine tuning of oxygen levels may result in a preponderant effect of oxygen in either cell protection or cell death.

4.1.2 Reversible effect of oxygen on cell growth and volume

HSCs respond to oxygen levels by reprogramming erythropoiesis as seen in the effect of high altitude. A single donor test was tried in culture to assess the response of cells to sudden oxygen changes without any EPO concentration modification. Results showed the adaptation ability of cells to changed oxygen levels, where proerythroblasts formed at $3\%\,O_2$ moved to $20\%\,O_2$ recovered their expansion potential, while a loss was observed when proerythroblasts were moved from hyperoxia to low oxygen. The response in terms of cell volume occurred already after 24 hours, while it required at least 48 hours to affect cell growth. The expansion potential recovery was also seen by Cipolleschi et al. [33] when they moved cell from hypoxia to atmospheric oxygen. These results demonstrate the adaptation ability of erythroid precursors, in particular of HSCs. These latter cultured at $3\%\,O_2$ resulted indeed in a 1.4 times higher cell yield than proerythroblasts moved to low oxygen. This more relevant response of HSCs to oxygen levels was also seen by Vlaski et al. [167] and explained by Cipolleschi et al. [33] as an inverse effect of oxygen on cell cultures, where low levels favour BFU-E and CFU-E early development but inhibit their terminal expansion, therefore explaining the results observed here. On the other hand, moving proerythroblasts at low oxygen to atmospheric levels did not fully recover proerythroblasts expansion potential, confirming their higher susceptibility to oxygen levels because of their lower adaptation capacity compared to HSCs. This may indicate that HCSc can be reprogrammed for reducing their expansion potential to push towards favoring an earlier cell differentiation in necessary conditions.

4.1.3   Characterization of erythroid precursors grown at high and low oxygen comparison with the precursors from high altitude

4.1.3.1   Growth and volume curves

After that preliminary tests confirmed the possibility to culture PBMCs from day 0 expansion at $3\%\,O_2$, the donors involved in the neocytolisis study were cultured at high and low oxygen from pre-altitude isolated PBMCs and only at atmospheric oxygen for PBMCs isolated at high altitude.

While $20\%\,O_2$ and $3\%\,O_2$ confirmed the preliminary results with a significant reduced cell growth and volume at $3\%\,O_2$, pre-altitude cultures compared to high altitude ones differed in cell growth but not in cell volumes. The reduced volume at low oxygen is an indication of decreased protein synthesis as a consequence of lower oxygen availability, while energy production for anabolic and catabolic processes was equal for "Pre" and "JJ" samples.

A different consideration should be done regarding cell growth. Hypoxia may induce HSCs mobilization to the circulation or a major commitment of these cells to the erythroid lineage, resulting in both cases in a higher number of CD34+ cells in peripheral blood. This was indeed confirmed by flow cytometry measurements in fresh blood performed at high altitude and post-altitude. Studies support the hypothesis of cell mobilization. In one study [114], tests were performed on a cell line with erythroid characteristics, which exhibited active pseudopodial extensions in cultures at $1\%\,PO_2$ and supported the hypothesis that in hypoxia erythroid progenitors migrate to contact stromal cells, which protect them from apoptosis induced by the lack of oxygen. These cells indeed communicate with erythroid progenitors to favour erythropoiesis. In the bone marrow, stromal cells are endothelial, mesenchymal and neural cells which are part of HSCs niches. HSCs motility favours the formation of the niches because erythroid progenitors can better contact the central macrophage. These niches are either located in the endosteum, containing long-term quiescent HSCs, or in the venous sinusoids, containing vascular niches where differentiating HSCs prevail. The vascular endothelium in these vessels is more permeable, therefore allowing the entrance of HSCs in the circulation. Mobilization from endosteal to vascular niches occurs in the hypoxic bone marrow in order to stimulate cell differentiation [72], explaining the higher detection of CD34+ cells during the high altitude. The general reason for HSCs and erythroid precursors presence in the circulation is thought to be for the communication between different BM areas and this cell signaling system may be enhanced in hypoxia.

4.1.3.2   Hemoglobinization and hemoglobin types expression

Hemoglobinization was assessed to evaluate if oxygen could affect Hb concentration in cells. The same number of cells was evaluated to check for differences in spectrophotometry and none was ob-

served in any culture condition at terminal differentiation. However, results at day 0 differentiation between 20 % O_2 and 3 % O_2 cultures indicate an accelerated differentiation tendency for low oxygen cultures, also confirmed by the observation of reticulocytes in cytospins. Interestingly, no significant difference was observed between low oxygen and "JJ" cultures. This may depend on a slightly higher preserved accelerated differentiation in "JJ" samples which could derive from possible epigenetic modifications caused by high altitude.

The following analysis of the expressed Hb types revealed differences between cultures at 20 % O_2 and 3 % O_2. HbF was indeed doubled at low oxygen, while in same percentage at 20 % O_2, reflecting Hb type expression as oxygen-dependent. This result is in accordance with detection of γ-globin mRNA expression by qPCR in a study [167]. HbF is expressed in immature erythroid progenitors and is progressively switched to HbA during maturation [126, 60]. This may explain that cells cultured at low oxygen are pushed to early differentiation [167]. HbA measurements confirmed higher expression of HbA at 20 % O_2 cultures. HbA_2 was also found to be significantly higher in cultures at low oxygen, supporting an early erythroid differentiation since its expression levels decrease with maturation [160]. From the physiological point of view, HbF expression in hypoxic cells could be useful because of its higher affinity for oxygen compared to HbA and could be a complementary response to the enhanced erythropoiesis to increase oxygen carrying capacity. On the other hand, higher oxygen affinity means less release of oxygen to peripheral tissues. However, hypoxic peripheral tissues are more acidic than in steady condition, increasing Hb oxygen release by Bohr effect and therefore justifying a possible role of HbF to contrast hypoxia.

4.1.3.3   Assessment of enucleation and CD71 vs CD235 expression via flow cytometry

Flow cytometry was employed to follow cell differentiation by assessing the degree of enucleation and the expression of differentiation markers during maturation. Enucleation meant as the amount of formed reticulocytes, was significantly higher already at day 0 until day 9 in 3 % O_2 cultures but not at day 13. Calculating expelled nuclei percentage at this last time point explained a significantly higher nuclei extrusion in 20 % O_2 cultures. This means that reticulocytes formed at low oxygen were more stable than the ones at atmospheric oxygen, a result that may be caused by the lower amount of Reactive Oxygen Species (ROS) in 3 % O_2 cultures.

ROS levels are important throughout cell maturation: long-term HSCs located in the endosteal BM niche were described to produce low ROS as a result of reduced metabolic activity and quiescent state. Here low ROS maintain the long-term repopulating potential of HSCs to protect genomic integrity [173, 72]. On the contrary, vascular niche includes high-ROS HSCs, where the greater

metabolism reflects cell maturation, explaining ROS role in promoting cell differentiation. However, a study showed that at the stage of enucleation ROS levels, which formation is promoted by EPO [172], decrease. Inhibition of ROS by addition of the anti-oxidant N-acetyl-cysteine (NAC) promoted enucleation, thus underlining the close relation between EPO effect and oxygen levels. This may elucidate the EPO-independent erythropoiesis, known as EPO-paradox [115] observed at high altitude, where EPO initial increase gets reduced (but still higher than at sea levels) but erythropoiesis remains highly stimulated. Oxygen and ROS formation could be the explanation for such an effect and these results from cell cultures confirmed an accelerated erythropoiesis despite EPO levels where unchanged. Moreover, the activation of HIF factors in hypoxia reduces ROS mitochondrial production [150], supporting the lower ROS levels at $3\,\%\,O_2$ cultures to explain their faster enucleation.

Assessment of CD71 and CD235 confirmed the accelerated differentiation of $3\,\%\,O_2$ cultures and the same final reticulocyte percentage obtained in both high and low oxygen cultures. "Pre" compared to "JJ" cultures did not show any difference at any timepoint in maturation, confirming the adaptation of "JJ" samples to high oxygen conditions.

4.1.3.4   Cell survival

Cell viability was compared between the tested culture conditions by assessing reticulocytes and nuclei ratio (R/N) representing the survival of enucleated cells (i.e. reticulocytes). This ratio resulted significantly higher throughout differentiation for $3\,\%\,O_2$ cultures. The fact that at day 13 R/N ratio in cultures at $20\,\%\,O_2$ was below 1 indicates that a percentage of formed reticulocytes is unstable at such oxygen levels, leading to cell death that overcomes nuclei degradation simultaneously occurring in the culture. Pre-altitude compared to "JJ" cultures did not differ at any timepoint. These results demonstrate the role of oxygen level in cultured reticulocytes stability, and suggest rather a toxic effect that an advantage over cells formed at low oxygen.

4.1.3.5   Metabolic activity

Measurements of extracellular glucose and lactate from culture medium revealed a higher metabolic glucose consumption and lactate production in $3\,\%\,O_2$ cultures. Expecting an increased glycolitic activity in cells during their maturation while still preserving the organelle apparatus for cellular respiration is reasonable because of a reduced availability of oxygen that cannot be consumed by mitochondria. On the other hand, also in reticulocytes, glycolysis is enhanced in hypoxic cells at the expense of the Hexose Monphosphate Pathway (HMP), which competes with glycolysis. In fact, in RBCs and reticulocytes, NADPH production occurs only through HMP pathway and is used to reduce

thiols, the main RBCs protection system against oxidative stress damage. This pathway is in close balance with glycolysis and the regulation of both depends on the oxygenation state of Hb [147]. Deoxy-Hb competes for the binding to the cytosolic domain of band 3 protein with some glycolitic enzymes, while oxy-Hb does not interact with the protein. The result is that during oxygenation, these enzymes are sequestered on band 3, favouring NADPH production to maintain thiol reduction against oxidative stress. On the contrary, deoxyHb allows glycolitic enzymes to metabolize glucose for ATP production (figure 79).

Relation between antioxidant ability and oxygen level
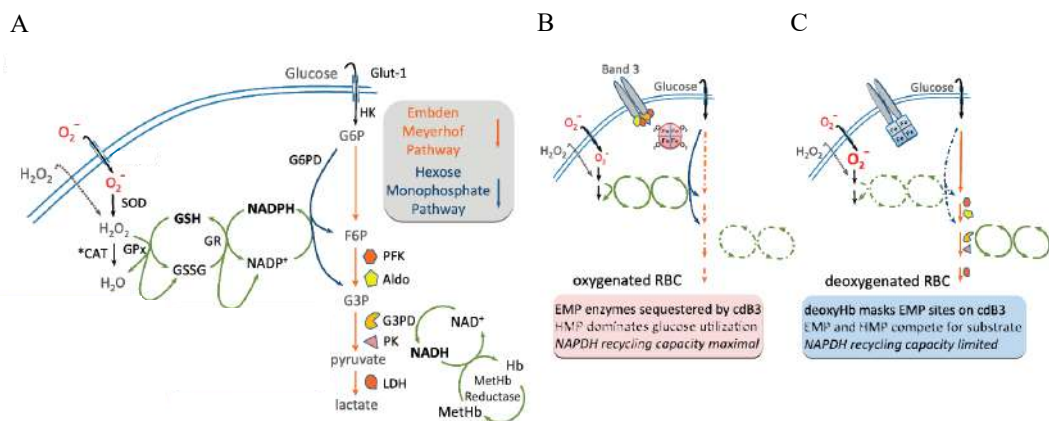
Figure 79: Antioxidant cell ability dependance on oxygen levels. (A) Scheme of Embden Meyerhof Pathway, i.e. glycolysis, and HMP competition. Glycolisis reactions can indeed be directed to HMP to reduce NADP$^+$ to NADPH, which in turn reduces thiols, such as glutathione (GSH if reduced and GSSG when oxidated), to protects against ROS. (B) Band 3 protein sequesters some key glycolitic enzymes, favouring HMP and antioxidant ability enhancement, to the detriment of ATP production when Hb is oxygenated. (C) DeoxyHb interacts with band 3 and this competition binding releases glycolitic enzymes, favouring ATP production rather than thiol reduction. Adapted from [147].

This can therefore explain the higher ratio Na/K observed in cell culture media: the higher production of ATP in hypoxic cells increases Na/K pump activity. In fact, this pump has been defined as capable of oxygen and redox state sensing, meaning that it adjusts its ATP consumption according to ATP rate formation [20]. In reticulocytes this is regulated by redox state since no oxygen consumption occurs, and in particular the upregulation of free radicals inhibits the transport activity of Na/K ATPase [18]. Hypoxic cells have lower oxidative stress tolerance due to less reduced thiol production, an observation that brought to support the theory of neocytolisis, where high altitude formed cells have a limited antioxidant ability and upon return to high oxygen levels cannot stand oxidative stress. However, a higher oxidative stress occurs in $20\,\%\,O_2$ cultures, and even if reduced thiols are higher, cells need to stand the caused oxidative damage, probably too high and explaining the reduced reticulocytes viability in such cultures.

But why does Na/K pump need to increase its activity upon hypoxia? It has been shown that hypoxia is one of the major triggers for ATP release from RBCs [102]. ATP stimulates endothelial receptors for production of nitric oxide (NO) which contributes to vasodilation to increase oxygen delivery to peripheral tissues during hypoxia. How ATP release occurs in RBCs is not fully understood but must involve channels with large pores, between 0.6 and 1.1. nm [148], which allow permeation of small ions, such as Na^+ and K^+. This would therefore affect membrane gradients, requiring an increased pump activity to restore resting gradient [61].

Besides glycolysis regulation, low oxygen affects membrane functions. Lactate production resulted in the acidification of the medium, visually noted by its orange-turning color. Every medium change was done in the same manner for $20\%\,O_2$ and $3\%\,O_2$ cultures to keep any observed difference exclusively due to oxygen influence on cells. Acidification of the medium determines cell swelling and increased activity of the Na/H exchanger, where protons are removed by introducing Na. Na/H exchanger is coupled with band 3 protein activity because the dissociation of H_2CO_3 into HCO_3^- and H^+ results in the extrusion of HCO_3^- and the entrance of Cl^- anion [28]. This is demonstrated by the significantly reduced chloride concentration in the culture medium in $3\%\,O_2$ cultures. A consequence of cell acidification is its swelling caused by the inability of Na/H exchange to regulate all the formed H^+, which induces water entrance by osmotic effect [28].

4.1.3.6   Cell morphology comparison by 3D confocal imaging

3D imaging of fixed cells was used to evaluate their morphology, revealing a more than doubled amount of biconcave and monoconcave reticulocytes in cells grown at low oxygen. Typical reticulocytes appear with irregular shapes presenting multilobes [86] which further rearrange their membrane to become discocytes. Between these two shapes a spectrum of different morphological configurations of reticulocytes is known in literature: a study [108] showed that cells CD71low, i.e. a step before maturation to RBCs, assume concavity, which later evolves to a proto-biconcavity, meaning a large biconcave cell with irregular borders (see figure 43 and [108]). The major abundance of such morphological features may therefore be a sign of a higher maturity of reticulocytes formed at $3\%\,O_2$, where their increased survival may allow for a more advanced maturation. This possible difference could be futher assessed by determining the levels of CD71 expression in the two set of cultures.

4.1.3.7   Cell deformability measurement

RBCs are characterized by high deformability to stand elevated shear stress in circulation and to pass through narrow vessels such as capillaries. Thanks to the elasticity conferred by the particular

structure of their cytoskeleton, they adapt their shape to be hydrodynamic to favour blood flow [96]. When deformability is reduced RBCs life span is shortened, as observed in hemolytic anemias [69]. Therefore, this parameter is an indicator of RBCs functionality and was here assessed on the *in vitro* obtained reticulocytes at the end of differentiation. No significant differences were observed between both 20 % and 3 % O_2, 3 % O_2 and "JJ" and 20 % O_2 and "JJ", indicating that oxygen level did not affect cell deformability. This observation is in accordance with the *in vivo* results on the 12 donors, where the measurements of the two isotopes' decay revealed that no neocytolisis occurred after the stay at 3450 m (publication in preparation).

4.1.3.8 Conclusions

Overall, these results suggest the importance of low oxygen during different erythropoiesis steps, where cell cultures could be optimized by adapting oxygen concentrations at different phases of maturation: 20 % O_2 for a better cell expansion and 3 % O_2 for an improved differentiation and stability of formed reticulocytes. From the physiological perspective, cell culture represents a simplified model of what occurs in the bone marrow and cannot fully explain the mechanisms induced by hypoxia. However, cultures at lower oxygen elucidated an accelerated erythropoiesis in hypoxia, highlighting a direct effect of oxygen that is not mediated by EPO, and therefore confirming the existance of an EPO-independent erythropoiesis. The resulting comparable reticulocytes' deformability excluded a difference in cell resistance to shear stress, and may be comparable to the observed lack of neocytolisis in the 12 donors after return from high altitude.

4.1.4 Development of a methodology for reticulocytes' RNA-seq

Reticulocytes are distinguished from RBCs for the presence of remnant RNA after nucleus extrusion. RNA content can be visualized on blood smears by staining with methylene blue which causes its precipitation, giving it a reticular aspect. When RNA is not anymore detectable, cells are defined as RBCs. Despite RNA can't be detected in RBCs' blood smears or by flow cytometry, RBC *de novo* protein synthesis during their 120 days lifespan has not been excluded [74]. Remnant RNA in reticulocytes was traditionally considered a cell degradation product but a study demonstrated that is necessary for the final maturation to RBCs [93]. Moreover, transcriptome analysis was performed, revealing most of gene expression being for ribosomal units and globins [57]. Because of established hypoxia-induced gene expression in mammalian cells [153, 53, 151], transcriptome analysis of reticulocytes formed at high altitude may highlight pathways involved in their possible premature clearance

upon return to atmospheric oxygen.

4.1.4.1   Enrichment and isolation of reticulocytes' RNA

Sequencing RNA from reticulocytes is a challenge because of both the reduced amount of these cells in blood, accounting on average for 1% of red cells, and the very low RNA abundance per cell. While being blood samples easily accessible through venipuncture or by finger prick, reticulocytes need to be isolated from a large amount of various blood material: platelets, RBCs and especially WBCs, which may affect the outcome of the transcriptome because of their active protein synthesis in contrast to reticulocytes.

Separation of blood components can firstly be helped by centrifugation to remove the buffy coat, and improved by RBCs density gradient separation by percoll, where the light fraction is enriched with reticulocytes. However, these latter can also distribute over other RBCs fractions [16, 24], bringing to a selection of the isolated reticulocyte population when using the light fraction. Moreover, conditions such as high altitude, which increases cell Hb content [149] may affect reticulocytes density, causing a misselection of the cells compared to pre-altitude samples. Density fractions can also contain contaminant WBCs [116, 32].

Another method consists in high-efficiency WBCs reduction by filtration [57]. Despite their lack of observed WBCs during blood count, a single WBC out of a million reticulocytes may exist and contaminate the sample [116].

The most accurate current method for obtaining the purest reticulocytes isolation is cell sorting of antibody-stained reticulocytes for CD71 or RNA staining in addition to negative sorting for CD45+ detected by FACS. However, reticulocytes constitute only 1% of RBCs, meaning about 50 000 cells out of 5 million RBCs in $1\,\mu$l of blood. Sorting a reasonable amount of reticulocytes to reach a good yield in RNA requires too much time. The study on neocytolisis included the simultaneous involvement of 12 donors, and required the sorting of 6 donors in a working day. In addition, RNA is subjected to degradation and a slow purification procedure could affect its final quantity and quality. Percoll fractioning enrichment could be useful but does not result time-efficient in this context. MACS separation from a small blood samples resulted an efficient enrichment technique for sample preparation for sorting. This technique was used to select cells that express CD71, a marker also present in hypoxia-formed reticulocytes (see chapter "The role of oxygen in erythropoiesis"). CD71 is also expressed on other cells, including WBCs, therefore the additional CD45 staining was added to select the right reticulocytes population during sorting. MACS separation resulted in a 60 to 70% reticulocytes enrichment and later tests on RNA isolation resulted in a minimal requirement of 200

000 cells per sample for a sufficient amount of RNA extraction for transcriptome analysis. Of note, these sorted reticulocytes were the youngest, because still expressing CD71, and therefore containing the highest amounts of RNA.

Cell sorting also resulted highly-time efficient, requiring only 15 minutes per sample, yielding from 200 000 to 3 million reticulocytes. This particularly high number only occurred for high-altitude samples, starting with an increased reticulocytes percentage in whole blood.

4.1.4.2   Reticulocytes sorting and RNA isolation

RNA isolation procedure was also tested because of the low amounts in reticulocytes and its ongoing degradation. Traditional TRIzol-based separation requires an optimized proportion with RNA amount to be efficient. In literature, TRIzol volumes per number of cells are suggested but this was not working for reticulocytes, containing only RNA remnants. Qiagen kit miRNeasy from serum or plasma is optimized for short RNAs (¡200 nucleotides), e.g. miRNA, and resulted in the isolation of sufficient RNA yields and integrity. The observation that erythroid precursors until reticulocytes contain large amounts of circular RNA [117] justified the decision to isolate the total RNA rather than only the messenger. Comparison of RNA quality between TRIzol method and the use of a kit for short RNA isolation resulted in a reproducible improved ratio of 28S over 18S RNA, typically observed to check RNA integrity. TRIzol-isolated RNA was not particularly degraded but 18S peaks was higher than 28S. This result was also previously obtained in a study aiming to analyze RNA in RBCs [74]. It could be that in mature cells RNA extraction results in a higher degradation, but the same trend in reticulocytes was observed (personal communication with Benoit Nicolet). Therefore, results from the use of the kit may indicate an improved integrity of the obtained RNA. High altitude samples all resulted in slight but consistent reduced RNA quality, hypothetically caused by the sudden oxidative damage that cells may have experienced during sample preparation (RNA enrichment procedure), due to less antioxidant ability of reticulocytes formed in hypoxia compared to normoxic ones.

4.1.4.3   RNA sequencing results

Ribosomal RNA depletion was performed to avoid masking of other transcripts but no Hb depletion was applied in order to check for any changes in Hb type expression, in particular any increase for HbF. The library was done for all RNAs by adding a poly-A tail to all transcripts for DNA synthesis. The final reads resulted in a high amount of duplicates, probably referring to Hb. No differences in Hb types expression were detected. Preliminary results here shown highlighted a depletion of the EPO receptor signaling pathway, a consequence that may be due to the higher amount of available EPO, which may not require many receptors for cell activation pathways. Considering that EPO

increases ROS contents, which reduced amount triggers enucleation [172], a lower EPO receptor expression may accelerate erythroid progenitor differentiation, in accordance to the effect of hypoxia. Such results need further investigation for a deeper understanding of reticulocytes' protein signaling changes due to hypoxia. The challenge here faced was the requirement to perform a fast reticulocytes enrichment and sorting, meaning using a small amount of blood (few μl). This affects RNA obtained quantity, and if this latter degrades it may not lead to the possibility to map the reads to the genome. Despite the need for improvements of the detection of the expressed genes, reticulocytes enrichment and an RNA extraction method were established. Next steps will involve a higher starting blood volume and Hb depletion avoiding duplicated reads.

4.2 Study of RBCs fixation

Especially in the context of rare anemias, the limited availability of patients samples mostly requires transportation from the hospital to the research laboratory of interest. Blood storage causes a series of modifications in RBCs, among which ATP-depletion which causes echinocytes formation [10]. Besides these artifacts, the buffer components, pH and temperature contribute to change RBCs shapes, and staining procedures (such as EMA) may also affect cell morphology. Therefore, immediate fixation after blood drawing is a desirable step to keep cells always comparable among different samples and allow long-term storage. However, the process of fixation also required several precautions. First of all, the choice of the fixative. Tests with formaldehyde showed poor fixation of cell membrane structures when imaging at high resolution via SEM. Therefore glutaraldehyde was preferred and became the fixative of choice for all next experiments. However, this powerful crosslinker also needs adjustments when concentrations are higher than 0.1%. In particular, the tested concentrations were mostly 0.1 and 1 %, revealing substantial differences in the obtained RBCs' shapes, where knizocytes were only observed in samples fixed in 1 % GA upon deliberate shear stress induced by strong pipetting.

4.2.0.1   Monomers and polymers in GA solutions

While adjusting osmolality of the fixation solutions, the use of different GA batches allowed to notice that cells containing the same nominal concentration of GA had different osmolality. This is due to differential monomer-polymer ratio of GA molecules, which depends on time and temperature. GA batches are often stored for long time before ending the product, therefore requiring that any new prepared solution is controlled for osmolality because it may change over time. One solution to delay GA polymerization is to preserve it at -20°C, since high temperature favors polymer formation, and in aliquots to avoid unnecessary repeated thawing steps. This would allow for more consistent results among samples.

Absorption spectroscopy is a tool that allows to check for monomer and polymer ratio to check GA stability and choose the preferred type. Regarding this point, literature is controversial and in the tests performed here no difference in fixation quality was observed. Most of quality variability in literature was actually noticed in transmission electron microscopy, where both membrane and cytoplasm details can be thoroughly examined. However, measuring such ratio and providing this detail in publications may help to understand better the effect of monomers and polymers on cell fixation quality.

4.2.0.2   Effect of shear stress

After understanding how to preserve cell shape, shear stress impact was assessed, noticing that cells fixed in 1% GA presented occasional knizocytes while the samples in 0.1% GA did not. These shapes are indeed artifacts formed during cell pipetting into the fixative. Pipetting causes shear stress high enough to deform cells to knizocytes, shown to appear at high shear rates [89]. Other known flow shapes such as "parachutes" and "croissants" were not observed because they form in the microvasculature (range of few μm) [136]. The fact that knizocytes can be observed at 1% GA explains that fixation occurs before cells can relax their shape to the static one, meaning that GA at this concentration fixes cells between 100 ms [4] and 1 second [25]. Avoiding the presence of artificial knizocytes is also important because in some blood diseases they may be really representative as static shapes. To overcome this issue the solution is to fix in 0.1% GA or to pipette gently and diluting blood to a hematocrit of about 5% for reducing its viscosity prior to fixation.

4.2.0.3   Autofluorescence affecting cell stainings

GA displays fluorescence only when binding RBCs, covering a wide range of wavelengths. The application of a suggested method [98] demonstrated a possible quenching with trypan blue, however not fully depleting autofluorescence signal. Moreover, cell staining may be affected by fixation, where GA bond to cell proteins may mask staining dye binding structures or antibodies epitopes, as observed for EMA, PKH67 and HbF staining. In particular for intracellular staining such as for HbF, requiring cell fixation, it is important to fine tune GA concentration to obtain reliable staining. The observation that PKH67 performed worse than in living cells and cannot be compared to CellMask efficiency may be due to the fact that PKH is a dye incorporated in a long aliphatic chain that may not be fully inserted in a crosslinked membrane, resulting in the formation of filament-like structures. A consideration deserves the heterogeneous autofluorescence of RBCs of the same sample fixed in the same solution: a higher autofluorescence in certain cells may reflect their higher protein abundance, considering that GA binds to amino groups. This may indicate GA as a tool for cell age detection, knowing that RBCs loose membrane proteins while aging [76].

4.2.0.4   Effect on cell projected area

A quantitative measurement was performed to evaluate the effect of GA fixation. Projected area was investigated since it is a commonly used parameter in microscopy data analysis. Cell fixation resulted in a shift of RBCs' projected area distribution towards smaller values and the two tested concentrations on same samples showed a difference, where cells fixed at 0.1% GA resulted in smaller

projected areas than the ones fixed in 1% GA. Therefore, despite osmolality correction allows for shape preservation, certain cell modifications are unavoidable and it is therefore necessary to make sure to fix samples in the same conditions (possibly using the same GA solution) for comparisons.

4.2.0.5 Summary of GA properties and use

In conclusion, the concentrations of GA to be used depend on the desired application. Between 0.1% and 1% GA fixes cells within minutes and this can be checked by suspending fixed cells in distilled water, where they can't burst nor change shape when appropriately fixed. The choice of a lower concentration and lower fixation time is desirable when autofluorescence is to be avoided. Despite trypan blue quenching option, long storage in GA increases autofluorescence, making the quenching less efficient. One way to reduce the autofluorescence emission spectrum is by using GA with high monomer concentration, especially reducing fluorescence at 488 nm. When fast fixation is desired, such as if aiming to fix flow shapes, is rather convenient to use 1% GA concentration. Also for applications such as SEM or TEM it is prefarable to fix at higher concentrations for a better preservation of cell structures, due to the abrasive methods required for sample preparation. 3D imaging for shape determination also benefits of autofluorescence of 1% GA, helping to increase the signal besides the used staining dye (e.g. CellMask). Finally, for quantitative image analysis, despite cell shape being preserved at both 0.1% and 1% GA, it is important to be consistent with the used GA concentrations between samples in comparison.

4.2.1 Morphological characterization of RBCs of sickle cell disease patients upon memantine treatment

4.2.1.1 *In vitro* deoxygenation compared to *in vivo* sickling events

A remark on the effect of prolonged deoxygenation in stasis compared to *in vivo* effects on SCD RBCs is necessary. The shapes observed *in vitro* do not correspond to the *in vivo* situation, where only classical "sickle" cells are observed. The reason for this difference depends on the fact that RBCs flowing through the circulation oxygenate and deoxygenate continuously. Therefore, while HbS fibers disaggregate upon oxygenation, a nucleation site containing molecules of aggregated HbS may remain by the time that the cell flows back to deoxygenated tissues. Therefore, crystallization of HbS rate would increase around the nucleation site, forming organized parallel fibers which give the sickle typical shape [120]. *In vitro* this cannot happen when cells are only exposed to hypoxia, therefore their deformations are a measure of cell hydration and hemoglobins expression. In fact, the more the cell is dehydrated, the more nucleation sites form in the time unit, causing the appearance

of "holly-leaf" cells, while the less dehydration is associated with the formation of a single nucleation site where all HbS molecule aggregate, a process occurring at a lower rate. Therefore, while in artificially deoxygenated RBCs cells with a sickle shape represent the ones which form latest, and therefore the mostly hydrated cells, *in vivo* this shape represents the most dehydrated cells. HbF cellular concentration is also influencing deoxygenation rate and degree of cell shape deformation, since is not included in the HbS fiber. Cells expressing high percentage of HbF appear indeed as regular discocyte also upon prolonged deoxygenation. The reason for such heterogeneity in HbF expression may be due to different delay in fetal γ-globin decay [12]. Discocytes in deoxygenation can still contain concentric HbS fibers [37], but the increased number of discocytes verified by incubation of RBCs with and without MEM in a calcium-containing medium suggests a high dependence of these shapes on sustained cell hydration.

4.2.1.2   Morphological characterization of RBCs of sickle cell disease patients upon memantine treatment

SCD is a genetic disease with recessive inheritance, originally described by the observation of RBCs with the shape of a sickle. Subjects with sickle cell trait, i.e. carrying only one mutated allele for the β-chain of Hb do not experience medical problems and are asymptomatic. In extreme cases, dehydration and high intense physical activity may cause health issues due to prolonged deoxygenation of peripheral tissues and higher acidity which induces Hb oxygen release. This increases the chances for sickling and triggers dehydration caused by ATP consumption, meaning a delayed activity of calcium pumps in re-establishing calcium intracellular content increased by NMDAR activity. Subjects affected by SCD can both be homozygous and heterozygous, but combined with another mutation in the β-chain, such as the ones causing HbC or β-thalassemia. This situation is also associated with SCD and can cause complications, such as VOCs. Therefore, therapeutic approaches are important also for different SCD genetic variants.

MemSID trial assessed, along with other clinical and experimental analysis, the effect of memantine on SCD RBCs and clinical symptoms of the treated patients. The major highlights from both morphological and other experimental results, are an observed increase in RBC hydration state and stabilization of their morphology to discocytes resulting in a decreased number of terminally sickle cells (ISCs). From the clinical aspect, patients benefit the lack of VOCs episodes [65], the worst complication they experience.

The parameters used for the quantitative evaluation of imaged RBCs highlighted a substantial change

in projected areas at a very early stage (see P5 and P6), not maintained after suspension of the treatment, where a shift of the distributions towards original curves occurred in two of the patients, and towards even smaller cells in the other two. This parameter therefore reflects fast changes in RBC population and may relate to cell hydration state. This latter was evaluated by percoll density gradient from the research group in Zurich and resulted in the presence of more dense cells in the post-treatment phase. This feature can be expected because of the lack of MEM binding to NMDAR. Along with this, intracellular calcium levels increased in the post-phase, another sign of lost effect of MEM on cell hydration. However, eccentricity and solidity are not only sustained but even improved in some cases, as well as the number of "non-sickle" cells and the decrease in "sickle" cell abundance. This can be explained by the additional action of MEM on erythroid cells, which are also expressing NMDAR and for which calcium may play a role in gene regulation [29]. Even though this aspect was not assessed throughout the study, several effects support the role of MEM on gene expression re-programming. In fact, P1 showed an increase in HbF expression while always being refractive to the effect of hydroxyurea treatment. Moreover, among the analysis performed, the number of NMDAR per cell and the Mean Cell Hemoglobin Content (MCHC) resulted reduced by the end of the treatment and this condition was sustained post-treatment [106]. A study showed the involvement of calcium in hemoglobin expression regulation [29], which could explain the increase in HbF in P1 and the sustained decrease in MCHC levels. Therefore, this latter does not depend, at least exclusively, on cell hydration but is rather an effect on hemoglobin S reduced expression. Such a response seems correlated to eccentricity and solidity, which may be seen as "morphological detectors" of sickling events. In fact, eccentricity represents cell elongation and its reduced values after treatment indicate the presence of more round cells. Solidity is a measure of cell roughness, caused in SCD by the continuous formation and disaggregation of HbS molecules, which provoke cell deformation and eventually generation of ISCs. The decrease in cell roughness is a sign of less sickling occurring. These quantitative parameters used to evaluate cells were confirmed by manual classification of RBCs shapes. In fact, what's seen from eccentricity and solidity plots is reflected in cell shapes, where the increase of the number of discocytes is even improved in the post-phase and related to a decrease in ISCs. A possible explanation for the observation that these parameters show a better condition post-treatment can be related to the effect of MEM on gene regulation. In fact, while its direct action on NMDAR is suspended at the end of the treatment, gene expression regulation may persist. The increase in the healthy aspect of cells can be speculated as the combined presence of RBCs with a longer life-span and the new generated ones with lower MCHC and NMDAR expression protracted after treatment.

Solidity, even though not being a highly sensitive parameter, showed a significant improvement in cell roughness for higher projected areas in P1, especially in the post phase. P4 resulted in a larger standard deviation and a slight decrease in solidity upon treatment, preserved in the post phase. Compared to the others, this patient started with homogeneous solidity values throughout the whole cell population. These values were preserved but the standard deviations became larger, indicating an acquired number of cells with rougher borders than in the pre-treatment condition. One could speculate that cells improving their hydration state can survive longer even when sickling events occur; at the same time, a new population of normally-shaped cells results from the re-programming effect of the drug; finally a small population of ISCs still exists, overall resulting in a variable RBCs population upon treatment. Therefore solidity, besides underlining RBCs' sickling history, could be a marker of cell heterogeneity along with projected area distribution width. This hypothesis is also supported by the data collected on P5 and P6. In fact, after 2 and 1 month of treatment respectively, their projected area and solidity distributions showed a significant difference while none existed on eccentricity. Projected area width remained large and solidity standard deviations increased. The evaluation of shape occurrence underlined a higher number of sickle cell presence in P5. This supports a better cell survival, even for sickle cells, due to their higher hydration despite the deformed shape. Projected area distributions, showing in 2 of the patients a reversed effect towards pre-treatment condition, may be a further indication that cell hydration state after suspension of the drug may start to be lost. However, the other two patients changed distributions towards even smaller values. This inter-patient variability may be due to a different response to the drug's effect on erythroid cells.

To summarize: projected area and solidity change faster because associated to the immediate effect of MEM on increasing cell hydration, while the effect on gene regulation may require a longer time and is mostly represented by cell eccentricity. Cell elongation is in fact high in ISCs, which can arrive to eccentricity values of 0.9 and their number showed to be lowest in the post phase rather than at the end of the treatment.

Projected area, as a 2D parameter, cannot easily be related to cell size. Indeed, bigger cells do not necessarily have larger projected areas: spherocytes and stomatocytes induced by swelling have lower projected areas than discocytes, and swelling is expected as a consequence of better cell hydration. This aspect is also represented by the reduced width of projected area distributions by the treatment, which correlates to the distribution on density gradients observed in the group in Zurich. On percoll gradients the whole cell population increased in the medium fraction of cells. Another interesting observation comes from the distributions of projected areas together with eccentricity: the changes

among the time points of the trial showed shifts of the whole RBC population towards the values of healthy subjects but no changes took place in the general characteristics of the population. Shape occurrence at different projected areas showed indeed that sickle cells are mostly the ones with lowest projections in all the three assessed phases and represent highly dehydrated cells.

4.2.1.3 Conclusions

These exploration of morphological parameters revealed useful information coherent with the results from other analysis performed during the trial, suggesting a possible use of morphological analysis in SCD for therapy efficiency assessment. The advantage of this method is the ease of application because the requirement is only to create cell projections before performing measurements and can be applied also on brightfield or darkfield microscopy. However, it has the limitation of inaccurate measurements and shape classification because of the limited view with the projections. Exploiting the potential of confocal microscopy 3D cell reconstructions could improve any of these evaluations.

4.2.2 Automated 3D shape recognition for morphological assessment of RBCs in hereditary spherocytosis

This project aimed to explore the information that 3D imaging adds to traditional 2D microscopy of RBCs by means of an automated tool to discover the relation between anemia and RBCs' shape. As demonstrated in Results, the fixation procedure does not affect the original cell shape and is actually a reliable method for its preservation since RBCs were directly fixed after blood drawing. Staining procedures with fluorescent dyes, necessary for 3D imaging, preserve it as well, as demonstrated by the retained shapes of cells produced by osmolality changes. Furthermore, 3D imaging was tested on several samples fixed at two concentrations of GA (1 % and 0.1 %) for comparison. On the other hand, the lack of spherocytes in 3D patients' samples could be expected because of their fragile nature. This conformation is in fact defined as a pre-lysis shape [134]. While literature on blood smears regularly uses the term "spherocytes" because of the general round aspect of such cells, a detailed research resulted in the single statement that "*Spherocytes* is a historical term. The cells it describes are actually not spheres... *Hereditary spherocytosis* is a condition in which the red cells tend to be stomato-spherocytes." [15]. Bessis' observation may have been unconsidered, thinking this distinction can only be observed at high resolution microscopy, such as in SEM. However, confocal resolution here used (320 nm in x and y) allowed to observe this difference from blood smears rather as a rotation-dependence of 2D images, since other shapes besides stomatocytes may look like

spherocytes. Concerning such shapes, there exist literature about "mushroom-shaped" cells and presence of acanthocytes in blood smears. Their amounts was related to the type of mutation [50, 130]. However, such shapes are mentioned secondarily to the spherocytes, and their count (see mushroom cells in figure 10) might be erroneous because of cell rotation. During the process of smearing many cells deform and might be counted as spherocytes even though they do not completely look round. In this case, it is not detectable if cells were deforming during the smearing process or were originally affected. Despite these drawback, blood smears remain an inexpensive method for preliminary diagnoses. 3D imaging followed by automated shape recognition is a more sophisticated method that can be used to investigate further the role of shape deformations in anemias. HS, a complex disease in terms of involved mutations and severity of patients, is an interesting example for such deeper investigations. The two-stage ANN can always be updated by re-training with new classes or new shape transition scales. The evaluation of these first patients does not yet allow to conclude if the amount and presence of certain deformed shapes is linked to a specific mutation and needs further sampling, but the automation was developed and will make it possible a routine use in research laboratories. Furthermore, it opens to the possibility to standardize RBCs shape classification.

4.2.2.1 Conclusions

This study, a combination of biological questions with new methodical advances, was a driving force to explore more in detail the traditional knowledge on RBCs shapes. Thorough morphological analysis by means of automated tools, both with traditional programs as applied in MemSID trial, and by means of artificial intelligence, enhanced the amount of data that can be obtained exclusively by imaging. Next research works will exploit the knowledge acquired in these first tests for further understanding of the pathophysiology of anemias. In particular, sickle cell disease manual classification that was applied in this thesis work, can be substituted by the automated shape recognition by ANN, provided the creation of an adequate training data. Oxygen effect in SCD may therefore be further evaluated with a detailed morphological analysis of deoxygenated sickle shapes to understand the pathophysiological and clinical meaning of their heterogeneous shapes.

Abbreviations

2,3-DPG	2-3-diphospoglycerate
18, 28 S	18 and 28 Svedberg (rRNA)
ANK-1	Ankyrin 1
ANN	Artificial Neural Network
ANOVA	Analysis of variance
ARCA	Automated Rheoscope and Cell Analyzer
ATP	Adenosine triphosphate
BFU-E	Burst Forming Unit-Erythroid
BM	Bone Marrow
BSA	Bovine Serum Albumine
BSE	Back-Scattering Electrons
C	Cytosine
CATS	Capture and Amplification by Tailing and Switching
CD	Cluster of Differentiation
cDNA	Complementary desoxyribonucleic acid
CE	Cross-Entropy
CFU-E	Colony Forming Unit-Erythroid
Cl^-	Chloride ion
CO_2	Carbon dioxide
Dex	Dexamethasone
DRAQ5	Deep Red Anthraquinone 5
ε	Eccentricity
EBL	Erythroblast
EDTA	Ethylenediaminetetraacetic acid
e.g.	Given example (exempli gratia)
ELISA	Enzyme-linked immunosorbent assay
EMA	Eosin-5'-maleimide
EPO	Erythropoietin
EpoR	Erythropoietin Receptor
et al.	And others (et alii)
FA	Formaldehyde

FACS	Fluorescence-activated cell sorting
Fe_2^+, Fe_3^+	Oxidized iron
FITC	Fluorescein-5-isothiocyanate
fl	Femtoliter
FSC	Forward scatter
g	gram or accelerated gravity force
G	Guanine
GA	Glutaraldehyde
GPA (B, C, D)	Glycophorin A (B, C, D)
GSH	Reduced glutathione
GSSG	Oxidated glutathione
H^+	Hydrogen ion
H_2CO_3	Carbonic acid
HCO_3^-	Bicarbonate
H_2O	Water molecule
Hb	Hemoglobin
HbA	Adult hemoglobin
HbF	Fetal hemoglobin
HbS	Sickle hemoglobin
HEPES	4-(2-hydroxyethyl)-1-piperazineethanesulfonic acid
HIF	Hypoxia Inducible Factor
HMP	Hexose Monphosphate Pathway
HPLC	High Performance Liquid Chromatography
HS	Hereditary Spherocytosis
HSC	Hematopoietic Stem Cell
i.e.	That is (id est)
ISC	Irreversible Sickle Cell
ISE	Ion Selective Electrode
IU	International unit for enzyme
JJ	Jungfraujoch
K^+	Potassium ion
KCC	Potassium chloride cotransporter
KCl	Potassium chloride
kDa	Kilodalton

KHCO$_3$	Potassium bicarbonate
K$_2$HPO$_4$	Dipotassium hydrogen phosphate
Lys430	Lysine in position 430
M	Molar
MACS	Magnetic-activated Cell Sorting
MCHC	Mean Cell Hemoglobin Content
MEM	Memantine
MemSID	Clinical trial for safety and tolerability of memantine in sickle cell disease
MgSO$_4$	Magnesium sulfate
miRNA	micro RNA
μl	Microliter
ML	Machine Learning
μm	Micrometer
MMLV	Moloney Murine Leukemia Virus
MPP	Multi-Potent Progenitor
MSE	Mean Squared Error
mV	Millivolt
N	Nuclei
Na$^+$	Sodium ion
NAC	N-acetyl-cystein
NaCl	Sodium chloride
NADP(H)	Nicotinamide adenine dinucleotide phosphate (reduced)
NaHCO$_3$	Sodium bicarbonate
(-)NH$_2$	Amino group
NH$_4$Cl	Ammonium chloride
NMDAR	N-Methyl D-Aspartate Receptor
ns	not significant
Na$_2$S$_2$O$_4$	Sodium dithionite
O$_2$	Molecular oxygen
PBMC	Peripheral Blood Mononuclear Cell
PBS	Phosphate Buffer Saline
PCR	Polymerase Chain Reaction
poly-A	Adenine polypeptide
poly-T	Thymine polypeptide

R	Reticulocyte(s)
RBC	Red Blood Cell
ReLU	Rectified Linear Unit
RIN	RNA Integrity Number
RNA	Ribonucleic acid
rRNA	Ribosomal ribonucleic acid
RNA-Seq	RNA sequencing
ROS	Reactive oxygen species
R-state	Relaxed state
P	Patient or P-value
PB	Pacific Blue
PE	Phycoerythrin
pH	potential of hydrogen
pO_2	Partial pressure of oxygen
Pre	Pre-altitude or pre-treatment
P-value	Probability value
px	Pixel
s	Solidity
SCA	Sickle Cell Anemia
SCD	Sickle Cell Disease
SCF	Stem Cell Factor
SDE	Stomatocyte-Discocyte-Echinocyte
SE	Secondary Electrons
SEM	Scanning Electron Microscopy
SHA	Spherical Harmonics Analysis
SHS	Spherical Harmonics Spectrum
SLC4A1	Solute Carrier Family 4 Member 1
SPTA1	Spectrin Alpha Chain, erythrocytic 1
SSC	Side scatter
T3	Triiodothyronine
TEM	Transmission Electron Microscopy
T-state	Tense state
VOC	Vaso-Occlusive Crisis
WBC	White Blood Cell

Other

°C	Degree Celsius
%	Percentage

List of Figures

List of Tables

References

[1] Abay, A., Simionato, G., Chachanidze, R., Bogdanova, A., Hertz, L., Bianchi, P., Van Den Akker, E., Von Lindern, M., Leonetti, M., Minetti, G., Wagner, C., and Kaestner, L. Glutaraldehyde–a subtle tool in the investigation of healthy and pathologic red blood cells. *Frontiers in physiology*, 10, 2019.

[2] Alfrey, C. P., Rice, L., Udden, M. M., and Driscoll, T. B. Neocytolysis: physiological down-regulator of red-cell mass. *The Lancet*, 349(9062):1389–1390, 1997.

[3] Ambriz-Colin, F., Torres-Cisneros, M., Avina-Cervantes, J. G., Saavedra-Martinez, J. E., Debeir, O., and Sanchez-Mondragon, J. J. Detection of biological cells in phase-contrast microscopy images. In *Fifth Mexican International Conference on Artificial Intelligence*, pages 68–77. IEEE, 2006.

[4] Amirouche, A., Ferrigno, R., and Faivre, M. Impact of channel geometry on the discrimination of mechanically impaired red blood cells in passive microfluidics. *Proceedings*, 1(4):512, 2017.

[5] An, X. and Mohandas, N. Erythroblastic islands, terminal erythroid differentiation and reticulocyte maturation. *International journal of hematology*, 93(2):139–143, 2011.

[6] Angelini, F., Botti, D., Colombo, R., Gornati, R., Monaco, G., Odierna, G., Olmo, E., Ottaviani, E., Panzica, G. C., Rosati, F., Sottile, L., Stingo, V., and Venturini, G. *Biologia dei tessuti*. Edi.Ermes, 2007.

[7] Arganda-Carreras, I., Kaynig, V., Rueden, C., Eliceiri, K. W., Schindelin, J., Cardona, A., and H., S. S. Trainable Weka Segmentation: a machine learning tool for microscopy pixel classification. *Bioinformatics*, 33(15):2424–2426, 2017.

[8] Asakura, T. and Mayberry, J. Relationship between morphologic characteristics of sickle cells and method of deoxygenation. *The Journal of laboratory and clinical medicine*, 104(6):987–994, 1984.

[9] Ataga, K. I., Reid, M., Ballas, S. K., Yasin, Z., Bigelow, C., James, L. S., Smith, W. R., Galacteros, F., Kutlar, A., Hull, J. H., et al. Improvements in haemolysis and indicators of erythrocyte survival do not correlate with acute vaso-occlusive crises in patients with sickle cell disease: a phase III randomized, placebo-controlled, double-blind study of the gardos channel blocker senicapoc (ICA-17043). *British journal of haematology*, 153(1):92–104, 2011.

[10] Bernhardt, I. and Ellory, J. C. *Red cell membrane transport in health and disease*. Springer Science & Business Media, 2013.

[11] Bertles, J. F. and Döbler, J. Reversible and irreversible sickling: a distinction by electron microscopy. *Blood*, 33(6):884–898, 1969.

[12] Bertles, J. F. and Milner, P. F. Irreversibly sickled erythrocytes: a consequence of the heterogeneous distribution of hemoglobin types in sickle-cell anemia. *The Journal of clinical investigation*, 47(8):1731–1741, 1968.

[13] Bessis, M. Erythroblastic island, functional unity of bone marrow. *Revue d'hematologie*, 13 (1):8, 1958.

[14] Bessis, M. *Red cell shapes. An illustrated classification and its rationale*. Springer, 1973.

[15] Bessis, M. *Corpuscles: Atlast of Red Blood Blood Cell Shape*. Springer Science & Business Media, 2012.

[16] Bhardwaj, N. and Saxena, R. K. Heterogeneity of reticulocyte population in mouse peripheral blood. *Current Science*, pages 1611–1614, 2013.

[17] Bodénès, P., Wang, H.-Y., Lee, T.-H., Chen, H.-Y., and Wang, C.-Y. Microfluidic techniques for enhancing biofuel and biorefinery industry based on microalgae. *Biotechnology for biofuels*, 12(1):33, 2019.

[18] Bogdanova, A., Petrushanko, I., Boldyrev, A., and Gassmann, M. Oxygen-and redox-induced regulation of the Na-K ATPase. *Current Enzyme Inhibition*, 2(1):37–59, 2006.

[19] Bogdanova, A., Makhro, A., and Kaestner, L. Calcium handling in red blood cells of sickle cell disease patients. *Sickle Cell Disease, ed ME Lewis (Hauppauge, NY: Nova Science Publishers)*, pages 29–60, 2015.

[20] Bogdanova, A., Petrushanko, I. Y., Hernansanz-Agustín, P., and Martínez-Ruiz, A. 'oxygen sensing' by Na, K-ATPase: these miraculous thiols. *Frontiers in physiology*, 7:314, 2016.

[21] Bookchin, R. M. and Lew, V. L. Effect of a 'sickling pulse' on calcium and potassium transport in sickle cell trait red cells. *The Journal of physiology*, 312(1):265–280, 1981.

[22] Boyer, R. F. *Concepts in Biochemistry*. Wiley, 2005. ISBN 9780471661795. URL https://books.google.de/books?id=bQqcQgAACAAJ.

[23] Bradley, T. R., Hodgson, G. S., and Rosendaal, M. The effect of oxygen tension on haemopoietic and fibroblast cell proliferation in vitro. *Journal of cellular physiology*, 97(3):517–522, 1978.

[24] Branch, D. R., Sy Siok Hian, A. L., Carlson, F., Maslow, W. C., and Petz, L. D. Erythrocyte age-fractionation using a Percollκ-Renografin® density gradient: Application to autologous red cell antigen determinations in recently transfused patients. *American journal of clinical pathology*, 80(4):453–458, 1983.

[25] Braunmüller, S., Schmid, L., and Franke, T. Dynamics of red blood cells and vesicles in microchannels of oscillating width. *Journal of Physics: Condensed Matter*, 23(18):184116, 2011.

[26] Bridges, K. R., Pearson, H. A., et al. *Anemias and other red cell disorders*. New York: McGraw-Hill Medical,, 2008.

[27] Brownlee, J. *Clever algorithms: nature-inspired programming recipes*. Jason Brownlee, 2011.

[28] Cala, P. M., Anderson, S. E., and Cragoe, J. E. J. Na-H exchange-dependent cell volume and pH regulation and disturbances. *Comparative biochemistry and physiology. A, Comparative physiology*, 90(4):551–555, 1988.

[29] Caulier, A., Jankovsky, N., Demont, Y., Ouled-Haddou, H., Demagny, J., Guitton, C., Merlusca, L., Lebon, D., Vong, P., Aubry, A., et al. PIEZO1 activation delays erythroid differentiation of normal and hereditary xerocytosis-derived human progenitors. *Haematologica*, pages haematol–2019, 2019.

[30] Chasis, J. A., Prenant, M., Leung, A., and Mohandas, N. Membrane assembly and remodeling during reticulocyte maturation. *Blood*, 74(3):1112, 1989.

[31] Christoph, G. W., Hofrichter, J., and Eaton, W. A. Understanding the shape of sickled red cells. *Biophysical journal*, 88(2):1371–1376, 2005.

[32] Ciana, A., Achilli, C., Balduini, C., and Minetti, G. On the association of lipid rafts to the spectrin skeleton in human erythrocytes. *Biochimica et Biophysica Acta (BBA)-Biomembranes*, 1808(1):183–190, 2011.

[33] Cipolleschi, M. G., D'Ippolito, G., Bernabei, P. A., Caporale, R., Nannini, R., Mariani, M., Fabbiani, M., Rossi-Ferrini, P., Olivotto, M., and Dello, P. S. Severe hypoxia enhances the

formation of erythroid bursts from human cord blood cells and the maintenance of BFU-E in vitro. *Experimental hematology*, 25(11):1187–1194, 1997.

[34] Collins, J.-A., Rudenski, A., Gibson, J., Howard, L., and O'Driscoll, R. Relating oxygen partial pressure, saturation and content: the haemoglobin–oxygen dissociation curve. *Breathe*, 11(3):194–201, 2015.

[35] Commons, W. https://commons.wikimedia.org/wiki/File: Risk-Factors-for-Sickle-Cell-Anemia_(1)2.jpg, 2020. Accessed: 2020.03.08.

[36] Commons, W. https://commons.wikimedia.org/wiki/File:H%C3%A4moglobin_bei_der_ Sichelzellenan%C3%A4mie.svg, 2020. Accessed: 2020.03.08.

[37] Corbett, J. D., Mickols, W. E., and Maestre, M. F. Effect of hemoglobin concentration on nucleation and polymer formation in sickle red blood cells. *Journal of biological chemistry*, 270(6):2708–2715, 1995.

[38] D'Angelo, E. and Peres, A. *Fisiologia. Molecole, cellule e sistemi*. Edi.Ermes, 2006.

[39] Danielczok, J., Hertz, L., Ruppenthal, S., Kaiser, E., Petkova-Kirova, P., Bogdanova, A., Krause, E., Lipp, P., Freichel, M., Birnbaumer, L., et al. Does erythropoietin regulate TRPC channels in red blood cells? *Cellular Physiology and Biochemistry*, 41(3):1219–1228, 2017.

[40] Davies, J., Evans, R. H., Francis, A. A., and Watkins, J. C. Excitatory amino acid receptors and synaptic excitation in the mammalian central nervous system. *Journal de physiologie*, 75 (6):641–654, 1979.

[41] Diez-Silva, M., Dao, M., Han, J., Lim, C.-T., and Suresh, S. Shape and biomechanical characteristics of human red blood cells in health and disease. *MRS bulletin*, 35(5):382–388, 2010.

[42] Dobbe, J. G. G., Streekstra, G. J., Hardeman, M. R., Ince, C., and Grimbergen, C. A. Measurement of the distribution of red blood cell deformability using an automated rheoscope. *Cytometry: The Journal of the International Society for Analytical Cytology*, 50(6):313–325, 2002.

[43] Dorn, I., Lazar-Karsten, P., Boie, S., Ribbat, J., Hartwig, D., Driller, B., Kirchner, H., and Schlenke, P. In vitro proliferation and differentiation of human CD34+ cells from peripheral blood into mature red blood cells with two different cell culture systems. *Transfusion*, 48(6): 1122–1132, 2008.

[44] Du, E., Diez-Silva, M., Kato, G. J., Dao, M., and Suresh, S. Kinetics of sickle cell biorheology and implications for painful vasoocclusive crisis. *Proceedings of the National Academy of Sciences*, 112(5):1422–1427, 2015.

[45] Dykes, G., Crepeau, R. H., and Edelstein, S. J. Three-dimensional reconstruction of the fibres of sickle cell haemoglobin. *Nature*, 272(5653):506, 1978.

[46] Dzierzak, E. and Philipsen, S. Erythropoiesis: development and differentiation. *Cold Spring Harbor perspectives in medicine*, 3(4):a011601, 2013.

[47] Eaton, J. W., Berger, E., White, J. G., and Jacob, H. S. Calcium-induced damage of haemoglobin ss and normal erythrocytes. *British journal of haematology*, 38(1):57–62, 1978.

[48] Eaton, W. A. Linus Pauling and sickle cell disease. *Biophysical chemistry*, 100(1-3):109–116, 2002.

[49] Eaton, W. A. and Hofrichter, J. Sickle cell hemoglobin polymerization. In *Advances in protein chemistry*, volume 40, pages 63–279. Elsevier, 1990.

[50] Eber, S. and Lux, S. E. Hereditary spherocytosis–defects in proteins that connect the membrane skeleton to the lipid bilayer. *Seminars in hematology*, 41(2):118–141, 2004.

[51] Eckardt, K.-U., Boutellier, U., Kurtz, A., Schopen, M., Koller, E. A., and Bauer, C. Rate of erythropoietin formation in humans in response to acute hypobaric hypoxia. *Journal of applied physiology*, 66(4):1785–1788, 1989.

[52] Eckmann, D. M., Bowers, S., Stecker, M., and Cheung, A. T. Hematocrit, volume expander, temperature, and shear rate effects on blood viscosity. *Anesthesia & Analgesia*, 91(3):539–545, 2000.

[53] Fandrey, J. and Gassmann, M. Oxygen sensing and the activation of the hypoxia inducible factor 1 (HIF-1)–invited article. In *Arterial Chemoreceptors*, pages 197–206. Springer, 2009.

[54] Farashi, S. and Harteveld, C. Molecular basis of α-thalassemia. *Blood Cells, Molecules, and Diseases*, 70, 09 2017. doi: 10.1016/j.bcmd.2017.09.004.

[55] Fryers, G. R. and Berlin, N. I. Mean red cell life of rats exposed to reduced barometric pressure. *American Journal of Physiology-Legacy Content*, 171(2):465–470, 1952.

[56] Gillett, R. and Gull, K. Glutaraldehyde–its purity and stability. *Histochemie*, 30(3):162–167, 1972.

[57] Goh, S.-H., Josleyn, M., Lee, Y. T., Danner, R. L., Gherman, R. B., Cam, M. C., and Miller, J. L. The human reticulocyte transcriptome. *Physiological genomics*, 30(2):172–178, 2007.

[58] Gräf, R., Rietdorf, J., and Zimmermann, T. Live cell spinning disk microscopy. In *Microscopy techniques*, pages 57–75. Springer, 2005.

[59] Griffiths, G. *Fine structure immunocytochemistry*. Springer Science & Business Media, 2012.

[60] Groudine, M., Peretz, M., Nakamoto, B., Papayannopoulou, T., and Stamatoyannopoulos, G. The modulation of Hb F synthesis in adult erythroid progenitor (burst-forming unit) cultures reflects changes in gamma-globin gene transcription and chromatin structure. *Proceedings of the National Academy of Sciences*, 83(18):6887–6891, 1986.

[61] Grygorczyk, R. and Orlov, S. N. Effects of hypoxia on erythrocyte membrane properties–implications for intravascular hemolysis and purinergic control of blood flow. *Frontiers in physiology*, 8:1110, 2017.

[62] Guillochon, D., Vijayalakshmi, M. W., Thiam-Sow, A., Thomas, D., and Chevalier, A. Effect of glutaraldehyde on hemoglobin: functional aspects and Mössbauer parameters. *Biochemistry and Cell Biology*, 64(1):29–37, 1986.

[63] Hänggi, P., Makhro, A., Gassmann, M., Schmugge, M., Goede, J. S., Speer, O., and Bogdanova, A. Red blood cells of sickle cell disease patients exhibit abnormally high abundance of N-methyl D-aspartate receptors mediating excessive calcium uptake. *British journal of haematology*, 167(2):252–264, 2014.

[64] Hardy, P. M., Nicholls, A. C., and Rydon, H. N. The nature of glutaraldehyde in aqueous solution. *Journal of the Chemical Society D: Chemical Communications*, 565(10):565–566, 1969.

[65] Hegemann, I., Sasselli, C., Valeri, F., Makhro, A., Müuller, R., Bogdanova, A., Manz, M. G., Gassman, M., and Goede, J. S. Memantine treatment is well tolerated by sickle cell patients and improves erythrocyte stability: phase II study MemSID. *HemaSphere*, 2020.

[66] Heideveld, E. and van den Akker, E. Digesting the role of bone marrow macrophages on hematopoiesis. *Immunobiology*, 222(6):814–822, 2017.

[67] Hertz, L., Huisjes, R., Llaudet-Planas, E., Petkova-Kirova, P., Makhro, A., Danielczok, J. G., Egee, S., del Mar Mañú-Pereira, M., Van Wijk, R., Vives C., J.-L., et al. Is increased intra-

cellular calcium in red blood cells a common component in the molecular mechanism causing anemia? *Frontiers in physiology*, 8:673, 2017.

[68] Hickman, C. P., Roberts, L. S., Keen, S. L., Eisenhour, D. J., Larson, A., and L. Anson, H. *Diversita animale*. McGraw Hill, 2016.

[69] Huisjes, R., Bogdanova, A., van Solinge, W. W., Schiffelers, R. M., Kaestner, L., and Van Wijk, R. Squeezing for life–properties of red blood cell deformability. *Frontiers in physiology*, 9: 656, 2018.

[70] Inaba, M. and Maede, Y. Correlation between protein 4.1 a/4.2 b ratio and erythrocyte life span. *Biochimica et Biophysica Acta (BBA)-Biomembranes*, 944(2):256–264, 1988.

[71] Ishikawa, Y. and Ito, T. Kinetics of hemopoietic stem cells in a hypoxic culture. *European journal of haematology*, 40(2):126–129, 1988.

[72] Itkin, T., Gur-Cohen, S., Spencer, J. A., Schajnovitz, A., Ramasamy, S. K., Kusumbe, A. P., Ledergor, G., Jung, Y., Milo, I., Poulos, M. G., et al. Distinct bone marrow blood vessels differentially regulate haematopoiesis. *Nature*, 532(7599):323–328, 2016.

[73] Jesper Sjöström, P., Frydel, B. R., and Wahlberg, L. U. Artificial neural network-aided image analysis system for cell counting. *Cytometry: The Journal of the International Society for Analytical Cytology*, 36(1):18–26, 1999.

[74] Kabanova, S., Kleinbongard, P., Volkmer, J., Andrée, B., Kelm, M., and Jax, T. W. Gene expression analysis of human red blood cells. *International journal of medical sciences*, 6(4): 156, 2009.

[75] Kaestner, L. and Egee, S. Commentary: voltage gating of mechanosensitive PIEZO channels. *Frontiers in physiology*, 9:1565, 2018.

[76] Kaestner, L. and Minetti, G. The potential of erythrocytes as cellular aging models, 2017.

[77] Kaestner, L., Bogdanova, A., and Egee, S. Calcium channels and calcium-regulated channels in human red blood cells. *Advances in experimental medicine and biology*, 1131:625, 2020.

[78] Kapoor, S., Little, J. A., and Pecker, L. H. Advances in the treatment of sickle cell disease. In *Mayo Clinic Proceedings*. Elsevier, 2018.

[79] Kazhdan, M., Funkhouser, T., and Rusinkiewicz, S. Rotation invariant spherical harmonic representation of 3D shape descriptors. In *Symposium on geometry processing*, volume 6, pages 156–164, 2003.

[80] Kedar, P. S., Colah, R. B., Kulkarni, S., Ghosh, K., and Mohanty, D. Experience with eosin-5'-maleimide as a diagnostic tool for red cell membrane cytoskeleton disorders. *Clinical & Laboratory Haematology*, 25(6):373–376, 2003.

[81] Khairy, K., Foo, J., and Howard, J. Shapes of red blood cells: Comparison of 3D confocal images with the bilayer-couple model. *Cellular and molecular bioengineering*, 1(2-3):173, 2008.

[82] Kihm, A., Kaestner, L., Wagner, C., and Quint, S. Classification of red blood cell shapes in flow using outlier tolerant machine learning. *PLoS computational biology*, 14(6):e1006278, 2018.

[83] Kikuchi-Taura, A., Soma, T., Matsuyama, T., Stern, D. M., and Taguchi, A. A new protocol for quantifying CD34+ cells in peripheral blood of patients with cardiovascular disease. *Texas Heart Institute Journal*, 33(4):427, 2006.

[84] Kim, Y., Kim, K., and Park, Y. Measurement techniques for red blood cell deformability: recent advances. *Blood Cell–An Overview of Studies in Hematology*, 10:167–194, 2012.

[85] Kingma, D. P. and Ba, J. Adam: A method for stochastic optimization. *arXiv preprint arXiv:1412.6980*, 2014.

[86] Kono, M., Kondo, T., Takagi, Y., Wada, A., and Fujimoto, K. Morphological definition of CD71 positive reticulocytes by various staining techniques and electron microscopy compared to reticulocytes detected by an automated hematology analyzer. *Clinica Chimica Acta*, 404(2): 105–110, 2009.

[87] Koury, M. J., Koury, S. T., Kopsombut, P., and Bondurant, M. C. In vitro maturation of nascent reticulocytes to erythrocytes. *Blood*, 105(5):2168–2174, 2005.

[88] Krizhevsky, A., Sutskever, I., and Hinton, G. E. Imagenet classification with deep convolutional neural networks. In *Advances in neural information processing systems*, pages 1097–1105, 2012.

[89] Lanotte, L., Mauer, J., Mendez, S., Fedosov, D. A., Fromental, J. M., Claveria, V., Nicoud, F., Gompper, G., and Abkarian, M. Red cells' dynamic morphologies govern blood shear thinning under microcirculatory flow conditions. *Proceedings of the National Academy of Sciences*, 113 (47):13289–13294, 2016.

[90] Leberbauer, C., Boulmé, F., Unfried, G., Huber, J., Beug, H., and Mùĺ^llner, E. W. Different steroids co-regulate long-term expansion versus terminal differentiation in primary human erythroid progenitors. *Blood*, 105(1):85–94, 2005.

[91] LeCun, Y., Touresky, D., Hinton, G., and Sejnowski, T. A theoretical framework for backpropagation. In *Proceedings of the 1988 connectionist models summer school*, volume 1, pages 21–28. CMU, Pittsburgh, Pa: Morgan Kaufmann, 1988.

[92] LeCun, Y., Bengio, Y., and Hinton, G. Deep learning. *Nature*, 521(7553):436–444, 2015.

[93] Lee, E., Choi, H. S., Hwang, J. H., Hoh, J. K., Cho, Y.-H., and Baek, E. J. The RNA in reticulocytes is not just debris: it is necessary for the final stages of erythrocyte formation. *Blood Cells, Molecules, and Diseases*, 53(1-2):1–10, 2014.

[94] Li, H., Xu, Z., Taylor, G., Studer, C., and Goldstein, T. Visualizing the loss landscape of neural nets. In *Advances in Neural Information Processing Systems*, pages 6389–6399, 2018.

[95] Li, J., Hale, J., Bhagia, P., Xue, F., Chen, L., Jaffray, J., Yan, H., Lane, J., Gallagher, P. G., Mohandas, N., et al. Isolation and transcriptome analyses of human erythroid progenitors: BFU-E and CFU-E. *Blood, The Journal of the American Society of Hematology*, 124(24): 3636–3645, 2014.

[96] Lim H. W., G., Wortis, M., and Mukhopadhyay, R. *Red Blood Cell Shapes and Shape Transformations: Newtonian Mechanics of a Composite Membrane: Sections 2.5–2.8*, pages 139–204. Wiley-VCH Verlag GmbH & Co. KGaA, 2009.

[97] Lodish, H., Flygare, J., and Chou, S. From stem cell to erythroblast: regulation of red cell production at multiple levels by multiple hormones. *IUBMB life*, 62(7):492–496, 2010.

[98] Loike, J. D. and Silverstein, S. C. A fluorescence quenching technique using trypan blue to differentiate between attached and ingested glutaraldehyde-fixed red blood cells in phagocytosing murine macrophages. *Journal of immunological methods*, 57(1-3):373–379, 1983.

[99] Lux, S. E. Anatomy of the red cell membrane skeleton: unanswered questions. *Blood, The Journal of the American Society of Hematology*, 127(2):187–199, 2016.

[100] Lynch, E. C. Peripheral blood smear. In *Clinical Methods: The History, Physical, and Laboratory Examinations*. Butterworths, 1990.

[101] MacDonald, S. L. and Pepper, D. S. [19] hemoglobin polymerization. In *Methods in enzymology*, volume 231, pages 287–308. Elsevier, 1994.

[102] Mairbäurl, H., Ruppe, F. A., and Bärtsch, P. Role of hemolysis in red cell adenosine triphosphate release in simulated exercise conditions in vitro. *Medicine & Science in Sports & Exercise*, 45(10):1941–1947, 2013.

[103] Makhro, A., Wang, J., Vogel, J., Boldyrev, A. A., Gassmann, M., Kaestner, L., and Bogdanova, A. Functional NMDA receptors in rat erythrocytes. *American Journal of Physiology-Cell Physiology*, 298(6):C1315–C1325, 2010.

[104] Makhro, A., Hänggi, P., Goede, J. S., Wang, J., Brüggemann, A., Gassmann, M., Schmugge, M., Kaestner, L., Speer, O., and Bogdanova, A. N-methyl-D-aspartate receptors in human erythroid precursor cells and in circulating red blood cells contribute to the intracellular calcium regulation. *American Journal of Physiology-Cell Physiology*, 305(11):C1123–C1138, 2013.

[105] Makhro, A., Huisjes, R., Verhagen, L. P., del Mar Mañú-Pereira, M., Llaudet-Planas, E., Petkova-Kirova, P., Wang, J., Eichler, H., Bogdanova, A., van Wijk, R., et al. Red cell properties after different modes of blood transportation. *Frontiers in physiology*, 7:288, 2016.

[106] Makhro, A., Hegemann, I., Seiler, E., Simionato, G., Claveria, V., Bogdanov, N., Sasselli, C., Torgeson, P., Kaestner, L., Manz, M. G., Goede, J. S., Gassman, M., and Bogdanova, A. A pilot clinical phase II trial MemSID: Acute and durable changes of red blood cells of sickle cell disease patients on memantine treatment. *British Journal of Hematology*, 2020.

[107] Malik, P., Fisher, T. C., Barsky, L. L. W., Zeng, L., Izadi, P., Hiti, A. L., Weinberg, K. I., Coates, T. D., Meiselman, H. J., and Kohn, D. B. An in vitro model of human red blood cell production from hematopoietic progenitor cells. *Blood, The Journal of the American Society of Hematology*, 91(8):2664–2671, 1998.

[108] Malleret, B., Xu, F., Mohandas, N., Suwanarusk, R., Chu, C., Leite, J. A., Low, K., Turner, C., Sriprawat, K., Zhang, R., et al. Significant biochemical, biophysical and metabolic diversity in circulating human cord blood reticulocytes. *PloS one*, 8(10), 2013.

[109] Manwani, D. and Bieker, J. J. The erythroblastic island. *Current topics in developmental biology*, 82:23–53, 2008.

[110] Matsunaga, S., Kishi, T., and Iwata, N. Memantine monotherapy for Alzheimer's disease: a systematic review and meta-analysis. *PloS one*, 10(4), 2015.

[111] McCarthy, J. and Feigenbaum, E. A. In memoriam: Arthur Samuel: Pioneer in machine learning. *AI Magazine*, 11(3):10–10, 1990.

[112] McKinnon, K. M. Flow cytometry: An overview. *Current protocols in immunology*, 120(1): 5–1, 2018.

[113] Merino, C. F. Studies on blood formation and destruction in the polycythemia of high altitude. *Blood*, 5(1):1–31, 1950.

[114] Mikami, M., Sadahira, Y., Haga, A., Otsuki, T., Wada, H., and Sugihara, T. Hypoxia-inducible factor-1 drives the motility of the erythroid progenitor cell line, UT-7/Epo, via autocrine motility factor. *Experimental hematology*, 33(5):531–541, 2005.

[115] Milledge, J. S. and Bärtsch, P. Blood and haemostasis. *High Altitude: Human Adaptation to Hypoxia*, pages 203–216, 2014.

[116] Minetti, G., Egée, S., Mörsdorf, D., Steffen, P., Makhro, A., Achilli, C., Ciana, A., Wang, J., Bouyer, G., Bernhardt, I., et al. Red cell investigations: art and artefacts. *Blood reviews*, 27 (2):91–101, 2013.

[117] Nicolet, B. P., Engels, S., Aglialoro, F., van den Akker, E., von Lindern, M., and Wolkers, M. C. Circular RNA expression in human hematopoietic cells is widespread and cell-type specific. *Nucleic acids research*, 46(16):8168–8180, 2018.

[118] Nilsson, N. J. *Principles of artificial intelligence*. Morgan Kaufmann, 2014.

[119] Noguchi, C. T. and Schechter, A. N. The intracellular polymerization of sickle hemoglobin and its relevance to sickle cell disease. *Blood*, 58(6):1057–1068, 1981.

[120] Ohnishi, S. T. and Ohnishi, T. *Membrane abnormalities in sickle cell disease and in other red blood cell disorders*. CRC, 1994.

[121] Ohtsuki, M., White, S. L., Zeitler, E., Wellems, T. E., Fuller, S. D., Zwick, M., Makinen, M. W., and Sigler, P. B. Electron microscopy of fibers and discs of hemoglobin S having sixfold symmetry. *Proceedings of the National Academy of Sciences*, 74(12):5538–5542, 1977.

[122] Orkin, S. H. and Zon, L. I. Hematopoiesis: an evolving paradigm for stem cell biology. *Cell*, 132(4):631–644, 2008.

[123] Ovchynnikova, E., Aglialoro, F., Bentlage, A. E. H., Vidarsson, G., Salinas, N. D., von Lindern, M., Tolia, N. H., and van den Akker, E. DARC extracellular domain remodeling in maturing reticulocytes explains Plasmodium vivax tropism. *Blood, The Journal of the American Society of Hematology*, 130(12):1441–1444, 2017.

[124] Ovchynnikova, E., Aglialoro, F., Von Lindern, M., and Van Den Akker, E. The shape shifting story of reticulocyte maturation. *Frontiers in physiology*, 9, 2018.

[125] Pace, N., Meyer, L. B., and Vaughan, B. E. Erythrolysis on return of altitude acclimatized individuals to sea level. *Journal of applied physiology*, 9(2):141–144, 1956.

[126] Papayannopoulou, T., Kalmantis, T., and Stamatoyannopoulos, G. Cellular regulation of hemoglobin switching: evidence for inverse relationship between fetal hemoglobin synthesis and degree of maturity of human erythroid cells. *Proceedings of the National Academy of Sciences*, 76(12):6420–6424, 1979.

[127] Patterson, D. W. *Artificial neural networks: theory and applications*. Prentice Hall PTR, 1998.

[128] Pauling, L., Itano, H. A., Singer, S. J., and Wells, I. C. Sickle cell anemia, a molecular disease. *Science*, 110(2865):543–548, 1949.

[129] Peacock, A. J. Oxygen at high altitude. *Bmj*, 317(7165):1063–1066, 1998.

[130] Perrotta, S., Gallagher, P. G., and Mohandas, N. Hereditary spherocytosis. *The Lancet*, 372 (9647):1411–1426, 2008.

[131] Piel, F. B., Patil, A. P., Howes, R. E., Nyangiri, O. A., Gething, P. W., Williams, T. N., Weatherall, D. J., and Hay, S. I. Global distribution of the sickle cell gene and geographical confirmation of the malaria hypothesis. *Nature communications*, 1:104, 2010.

[132] Piel, F. B., Steinberg, M. H., and Rees, D. C. Sickle cell disease. *New England Journal of Medicine*, 376(16):1561–1573, 2017.

[133] Pitari, G. https://slideplayer.it/slide/10622914/, 2020. Accessed: 2020-03-08.

[134] Ponder, E. H. et al. *Hemolysis and related phenomena*. Grune & Stratton, 1971.

[135] Prentø, P. Glutaraldehyde for electron microscopy: a practical investigation of commercial glutaraldehydes and glutaraldehyde-storage conditions. *The Histochemical Journal*, 27(11): 906–913, 1995.

[136] Quint, S., Christ, A. F., Guckenberger, A., Himbert, S., Kaestner, L., Gekle, S., and Wagner, C. 3D tomography of cells in micro-channels. *Applied Physics Letters*, 111(10):103701, 2017.

[137] Rasmussen, K. E. Fixation in aldehydes a study on the influence of the fixative, buffer, and osmolarity upon the fixation of the rat retina. *Journal of ultrastructure research*, 46(1):87–102, 1974.

[138] Rasmussen, K. E. and Albrechtsen, J. Glutaraldehyde. the influence of pH, temperature, and buffering on the polymerization rate. *Histochemistry*, 38(1):19–26, 1974.

[139] Rees, D. C., Williams, T. N., and Gladwin, M. T. Sickle-cell disease. *The Lancet*, 376(9757): 2018–2031, 2010.

[140] Reynafarje, C., Berlin, N. I., and Lawrence, J. H. Red cell life span in acclimatization to altitude. *Proceedings of the Society for Experimental Biology and Medicine*, 87(1):101–102, 1954.

[141] Rice, L., Ruiz, W., Driscoll, T., Whitley, C. E., Tapia, R., Hachey, D. L., Gonzales, G. F., and Alfrey, C. P. Neocytolysis on descent from altitude: a newly recognized mechanism for the control of red cell mass. *Annals of Internal Medicine*, 134(8):652–656, 2001.

[142] Rich, I. N. and Kubanek, B. The effect of reduced oxygen tension on colony formation of erythropoietic cells in vitro. *British journal of haematology*, 52(4):579–588, 1982.

[143] Richards, F. M. and Knowles, J. R. Glutaraldehyde as a protein cross-linking reagent. *Journal of molecular biology*, 37(1):231–233, 1968.

[144] Risso, A., Turello, M., Biffoni, F., and Antonutto, G. Red blood cell senescence and neocytolysis in humans after high altitude acclimatization. *Blood Cells, Molecules, and Diseases*, 38 (2):83–92, 2007.

[145] Robertson, E. A. and Schultz, R. L. The impurities in commercial glutaraldehyde and their effect on the fixation of brain. *Journal of ultrastructure research*, 30(3-4):275–287, 1970.

[146] Rogers, H. M., Yu, X., Wen, J., Smith, R., Fibach, E., and Noguchi, C. T. Hypoxia alters progression of the erythroid program. *Experimental hematology*, 36(1):17–27, 2008.

[147] Rogers, S. C., Said, A., Corcuera, D., McLaughlin, D., Kell, P., and Doctor, A. Hypoxia limits antioxidant capacity in red blood cells by altering glycolytic pathway dominance. *The FASEB Journal*, 23(9):3159–3170, 2009.

[148] Sabirov, R. Z. and Okada, Y. ATP release via anion channels. *Purinergic signalling*, 1(4): 311–328, 2005.

[149] Sanchis-Gomar, F., Martinez-Bello, V. E., Domenech, E., Nascimento, A. L., Pallardo, F. V., Gomez-Cabrera, M. C., and Vina, J. Effect of intermittent hypoxia on hematological parameters after recombinant human erythropoietin administration. *European journal of applied physiology*, 107(4):429–436, 2009.

[150] Semenza, G. L. Mitochondrial autophagy: life and breath of the cell. *Autophagy*, 4(4):534–536, 2008.

[151] Semenza, G. L. Hypoxia-inducible factors in physiology and medicine. *Cell*, 148(3):399–408, 2012.

[152] Sheikh, H., Zhu, B., and Micheli-Tzanakou, E. Blood cell identification using neural networks. In *Proceedings of the IEEE 22nd Annual Northeast Bioengineering Conference*, pages 119–120. IEEE, 1996.

[153] Shih, S.-C. and Claffey, K. P. Hypoxia-mediated regulation of gene expression in mammalian cells. *International journal of experimental pathology*, 79(6):347–357, 1998.

[154] Sidney, L. E., Branch, M. J., Dunphy, S. E., Dua, H. S., and Hopkinson, A. Concise review: evidence for CD34 as a common marker for diverse progenitors. *Stem cells*, 32(6):1380–1389, 2014.

[155] Singh, P., Doshi, S., Spaethling, J. M., Hockenberry, A. J., Patel, T. P., Geddes-Klein, D. M., Lynch, D. R., and Meaney, D. F. N-methyl-D-aspartate receptor mechanosensitivity is governed by C terminus of NR2B subunit. *Journal of Biological Chemistry*, 287(6):4348–4359, 2012.

[156] Sinha, N. and Ramakrishnan, A. G. Automation of differential blood count. In *TENCON 2003. Conference on Convergent Technologies for Asia-Pacific Region*, volume 2, pages 547–551. IEEE, 2003.

[157] spectrum, I. https://spectrum.ieee.org/static/ai-vs-doctors, 2020. Accessed: 2020.03.11.

[158] Stamatoyannopoulos, G. Control of globin gene expression during development and erythroid differentiation. *Experimental hematology*, 33(3):259–271, 2005.

[159] Steinberg, M. H. and Brugnara, C. Pathophysiological-based approaches to treatment of sickle cell disease. *Annual Review of Medicine*, 54(1):89–112, 2003.

[160] Steinberg, M. H. and Rodgers, G. P. HbA2: biology, clinical relevance and a possible target for ameliorating sickle cell disease. *British journal of haematology*, 170(6):781–787, 2015.

[161] Suemori, S., Wada, H., Nakanishi, H., Tsujioka, T., Sugihara, T., and Tohyama, K. Analysis of hereditary elliptocytosis with decreased binding of eosin-5-maleimide to red blood cells. *BioMed research international*, 2015, 2015.

[162] Sutera, S. P. and Mehrjardi, M. H. Deformation and fragmentation of human red blood cells in turbulent shear flow. *Biophysical journal*, 15(1):1–10, 1975.

[163] Thom, C. S., Dickson, C. F., Gell, D. A., and Weiss, M. J. Hemoglobin variants: biochemical properties and clinical correlates. *Cold Spring Harbor perspectives in medicine*, 3(3):a011858, 2013.

[164] Tomari, R., Zakaria, W. N. W., Jamil, M. M. A., Nor, F. M., and Fuad, N. F. N. Computer aided system for red blood cell classification in blood smear image. *Procedia Computer Science*, 42: 206–213, 2014.

[165] Topol, E. J. High-performance medicine: the convergence of human and artificial intelligence. *Nature medicine*, 25(1):44, 2019.

[166] van den Akker, E., Satchwell, T. J., Pellegrin, S., Daniels, G., and Toye, A. M. The majority of the in vitro erythroid expansion potential resides in CD34- cells, outweighing the contribution of CD34+ cells and significantly increasing the erythroblast yield from peripheral blood samples. *haematologica*, 95(9):1594–1598, 2010.

[167] Vlaski, M., Lafarge, X., Chevaleyre, J., Duchez, P., Boiron, J.-M., and Ivanovic, Z. Low oxygen concentration as a general physiologic regulator of erythropoiesis beyond the EPO-related downstream tuning and a tool for the optimization of red blood cell production ex vivo. *Experimental hematology*, 37(5):573–584, 2009.

[168] von Lindern, M., Zauner, W., Mellitzer, G., Steinlein, P., Fritsch, G., Huber, K., Loǐ̂wenberg, B., and Beug, H. The glucocorticoid receptor cooperates with the erythropoietin receptor and c-kit to enhance and sustain proliferation of erythroid progenitors in vitro. *Blood, The Journal of the American Society of Hematology*, 94(2):550–559, 1999.

[169] Walker, H. K., Hall, W. D., and Hurst, J. W. *Peripheral Blood Smear–Clinical Methods: The History, Physical, and Laboratory Examinations*. Butterworths, 1990.

[170] Wang, D. N. Band 3 protein: structure, flexibility and function. *FEBS letters*, 346(1):26–31, 1994.

[171] Witt, A., Macdonald, N., and Kirkpatrick, P. Memantine hydrochloride, 2004.

[172] Zhao, B., Mei, Y., Yang, J., and Ji, P. Erythropoietin-regulated oxidative stress negatively affects enucleation during terminal erythropoiesis. *Experimental hematology*, 44(10):975–981, 2016.

[173] Zhao, M. and Li, L. Dissecting the bone marrow HSC niches. *Cell research*, 26(9):975–976, 2016.

[174] Zhu, Y. Y., Machleder, E. M., Chenchik, A., Li, R., and Siebert, P. D. Reverse transcriptase template switching: A SMART™approach for full-length cdna library construction. *Biotechniques*, 30(4):892–897, 2001.

Publications

Abay A.*, **Simionato G.**, Chachanidze R., Bogdanova A., Hertz L., Bianchi P., Van den Akker E., Von Lindern M., Leonetti M., Minetti G., Wagner C., Kaestner L., 2019. Glutaraldehyde - a subtle tool in the investigation of healthy and pathologic red blood cells. Front Physiol. doi: 10.3389/fphys.2019.00514.
*These authors contributed equally to this work.

Hertz L., Ruppenthal S., **Simionato G.**, Quint S., Kihm A., Abay A., Petkova-Kirova P., Boehm U., Weissgerber P., Wagner C., Laschke M. W., Kaestner L., 2019. The evolution of erythrocytes becoming red in respect to fluorescence. Front Physiol. doi: 10.3389/fphys.2019.00753.

Bogdanova A., Kaestner L., **Simionato G.**, Wickrema A., Makhro A., 2020. Heterogeneity of red blood cells: causes and consequences. Front Physiol. Accepted for publication. doi: 10.3389/fphys.2020.00392.

Makhro A., Hegemann I., Seiler E., **Simionato G.**, Claveria V., Bogdanov N., Sasselli C., Torgeson P., Kaestner L., Manz M. G., Goede J. S., Gassman M., Bogdanova A, 2020. A pilot clinical phase II trial MemSID: Acute and durable changes of red blood cells of sickle cell disease patients on memantine treatment. Submitted to: eJHaem.

Acknowledgments

Appendix

Representative RBCs in three phases of the trial
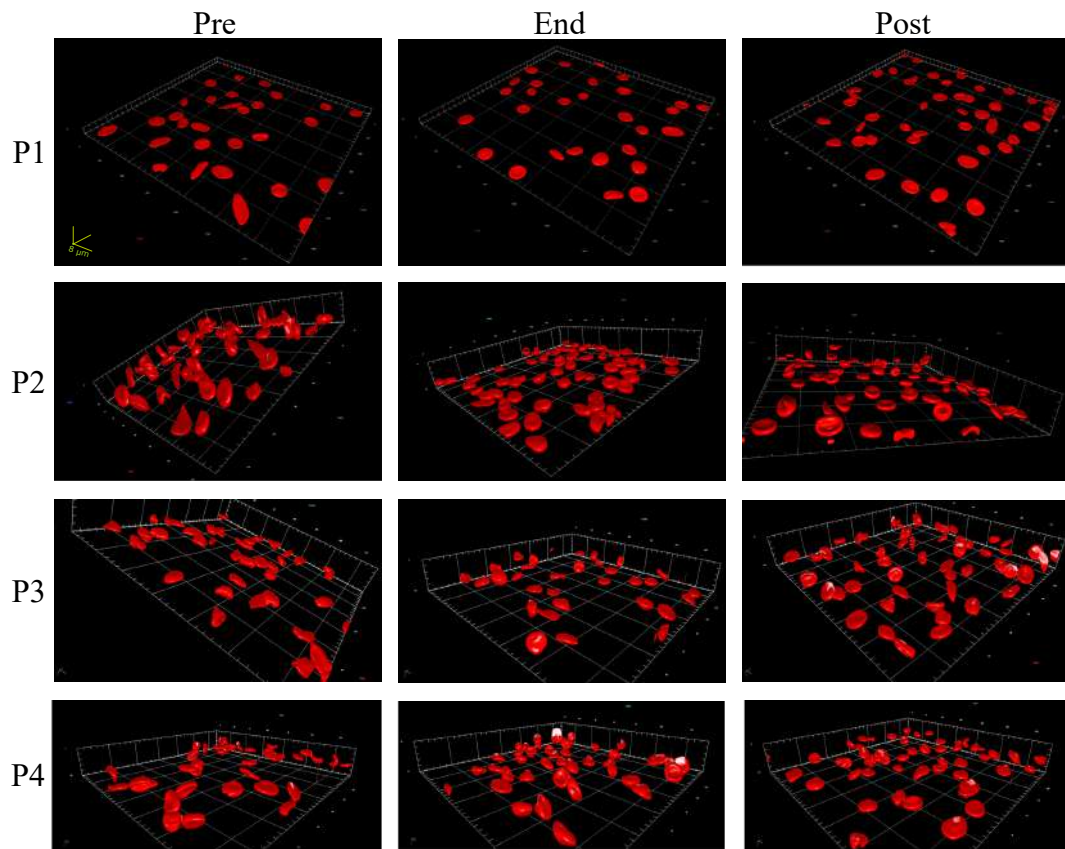
Figure 80: Example 3D confocal reconstruction of the 4 SCD patients finalizing MemSID trial. Representative images at different time points are illustrated. Pre=pre-treatment phase, End=end of treatment, Post=post-treatment. P=patient.

3D SDE shapes of RBCs and corresponding SHA for correct allocation by the ANN
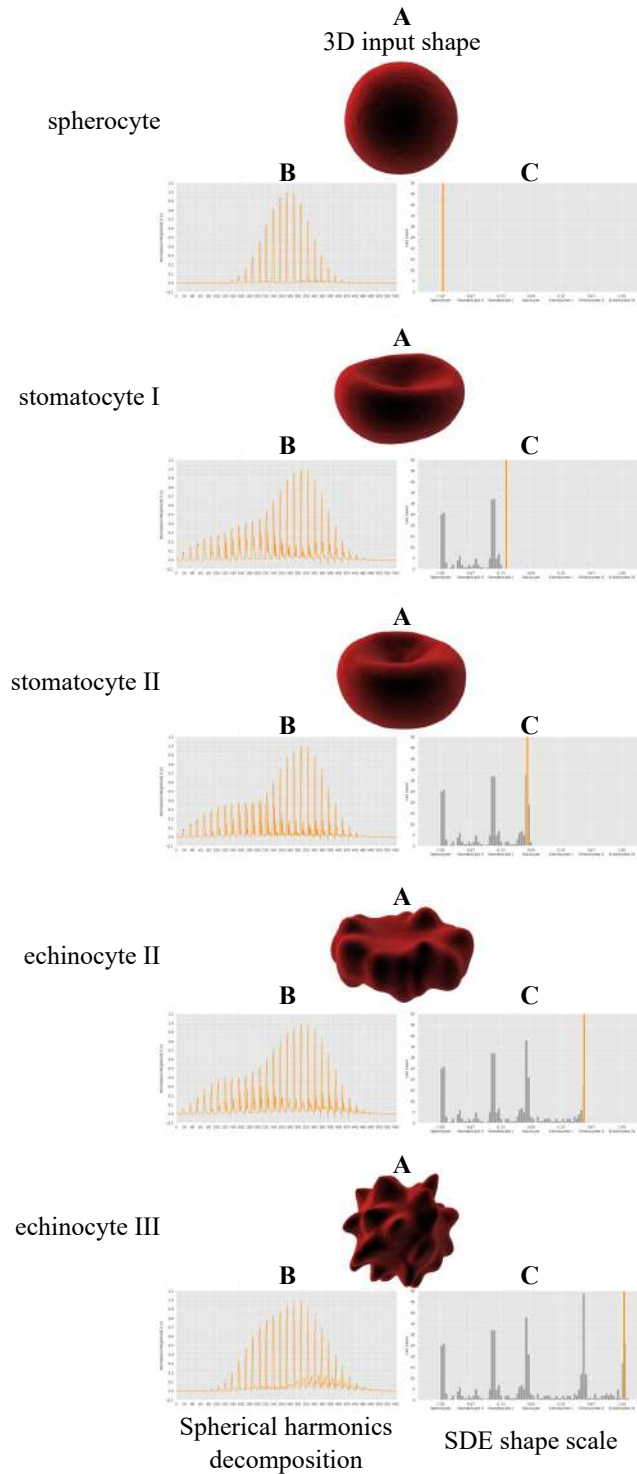
Figure 81: 3D reconstruction of healhty RBCs in different SDE configurations and corresponding SHA spectrum and automated SDE scale position. Note for each cell shape 3D reconstruction (A) and the corresponding SHA spectrum details are shown (B), highlighting different frequencies for each shape type. (C) The corresponding automated placement by the ANN assigning a score on the SDE scale is shown (yellow line) and occurs according to the SHA spectrum. Grey lines represent the position assigned to previous recognized cells during the automated process.

Curriculum vitae

The curriculum vitae was removed from the electronic version of the doctoral thesis for reasons of data protection.